Martian Chloride Salts in the Thermal Infrared

by

Jonathon Ryan Hill

A Dissertation Presented in Partial Fulfillment
of the Requirements for the Degree
Doctor of Philosophy

Approved March 2022 by the
Graduate Supervisory Committee:

Philip R. Christensen, Chair
Thomas G. Sharp
Steven W. Ruff
Molly N. Simon
Joseph G. O'Rourke

ARIZONA STATE UNIVERSITY

May 2022

ABSTRACT

Understanding the history of water on Mars is one of the highest priority goals of the international Mars exploration community. Water would have played a key role in any potential abiogenesis in the past and will play a key role in the future human exploration of the planet. Chloride salts are an indicator of past hydrologic activity in the Martian geologic record and have the potential to preserve fluid inclusions and organic material within their crystal structure over geologic timescales. This dissertation will describe an innovative method for identifying chloride salts on the Martian surface, explore the implication of their distribution within Early Noachian terrains, and document important opportunistic discoveries made in the process.

Decorrelation stretched Thermal Emission Imaging System (THEMIS) infrared images have long been used to identify chloride salts on Mars, but the process has been time-consuming, subjective, and qualitative. By analyzing the entire THEMIS dataset, acquired over more than twenty years at Mars, a globally-applicable covariance matrix was calculated that describes the geologic diversity of the Martian surface. This covariance matrix allows all THEMIS daytime infrared images to be translated into globally-consistent decorrelation stretch and principal component images, enabling an automatic, objective, and quantitative method for identifying chloride salts.

A new global survey located 1,605 chloride salt deposits across the Martian surface, a significant increase over previous surveys. In particular, the 257 deposits in Early Noachian terrains have characteristics that indicate they formed contemporaneously with the surrounding terrain. In addition, a chloride salt formation was identified on the floor

of Ares Vallis with a unique three-dimensional structure that has been interpreted as an exposed chloride salt diapir, which would indicate the presence of a significant subsurface chloride salt layer.

By improving our understanding of the distribution and diversity of chloride salts on the Martian surface, this work has provided future investigators with new tools and avenues of research to explore the history of water on Mars.

DEDICATION

This dissertation is dedicated to James B. Callaghan, Jr.

ACKNOWLEDGMENTS

This work was made possible by the support, encouragement, collaboration, mentorship, and friendship of the entire staff of the ASU Mars Space Flight Facility over the last seventeen years, which includes more individuals than could possibly be listed here. I deeply appreciate the trust they placed in me to operate our precious instruments throughout the solar system. Specifically, Margaret Hufford and Paige Valderrama Graff for first hiring me as a student worker in the Mars Education group, and Dr. Philip Christensen and Greg Mehall for believing that the kid in the mailroom could contribute to their world-class team.

I would not have been able to complete this odyssey without the added encouragement and friendship of multiple generations of fellow graduate students, both from the Christensen Research Group and the wider School of Earth and Space Exploration community, which are also too numerous to list. Without their support over the last twelve years, it would have been impossible to pursue a doctorate degree part-time while also working full-time.

And finally, I want to thank my family for supporting me throughout this entire journey, which lasted much longer than originally intended.

TABLE OF CONTENTS

Page

CHAPTER Page

CHAPTER Page

CHAPTER Page

CHAPTER Page

CHAPTER Page

CHAPTER Page

Page

APPENDIX Page

LIST OF TABLES

LIST OF FIGURES

Figure Page

Figure Page

Figure Page

Figure Page

Figure Page

Figure Page

CHAPTER 1

INTRODUCTION

Understanding the history of water on Mars is one of the highest priority goals of the international Mars exploration community. Water is required for all known forms of life and would have played a key role in any potential abiogenesis on the early surface of Mars. In the future, it will play a key role in the human exploration of the planet, providing in-situ drinking water, air, and fuel for early explorers.

Chloride salts are a strong indicator of past hydrologic activity in the Martian geologic record. They have the potential to preserve fluid inclusions within their crystal structure over geologic timescales, which would provide a record of early surface conditions and possibly pre-biotic chemistry. This dissertation will describe an innovative method for quantitatively identifying chloride salts on the Martian surface, explore the implication of their distribution within Early Noachian terrains, describe a unique three-dimensional chloride salt structure in Ares Vallis, and document important opportunistic discoveries that were made in the process.

Decorrelation stretched Thermal Emission Imaging System (THEMIS) infrared images have long been used to identify chloride salts on Mars, but the process has been time-consuming, subjective, and qualitative. By analyzing the entire THEMIS dataset, acquired over more than twenty years at Mars, a globally-applicable covariance matrix was calculated that describes the geologic diversity of the Martian surface in the infrared wavelengths. This covariance matrix enabled the calculation of a globally-applicable eigenvector matrix, which can be used to rotate THEMIS daytime infrared radiance

image data into globally-consistent decorrelation stretch images. The same eigenvector matrix can also be used to calculate globally-consistent principal component images, which were used to develop an automatic, objective, and quantitative method for identifying Martian chloride salts.

A new global survey was conducted using this method, which located 1,605 chloride salt deposits across the Martian surface, a significant increase over the 642 deposits from previous surveys. A total of 257 deposits are located in Early Noachian terrains and have characteristics that indicate they formed contemporaneously with the surrounding terrain.

In addition, a newly-identified chloride salt formation was located on the floor of Ares Vallis, which is unusual since the vast majority of chloride salt deposits are instead found in the southern highlands. This formation has a unique three-dimensional structure, which is significantly different from the superficial two-dimensional structures of all other identified chloride salt deposits. The three-dimensional polygonal fracturing and meter-scale layering observed in this formation led to its interpretation as an exposed chloride salt diapir, which was only revealed due to the erosion of Ares Vallis. The existence of a chloride salt diapir would necessarily require a significant subsurface chloride salt layer in the area, which would be over a kilometer below the surrounding Early Noachian terrain, indicating that it likely formed during the Pre-Noachian period. This conclusion is supported by the findings of previous researchers studying nearby regions, who came to the same conclusion based on independent evidence.

In the process of completing this work, a previously undescribed population of 4,024 small young impact craters surrounded by low thermal inertia ejecta deposits were identified scattered across the Martian surface. A global survey cataloged their locations

and a point density analysis revealed these craters are primarily located downrange of oblique young rayed craters. This led to the conclusion that they are the result of relatively low-velocity secondary impacts, which did not have enough energy to disperse their fine particulate ejecta over large areas.

Additionally, the completed THEMIS Daytime Infrared Global Mosaic, which served as the foundation of this work, was printed on a basketball court-sized vinyl mat so students and the general public could physically explore the full extent of the map. Over 8,000 participants have explored the "Walk on Mars" map so far, with either the assistance of volunteer planetary scientists or using a variety of self-guided tours. An educational assessment study was conducted and demonstrated that the "Walk on Mars" map and its associated lessons are effective tools for teaching junior high school students about the geography of Mars and the history of Mars exploration. However, future events would benefit from including a pre-lesson utilizing an augmented reality sandbox, to help students develop a more thorough understanding of colorized topography.

The following chapters will describe these efforts and how the various conclusions were reached. Hopefully, this dissertation will provide future investigators with new tools and avenues of research to explore the distribution and diversity of chloride salts on the Martian surface and their relationship with the history of water on Mars.

CHAPTER 2

VISUALIZING THE MAXIMUM COMPOSITIONAL VARIATION WITHIN THE THEMIS MULTISPECTRAL THERMAL INFRARED DATASET

2.1 Introduction

Decorrelation stretched (DCS) images are commonly used in the terrestrial and planetary remote sensing communities to visualize compositional variation within multispectral images. The DCS process is based on Principal Component Analysis (PCA), which seeks to separate information among the image bands that is highly correlated from the information that is less correlated. To create a DCS image, three image bands from a multispectral image are selected and subjected to PCA, which results in three principal component images: the first band contains the highly-correlated information, the second band contains information that is uncorrelated with the information in the first band but correlated amongst itself, and the third band contains the remaining image information. These three principal component images can then be assigned to the Red-Green-Blue (RGB) channels of an 8-bit color image to visualize the relationship between the highly-correlated, less-correlated, and uncorrelated image information.

The Thermal Emission Imaging System (THEMIS) has acquired thermal infrared (IR) images of the Martian surface for over 20 years, representing approximately one Martian decade. These infrared images contain ten spectral bands, although only eight bands are useful for analyzing surface compositions. The THEMIS Science Team has traditionally used DCS images to visualize spectral variation within these images, but only

qualitatively. It has not been possible to use THEMIS IR DCS images for quantitative analysis because the DCS process uses covariance matrices calculated on a per-image basis, leading to slight differences between DCS images that are not obvious or easy to characterize.

The goal of this work is to calculate a globally-applicable covariance matrix, which can be used in the calculation of DCS images to ensure that they are directly comparable and can therefore be used for quantitative analysis. A global covariance matrix will also identify the ideal three-band combination for THEMIS DCS images, which will capture the most compositional variation possible within a three-band set. This will give future researchers an easier method of accessing some of the compositional information contained within the massive THEMIS IR dataset.

2.2 Instrument and Dataset

2.2.1 Instrument Description

THEMIS is one of three science instruments on the 2001 Mars Odyssey spacecraft, which launched on April 7th, 2001 and entered orbit around Mars on October 24th, 2001. The instrument consists of two multispectral imaging subsystems: a ten-band thermal infrared imager and a five-band visible/near-infrared imager. The thermal infrared imager operates as a pushbroom scanner that acquires data at a nominal surface spatial resolution of 100m/pixel using an uncooled 320×240 pixel microbolometer array covered by ten ~1-μm-bandwidth strip filters (Figure 2.1) centered at nine different wavelengths between 6.8μm and 14.9μm (Christensen et al., 2004). The bandpasses are plotted in Figure 2.2 and quantitatively summarized in Table 1.

Over the first 20 years of its mission, which represents approximately one Martian decade, THEMIS has acquired a global dataset of over 300,000 multispectral infrared images.

Bands 1 and 2 cover the same spectral range and use the same filter material on two adjacent detector strips. The instrument was designed this way due to the detector's relatively low signal-to-noise ratio (SNR) in that wavelength range and the importance of a carbonate spectral feature in the same range. By averaging the two bands on the ground, the SNR of the combined spectral band can be improved by a factor of $\sqrt{2}$. However, this averaging is not performed in any of the standard THEMIS data products, so the user must perform this averaging themselves after map projecting the two bands. In this work, except where specified otherwise, "Band 2" will always represent the average of Bands 1 and 2.

Band 10 is spectrally located on the primary infrared absorption feature of carbon dioxide to obtain temperature measurements of the Martian atmosphere, which results in the Martian surface being completely obscured in this band.

Therefore, THEMIS infrared images only contain eight spectral bands that can be used for compositional analysis of the surface: the average of bands 1 & 2 and bands 3-9. An example of a 10-band THEMIS image is shown in Figure 2.3, which demonstrates the overall highly-correlated nature of the information in these closely-spaced spectral bands.

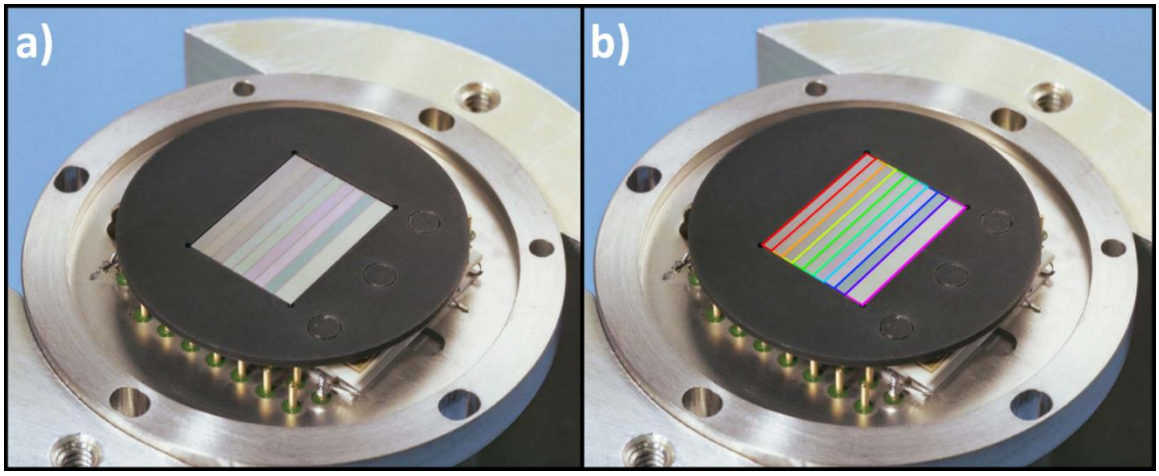

Figure 2.1. THEMIS infrared sensor: (a) THEMIS infrared sensor and spectral filters, (b) THEMIS infrared sensor with the spectral filters outlined in wavelength order (modified from Christensen et al., 2004).

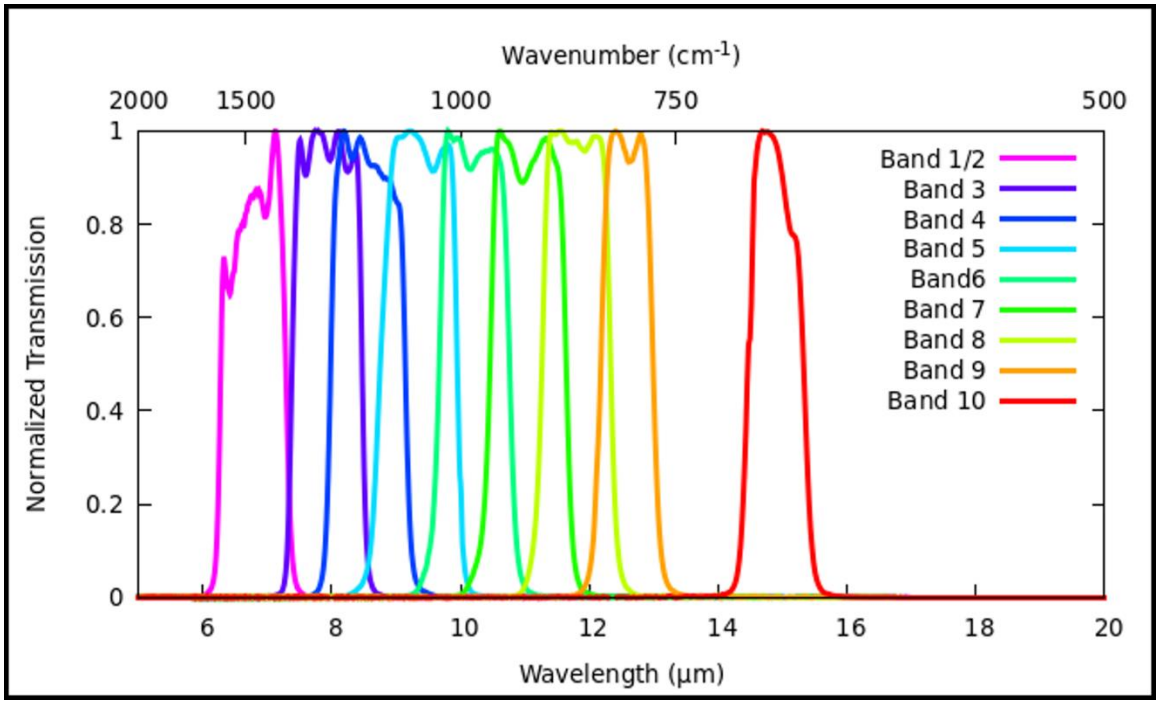

Figure 2.2. THEMIS infrared spectral bandpasses colored by wavelength order, consistent with Figure 2.1b (modified from Christensen et al., 2004).

Table 2.1. THEMIS infrared spectral band characteristics (modified from Christensen et al., 2004)

Band	Center Wavelength (µm)	Band Width (FWHM) (µm)	SNR
1	6.78	1.01	33
2	6.78	1.01	34
avg(1+2)	6.78	1.01	47
3	7.93	1.09	104
4	8.56	1.16	163
5	9.35	1.20	186
6	10.21	1.10	179
7	11.04	1.19	193
8	11.79	1.07	171
9	12.57	0.81	132
10	14.88	0.87	128

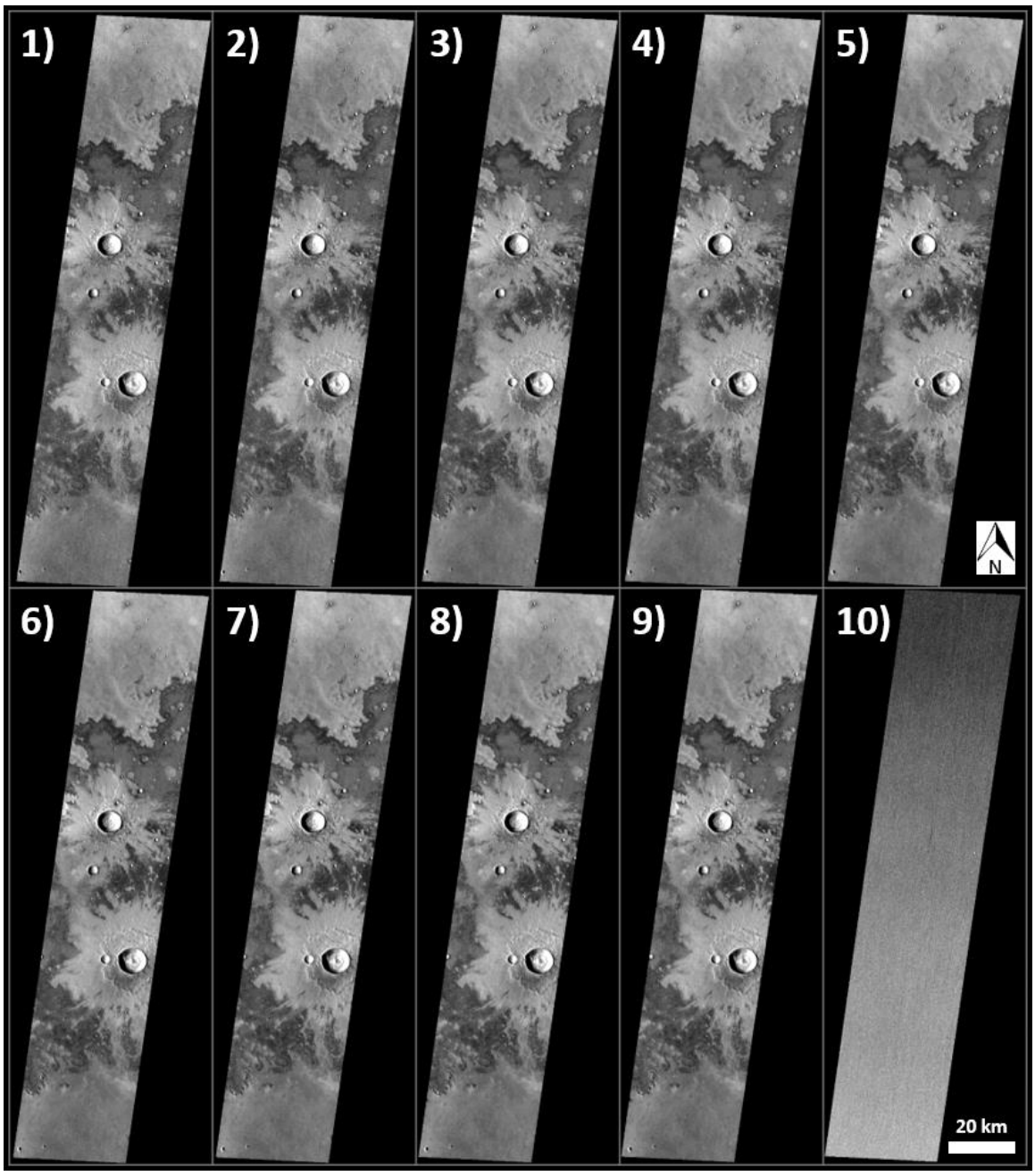

Figure 2.3. THEMS 10-band infrared image (I02685009) showing the data's highly-correlated nature, except band 10, which measures the CO_2 absorption feature.

2.2.2 Dataset Description

The THEMIS infrared images used in this study to derive a global covariance matrix were restricted to late-afternoon images acquired at full-resolution with all ten bands between 60°N and 60°S. This latitude range was selected because images with CO2 or H2O ice significantly skew the band-to-band covariance calculations, which effectively washes out all the variations in the non-ice surface materials when decorrelation stretches are applied to the images.

Additionally, only images with minimum surface brightness temperatures of 225K or greater were used, because the radiance correction in the standard THEMIS processing pipeline (Bandfield et al., 2004) often fails for colder images, resulting in decorrelation stretched images over-emphasizing sunlit and shadowed slopes. And finally, any images that failed during the standard THEMIS processing pipeline due to data dropouts, stray light artifacts, unusually high instrument noise, focal plane temperature instability, or any other issues were removed from the analysis. This resulted in a total of 29,922 images being available for this analysis.

2.2.3 Analytical Tool Descriptions

The Java Mission-planning and Analysis for Remote Sensing (JMARS) geospatial information system (http://jmars.asu.edu) (Christensen et al., 2009) was used to conduct THEMIS image reconnaissance and identify appropriate example images.
Image data were map-projected and analyzed using the Integrated Software for Imagers and Spectrometers (ISIS) maintained by the United States Geologic Survey's Astrogeology Science Center (http://isis.astrogeology.usgs.gov) [e.g., Anderson et al.,

2004; Becker et al., 2013], as well as the DaVinci generic array processing tool maintained by Arizona State University's Mars Space Flight Facility (http://davinci.asu.edu) [e.g., Edwards et al., 2011a,b].

2.3 Methods

2.3.1 The Decorrelation Stretch

The decorrelation stretch (DCS), which is based on principal component analysis (PCA), is a common technique used in remote sensing to emphasize and visualize subtle spectral variations in multispectral images.

Principal Component Analysis was independently developed by Karl Pearson (Pearson., 1901) and Harold Hotelling (Hotelling, 1933; Hotelling, 1936) as a way to transform a multivariate dataset into a new coordinate system such that the first dimension lies along the vector of greatest variance within the dataset and the subsequent dimensions lie along the vector of the greatest remaining variance while also remaining orthogonal to the previously-defined dimensions. This process has the effect of decorrelating, to the greatest extent possible, data that is otherwise highly correlated.

Taylor (1973) recognized that once a dataset is decorrelated by rotation to its principal component axes and equalizing the variances, any additional rotations to other coordinate systems do not re-introduce correlation to the data. Soha and Schwartz (1978) then determined that for multivariate (or multispectral/multiband) remote sensing images, simply rotating the data back to the original wavelength-based coordinates is the easiest way to visualize and interpret the results of the decorrelation process (Alley, 1996).

Gillespie et al. (1986) described the implementation of a decorrelation stretch on modern multiband digital remote sensing images, including images from the Landsat Multispectral Scanner System (MSS) and NASA's airborne Thermal Infrared Multispectral Scanner (TIMS). The decorrelation stretch process proved to be particularly useful for multiband remote sensing data, because the closely-spaced wavelength bands of most remote sensing instruments result in highly-correlated image data.

This method was later adapted and applied to THEMIS infrared images by Edwards et al. (2011a,b). The THEMIS standard data products include DCS images based on the band combinations 8/7/5, 9/6/4, and 6/4/2 (Murray, 2020). These band combinations were chosen early in the mission through a process of trial-and-error and a subjective determination of which combinations resulted in the most useful DCS images. At the time, a thorough study to identify the optimal DCS band combination that would display the maximum possible compositional variation using only a three-band set was not possible, since only a small percentage of the Martian surface had been imaged.

2.3.2 THEMIS Data Pre-Processing

Before performing a decorrelation stretch on a THEMIS IR image, it is necessary to perform a few instrument-specific pre-processing steps that will ultimately result in higher quality DCS images that are easier to interpret.

The pre-processing begins with the map-projected calibrated spectral radiance image data, which is referred to as the "GEO" product in the THEMIS standard data releases to NASA's Planetary Data System (PDS) (Murray, 2020). An example of a GEO data product is shown in Figure 2.3.

Because the THEMIS infrared imager is a pushbroom sensor with discrete filters, and the Martian surface is slowly rotating underneath the spacecraft during image acquisition, the resulting image bands do not perfectly overlap with each other after they have been map-projected. This can introduce significant artifacts to a DCS image, because pixels along the image edges can have spectral radiance values in some bands, but null values in others.

This issue can be solved by only using pixels that have non-null values in every band. Figure 2.4 shows the image pixels in each band of Figure 2.3 that have null values in at least one band, and therefore must be trimmed off. The offset between the non-overlapping pixels in each band is due to the rotation of Mars during images acquisition and the order in which the bands are acquired. Figure 2.5 shows all ten bands once these non-overlapping pixels have been removed, which preserves the vast majority of the original image data.

Next, the first 400 lines of the THEMIS infrared images must be set to null to remove potential artifacts caused by an internal reflection within the THEMIS infrared imager's optics (Bandfield et al., 2004), as shown in Figure 2.6. While these "ghosts" are very rarely detectable in the spectral radiance data (ex: Figure 2.3), the DCS process greatly exaggerates them because they are essentially uncorrelated noise. For example, Figure 2.7 shows the three standard DCS products for THEMIS image I05414023. All three DCS images contain significant artifacts related to the "ghost" noise within the first 400 lines. In this case, the noise is easily identifiable because it produces particularly bright DCS colors that slightly shift position depending on which bands are used as inputs to the DCS process.

The “ghost” issue impacts DCS images to varying degrees and it is difficult to automatically identify which images, or even which band configurations, have been significantly affected. For example, Figure 2.8 shows the three standard DCS products for image I02685009. The first 400 lines appear unaffected in the DCS 875 and DCS 964 images, but the DCS 642 image shows some slight “ghost” noise along the image’s top-left corner, which manifests as increased values in the green band of the DCS RGB image.

Because of this variability, users must make a subjective determination regarding whether the first 400 lines of a THEMIS IR DCS image should be analyzed or not. The first 400 lines of each THEMIS IR image are included in the standard DCS data products so that users can make this determination for themselves. However, for this study, the first 400 lines of each IR image will be set to null before the covariance matrix is calculated to prevent the “ghost” noise from skewing the covariance calculations.

Finally, users must decide how to use the standard THEMIS “white noise removal”, or “WNR”, algorithm. This algorithm is designed to remove, or at least reduce, completely uncorrelated pixel-level noise throughout all image bands, as documented by Nowicki et al., (2013). The use of the WNR algorithm significantly impacts the calculation of DCS images, because the DCS process is inherently designed to emphasize uncorrelated data.

By empirical trial and error, the THEMIS Science Team determined that the best-quality DCS images are produced using image data that has had the WNR algorithm applied to it, but with the covariance matrix calculated from the unaltered spectral

radiance image data, or “RAD” data, before the WNR algorithm was applied (Edwards et al., 2011a,b).

Figure 2.9 shows the results of performing a decorrelation stretch on WNR image data, using both the RAD and WNR covariance matrices. Using the WNR covariance matrix causes the remaining random pixel-level noise to be over-emphasized to a distracting degree. The standard THEMIS DCS data products use WNR image data and the RAD covariance matrix, as shown in Figure 2.9a. In this work, we calculate both the globally-applicable RAD and WNR covariance matrices so users can determine how to calculate their own globally-consistent THEMIS DCS images.

Once these pre-processing steps have been applied to the THEMIS IR image data, it is ready for the DCS process.

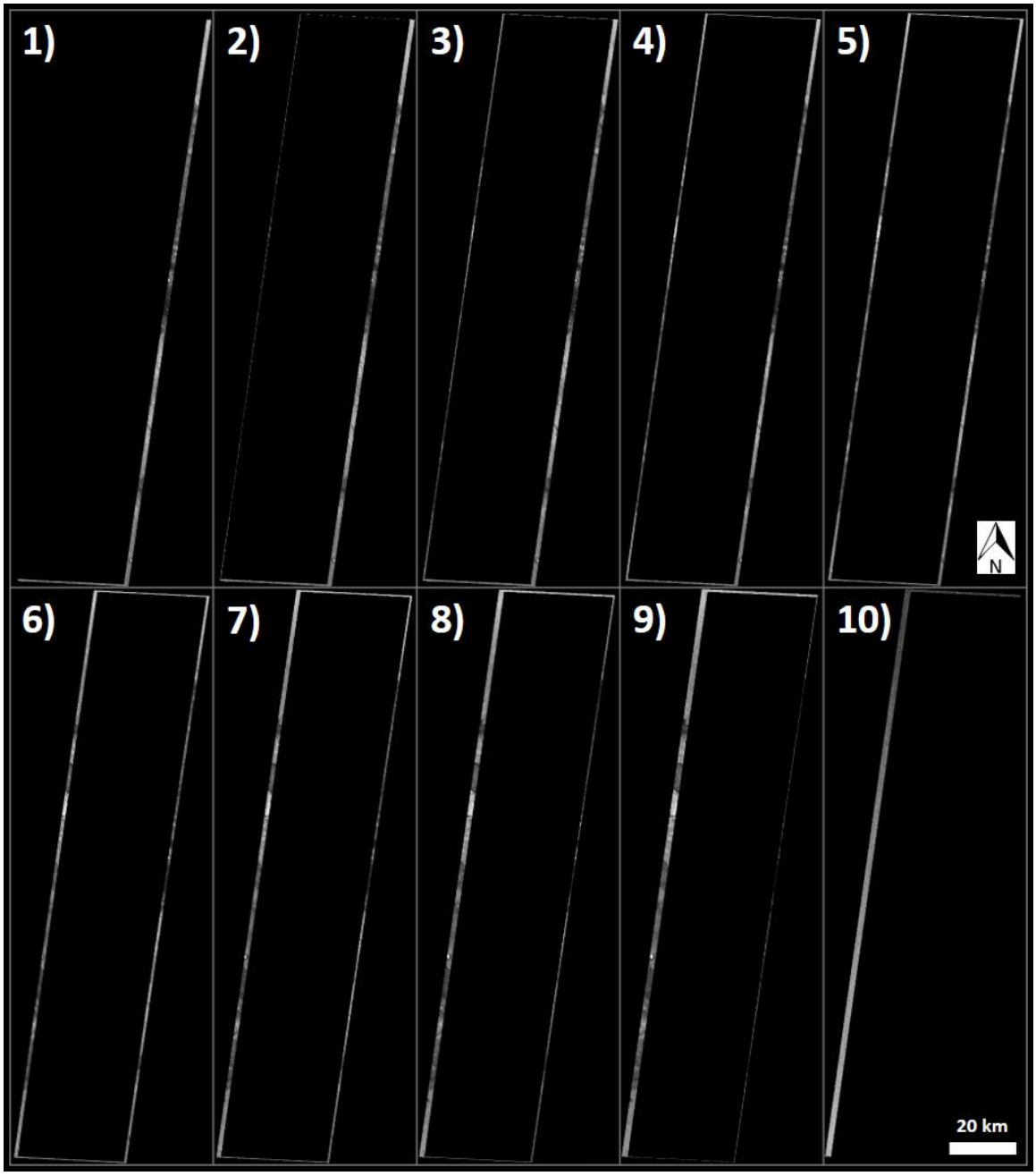

Figure 2.4. THEMS 10-band infrared image (I02685009) showing image pixels containing null values in at least one other band.

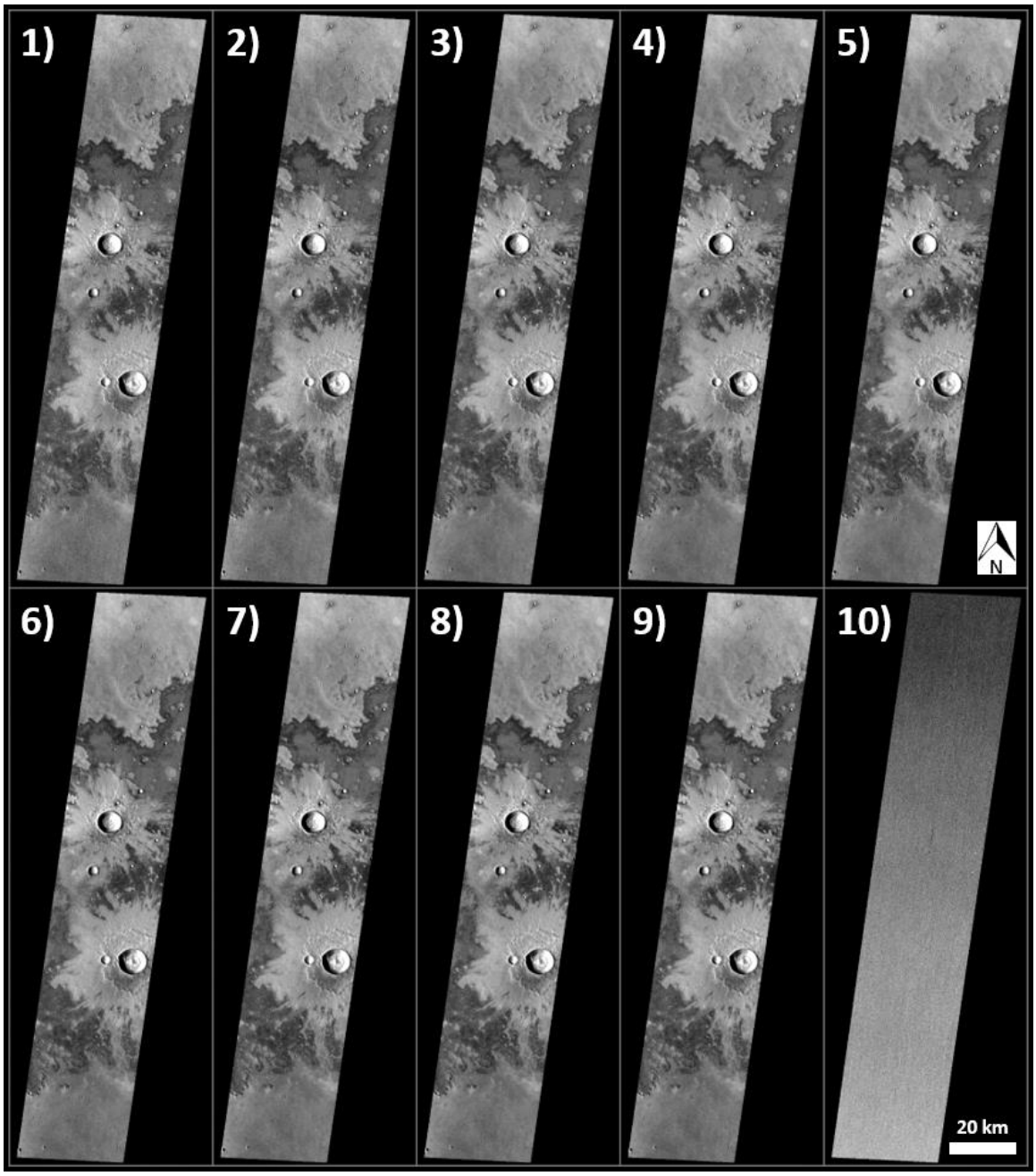

Figure 2.5. THEMS 10-band infrared image (I02685009) showing only image pixels containing data in all ten bands, which preserves the vast majority of the original image data.

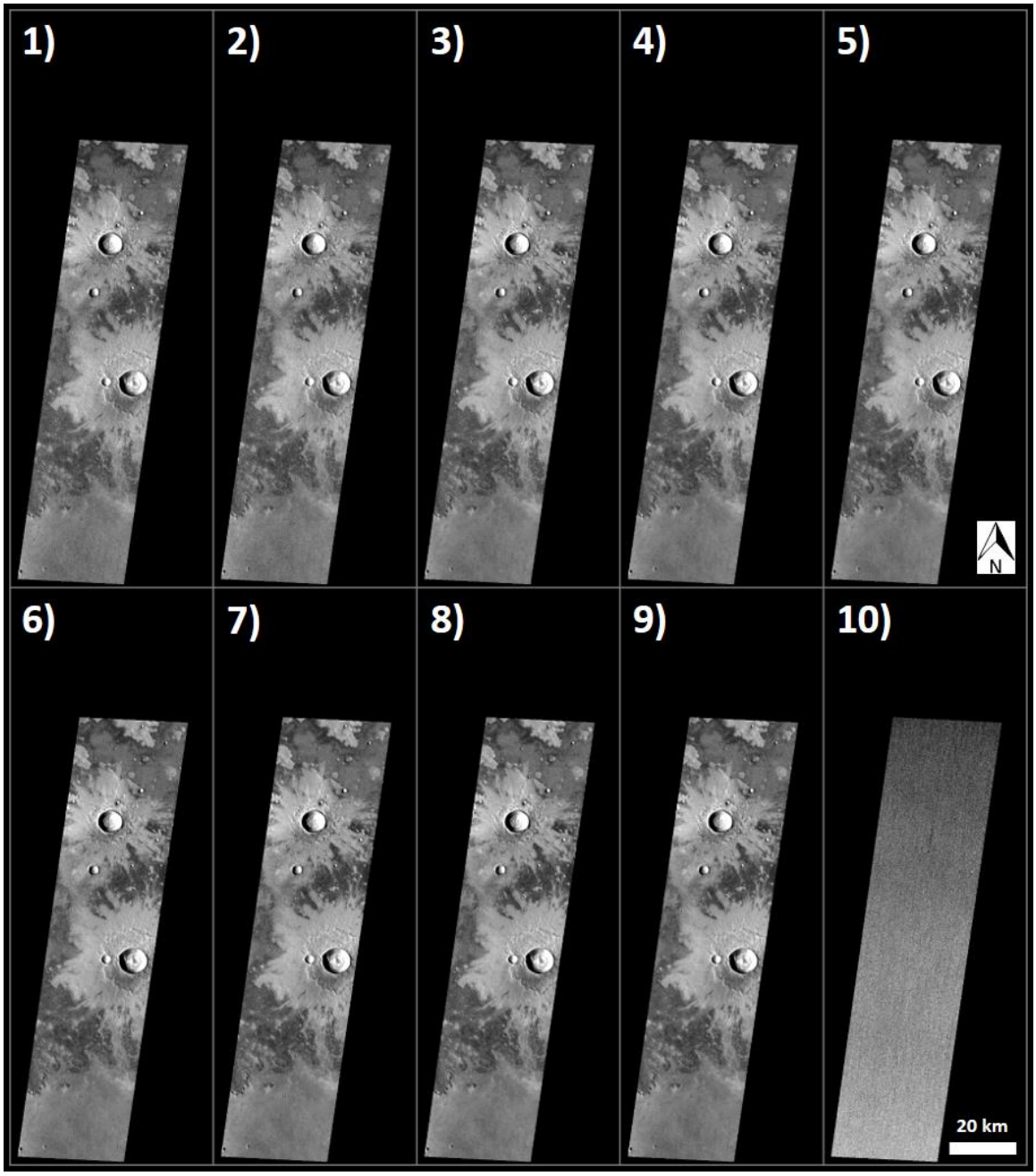

Figure 2.6. THEMS 10-band infrared image (I02685009) showing only image pixels that contain data in all ten bands, with the first 400 lines removed to eliminate DCS artifacts due to the THEMIS-specific uncorrectable internal reflection noise (a.k.a. “ghost”).

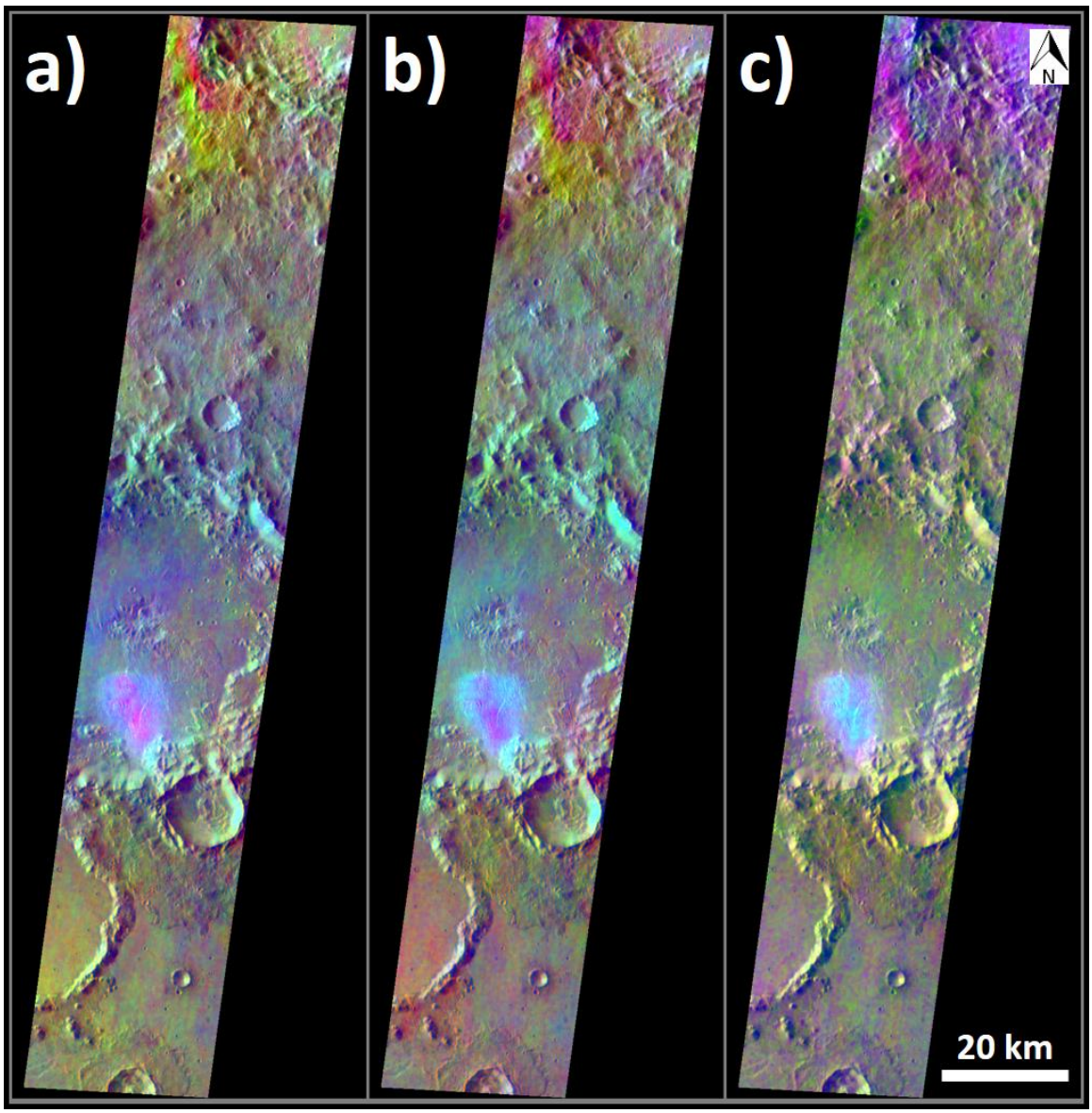

Figure 2.7. Standard THEMIS 3-band DCS products for image I05414023 with σ = 50, including the "ghost" artifacts at the start of the images: (a) DCS 875, (b) DCS 964 and (c) DCS 642.

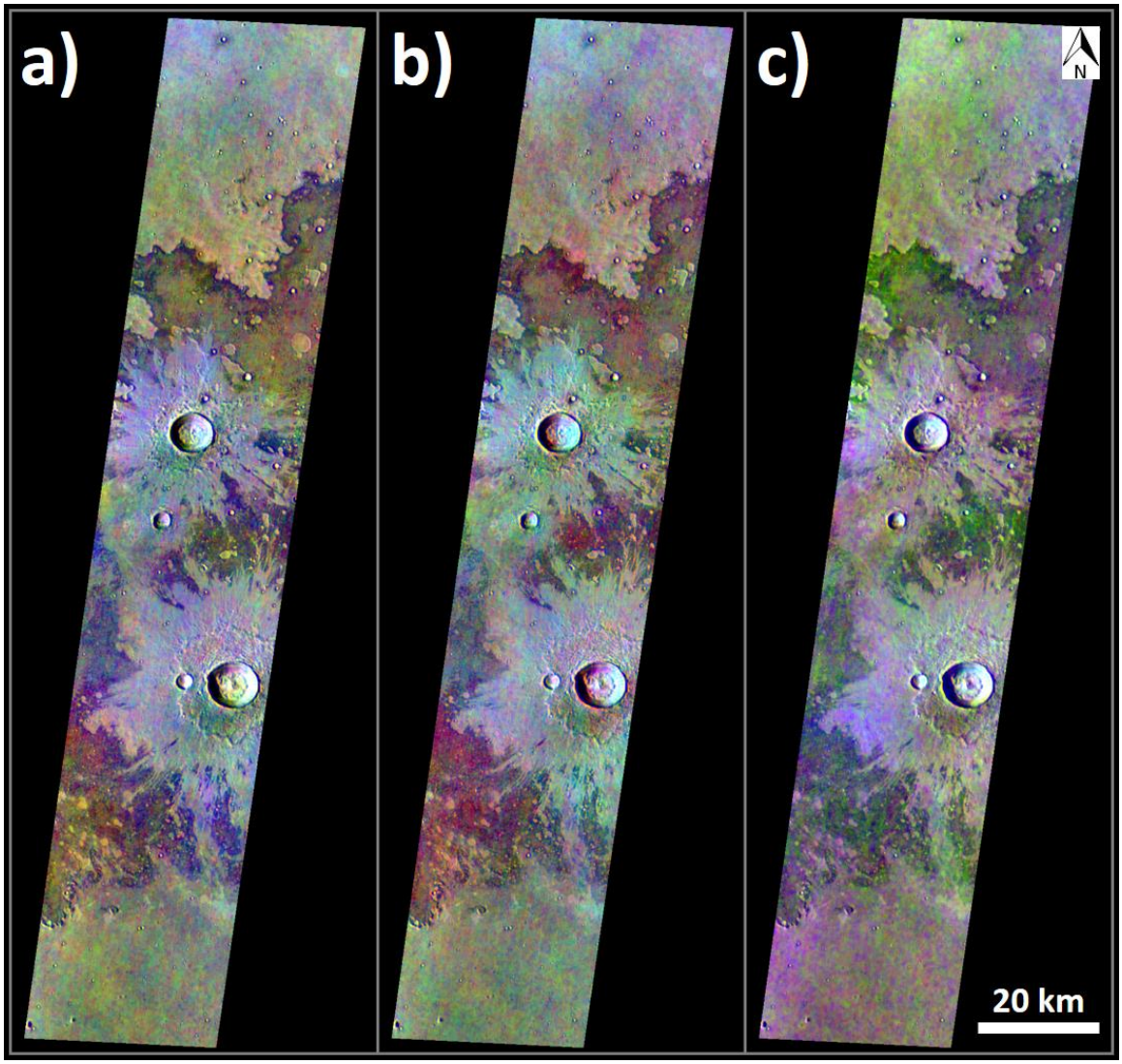

Figure 2.8. Standard THEMIS 3-band DCS products for image I02685009 with σ = 50, including only minimal "ghost" artifacts: (a) DCS 875, (b) DCS 964 and (c) DCS 642.

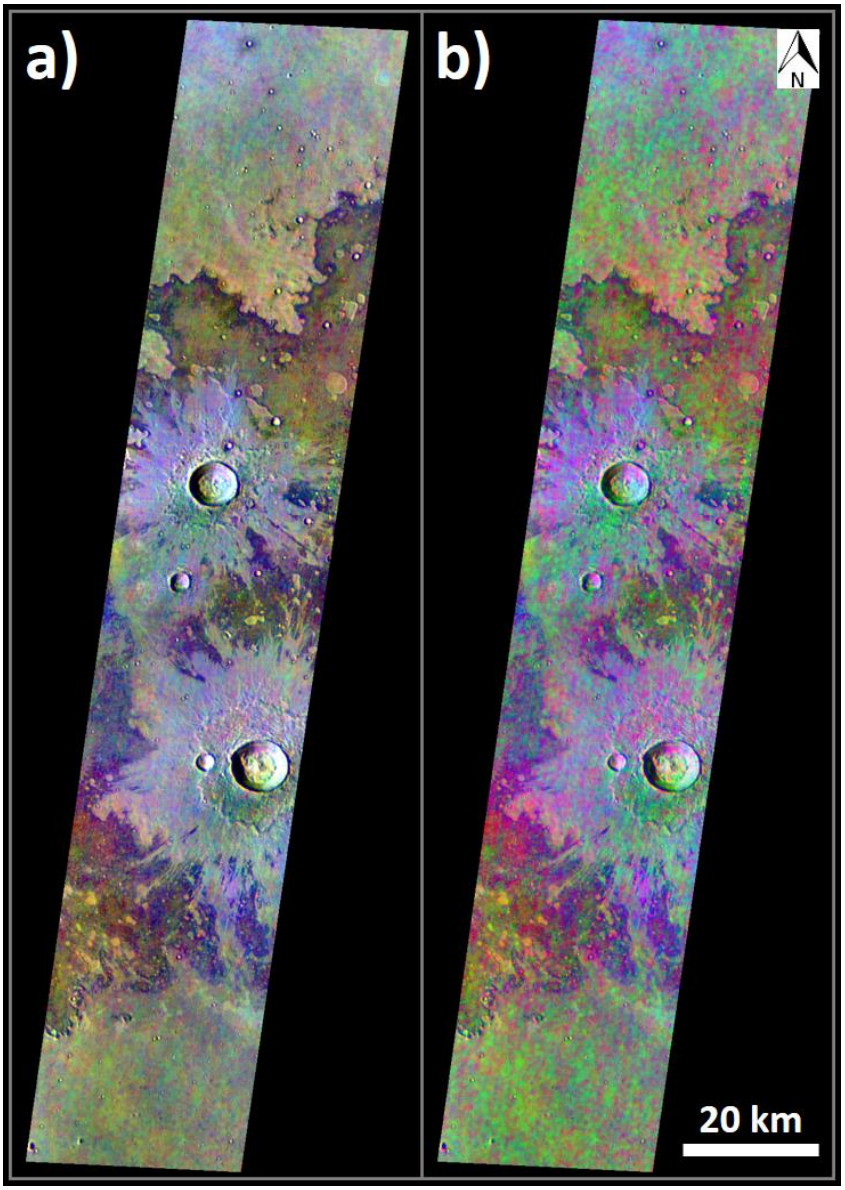

Figure 2.9. THEMIS DCS 875 of image I02685009 calculated using WNR image data along with: (a) the RAD covariance matrix; and (b) the WNR covariance matrix.

2.3.3 Calculating a Decorrelation Stretch Image

Calculating a decorrelation stretch image begins with the input data, which is often a multiband remote sensing image. This input image can be treated as a three-dimensional matrix, where each XY plane represents a two-dimensional image from a single spectral band and the Z dimension represents the numbers of spectral bands within the image. This organizational framework is illustrated in Figure 2.10.

The decorrelation stretch is based on the relationship between the values of a specific pixel, defined by an (x,y) coordinate, across different spectral bands in the z-dimension. The relationship between pixels within a particular XY plane is not relevant. Therefore, to greatly simplify the linear algebra calculations, it helps to reorganize the data into a two-dimensional matrix with dimensions defined as Z × (X*Y), where each row vector contains the values of a specific image pixel (j) in each of the available bands (i). This reorganization does not affect the decorrelation process because it only changes the relationship between pixels within each XY plane. However, it will need to be reversed at the end in order to properly interpret the results of the DCS process.

The result of this reorganization is a matrix A with dimensions i × j, where j >> i, as shown in Equation 2.1.

$$A = \begin{bmatrix} a_{1,1} & \cdots & a_{i,1} \\ \vdots & \ddots & \vdots \\ a_{1,j} & \cdots & a_{i,j} \end{bmatrix} \quad \text{Eq. 2.1}$$

Before a decorrelation stretch is calculated, the input data should be normalized, as described by Equation 2.2. This will prevent the image statistics from being skewed if the input bands have significantly different variances.

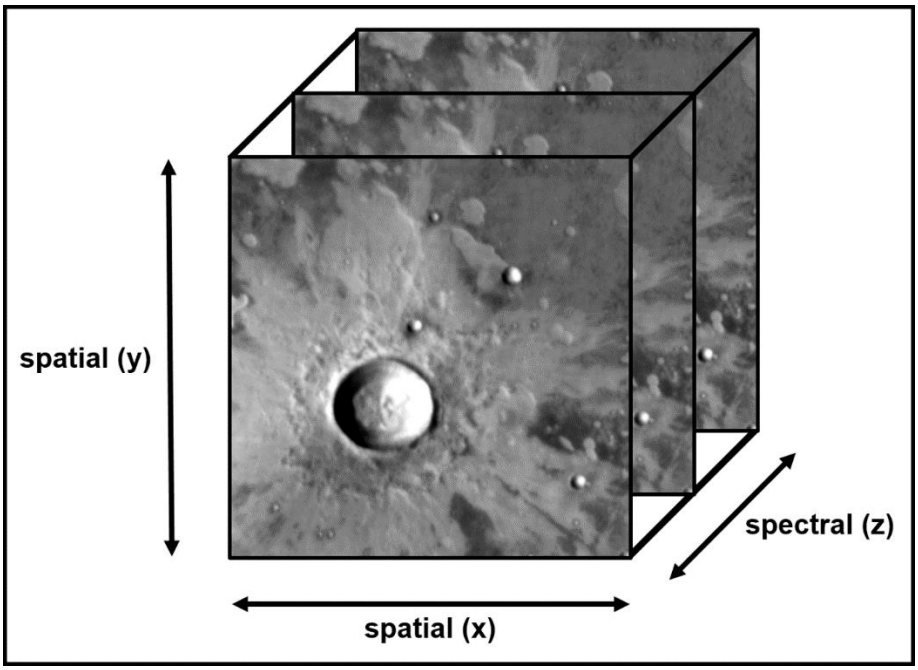

Figure 2.10. Illustration of a multiband image as a three-dimensional matrix

$$N = \frac{A - avg(A)}{stdev(A)} \qquad \text{Eq. 2.2}$$

A covariance matrix can then be calculated from the normalized input data using Equation 2.3, where the covariance between each pair of variables (bands) is calculated using all the available row vectors (pixels) as samples. The result is an i × i covariance matrix, which is a symmetric square matrix by definition. If the samples (pixels) used in the calculation represent the entire possible set of samples, then Equation 2.4 can be used, which will result in the diagonal values of the covariance matrix all equaling unity, since each variable will be known to always have a one-to-one correlation, or covariance, with itself.

$$C_{x,y} = \frac{\sum_{i=1}^{n}(X_i - \bar{x})(Y_i - \bar{y})}{n-1} \qquad \text{Eq. 2.3}$$

$$C_{x,y} = \frac{\sum_{i=1}^{n}(X_i - \bar{x})(Y_i - \bar{y})}{n} \qquad \text{Eq. 2.4}$$

For a THEMIS IR image with eight usable spectral bands (Bands 2-9), the covariance matrix will be in the form of a symmetric 8x8 square matrix, as shown in Equation 2.5.

$$C = \begin{matrix} C_{2,2} & C_{3,2} & C_{4,2} & C_{5,2} & C_{6,2} & C_{7,2} & C_{8,2} & C_{9,2} \\ C_{2,3} & C_{3,3} & C_{4,3} & C_{5,3} & C_{6,3} & C_{7,3} & C_{8,3} & C_{9,3} \\ C_{2,4} & C_{3,4} & C_{4,4} & C_{5,4} & C_{6,4} & C_{7,4} & C_{8,4} & C_{9,4} \\ C_{2,5} & C_{3,5} & C_{4,5} & C_{5,5} & C_{6,5} & C_{7,5} & C_{8,5} & C_{9,5} \\ C_{2,6} & C_{3,6} & C_{4,6} & C_{5,6} & C_{6,6} & C_{7,6} & C_{8,6} & C_{9,6} \\ C_{2,7} & C_{3,7} & C_{4,7} & C_{5,7} & C_{6,7} & C_{7,7} & C_{8,7} & C_{9,7} \\ C_{2,8} & C_{3,8} & C_{4,8} & C_{5,8} & C_{6,8} & C_{7,8} & C_{8,8} & C_{9,8} \\ C_{2,9} & C_{3,9} & C_{4,9} & C_{5,9} & C_{6,9} & C_{7,9} & C_{8,9} & C_{9,9} \end{matrix} \qquad \text{Eq. 2.5}$$

The Eigen Decomposition Theorem states that if C is a symmetric matrix, then Λ must be a diagonal matrix of the eigenvalues and the columns of U must be the orthogonal eigenvectors of the original dataset (Equations 2.6, 2.7, and 2.8). The eigenvectors represent the principal component axes that will be the basis of the decorrelation stretch calculation.

$$C = U\Lambda U^{-1} \qquad \text{Eq. 2.6}$$

where:

$$U = [\bar{u}_1 \quad \dots \quad \bar{u}_i] \qquad \text{Eq. 2.7}$$

$$\Lambda = \begin{bmatrix} \lambda_1 & \cdots & 0 \\ \vdots & \ddots & \vdots \\ 0 & \cdots & \lambda_i \end{bmatrix} \qquad \text{Eq. 2.8}$$

To solve for the eigenvalues and eigenvectors, Equation 2.6 must be reorganized and set equal to zero, as shown in Equations 2.9-2.12.

$$CU = U\Lambda \qquad \text{Eq. 2.9}$$

$$C\bar{u}_i = \lambda_i \bar{u}_i \qquad \text{Eq. 2.10}$$

$$(C - \lambda_i)\bar{u}_i = 0 \qquad \text{Eq. 2.11}$$

$$(C - \lambda_i) = 0 \qquad \text{Eq. 2.12}$$

Equation 2.12 can then be re-written in the more general form of Equation 2.13, which accounts for all possible eigenvalues (λ_i) as part of the eigenvalue matrix (λ).

$$(C - \lambda I) = 0 \qquad \text{Eq. 2.13}$$

By definition, the characteristic equation of matrix C is found by taking the determinant of both sides of Equation 2.13. The determinant of a 1×1 matrix, such as zero, is the same 1×1 matrix, so Equation 2.14 is still set equal to zero.

$$\det(C - \lambda_i I) = \det(0) = 0 \qquad \text{Eq. 2.14}$$

The determinant of a matrix is defined by Equation 2.15.

$$\det(A) = \sum_{j=1}^{j=n} a_{ij} A_{ij} \qquad \text{Eq. 2.15}$$

For the case of a three-band input image, Equation 2.15 can be simplified and re-written as Equation 2.16.

$$\det(A) = \begin{vmatrix} a & b & c \\ d & e & f \\ g & h & i \end{vmatrix} = a \begin{vmatrix} e & f \\ h & i \end{vmatrix} - b \begin{vmatrix} d & f \\ g & i \end{vmatrix} + c \begin{vmatrix} d & e \\ g & h \end{vmatrix}$$

$$= a(ei - hf) - b(di - gf) + c(dh - ge) \qquad \text{Eq. 2.16}$$

Therefore, Equation 2.14 can be simplified and re-written as Equation 2.17.

$$\det\left(\begin{bmatrix} c_{1,1} - \lambda_1 & \cdots & c_{i,1} \\ \vdots & \ddots & \vdots \\ c_{1,j} & \cdots & c_{i,y} - \lambda_i \end{bmatrix}\right) = 0 \qquad \text{Eq. 2.17}$$

In practice, expanding and solving Equation 2.17 for λ_i can be difficult and time-consuming. For the special case of a three-band input image, it is often easier to instead

use the generalized polynomial form of the characteristic equation of a 3x3 matrix, given by Equation 2.18.

$$\lambda^3 - \mathrm{tr}(\mathrm{C})\lambda^2 + \tfrac{1}{2}\left(\mathrm{tr}(\mathrm{C})^2 - \mathrm{tr}(\mathrm{C}^2)\right)\lambda - \det(\mathrm{C}) = 0 \qquad \text{Eq. 2.18}$$

In Equation 2.18, the mathematical operation "tr" refers to the "trace" of a matrix, which is defined as the sum of the values along the main diagonal (upper left to lower right) of a matrix, as defined in Equation 2.19.

$$\mathrm{tr}(\mathrm{A}) = \mathrm{tr}\left(\begin{bmatrix} a_{1,1} & \cdots & a_{i,1} \\ \vdots & \ddots & \vdots \\ a_{1,i} & \cdots & a_{i,i} \end{bmatrix}\right) = \mathrm{sum}\left(a_{1,1} \ldots a_{i,i}\right) \qquad \text{Eq. 2.19}$$

Solving the characteristic equation in Equation 2.18 for each possible eigenvalue λ_i will result in the matrix Λ, as shown in Equation 2.8. With matrix Λ known, it is possible to solve for the eigenvector matrix U, by using Equation 2.11 to solve for the eigenvector $\bar{u}_i$ corresponding to each eigenvalue λ_i.

With both the eigenvalue matrix (Λ) and eigenvector matrix (U) calculated, a decorrelation stretch of the normalized input data (N) can be performed. Begin by calculating the scaling matrix, as defined by Equation 2.20, where σ is the user-desired standard deviation of the data in the final DCS image.

$$\mathrm{S} = \frac{\sigma}{\sqrt{\Lambda}} \qquad \text{Eq. 2.20}$$

Then, a transformation matrix can be computed using Equation 2.21.

$$\mathrm{T} = \mathrm{U}^{\mathrm{T}}\mathrm{S}\mathrm{U} \qquad \text{Eq. 2.21}$$

The normalized image data can then be rotated to the eigenvector (principal component) axes using Equation 2.22.

$$\mathrm{D} = \mathrm{N}\mathrm{T} \qquad \text{Eq. 2.22}$$

The normalized image data will be centered around zero, so an offset of 127 is necessary to re-center the data at the middle of the 8-bit color range (0-255), as shown in Equation 2.23.

$$D' = D + 127 \qquad \text{Eq. 2.23}$$

Each pixel value will also need to be truncated to an integer, in order to later be displayed as an 8-bit color image, as described by Equation 2.24.

$$D'' = \text{integer}(D') \qquad \text{Eq. 2.24}$$

Then, any pixel values above "255" must be set to "255", and similarly, any pixel values below "0" must be set to "0", to fit within the acceptable value range (0-255) of an 8-bit image, as described by Equation 2.25.

$$D''' = \text{byte}(D'') \qquad \text{Eq. 2.25}$$

Finally, the image data must be reorganized into a three-dimensional matrix with dimensions X × Y × Z), so that the individual XY planes once again represent images and the Z dimension separates images from different spectral bands, as described by Equation 2.26.

$$A' = \begin{bmatrix} a_{1,1,1} & \cdots & a_{i,1,1} \\ \vdots & \ddots & \vdots \\ a_{1,j,1} & \cdots & a_{i,j,1} \end{bmatrix}; \begin{bmatrix} a_{1,1,2} & \cdots & a_{i,1,2} \\ \vdots & \ddots & \vdots \\ a_{1,j,2} & \cdots & a_{i,j,2} \end{bmatrix}; \begin{bmatrix} a_{1,1,3} & \cdots & a_{i,1,3} \\ \vdots & \ddots & \vdots \\ a_{1,j,3} & \cdots & a_{i,j,3} \end{bmatrix} \qquad \text{Eq. 2.26}$$

The resulting DCS image data can then be displayed as an 8-bit RGB image.

2.3.4 Running Decorrelation Stretch Calculation

DCS images are typically calculated using remote sensing image data covering only a relatively discrete area. However, this is not the case for THEMIS IR images, which are

sometimes long enough to cover a significant range of latitudes within a single image. This is problematic because Martian daily surface temperatures are largely a function of latitude.

THEMIS IR images can be acquired with lengths between 8.5 and 1,785 seconds (0.14 and 36.43 minutes). Mars Odyssey and THEMIS are in a near-polar orbit around Mars, so long image durations result in a wide range of latitudes within the images. This often results in regional-scale, latitude-dependent temperature changes along the images, as shown in Figures 2.11a and 2.11b.

If the image data is normalized as a whole, these along-image temperature changes will skew the calculation of the covariance matrix and result in eigenvectors that do not accurately represent the actual principal components of the image data, resulting in DCS images like the one shown in Figure 2.11c. Note that the effects of the along-image temperature drift are not immediately apparent.

The solution is to perform the DCS calculation in a running fashion: working along the image in sections of 1,000 lines, while moving forward in steps of 500 lines and blending the overlaps. This prevents latitude-dependent temperature changes from skewing the covariance matrix and washing out the spectral characteristics of the surface materials, as seen in Figure 2.11c. The process is analogous to the running contrast stretches developed by Edwards et al. (2011a,b) for single-band THEMIS IR images.

This "running DCS" calculation will result in covariance matrices and eigenvectors that more accurately and consistently describe the spectral variation of the surface materials within the image, as shown in Figure 2.11d.

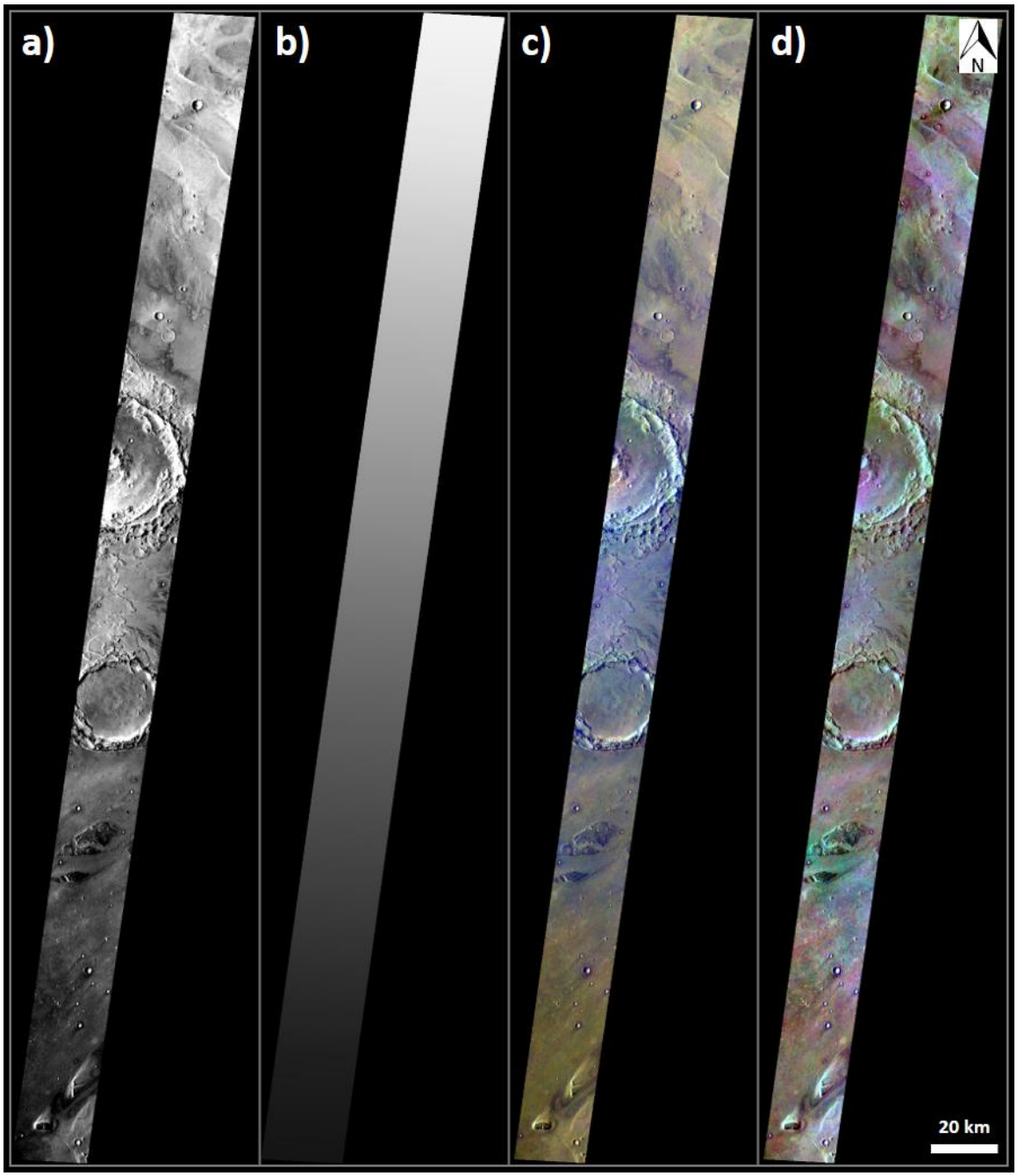

Figure 2.11. THEMIS IR image I03359002: (a) sigma stretch of band 9 spectral radiance with $\sigma = 70$, (b) cross-track averaged and smoothed spectral radiances, showing latitude-dependent temperature change along the length of the image, (c) a DCS 963 image processed using a single covariance matrix, (d) a DCS 963 image processed using a running covariance matrix calculation with a bin size of 1,000 lines and advancing in steps of 500 lines (5392 image lines total).

2.4 Results

2.4.1 Calculation of a Global Covariance Matrix

One of the common criticisms of decorrelation stretch image analysis is that the individual images are "scene dependent", meaning that the data within each image has been rotated to different principal component axes. These differences are usually so minor that they are unnoticeable to the human eye, as long as the images contain similar content (ex: images of a desert and a rainforest would likely result in significantly different principal component axes, while two images of the same desert would likely result in an insignificant difference between the principal component axes), but it is still a valid criticism, particularly when the goal is to perform a quantitative analysis of the DCS images.

This "scene dependence" results from calculating different covariance matrices for each image, which then yield different eigenvectors, which then rotate the original data to different principal component axes. A solution to the "scene dependence" problem is to apply the same covariance matrix to all images during the decorrelation stretch calculation, resulting in the normalized data from all images being rotated to the exact same principal component axes. However, for this to be an effective solution, this common covariance matrix needs to represent the full diversity of data within the images to which it is being applied.

Equation 2.3 describes how the covariance between two variables can be calculated. Both the numerator and denominator are sums and are typically summed across all pixels within an image. However, they can just as easily be summed across all pixels within multiple images as well. To that end, Equation 2.4 describes how the covariance between two variables can be calculated if all possible pixels are being considered.

To calculate this common "global" covariance matrix, the previously-described pre-processing steps were applied to each image in the THEMIS IR dataset described in Section 2.2. Two copies of each image were produced, one with the white noise removal algorithm applied (WNR) and one without (RAD).

As an intermediate step, the covariance values for each possible two-band pair were calculated on a per-image basis by summing both sides of Equation 2.4 for each image. Histograms of the resulting covariance values across the entire dataset were then generated, showing how many of the 29,922 images resulted in a given covariance value. The results for the RAD images (without white noise removal applied) are shown in Figure 2.12, and the results for the WNR images are shown in Figure 2.13.

Note that all the covariance histograms have Gaussian distributions, with the WNR data having much smoother histograms than the RAD data.

Finally, both sides of Equation 2.4 were summed across the entire dataset, resulting in the global covariance matrix in Equation 2.5. Table 2 contains the global covariance matrix for the RAD data and Table 3 contains the global covariance matrix for the WNR data.

Performing eigen decompositions on these covariance matrices yields eigenvectors representing the principal component axes of both the RAD and WNR image datasets. Table 4 contains the eigenvector matrix for the RAD image dataset and Table 5 contains the eigenvector matrix for the WNR image dataset.

Table 6 lists the associated eigenvalues for both the RAD and WNR image datasets, along with the percentage of the eigenvalue sum that each eigenvalue represents. The relatively large first eigenvalue for both the RAD and WNR image datasets demonstrates that both datasets are highly correlated.

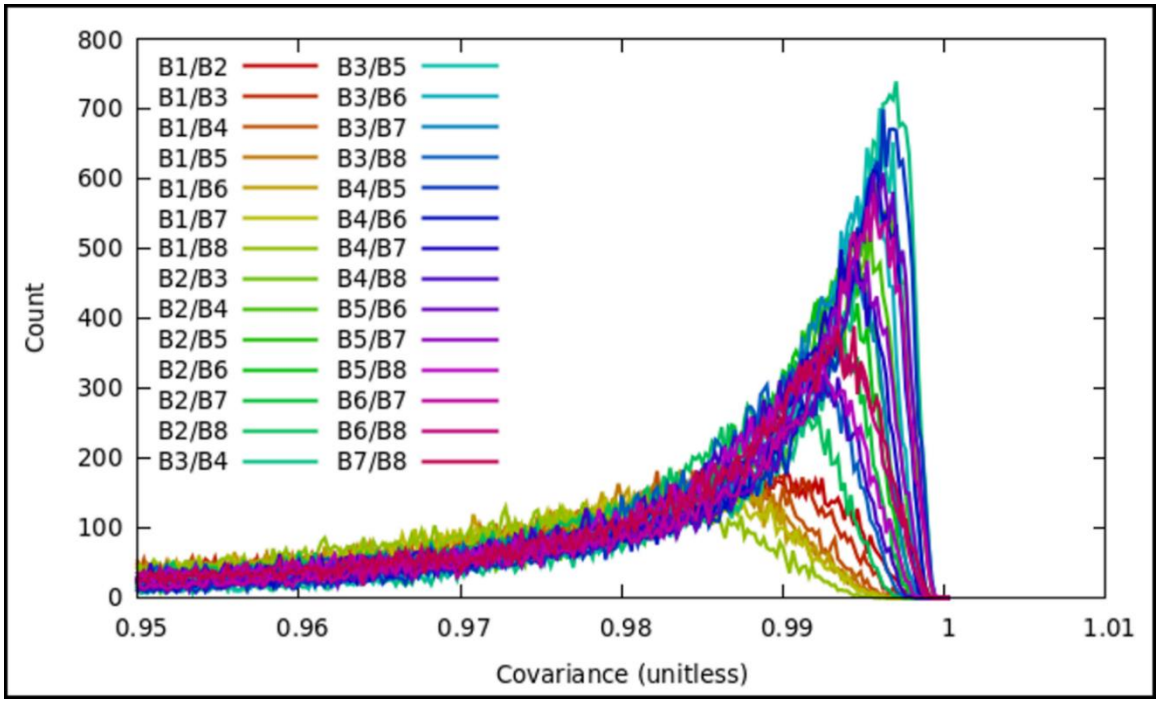

Figure 2.12. Band-to-band covariance distributions across all RAD images used to calculate the Global RAD Covariance Matrix.

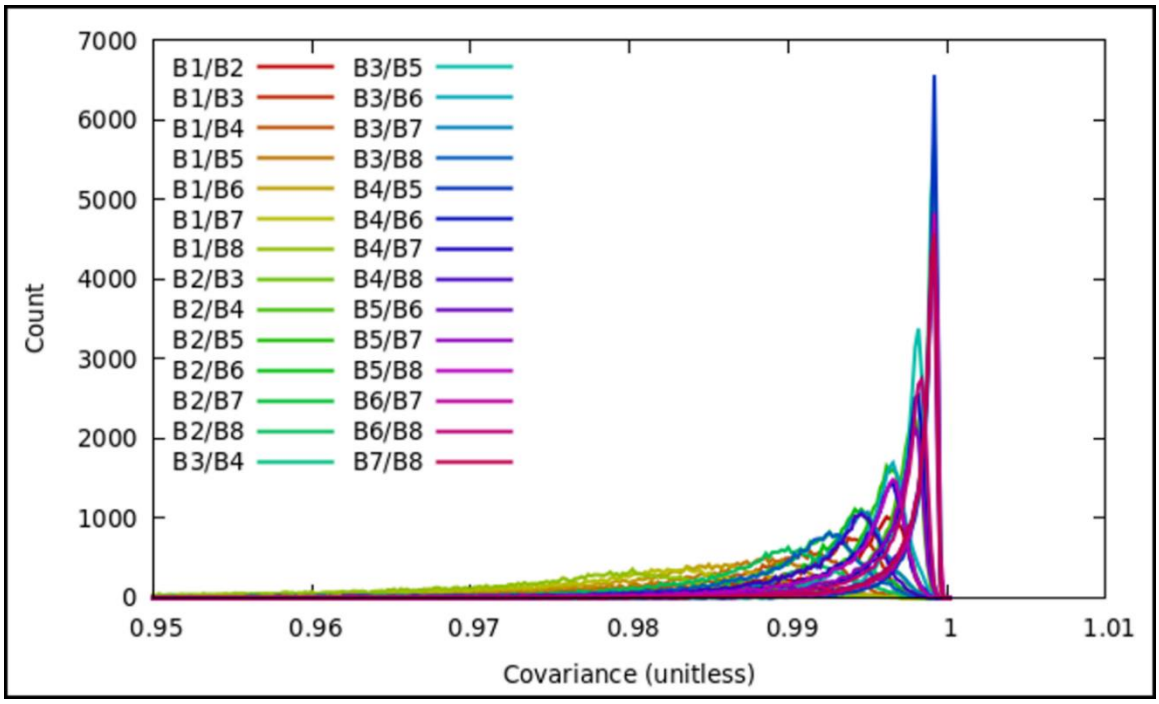

Figure 2.13. Band-to-band covariance distributions across all WNR images used to calculate the Global WNR Covariance Matrix.

Table 2.2. THEMIS IR - global RAD covariance matrix

	Band 2	**Band 3**	**Band 4**	**Band 5**	**Band 6**	**Band 7**	**Band 8**	**Band 9**
Band 2	**1.0000000**	0.9296726	0.9310298	0.9280695	0.9266264	0.9269063	0.9243046	0.9164545
Band 3	0.9296726	**1.0000000**	0.9755690	0.9734435	0.9721535	0.9720407	0.9688833	0.9592932
Band 4	0.9310298	0.9755690	**1.0000000**	0.9817803	0.9799774	0.9789953	0.9745404	0.9647437
Band 5	0.9280695	0.9734435	0.9817803	**1.0000000**	0.9808395	0.9790297	0.9738605	0.9638621
Band 6	0.9266264	0.9721535	0.9799774	0.9808395	**1.0000000**	0.9794613	0.9749901	0.9650594
Band 7	0.9269063	0.9720407	0.9789953	0.9790297	0.9794613	**1.0000000**	0.9789911	0.9698535
Band 8	0.9243046	0.9688833	0.9745404	0.9738605	0.9749901	0.9789911	**1.0000000**	0.9696570
Band 9	0.9164545	0.9592932	0.9647437	0.9638621	0.9650594	0.9698535	0.9696570	**1.0000000**

Table 2.3. THEMIS IR - global WNR covariance matrix

	Band 2	**Band 3**	**Band 4**	**Band 5**	**Band 6**	**Band 7**	**Band 8**	**Band 9**
Band 2	**1.0000000**	0.9767020	0.9737205	0.9688845	0.9675374	0.9633860	0.9604752	0.9570543
Band 3	0.9767020	**1.0000000**	0.9908979	0.9883217	0.9868095	0.9846615	0.9836701	0.9800970
Band 4	0.9737205	0.9908979	**1.0000000**	0.9948614	0.9937711	0.9896466	0.9823128	0.9789245
Band 5	0.9688845	0.9883217	0.9948614	**1.0000000**	0.9947567	0.9905128	0.9834892	0.9801135
Band 6	0.9675374	0.9868095	0.9937711	0.9947567	**1.0000000**	0.9930163	0.9854157	0.9823744
Band 7	0.9633860	0.9846615	0.9896466	0.9905128	0.9930163	**1.0000000**	0.9914924	0.9894048
Band 8	0.9604752	0.9836701	0.9823128	0.9834892	0.9854157	0.9914924	**1.0000000**	0.9958683
Band 9	0.9570543	0.9800970	0.9789245	0.9801135	0.9823744	0.9894048	0.9958683	**1.0000000**

Table 2.4. THEMIS IR - global RAD eigenvectors matrix

	PC 1	PC 2	PC 3	PC 4	PC 5	PC 6	PC 7	PC 8
PC 1	-0.3420712	-0.9342111	0.0789787	0.0603458	0.0010443	-0.0105964	-0.0154563	0.0023315
PC 2	-0.3545001	0.0504819	-0.3394956	-0.8369220	0.1729005	-0.0742759	-0.1427696	0.0170572
PC 3	-0.3561378	0.0954366	-0.2573375	0.0591360	-0.2303719	0.6533332	0.5586313	-0.0485140
PC 4	-0.3558786	0.1232370	-0.2763912	0.2126543	-0.3276275	-0.7264338	0.3105156	-0.0712973
PC 5	-0.3557988	0.1407699	-0.2025427	0.2937783	-0.2247442	0.1892750	-0.7196583	-0.3493121
PC 6	-0.3551603	0.1573496	0.1807156	0.2182446	0.7821087	-0.0531624	0.1604090	-0.3585557
PC 7	-0.3525737	0.1816133	0.8136705	-0.2429536	-0.3443118	-0.0116523	0.0117881	-0.0528851
PC 8	-0.3560806	0.1511533	0.0122074	0.2328910	0.1701142	0.0321466	-0.1646544	0.8595864

Table 2.5. THEMIS IR - global WNR eigenvectors matrix

	PC 1	PC 2	PC 3	PC 4	PC 5	PC 6	PC 7	PC 8
PC 1	0.3486138	0.7864898	0.4131905	0.2957112	0.0160346	0.0233471	-0.0304717	-0.0001857
PC 2	0.3541791	0.1664331	-0.0177499	-0.8402536	-0.2881121	0.1913499	-0.0529688	0.1344875
PC 3	0.3547667	0.1052077	-0.3733377	-0.0876737	0.1384395	-0.7086538	0.3921028	-0.2022470
PC 4	0.3546263	0.0039396	-0.4250258	0.0639066	0.5337684	0.1231981	-0.6098169	0.1324034
PC 5	0.3547502	-0.0638635	-0.3681195	0.2770177	-0.0937046	0.6099719	0.5251315	-0.0348360
PC 6	0.3546810	-0.2391583	-0.0715303	0.3397610	-0.7064792	-0.2349163	-0.3405196	0.1618595
PC 7	0.3538075	-0.3467717	0.3788112	-0.0504827	0.0911382	0.0935303	-0.1316501	-0.7577186
PC 8	0.3529595	-0.4014024	0.4741352	0.0057638	0.3105810	-0.0973280	0.2481856	0.5673879

Table 2.6. THEMIS IR - global RAD and WNR eigenvalues, with associated percentages of the eigenvalue sums.

RAD Eigenvalues	RAD Eigen Percentages	WNR Eigenvalues	WNR Eigen Percentages
7.731241	96.64	7.877284	98.47
0.108784	1.36	0.058340	0.73
0.045858	0.57	0.031602	0.40
0.030774	0.38	0.013381	0.17
0.026309	0.33	0.006244	0.08
0.019817	0.25	0.004882	0.06
0.019287	0.24	0.004493	0.06
0.017930	0.22	0.003774	0.05

2.4.2 Reducing the Global Covariance Matrices for DCS Calculations

The Global RAD and WNR Covariance Matrices in Tables 2 and 3 describe how all eight variables (bands) in THEMIS IR images vary with respect to each other. These matrices can be reduced to 3×3 matrices to create global covariance matrices for any three-band combination being used to calculate a DCS image.

The 8×8 global covariance matrices have the form of Equation 2.5 and need to be reduced to 3×3 covariance matrices of the form in Equation 2.27. For example, the reduced form of a global covariance matrix for Bands 3, 6, and 9 is given by Equation 2.28, where the bands have been ordered by wavelength rather than band number.

Note that all of the band-to-band covariance values in Equation 2.28 are available in Equation 2.5. Similarly, the covariance values for any three-band combination simply need to be taken from the global covariance matrices and re-ordered according to Equation 2.27.

The global eigenvectors can then be calculated normally from this reduced 3×3 global covariance matrix and applied to the calculation of multiple DCS images, which will rotate all the images to the exact same principal component axes. This will result in DCS images that are directly and quantitatively comparable.

$$C = \begin{matrix} C_{i,i} & C_{j,i} & C_{k,i} \\ C_{i,j} & C_{j,j} & C_{k,j} \\ C_{i,k} & C_{j,k} & C_{k,k} \end{matrix} \quad \text{Eq. 2.27}$$

$$C = \begin{matrix} C_{9,9} & C_{6,9} & C_{3,9} \\ C_{9,6} & C_{6,6} & C_{3,6} \\ C_{9,3} & C_{6,3} & C_{3,3} \end{matrix} \quad \text{Eq. 2.28}$$

2.4.3 Maximizing Covariance for a Three-Band Set

The Global Covariance Matrices make it possible to quantitatively determine the three-band combination that will capture the maximum possible compositional variation within a single DCS image. The band-to-band global RAD covariance matrix values from Table 2 are displayed in Table 7, ordered by increasing covariance value.

All of the two-band combinations that include Band 2 are at the top of the list, indicating that they are the least-correlated band combinations in the THEMIS IR dataset. This is not due to spectral differences of Martian surface materials between those two wavelength bands, but instead, the much lower SNR of Band 1/2, as shown in Table 1. With such a relatively low SNR compared to the other bands, Band 1/2 will have the most uncorrelated noise, which will lead to low covariance values when compared to other bands, even though that low covariance is not geologically meaningful. For this reason, all two-band combinations that include Band 2 will not be considered in this optimization.

It is not immediately apparent from Table 7 which three-band combination will result in the lowest total covariance. Therefore, the total RAD covariances for each possible three-band combination (excluding Band 1/2) are listed in Table 8, ordered by increasing summed covariance. This shows that the three-band combination of Bands 3, 6, and 9 has the lowest summed covariance, which means that a DCS image using that band combination will display the maximum possible variability in Martian surface geology on a global scale. Therefore, DCS 963 images should be used as the default THEMIS IR DCS band combination in the future.

This optimization was first carried out for the Global RAD Covariance Matrix, since it has been established that the best quality THEMIS IR DCS images are generated using WNR image data with the associated RAD covariance matrix.

However, a similar optimization can be performed using the Global WNR Covariance Matrix, as shown in Tables 9 and 10. When all possible two-band covariances are ordered by increasing value (Table 9), the lowest WNR covariance values are all combinations that include Band 1/2. The band combinations are in a slightly different order than for the RAD covariances, but again, all combinations including Band 1/2 can be disregarded due to its relatively low SNR.

When all possible WNR three-band combinations (excluding Band 1/2) are ordered by summed covariance (Table 10), the resulting order is very close to, but slightly different from, the order for the RAD covariances.

Table 2.7. THEMIS IR 2-band combinations ordered by increasing global RAD covariance matrix values.

Band Combination	RAD Covariance
2,9	0.916454
2,8	0.924305
2,6	0.926626
2,7	0.926906
2,5	0.928069
2,3	0.929673
2,4	0.931030
3,9	0.959293
5,9	0.963862
4,9	0.964744
6,9	0.965059
3,8	0.968883
8,9	0.969657
7,9	0.969854
3,7	0.972041
3,6	0.972154
3,5	0.973444
5,8	0.973860
4,8	0.974540
6,8	0.974990
3,4	0.975569
7,8	0.978991
4,7	0.978995
5,7	0.979030
6,7	0.979461
4,6	0.979977
5,6	0.980840
4,5	0.981780

Table 2.8. THEMIS IR 3-band combinations, excluding band 1/2, ordered by increasing summed global RAD covariance matrix values.

Band Combination	1st / 2nd Band Covariance	2nd / 3rd Band Covariance	1st / 3rd Band Covariance	Total Covariance
3,6,9	0.972154	0.959293	0.965059	2.896506
3,5,9	0.973444	0.959293	0.963862	2.896599
3,8,9	0.968883	0.959293	0.969657	2.897834
3,4,9	0.975569	0.959293	0.964744	2.899606
3,7,9	0.972041	0.959293	0.969854	2.901187
5,8,9	0.973860	0.963862	0.969657	2.907380
4,8,9	0.974540	0.964744	0.969657	2.908941
6,8,9	0.974990	0.965059	0.969657	2.909707
5,6,9	0.980840	0.963862	0.965059	2.909761
4,6,9	0.979977	0.964744	0.965059	2.909780
4,5,9	0.981780	0.964744	0.963862	2.910386
5,7,9	0.979030	0.963862	0.969854	2.912745
4,7,9	0.978995	0.964744	0.969854	2.913593
6,7,9	0.979461	0.965059	0.969854	2.914374
3,6,8	0.972154	0.968883	0.974990	2.916027
3,5,8	0.973444	0.968883	0.973860	2.916187
7,8,9	0.978991	0.969854	0.969657	2.918502
3,4,8	0.975569	0.968883	0.974540	2.918993
3,7,8	0.972041	0.968883	0.978991	2.919915
3,6,7	0.972154	0.972041	0.979461	2.923655
3,5,7	0.973444	0.972041	0.979030	2.924514
3,5,6	0.973444	0.972154	0.980840	2.926437
3,4,7	0.975569	0.972041	0.978995	2.926605
3,4,6	0.975569	0.972154	0.979977	2.927700
4,6,8	0.979977	0.974540	0.974990	2.929508
5,6,8	0.980840	0.973860	0.974990	2.929690
4,5,8	0.981780	0.974540	0.973860	2.930181
3,4,5	0.975569	0.973444	0.981780	2.930793
5,7,8	0.979030	0.973860	0.978991	2.931881
4,7,8	0.978995	0.974540	0.978991	2.932527
6,7,8	0.979461	0.974990	0.978991	2.933443
4,6,7	0.979977	0.978995	0.979461	2.938434
5,6,7	0.980840	0.979030	0.979461	2.939330
4,5,7	0.981780	0.978995	0.979030	2.939805
4,5,6	0.981780	0.979977	0.980840	2.942597

Table 2.9. THEMIS IR 2-band combinations ordered by increasing global WNR covariance matrix values.

Band Combination	RAD Covariance
2,9	0.957054
2,8	0.960475
2,7	0.963386
2,6	0.967537
2,5	0.968884
2,4	0.973721
2,3	0.976702
4,9	0.978924
3,9	0.980097
5,9	0.980113
4,8	0.982313
6,9	0.982374
5,8	0.983489
3,8	0.98367
3,7	0.984662
6,8	0.985416
3,6	0.98681
3,5	0.988322
7,9	0.989405
4,7	0.989647
5,7	0.990513
3,4	0.990898
7,8	0.991492
6,7	0.993016
4,6	0.993771
5,6	0.994757
4,5	0.994861
8,9	0.995868

Table 2.10. THEMIS IR 3-band combinations, excluding band 1/2, ordered by increasing summed global WNR covariance matrix values.

Band Combination	1st / 2nd Band Covariance	2nd / 3rd Band Covariance	1st / 3rd Band Covariance	Total Covariance
3,5,9	0.988322	0.980097	0.980113	2.948532
3,6,9	0.98681	0.980097	0.982374	2.949281
3,4,9	0.990898	0.980097	0.978924	2.949919
4,5,9	0.994861	0.978924	0.980113	2.953899
3,7,9	0.984662	0.980097	0.989405	2.954163
4,6,9	0.993771	0.978924	0.982374	2.95507
3,5,8	0.988322	0.98367	0.983489	2.955481
3,6,8	0.98681	0.98367	0.985416	2.955895
3,4,8	0.990898	0.98367	0.982313	2.956881
4,8,9	0.982313	0.978924	0.995868	2.957106
5,6,9	0.994757	0.980113	0.982374	2.957245
4,7,9	0.989647	0.978924	0.989405	2.957976
5,8,9	0.983489	0.980113	0.995868	2.959471
3,8,9	0.98367	0.980097	0.995868	2.959636
3,7,8	0.984662	0.98367	0.991492	2.959824
5,7,9	0.990513	0.980113	0.989405	2.960031
4,5,8	0.994861	0.982313	0.983489	2.960663
4,6,8	0.993771	0.982313	0.985416	2.9615
4,7,8	0.989647	0.982313	0.991492	2.963452
3,5,7	0.988322	0.984662	0.990513	2.963496
6,8,9	0.985416	0.982374	0.995868	2.963658
5,6,8	0.994757	0.983489	0.985416	2.963662
3,6,7	0.98681	0.984662	0.993016	2.964487
6,7,9	0.993016	0.982374	0.989405	2.964795
3,4,7	0.990898	0.984662	0.989647	2.965206
5,7,8	0.990513	0.983489	0.991492	2.965494
3,5,6	0.988322	0.98681	0.994757	2.969888
6,7,8	0.993016	0.985416	0.991492	2.969924
3,4,6	0.990898	0.98681	0.993771	2.971479
3,4,5	0.990898	0.988322	0.994861	2.974081
4,5,7	0.994861	0.989647	0.990513	2.975021
4,6,7	0.993771	0.989647	0.993016	2.976434
7,8,9	0.991492	0.989405	0.995868	2.976766
5,6,7	0.994757	0.990513	0.993016	2.978286
4,5,6	0.994861	0.993771	0.994757	2.983389

2.4.4 Global DCS 963 – Individual Images

The Global RAD and WNR Covariance Matrices for the DCS 963 band combination can be found by reducing and re-ordering the covariances in Tables 2 and 3 according to Equation 2.28, which yields the covariance matrices in Equations 2.29 and 2.30, respectively.

$$C_{RAD,963} = \begin{matrix} 1.0000000 & 0.9650594 & 0.9592932 \\ 0.9650594 & 1.0000000 & 0.9721535 \\ 0.9592932 & 0.9721535 & 1.0000000 \end{matrix} \quad \text{Eq. 2.29}$$

$$C_{WNR,963} = \begin{matrix} 1.0000000 & 0.9823744 & 0.9800970 \\ 0.9823744 & 1.0000000 & 0.9868095 \\ 0.9800970 & 0.9868095 & 1.0000000 \end{matrix} \quad \text{Eq. 2.30}$$

An eigen decomposition can then be performed on both covariance matrices to find the associated eigenvectors that will serve as the principal component axes for a DCS 963 image. These eigenvector matrices are shown in Equations 2.31 and 2.32, respectively.

$$\Lambda_{RAD,963} = \begin{matrix} -0.5760212 & -0.7953628 & 0.1886732 \\ -0.5785854 & 0.2336559 & -0.7814370 \\ -0.5774413 & 0.5592880 & 0.5947761 \end{matrix} \quad \text{Eq. 2.31}$$

$$\Lambda_{WNR,963} = \begin{matrix} -0.5766218 & -0.8051775 & 0.1385518 \\ -0.5779365 & 0.2821144 & -0.7657682 \\ -0.5774918 & 0.5216327 & 0.6280147 \end{matrix} \quad \text{Eq. 2.32}$$

Figure 2.14 shows examples of eight different THEMIS IR images processed into DCS 963 images using their respective image-dependent RAD covariance matrices. In contrast, Figure 2.15 shows the same images processed into DCS 963 images using the Global RAD Covariance Matrix (Equation 2.29). Using the global covariance matrix can slightly mute

the colors associated with different surface compositions, although now the colors indicate the same composition in all images.

A solution to this color muting is to convert the image from RGB space to Hue-Saturation-Value (HSV) space, increase the color saturation (ex: by a factor of 2.5) and then convert the image back into RGB space. Figure 2.16 shows the same images as Figure 2.15, using the same Global RAD Covariance Matrix and the same DCS variance, but with the color saturations increased by a factor of 2.5. At the risk of making the images appear garish, it is now much easier to visually distinguish the subtle variations in surface compositions depicted in the DCS images.

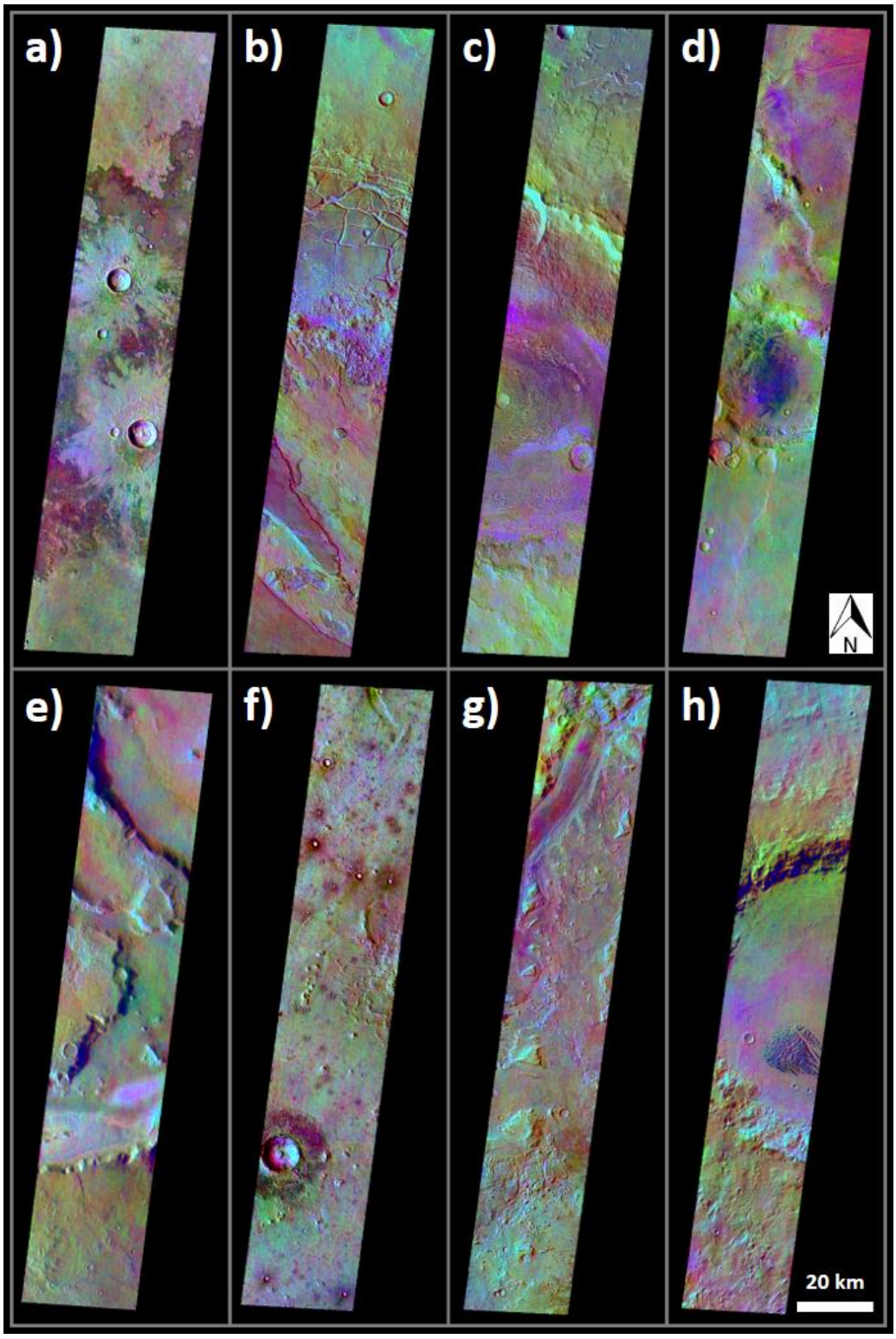

Figure 2.14. DCS 963 images processed with image-dependent RAD covariance matrices and σ = 50: (a) I02685009, (b) I01511012, (c) I00899005, (d) I00864002, (e) I05442017, (f) I02685007, (g) I01512003, and (h) I03233001.

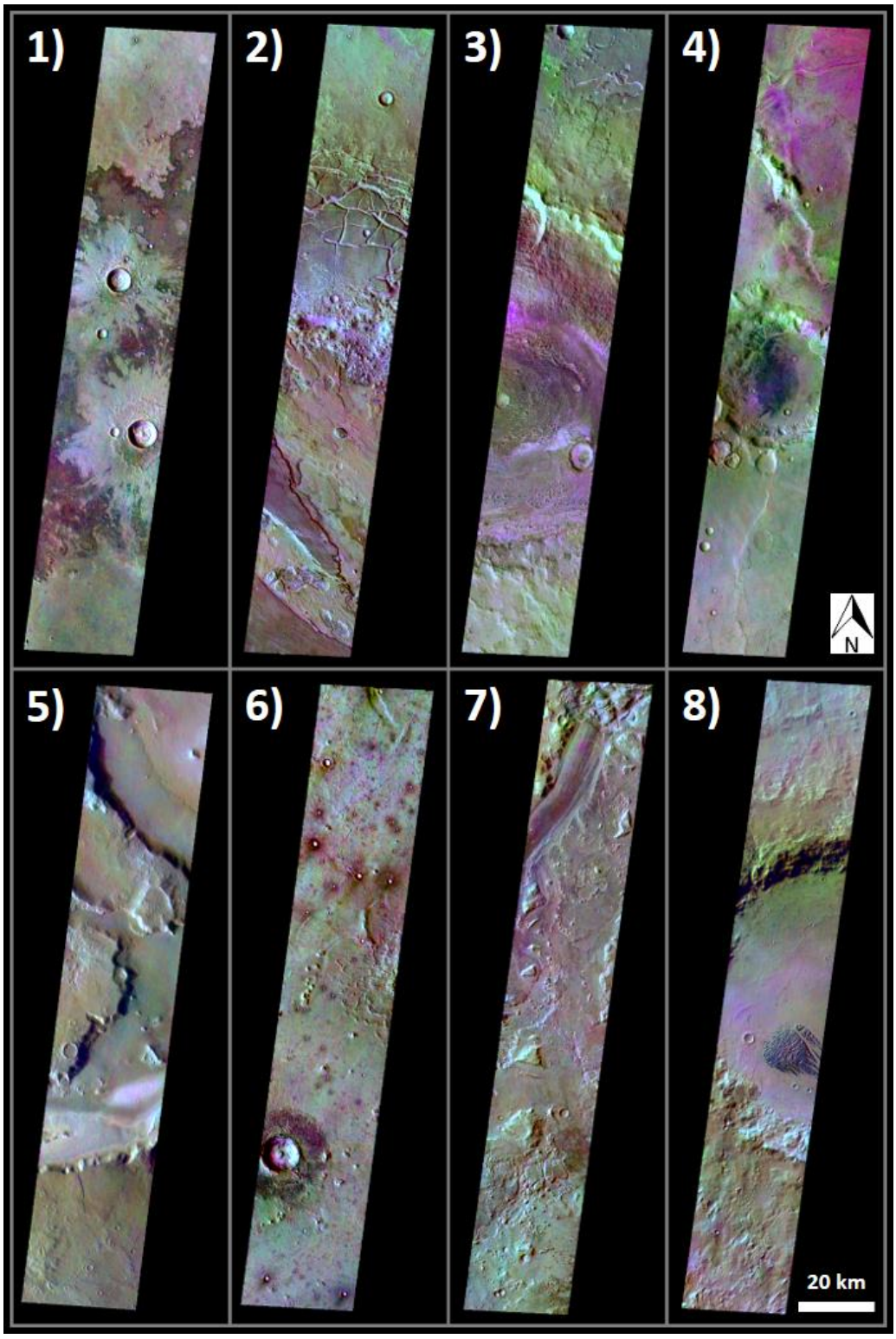

Figure 2.15. DCS 963 images processed with the Global RAD Covariance Matrix and σ = 50: (a) I02685009, (b) I01511012, (c) I00899005, (d) I00864002, (e) I05442017, (f) I02685007, (g) I01512003, and (h) I03233001.

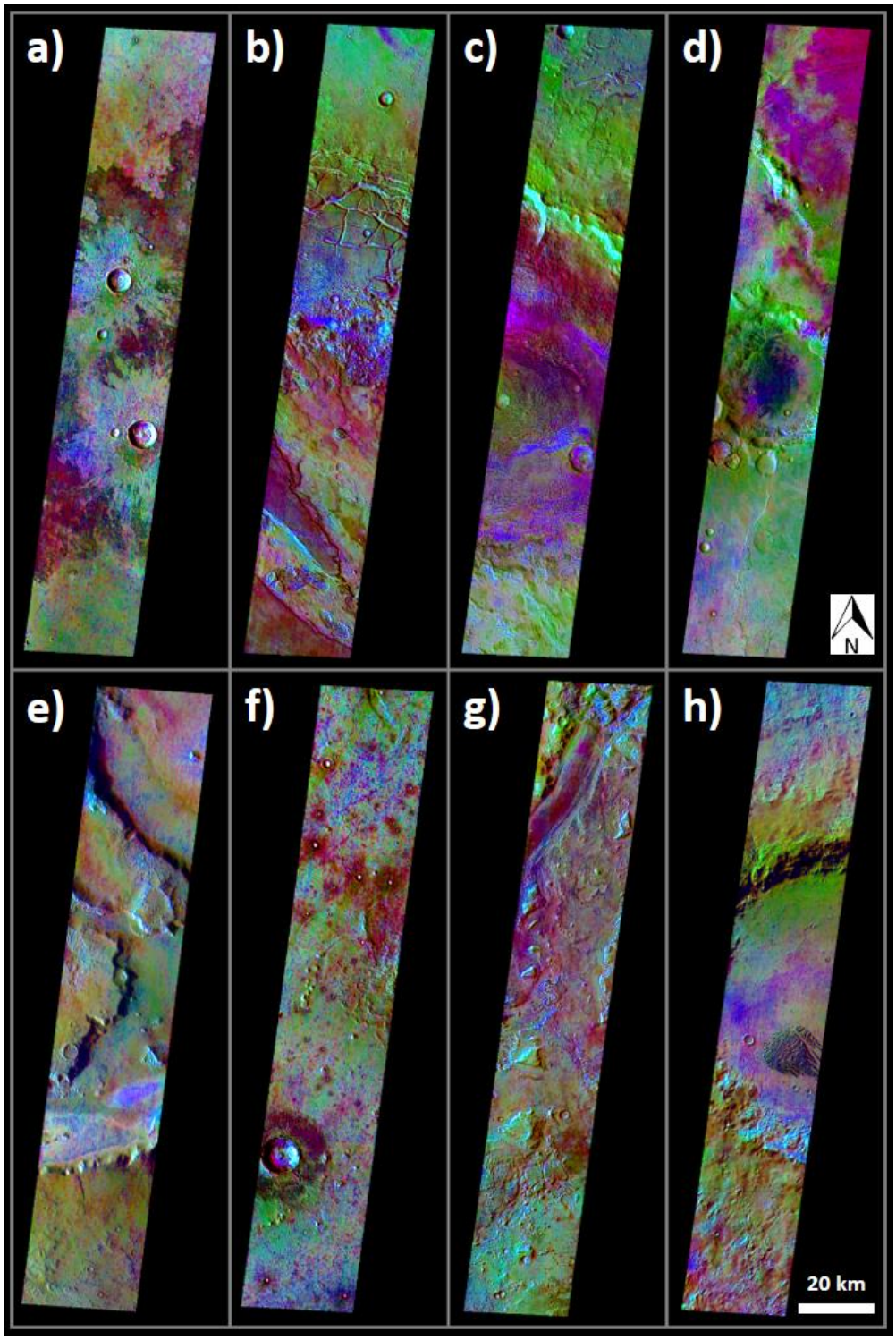

Figure 2.16. DCS 963 images processed with the Global RAD Covariance Matrix, with σ = 50 and saturation increased by a factor of 2.5: (a) I02685009, (b) I01511012, (c) I00899005, (d) I00864002, (e) I05442017, (f) I02685007, (g) I01512003, and (h) I03233001.

2.4.5 Global DCS 963 - Regional Mosaics

Using a global covariance matrix in the DCS image calculations removes the image-dependent nature of the resulting DCS images, so they can now be easily mosaicked together to create consistent images of larger-scale compositional features on the Martian surface. Figure 2.17 shows a DCS 963 mosaic composed of 73 individual THEMIS IR images processed into DCS 963 images using the Global RAD Covariance Matrix, which allows them to be assembled into a seamless mosaic with only the minimal use of blending algorithms, such as those described by Edwards et al. (2011a,b).

In the case of Figure 2.17, the DCS 963 images were mosaicked together, and then the saturation of the resulting mosaic was increased by a factor of 2.5, making the compositional features easier to identify.

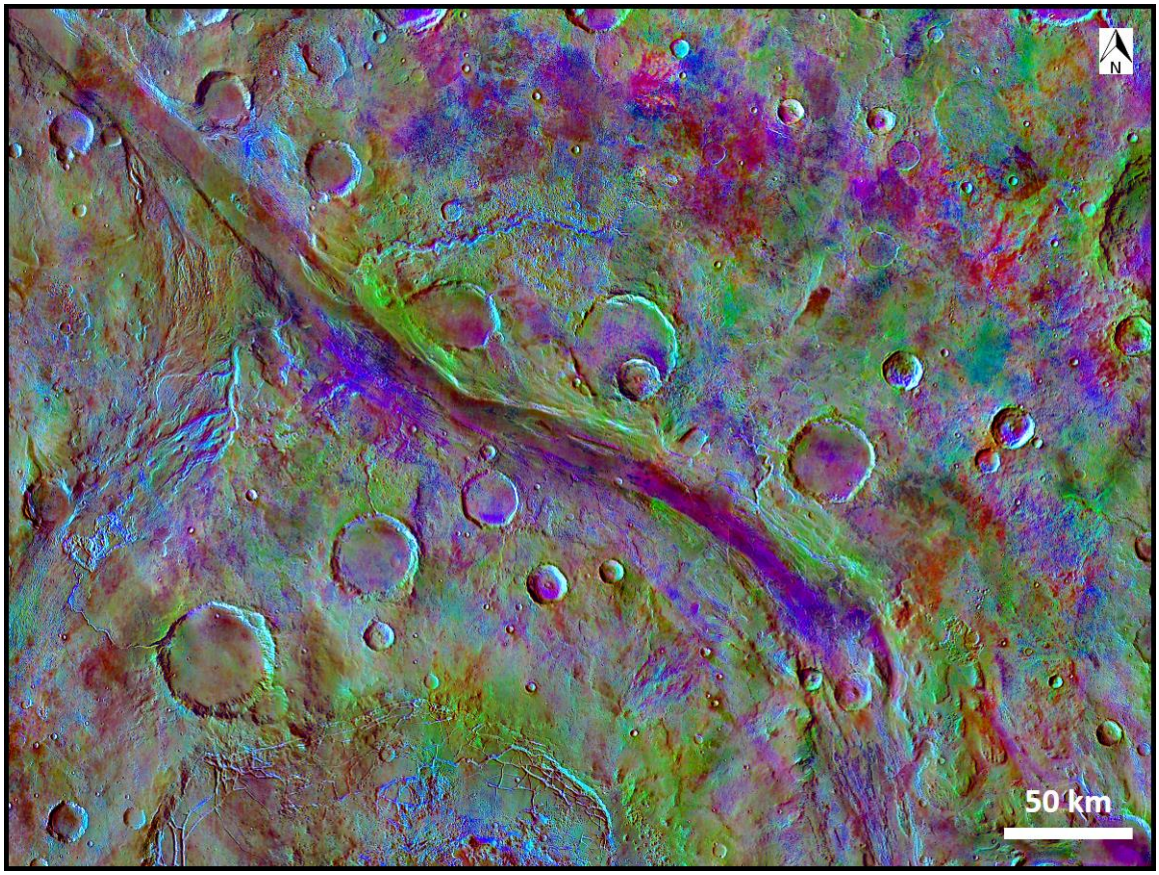

Figure 2.17. DCS 963 mosaic of Ares Vallis, composed of 73 images processed with the Global RAD Covariance Matrix, σ = 50 and with saturation increased by 2.5x.

2.5 Discussion

2.5.1 Easy Access to THEMIS Compositional Information

The THEMIS IR dataset has not been as widely utilized within the planetary science community as it could be. One reason for this is the relatively steep learning curve that new data users must overcome in order to process and analyze the data for themselves. This is particularly difficult and time-consuming for users who have not previously worked with thermal infrared data and must learn about the technique as well as the THEMIS data products themselves.

One goal of the THEMIS DCS 963 Global Mosaic is to give new users easy access to some of the compositional information contained within the THEMIS IR dataset. They will be able to quickly and easily perform reconnaissance in their area of interest, see the spatial relationships between different compositional units and correlate compositional boundaries with geomorphic features. Hopefully, this will provide new users with enough information to determine whether THEMIS infrared data would be valuable in their particular area of research and serve as the impetus for them to spend the time and effort to learn how to utilize the full potential of the THEMIS IR dataset.

2.5.2 Correlating DCS Features with Mineral Compositions

The comparison of data from THEMIS (high spatial resolution, low spectral resolution) and the Thermal Emission Spectrometer (TES) (Christensen et al., 2001) (low spatial resolution, high spectral resolution) is particularly powerful. To demonstrate this, a subsection of the Ares Vallis mosaic in Figure 2.17 is shown in Figure 2.18a, with footprints from three different atmospherically-corrected TES observations overlaid on

regions with significantly different colors in the DCS 963 mosaic. The averaged TES spectra from these three observations were linearly deconvolved using the methods and spectral library of Rogers and Christensen, (2007).

The solid lines represent the six spectral footprints of TES observation ock8983_ick1804, which were averaged together and linearly deconvolved in Figure 2.18b. The relatively high olivine-to-clinopyroxene ratio in this averaged spectrum can be correlated with the purple/violet colors in the DCS 963 image, which lie along the bottom of Ares Vallis. This correlation can then be extrapolated to apply to all the purple/violet pixels in the image, which shows the spatial distribution of the high-olivine unit in much higher resolution than would be possible using only TES observations.

Similarly, the dashed lines represent the six spectral footprints of TES observation ock8983_ick1809, which were averaged together and linearly deconvolved in Figure 2.18c. The lower olivine-to-clinopyroxene ratio can be correlated with the green colors in the DCS 963 image, which tend to lie along the walls of Ares Vallis. Not only is the boundary between the low and high olivine-to-clinopyroxene ratio units easily visible in the DCS 963 mosaic, but we can infer a similar composition in areas further outside Ares Vallis with similar colors.

Finally, the dotted lines represent the six spectral footprints of TES observation ock8392_ick1807, which were averaged together and linearly deconvolved in Figure 2.18d. Unlike the first two areas, this area contains a significant percentage of high silica material, which only appears to occur in splotchy patches along one part of the eastern edge of Ares Vallis and is correlated with the reddish-orange color. The DCS 963 mosaic is

particularly useful in this case, because it allows the variability within this compositional unit to be seen, which would not have been visible if only TES observations had been used.

An interpretation of what these compositional units can tell us about the evolution of Ares Vallis and the surrounding terrain is beyond the scope of this work. Still, hopefully this example will provide researchers with an idea of how to extract additional compositional information from the THEMIS IR dataset using the TES dataset.

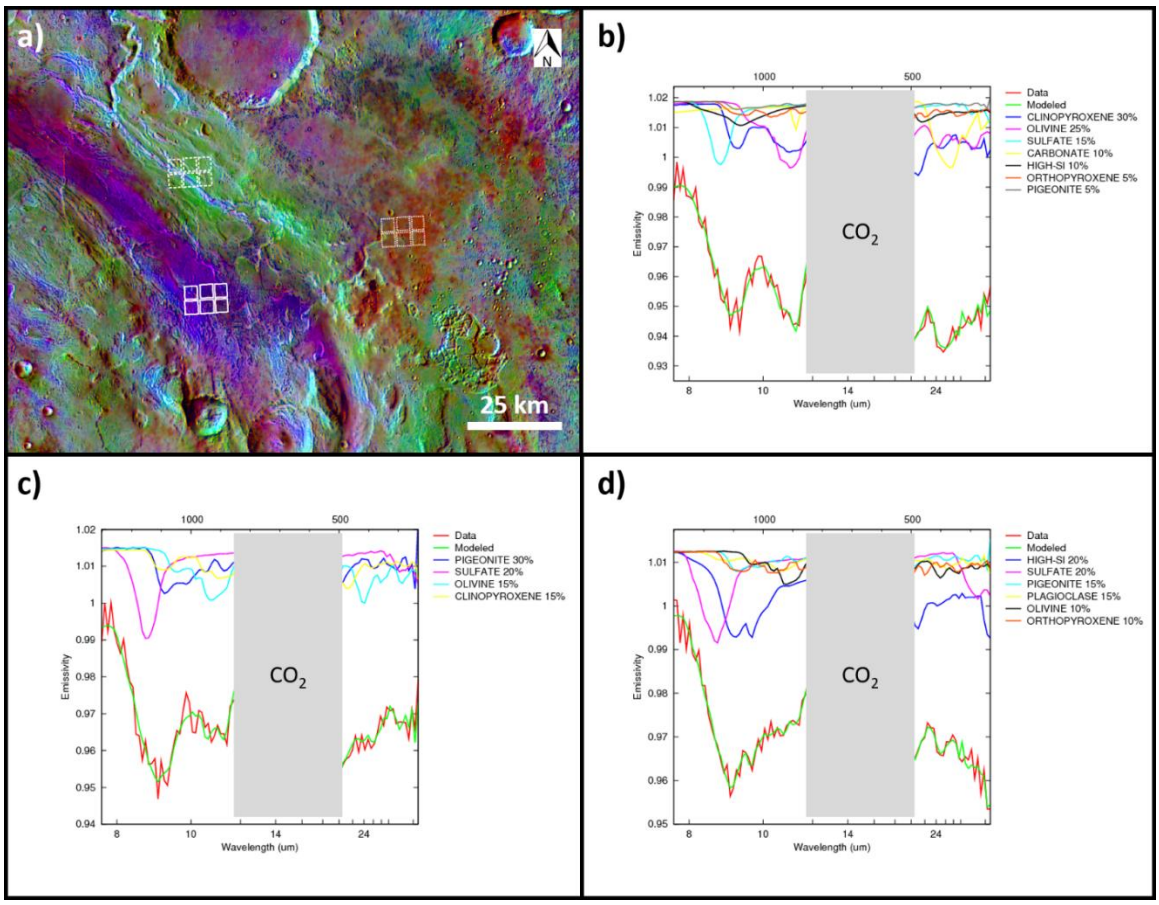

Figure 2.18. Deconvolving TES spectra associated with DCS 963 units: a) subsection of Figure 2.17 with outlines for TES observations ock8983_ick1804 (solid lines), ock8983_ick1809 (dashed lines) and ock8392_ick1807 (dotted lines); b) spectral deconvolution of TES observation ock8983_ick1804, showing a relatively high olivine-to-clinopyroxene ratio; c) spectral deconvolution of TES observation ock8983_ick1809, showing a relatively low olivine-to-clinopyroxene ratio; d) spectral deconvolution of TES observation ock8392_ick1807, showing the presence of high-silica materials that are not seen in the other two TES observations.

2.5.3 Global Principal Component Analysis

The Global RAD and WNR Covariance Matrices for the THEMIS IR dataset have additional applications beyond creating globally-consistent DCS images and mosaics. Using the full 8×8 matrices and their associated eigenvectors, it is possible to rotate an

entire 8-band THEMIS IR image from spectral radiance coordinates to principal component coordinates.

Figure 2.20 shows the eight-band THEMIS IR image I02685009, which has had the WNR algorithm applied and been rotated into principal component images using the 8×8 Global WNR Covariance Matrix in Table 3. The first principal component image appears very similar to all of the highly-correlated band images in Figure 2.6. This is consistent with the relatively large first WNR eigenvalue in Table 6, which represents 98.47% of the variance within the original eight-band image. This means the first principal component image likely roughly corresponds to an image of temperature distributions, since temperature will have a much more significant impact on the appearance of the surface in each band than any slight spectral differences.

However, principal component images 2 and 3, and possibly 4, show additional compositional structures that are uncorrelated with the first principal component image. Although it is not within the scope of this paper, it should be possible to determine what compositions these principal components represent, which could make it easier to locate and identify unique compositions on the Martian surface.

The final four principal component images appear to be composed of uncorrelated noise. The associated eigenvalues in Table 6 show that they represent extremely small fractions of the total variation within the WNR image data and are most likely insignificant when it comes to compositional analysis.

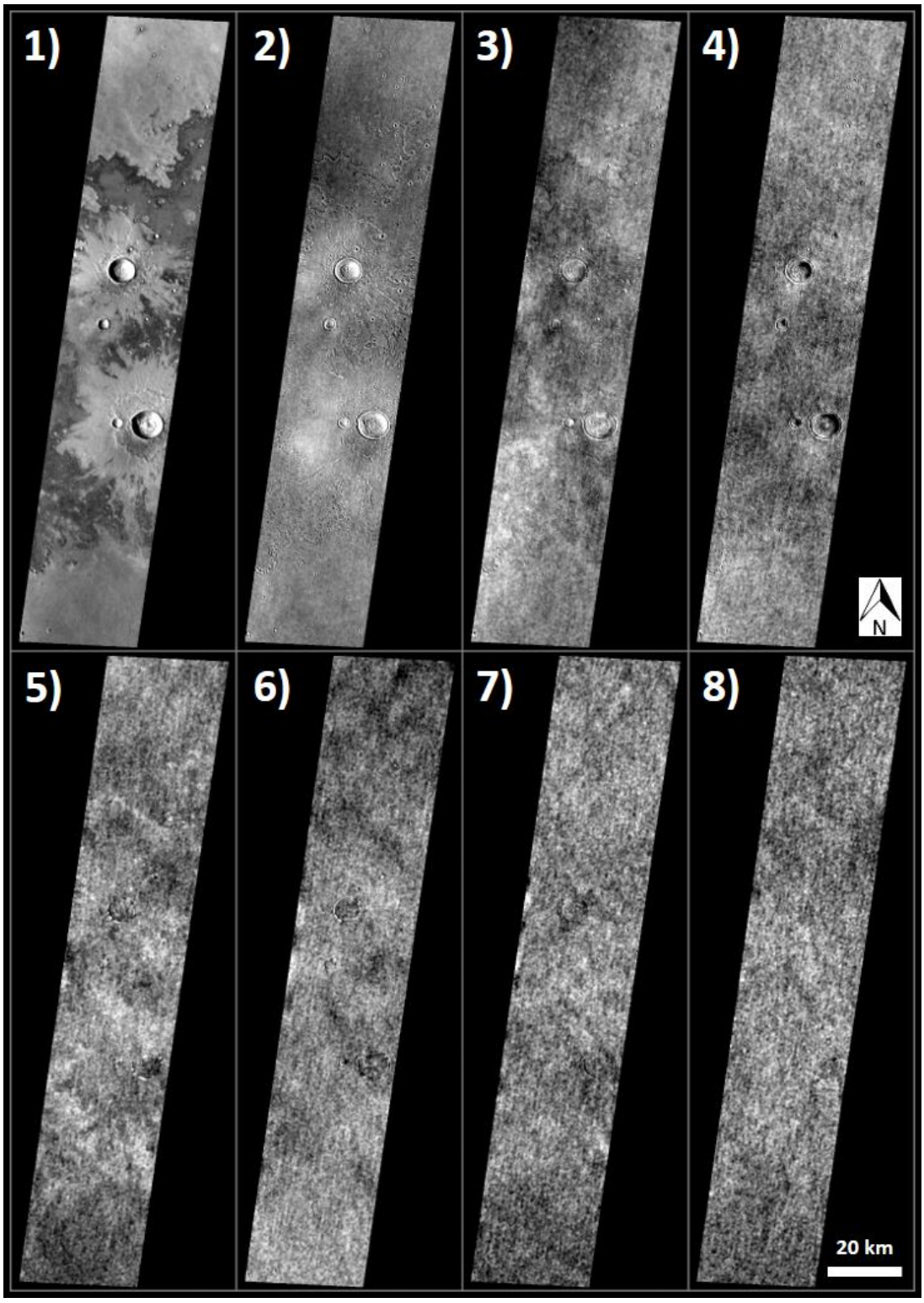

Figure 2.19. Principal component images of THEMIS IR image I02685009, calculated using WNR image data and the Global WNR Covariance Matrix.

2.6 Conclusions

The compositional variation within THEMIS eight-band IR images can be partially visualized using three-band decorrelation stretch images. Traditionally, DCS images were calculated on a per-image basis, which resulted in image-dependent covariance and eigenvector matrices. Researches had previously noted that THEMIS DCS images appear mostly consistent across the planet, with similar colors representing similar compositions. Still, since the DCS colors could not be definitively associated with a consistent composition, they had limited usefulness.

By analyzing all high-quality late-afternoon THEMIS IR images acquired between 60°N and 60°S, we have calculated global covariance matrices based on image data with and without applying the standard white noise removal (WNR) algorithm. This allowed global eigenvector matrices to be calculated for both the RAD and WNR datasets. By using the same global eigenvector matrix to rotate the individual THEMIS IR images into principal component axes, the DCS colors can be consistently and definitively correlated with specific compositions, particularly with the help of TES spectra.

The global covariance matrices also made it possible to determine that the three-band combination of 9/6/3 results in DCS images that visualizes the most spectral diversity possible within a three-band set. A globally-consistent THEMIS DCS 963 Global Mosaic was then compiled, giving researchers easy access to the compositional information within the THEMIS IR dataset. Similarly, globally-consistent THEMIS DCS 875, DCS 964, and DCS 642 Global Mosaics were compiled.

The global covariance and eigenvector matrices should also enable future research by allowing THEMIS eight-band IR images to be processed into globally-consistent principal

component images that could be used to identify minerals with unique spectral signatures on the Martian surface.

CHAPTER 3

A PRINCIPAL COMPONENT INDEX FOR IDENTIFYING CHLORIDE MINERALS USING THEMIS MULTISPECTRAL THERMAL INFRARED IMAGES

3.1 Introduction

Chloride salts were first identified on Mars by Osterloo et al. (2008) and were first surveyed on a global scale by Osterloo et al. (2010), which identified 642 distinct sites primarily located in the Martian southern highlands. Over the subsequent twelve years, this catalog of chloride sites was used to further investigate the origin and evolution of chloride salts and constrain the conditions on early Mars that would have enabled their precipitation. However, the Osterloo et al. (2010) survey was critically constrained by significant gaps in global datasets, making it difficult to determine whether their survey accurately described the true distribution of chloride salts on the Martian surface.

Over the subsequent twelve years, the orbital remote sensing instruments used to identify and analyze the chloride salts have greatly expanded their coverage of Mars: the THEMIS instrument onboard Mars Odyssey has reached full global coverage of late-afternoon infrared images and the CTX camera onboard the Mars Reconnaissance Orbiter has effectively reached full global coverage. In addition, the HiRISE camera onboard the Mars Reconnaissance Orbiter has greatly increased their areal coverage, which was partially guided by the desire to investigate the sites in the original chloride salt survey.

These expanded datasets have been used to perform a new survey that more accurately describes the global distribution of Martian chloride salt sites. Improved analysis techniques were also developed, enabling more objective identification of

chloride salts and quantification of the identification certainty. In particular, the chloride salts were found to have nearly diagnostic features in THEMIS infrared principal component images, even though chloride salts do not have any spectral features in the thermal infrared wavelength range.

This paper will describe the development of a principal component-based index for identifying chloride salts, the validation and verification of that index against the original survey results of Osterloo et al. (2010), describe the results of an improved global survey of chloride salt sites, and re-assess correlations between the chloride sites and global properties observed by independent instruments.

3.2 Datasets

3.2.1 Instrument Descriptions

The THEMIS instrument onboard the 2001 Mars Odyssey spacecraft consists of two multispectral imaging subsystems: a ten-band thermal infrared (IR) imager and a five-band visible/near-infrared imager. The thermal infrared (IR) subsystem is a pushbroom imager that acquires data at a nominal spatial resolution of 100m/pixel using an uncooled 320x240 pixel microbolometer array covered by ten ~1-μm-bandwidth strip filters centered at nine different wavelengths between 6.8μm and 14.9μm (Christensen et al., 2004).

The Gamma Ray Spectrometer (GRS) is also onboard the 2001 Mars Odyssey spacecraft and consists of three subsystems: the gamma subsystem (GS), the neutron spectrometer (NS), and the high-energy neutron detector (HEND) (Boynton et al., 2004). Data from the gamma subsystem were used to produce 5°x5° binned global elemental

concentration maps for H, Si, Fr, K, Th, and, most importantly for this study, Cl (Boynton et al., 2007).

The Context Camera (CTX), onboard the Mars Reconnaissance Orbiter (MRO), is a pushbroom imager that acquires data at a nominal spatial resolution of ~6m/pixel using a 5056-pixel linear CCD centered at a wavelength of 0.611μm with a full-width half-maximum (FWHM) bandpass of ±0.189μm (Malin et al., 2007; Bell et al., 2013). CTX images were used in this study to qualitatively assess the chloride sites' visible wavelength appearance and provide geologic context at a higher spatial resolution than is possible with THEMIS IR images.

The High Resolution Imaging Science Experiment (HiRISE), also onboard MRO, is a pushbroom imager that acquires data at a nominal spatial resolution of 0.25m/pixel using an array of 14 CCD detectors, with ten detectors centered at 0.694μm (red), two detectors centered at 0.536μm (blue-green) and two detectors centered at 0.874μm (near-infrared). The two blue-green and two near-IR detectors are in line with the center two red detectors, allowing the acquisition of approximate true color images along the center of the HiRISE image swath (McEwen et al., 2007). HiRISE images were used in this study to qualitatively assess the chloride sites' visible wavelength color and provide detailed geologic context at a higher spatial resolution than is possible with CTX images.

The Thermal Emission Spectrometer (TES) onboard the Mars Global Surveyor (MGS) spacecraft, is a Michelson interferometer covering the wavelength range from 6-50 μm (~1600–200 cm−1) with nominal 5 cm−1 and 10 cm−1 spectral resolution modes. Six 8.3-mrad fields-of-view pyroelectric detectors are arranged in a 3 × 2 array, each with 3-km resolution when pointed nadir (Christensen et al., 2001). TES-derived maps of

lambert albedo, nighttime thermal inertia (Putzig and Mellon, 2007), and Dust Cover Index (Ruff and Christensen, 2002) were used in this study to investigate possible correlations between the chloride site locations and these global properties.

Finally, the Magnetometer and Electron Reflectometer (MAG/ER) instrument onboard MGS consisted of dual triaxial flux gate magnetometers and a single electron reflectometer, which measured both the local and remote magnetic fields around Mars (Acuña et al., 1992). The resulting data were used to produce a global maps of the remnant Martian magnetic field strength in units of nano-Teslas (nT) (Connerney et al., 2005).

3.2.2 Dataset Descriptions

The HRSC-MOLA Blended 200m Digital Elevation Model (DEM) version 2.0 (Fergason et al., 2018) is a global digital elevation model that uses topographic data from the High Resolution Stereo Camera (HRSC) (Neukum and Jaumann, 2007; Jaumann et al., 2007) where it is available and topographic data from the Mars Orbital Laser Altimeter (MOLA) (Smith et al., 2001) where HRSC topographic data is not available. The spatial resolution of the blended product is 200 meters/pixel with a vertical accuracy of ±10 meters.

The Geologic Map of Mars (Tanaka et al., 2014) was developed using multiple remote sensing datasets and identifies the major geologic units on the planet's surface, along with their ages, based on crater size-frequency distribution statistics. These remote sensing datasets provided morphologic, topographic, spectral, and thermophysical observations for analysis and interpretation during the geologic mapping effort. The

THEMIS Day IR Global Mosaic (Edwards et al., 2011a,b) was used as the standard basemap for constructing this global geologic interpretation because it is mostly unaffected by atmospheric haze and thus allowed reliable analysis of surface morphology and texture at a higher resolution than other available global products could provide at the time.

3.2.3 Analytical Tool Descriptions

The Java Mission-planning and Analysis for Remote Sensing (JMARS) geospatial information system (http://jmars.asu.edu) (Christensen et al., 2009) was used to survey the global THEMIS Principal Component Chloride Index maps and to re-map chloride site extents.

Image data were analyzed using the Integrated Software for Imagers and Spectrometers (ISIS) maintained by the United States Geologic Survey's Astrogeology Science Center (http://isis.astrogeology.usgs.gov) [e.g., Anderson et al., 2004; Becker et al., 2013], as well as the DaVinci generic array processing tool maintained by Arizona State University's Mars Space Flight Facility (http://davinci.asu.edu) [e.g., Edwards et al., 2011a,b].

3.2.4 THEMIS IR Global Eigenvectors

The calculation of a global covariance matrix for the THEMIS late-afternoon infrared dataset, along with the associated global eigenvector matrix, is a critical pre-requisite for the work described in this paper. The calculation of the global covariance matrix and its use in generating globally-consistent principal component images is described in detail by Hill and Christensen (2022a).

3 Methods

3.3.1 Calculating the THEMIS Principal Component Chloride Index

As described in Hill and Christensen (2022a), the THEMIS global covariance matrix and associated global eigenvector matrix can be used to transform any normalized THEMIS infrared image into globally-consistent principal component images. Figure 3.1 shows an example 10-band THEMIS IR image of a chloride salt site and Figure 3.2 shows the same image transformed into the eight principal component images using the white-noise removed (WNR) global covariance matrix. The first 400 lines of the image have been masked, so the PC images are not affected by the THEMIS IR "ghost issue", as described by Hill and Christensen (2022a). Note that the chloride salts have extremely low values in the 3rd principal component (PC3), which serves as the foundation of the THEMIS Principal Component (PC) Chloride Index.

First, low values in PC3 are used as a proxy for chloride salts. Pixels with abnormally low values, as seen in Figure 3.3a, are identified according to Equation 3.1, which yields the mask in Figure 3.3b. Note that in addition to the chloride salts, this equation also highlights steep sun-facing and anti-sun-facing slopes.

$$\mathrm{PC3}\ [\ \text{where}\ \ \mathrm{PC3} < \mathrm{avg}_{\mathrm{PC3}} - (\mathrm{n}_3 \cdot \mathrm{stdev}_{\mathrm{PC3}}\ )] = 1.0 \qquad \text{Eq. 3.1}$$

Second, very high values in PC1 are used as a proxy for steep sun-facing slopes and very low values are used as a proxy for steep anti-sun-facing slopes, according to Equations 3.2 and 3.3. When applied to the PC1 image in Figure 3.4a, these equations

give the masks shown in Figures 3.4b and 3.4c, which can be combined into the single high-slope mask shown in Figure 3.4d.

$$\mathrm{PC1}\,[\text{ where }\ \mathrm{PC1} < \mathrm{avg}_{\mathrm{PC1}} - (\mathrm{n}_1 \cdot \mathrm{stdev}_{\mathrm{PC1}})] = 1.0 \qquad \text{Eq. 3.2}$$

$$\mathrm{PC1}\,[\text{ where }\ \mathrm{PC1} > \mathrm{avg}_{\mathrm{PC1}} + (\mathrm{n}_1 \cdot \mathrm{stdev}_{\mathrm{PC1}})] = 1.0 \qquad \text{Eq. 3.3}$$

where the ideal sensitivity parameters are:

$$\mathrm{n}_1 = 2.0 \qquad \text{Eq. 3.4a}$$

$$\mathrm{n}_3 = 3.0 \qquad \text{Eq. 3.4b}$$

The ideal values of the sensitivity parameters are given in Equations 3.4a and 3.4b, which strike a useful balance between maximizing true positive detections while minimizing false positive detections. Depending on the goal of the analysis, these values can be adjusted to either generally increase true positive detections (increasing n_1 and/or decreasing n_3) or to generally decrease false positive detections (decreasing n_1 and/or increasing n_3). However, the interplay of the two sensitivity parameters is not always so straightforward.

Finally, the THEMIS PC Chloride Index is calculated by subtracting the high-slope proxy mask from the chloride salt proxy mask, yielding pixels intended to highlight only the presence of chloride salts. Figure 3.5 shows the input masks, the resulting THEMIS PC Chloride Index mask, and the colorized THEMIS PC Chloride Index mask overlaid on the PC1 image for context.

3.3.2 THEMIS PC Chloride Index Confidence Levels

The confidence level of each chloride detection pixel can be quantified by calculating the THEMIS PC Chloride Index for multiple overlapping images and then adding the results. Figure 3.6a shows the previously-calculated THEMIS PC Chloride Index detections from THEMIS IR image I52251002. In contrast, Figure 3.6b shows the THEMIS PC Chloride Index detections calculated exactly the same way, but using THEMIS IR image I15559004. Figure 3.6c then shows the combination of the two THEMIS PC Chloride Index calculations.

A close inspection of Figure 3.6c, particularly along the crater's rim, shows that many false positive detections due to high slopes often occur in different pixels in different images. In contrast, the true positive detections reliably occur in the same pixels in different images. The false positive detections tend to be highly dependent on the image's solar incidence and solar azimuth angles. Overlapping THEMIS images are rarely from the same local time or solar longitude, so these angles vary between images. This prevents the vast majority of false positives from occurring in the same pixel multiple times.

Also, a close inspection of the main chloride salt site in Figure 3.6c shows that while many true positive detections occur in both images, there are slight differences. These differences can partially be attributed to variations in surface conditions over time, such as surface dust cover, atmospheric conditions, and surface temperatures. For example, the two images in Figure 3.6, I15559004 and I52251002, were acquired in June 2005 and September 2013, respectively. Therefore, it's not unexpected that surface conditions would change enough during those eight years, which included the global dust storm of

2007 (Smith, 2009), to result in slightly different THEMIS PC Chloride Index detections. This variation and its dependence on the sensitivity parameter values are explored in the next section.

Similarly, the THEMIS PC Chloride Index can be calculated using all available, high-quality late-afternoon THEMIS IR images, which gives a quantitative assessment of the confidence in each chloride detection pixel across the planet. Figure 3.7 shows the same chloride salt site, but with overlapping THEMIS PC Chloride Index detections from all available images. As in Figure 3.6, the false positives nearly always occur in different pixels in different images, resulting in a confidence value of 1. These single detections can easily be disregarded and only detections greater than one classified as true positive detections.

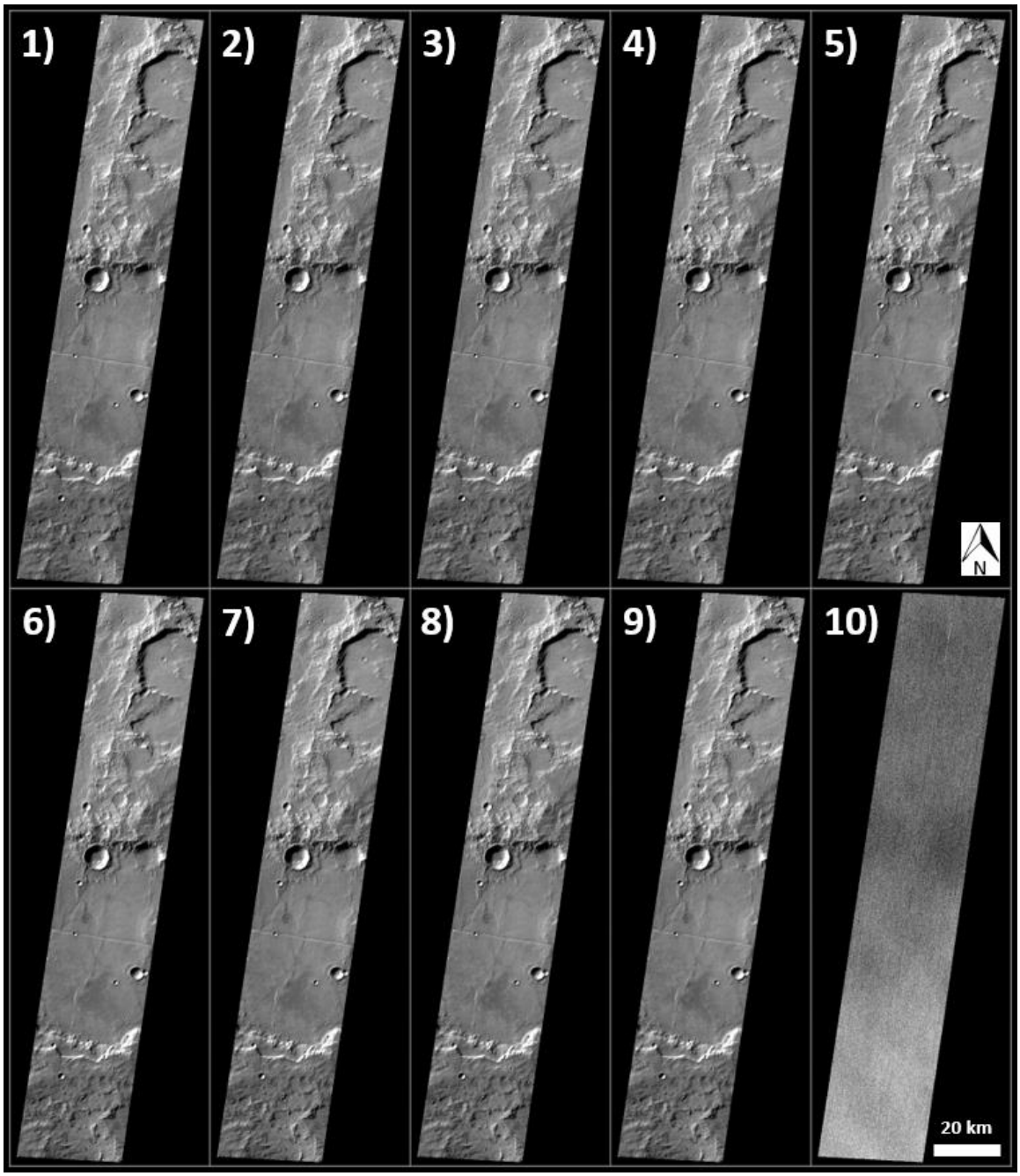

Figure 3.1. THEMS 10-band infrared image I52251002 of a chloride salt site, showing the highly-correlated nature of the THEMIS IR image data, with the exception of band 10, which measures the CO_2 absorption feature.

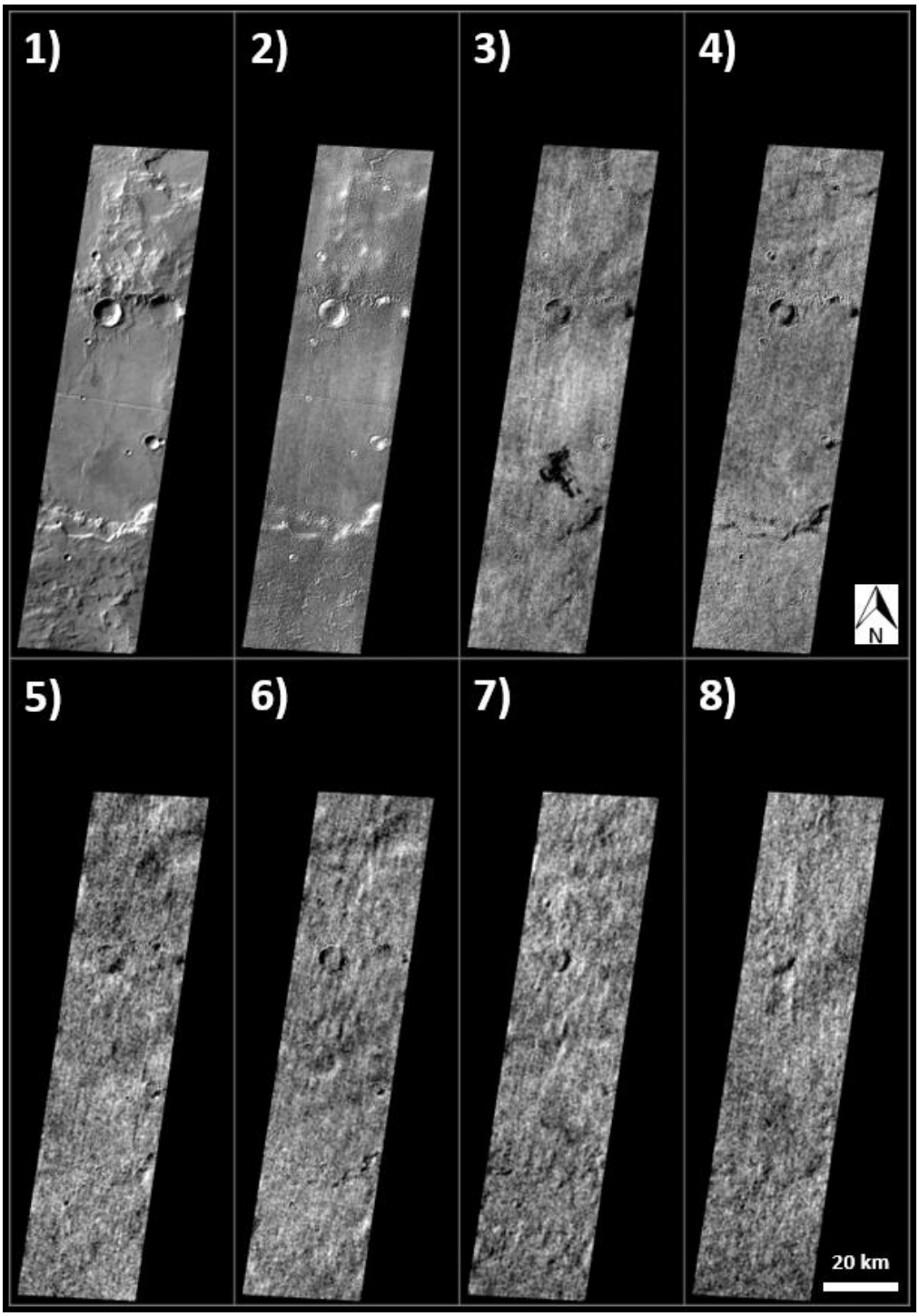

Figure 3.2. Principal component images of THEMIS IR image I52251002, calculated using WNR image data and the Global WNR Covariance Matrix. Note that the chloride salts have very low values in PC3.

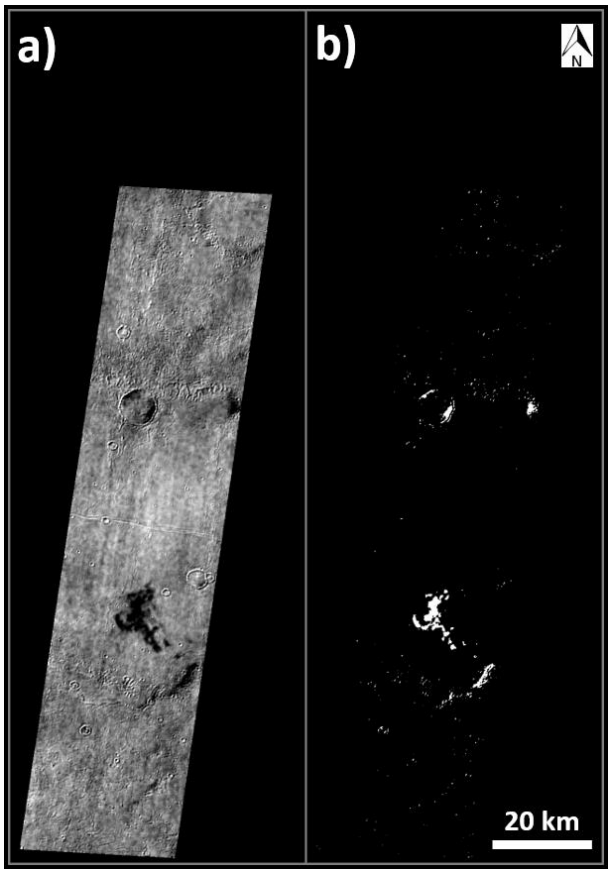

Figure 3.3. PC Proxy for chloride salts: (a) PC3 of THEMIS IR image I52251002; (b) mask of pixels less than three standard deviations below the mean, which acts as a proxy for chloride salts, even though it can also highlight high sunward and anti-sunward slopes.

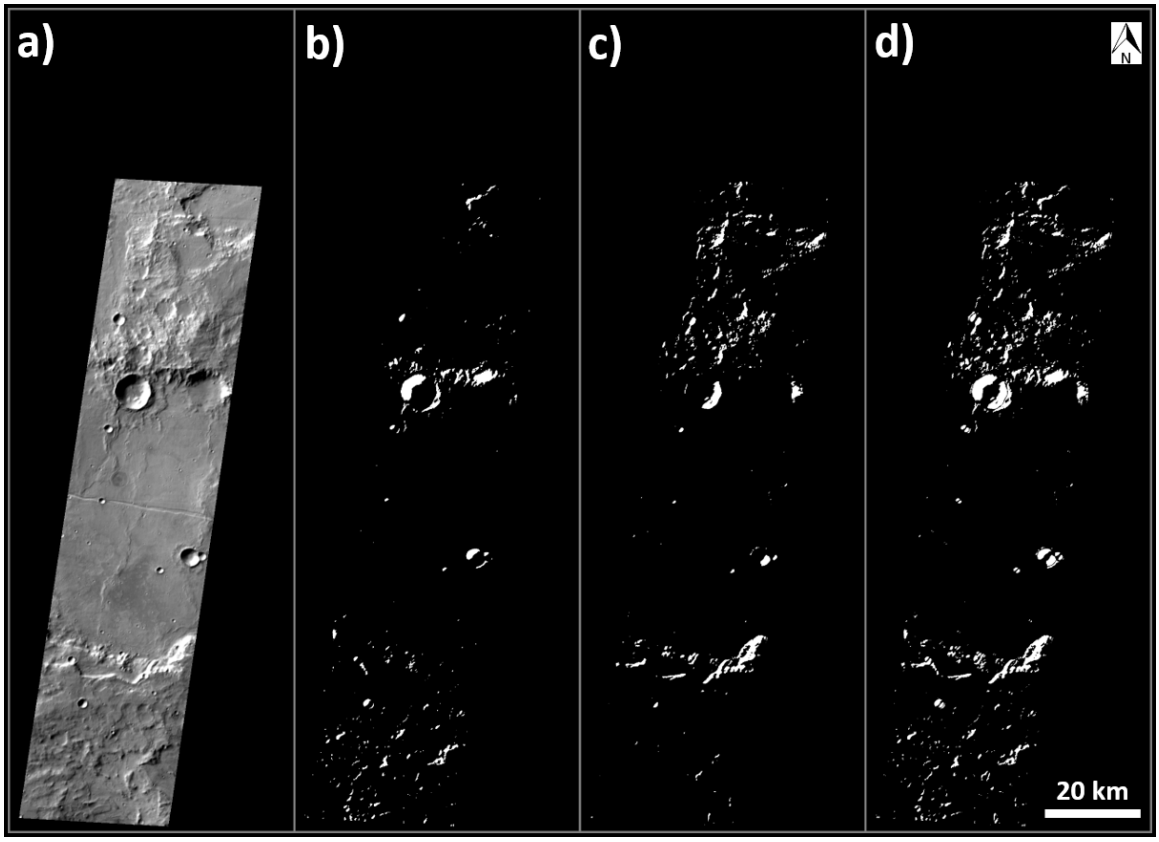

Figure 3.4. PC Proxy for high slopes: (a) PC1 of THEMIS IR image I52251002; (b) mask of pixels less than two standard deviations below the mean; (c) mask of pixels greater than two standard deviations above the mean; (d) combined mask of pixels more than two standard deviations outside the mean, which is a proxy for high slopes.

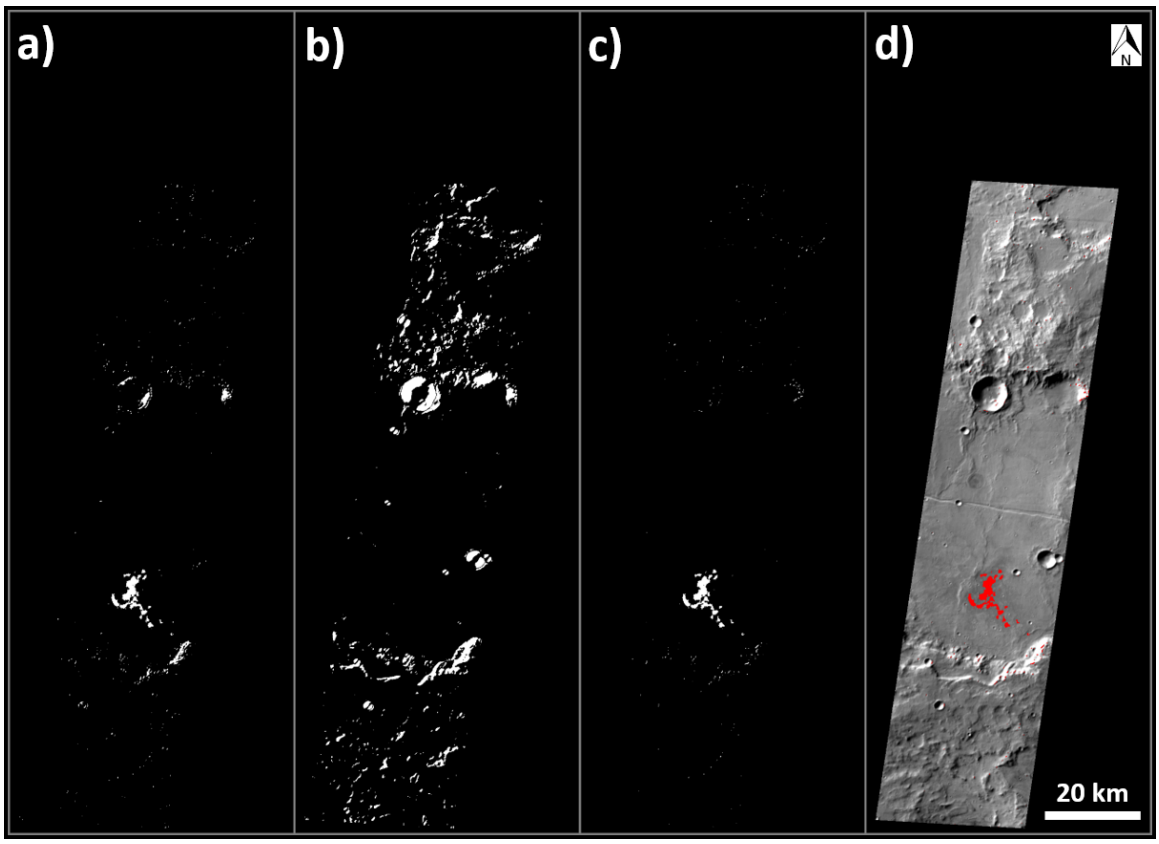

Figure 3.5. Calculating the THEMIS PC Chloride Index: (a) chloride salts proxy mask from PC3; (b) high slope proxy mask from PC1; (c) THEMIS PC Chloride Index mask, calculated by subtracting (b) from (a); (d) colorized THEMIS PC Chloride Index mask overlaid on the PC1 image for context.

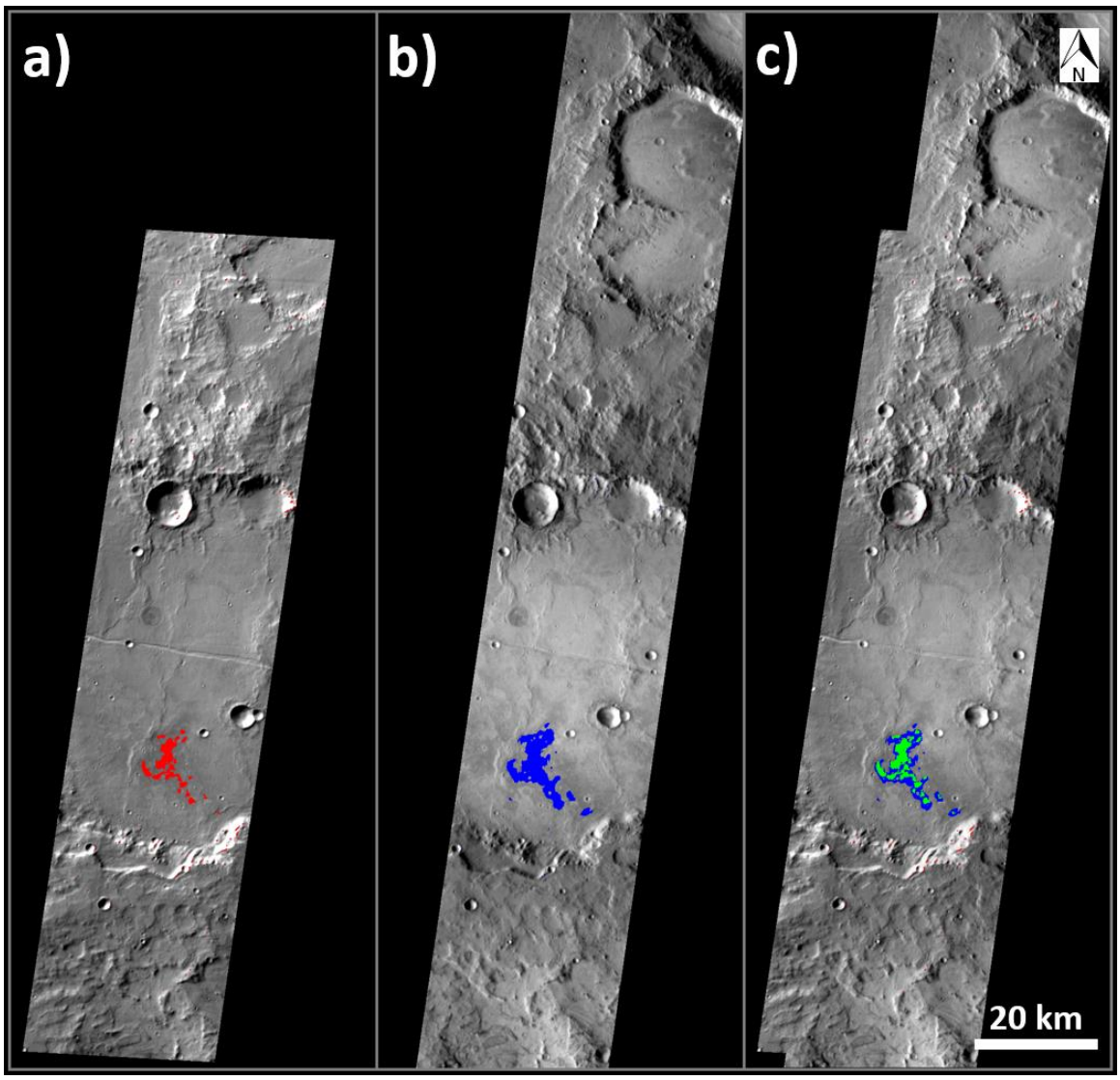

Figure 3.6. Increasing THEMIS PC Chloride Index detection confidence: (a) THEMIS PC Chloride Index mask calculated from THEMIS IR image I52251002 overlaid on the PC1 Image in red; (b) THEMIS PC Chloride Index mask calculated from THEMIS IR Image I15559004 overlaid on the PC1 image in blue; (c) combined THEMIS PC Chloride Index mask with pixels detected in both (a) and (b) shown in green overlaid on a PC1 image mosaic.

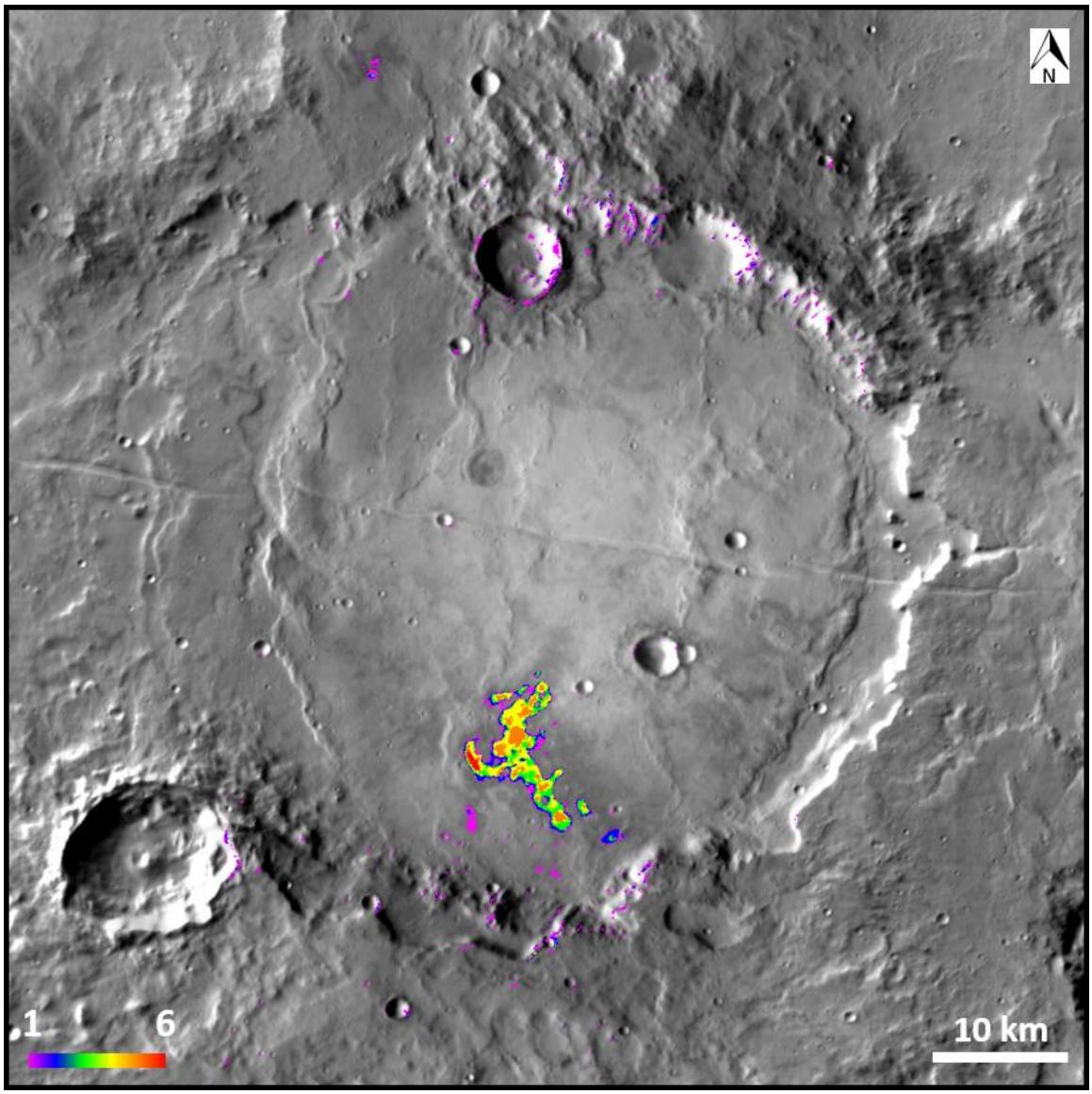

Figure 3.7. THEMIS PC Chloride Index confidence map calculated using all available overlapping high-quality late-afternoon THEMIS IR images overlaid on a THEMIS IR band 9 mosaic, with likely false positives at very low confidence levels.

3.3.3 Chloride Index Sensitivity Analysis

Equations 3.1-3.3 include two parameters, n1 and n3, that control the sensitivity of the THEMIS PC Chloride Index. In order to determine the optimal value of each parameter, a sensitivity analysis was performed by varying each parameter by ± 0.5 and calculating the resulting THEMIS PC Chloride Index confidence map for the chloride salt site shown in Figure 3.7. The results of this analysis are shown in Figure 3.8.

Figure 3.8e is a reproduction of Figure 3.7, with n1=2.0 and n3=3.0. The value of n1 is then varied along the y-axis and n3 is varied along the x-axis. Using these axes, the THEMIS PC Chloride Index becomes increasingly restrictive along the lower-left to upper-right diagonal, while also producing fewer false positive detections along that same diagonal. Therefore, a trade-off must be made regarding the sensitivity parameters: the index needs to be sensitive enough to maximize the number of true positive detections, while also minimizing the number of false positive detections.

Ultimately, the ideal sensitivity parameter values were determined to be n1=2.0 and n3=3.0, as shown in Equations 3.4a and 3.4b. This combination detects most of the known chloride sites while producing a relatively small number of false positive detections. However, it is still useful to consider the results from other parameter combinations along the lower-left to upper-right diagonal. Calculating the index with n1=1.5 and n3=3.5 produces essentially no false-positive identifications and can be used to further increase confidence in the validity of a particular chloride salt detection. Calculating the index with n1=2.5 and n3=2.5 produces an increased number of identifications that can help establish the true extent of a specific chloride salt site, even

though it tends to produce relatively large numbers of false positive identifications elsewhere in the images.

Moving forward, the chloride sites identified in the new global survey will be classified according to the least-restrictive set of these sensitivity parameters that results in their identification: 1) sites that are only identified using n1=2.5 and n3=2.5; 2) sites identified using n1=2.0 and n3=3.0 or less restrictive values; 3) sites identified using n1=1.5 and n3=3.5 or less restrictive values; and 4) sites not identified using any of these parameter combinations.

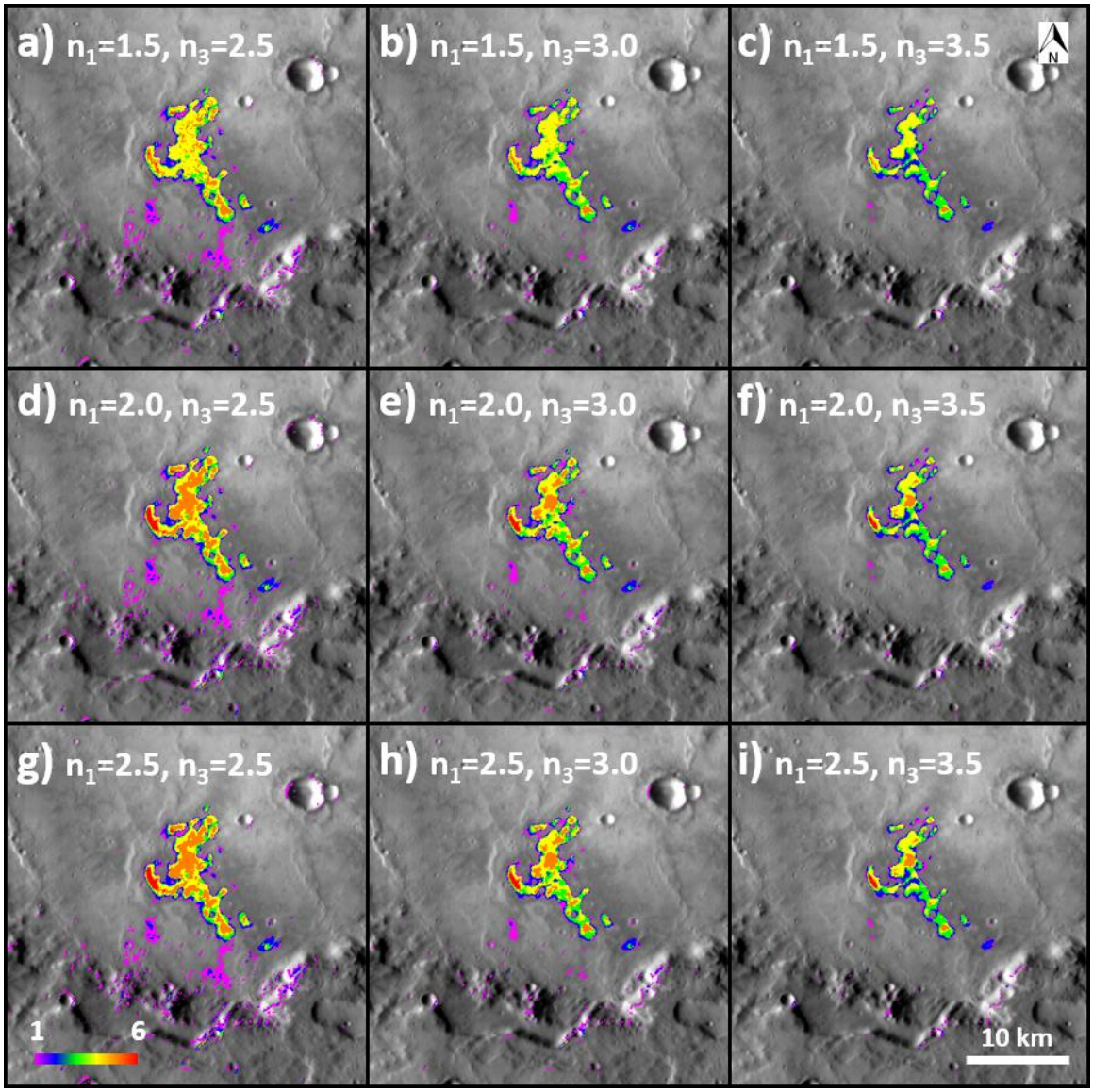

Figure 3.8. THEMIS PC Chloride Index confidence maps calculated using the same THEMIS IR images as Figure 3.7, but with varying sensitivity parameter (n_1 and n_3) values.

3.3.4 Re-Mapping Chloride Site Extents

When the Osterloo et al. (2010) chloride survey was conducted, polygons were drawn around each site using THEMIS DCS images as the primary guide for determining the boundaries. Now, with global CTX coverage and global THEMIS PC Chloride Index detections available, more accurate polygons can be drawn for each site, which will allow more accurate areal statistics to be calculated.

An example comparison of the original and updated chloride site polygons are shown in Figures 3.9a and 3.9b, with a closer view of the updated polygon in Figure 3.9c. Figures 3.9d-3.9f show THEMIS PC Chloride Index confidence maps using different sensitivity parameter combinations, which were used in conjunction with the underlying CTX image to determine more accurate boundaries for this particular chloride salt site. The final polygon shape was drawn based on a subjective geologic interpretation of the true bounds of the chloride salts at the spatial resolution of the CTX image mosaic, which is much higher spatial resolution than the THEMIS IR image data and accompanying THEMIS PC Chloride Index detections.

This re-drawing process was performed for all 642 chloride sites identified by Osterloo et al. (2010), which resulted in some sites being split and others being combined. The remaining sites identified by the updated survey were drawn using the same method from the start.

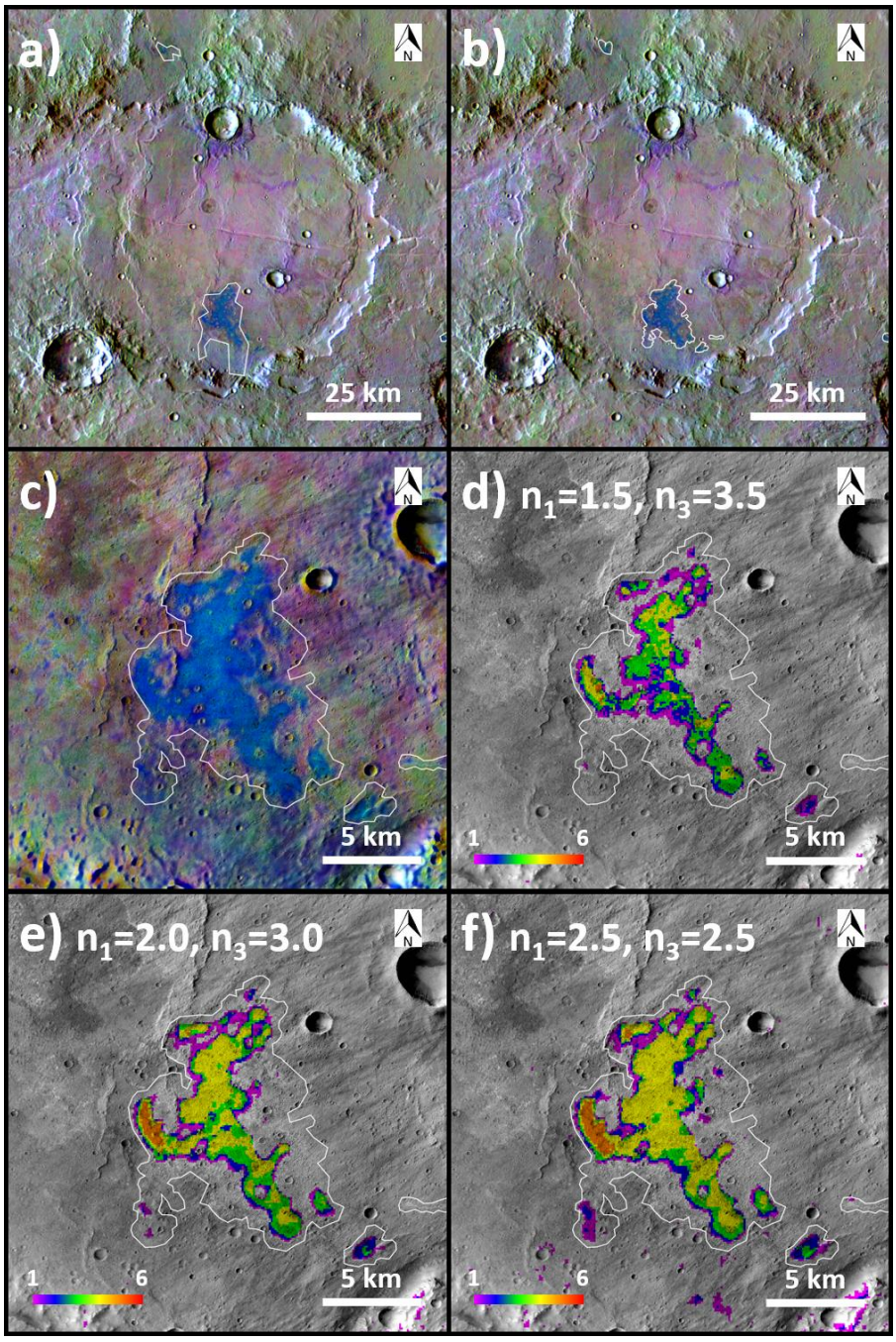

Figure 3.9. Example of a redrawn chloride salt site polygon at -27.25°N, 180.45°E: a) original polygon from Osterloo et al. (2010) overlaid on a THEMIS DCS 875 image mosaic; b) re-drawn polygon from this work overlaid on the same THEMIS DCS 875 image mosaic; c) a closer view of the re-drawn polygon from (b) overlaid on a saturation-enhanced THEMIS DCS 875 mosaic; d) THEMIS PC Chloride Index detections for n_1=1.5 and n_3=3.5 overlaid on a CTX mosaic; e) THEMIS PC Chloride Index detections for n_1=2.0 and n_3=3.0 overlaid on a CTX mosaic; f) THEMIS PC Chloride Index detections for n_1=2.5 and n_3=2.5 overlaid on a CTX mosaic.

3.3.5 THEMIS PC Chloride Index Validation

Validating the THEMIS PC Chloride Index is difficult because of the inherent uncertainty in identifying any Martian chloride salt site, particularly when there are no independent datasets capable of identifying chloride salts at these spatial scales. The best available dataset to judge the THEMIS PC Chloride Index results against is the global chloride survey conducted by Osterloo et al. (2010), which identified 642 chloride sites by manual inspection of THEMIS DCS images.

A close inspection of the original polygons used by Osterloo et al. (2010) found that many were slightly, but significantly, shifted away from the features they were meant to highlight. This is most likely due to slight image projection issues in the JMARS software's THEMIS Stamp Layer that existed at the time of the Osterloo et al. (2010) survey. To make an accurate assessment of the Osterloo et al. (2010) chloride sites, the original polygons were shifted slightly, where needed, to match the features they were meant to highlight.

Global maps of THEMIS PC Chloride Index detections were generated for each of the three combinations of sensitivity parameters previously discussed and compared against the shifted Osterloo et al. (2010) polygons to determine how many were re-identified.

The chloride sites were divided into four categories, as shown in Figure 3.10: 1) multiple detections (>=2 detections, indicating high confidence); 2) single detection (indicating marginal confidence); 3) single detections where only a single image is available (indicating marginal confidence, but due to lack of data); and 4) non-detections.

As expected, Figure 3.10a shows that the most restrictive version of the THEMIS PC Chloride Index only results in approximately two-thirds of the 642 Osterloo et al. (2010) chloride sites being re-identified with highly-confident detections, with a relatively large percentage of single detections and non-detections. The percentage of highly-confident detections increases to ~78% in Figure 3.10b and ~88% in Figure 3.10c, with increasingly less-restrictive sensitivity parameter combinations. The numbers of single detections and non-detections similarly decrease. In all cases, the number of single detections due to only a single image being available remained below 1%, indicating that lack of data does not significantly influence the overall results of these validation tests.

Interestingly, even when applying the least restrictive combination of sensitivity parameters, 19 sites identified by Osterloo et al. (2010) are still not re-identified by the THEMIS PC Chloride Index. One of these sites, located at -14.37°N and 142.53°E is covered by multiple HiRISE images, so it was investigated further.

Figure 3.11a shows the re-drawn polygon based on the original identification by Osterloo et al. (2010) overlaid on a mosaic of HiRISE Color, HiRISE Red, and CTX images. A heavily degraded channel-like feature is located at the center of the polygon, but only a few small white patches in the color image section appear consistent with chloride salts. Figure 3.11e shows the complete lack of THEMIS PC Chloride Index identifications in the area using n_1=2.5 and n_3=2.5, the least restrictive set of sensitivity parameters.

Figures 3.11b, 3.11c, and 3.11d show the same area in THEMIS DCS 875, 964, and 642 images, respectively, overlaid on a CTX image for improved geologic context. The largest occurrence of the white-toned units corresponds to a blue patch in the DCS 875

image, which is consistent with chloride salts. However, the same site does not correspond to a diagnostic teal color in the DCS 964 image or a diagnostic yellow/orange color in the DCS 642 image. Therefore, the identification of this feature as a chloride salt site by Osterloo et al. (2010) was originally relatively weak.

Figures 3.11f and 3.11g show the same area in PC1 and PC3 images, respectively, which were calculated using the global WNR covariance matrix. The channel-like feature has average values in PC1, but is not dark in PC3, which resulted in a lack of THEMIS PC Chloride Index detections.

Overall, it is likely that the small white-toned sites in this area are chloride salts. However, the lack of a quantitative identification is expected because they are small enough and dispersed enough that the spatial resolution of THEMIS IR images cannot detect them. It is possible, even likely, that higher resolution infrared data in the future could lead to PC Chloride Index identifications in this area.

For this reason, the chloride sites identified by either the Osterloo et al. (2010) survey or the updated global survey that do not result in THEMIS PC Chloride Index detections are still being kept in the survey results, but are classified as non-detections.

Ultimately, the THEMIS PC Chloride Index was determined to be sufficiently consistent with the results of the Osterloo et al. (2010) survey that it could be used to effectively survey the planet for additional occurrences of chloride salts.

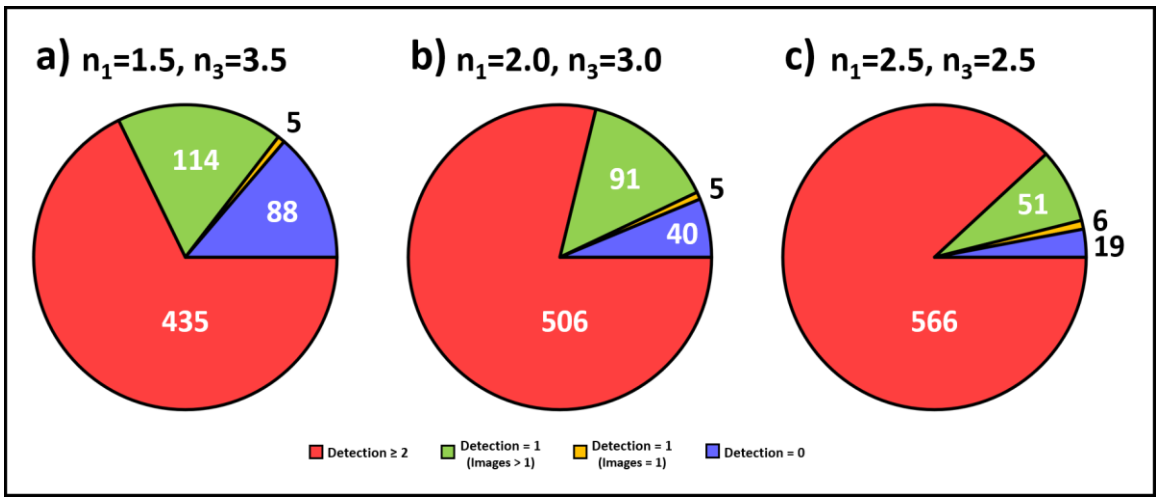

Figure 3.10. THEMIS PC Chloride Index detections of the 642 Osterloo et al. (2010) chloride sites using different sensitivity parameters.

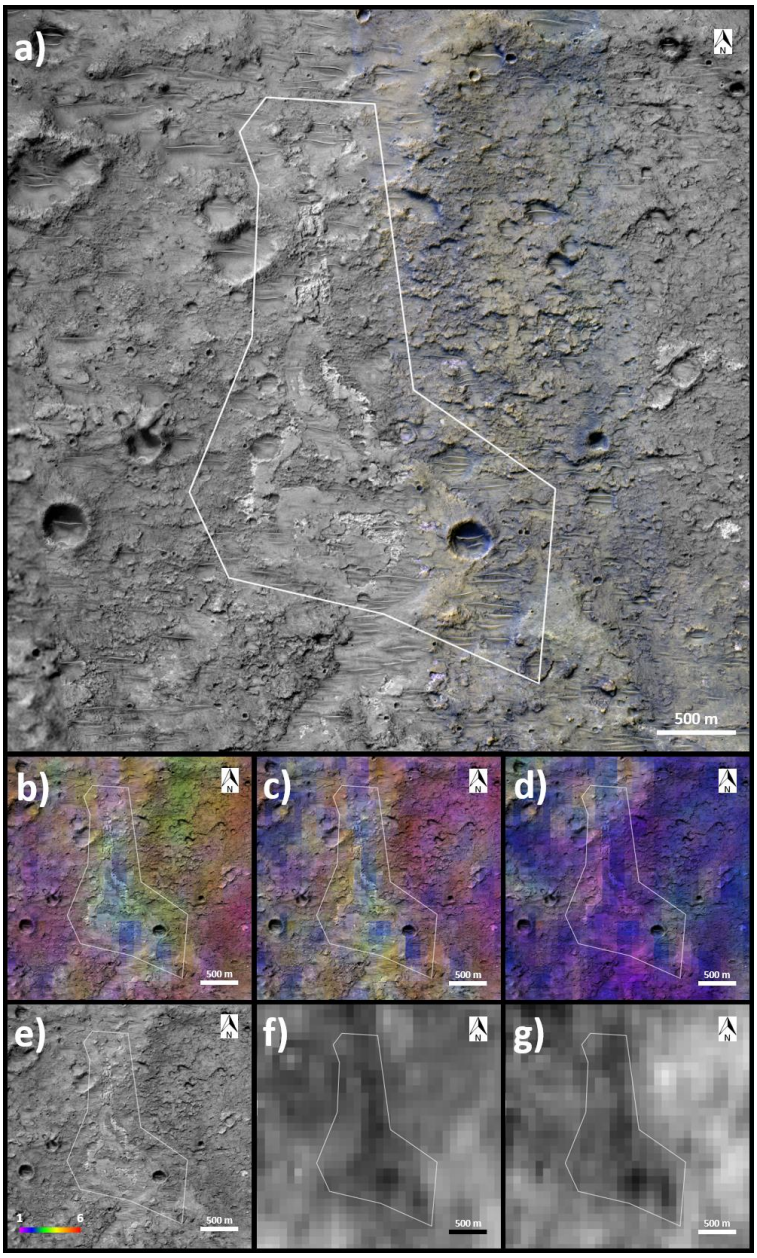

Figure 3.11. Investigation of THEMIS PC Chloride Index non-detection at -14.37°N, 142.53°E: a) re-drawn polygon overlaid on a HiRISE Red and Color image mosaic; b) global DCS 875 of THEMIS image I17632001, showing the diagnostic blue color within the polygon; c) global DCS 964 of THEMIS image, showing a lack of the diagnostic teal color within the polygon; d) global DCS 642 of THEMIS image, showing a lack of the diagnostic yellow/orange color within the polygon; e) THEMIS PC Chloride Index detections overlaid on a HiRISE Red image mosaic, showing no detections in the vicinity of the polygon; f) global PC1 of THEMIS image I17632001, with average value pixels within the polygon; g) global PC3 of THEMIS image, with no excessively dark pixels within the polygon, which resulted in the THEMIS PC Chloride Index non-detection.

3.4 Results

3.4.1 Global THEMIS PC Chloride Index Maps

The THEMIS PC Chloride Index was applied to the same dataset of THEMIS IR images used by Hill and Christensen (2022a) to calculate the Global WNR Covariance Matrix.

This included all high-quality, late-afternoon THEMIS IR images acquired at full-resolution with all ten bands between 60°N and 60°S. Additionally, only images with minimum surface brightness temperatures of 225K or greater were included, because the radiance correction in the standard THEMIS processing pipeline (Bandfield et al., 2004) often fails for colder images, resulting in decorrelation stretched images over-emphasizing sunlit and shadowed slopes. And finally, any images that failed during the standard THEMIS processing pipeline due to data dropouts, stray light artifacts, unusually high instrument noise, focal plane temperature instability, or any other issues were removed from the analysis. This resulted in a dataset of 29,922 images.

The resulting THEMIS PC Chloride Index images were then added together, accounting for their geographic location on the surface, to form a near-global map. This process was repeated for each of the three sensitivity parameter combinations used in Figure 3.10.

The three THEMIS PC Chloride Index maps are included in the supplementary material.

3.4.2 Improved Chloride Site Survey

The THEMIS PC Chloride Index global maps for the three sensitivity parameter combinations were used in conjunction with CTX global image coverage to conduct a near-global survey of chloride salts between 60°N and 60°S. The THEMIS PC Chloride Index global maps were used to guide the survey. Candidate detections were further investigated using CTX images and other datasets (HiRISE and HRSC) where the data was available. This new survey identified a total of 1,605 chloride salt sites.

Figure 3.12 shows a breakdown of how all 1,605 chloride sites were classified by the THEMIS PC Chloride Index using the different sensitivity parameter combinations, similar to the analysis of the original Osterloo et al. (2010) chloride sites in Figure 3.10.

When the sensitivity parameters n1=1.5 and n3=3.5 are used, the THEMIS PC Chloride Index identifies less than half of the chloride sites with multiple detections and over a quarter of the sites were completely undetected. This is expected since it has already been established that this parameter combination under-detects chlorides sites in an attempt to minimize false positive single detections.

When the sensitivity parameters n1=2.0 and n3=3.0 are used, the THEMIS PC Chloride Index performs better, identifying over half of the sites with multiple detections and leaving only ~ 16.5% of the sites undetected. However, when the sensitivity parameters n1=2.5 and n3=2.5 are used, the PC Chloride Index identifies ~75% of the sites with multiple detections and leaves only ~8.8% undetected. These undetected sites are suspect, but as previously shown, additional high-resolution data could later reveal that they do contain chloride salts as initially suspected by a subjective inspection of the data.

Similar to the previous analysis of the Osterloo et al. (2010) chloride sites, a very small number (~ 1.2%) of the sites identified in this survey have single detections due to only a single THEMIS IR image being available for analysis, indicating that gaps in THEMIS IR repeat coverage do not significantly affect this survey.

Figure 3.13a shows all 1,605 chloride sites plotted on a colorized MOLA topographic map of the Martian surface (Smith et al., 2001). The individual points have been color-coded: 1) white points are identified in all three sensitivity parameter combinations; 2) gray points are not identified using n1=1.5 and n3=3.5, but are identified using n1=2.0 and n3=3.0 and less-restrictive combinations; 3) black points are only identified using the least-restrictive combination of n1=2.5 and n3=2.5; and 4) red points not detected in any of these three standard parameter combinations.

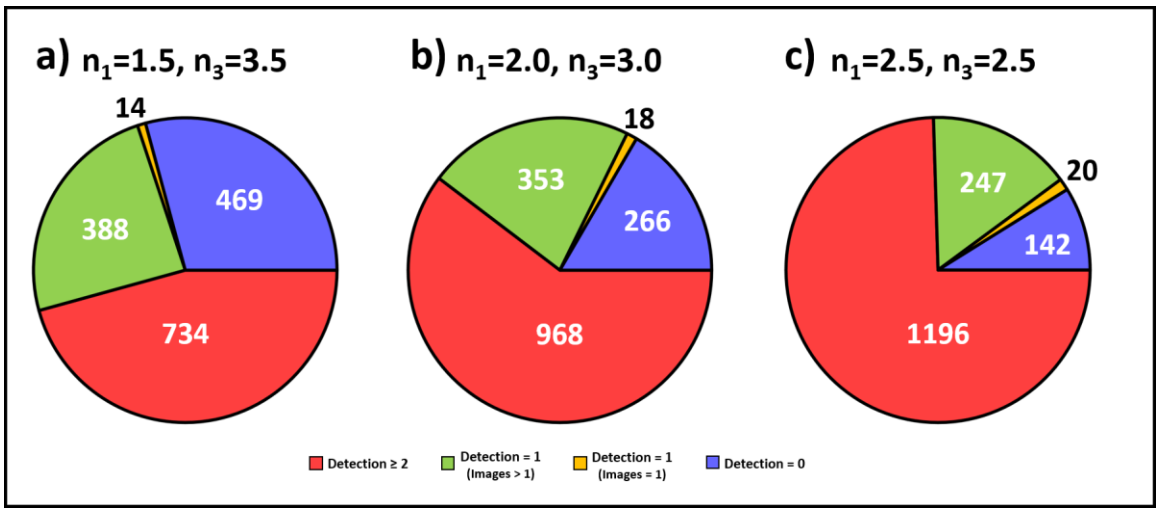

Figure 3.12. THEMIS PC Chloride Index detections of the chloride sites identified by this study using different sensitivity parameters.

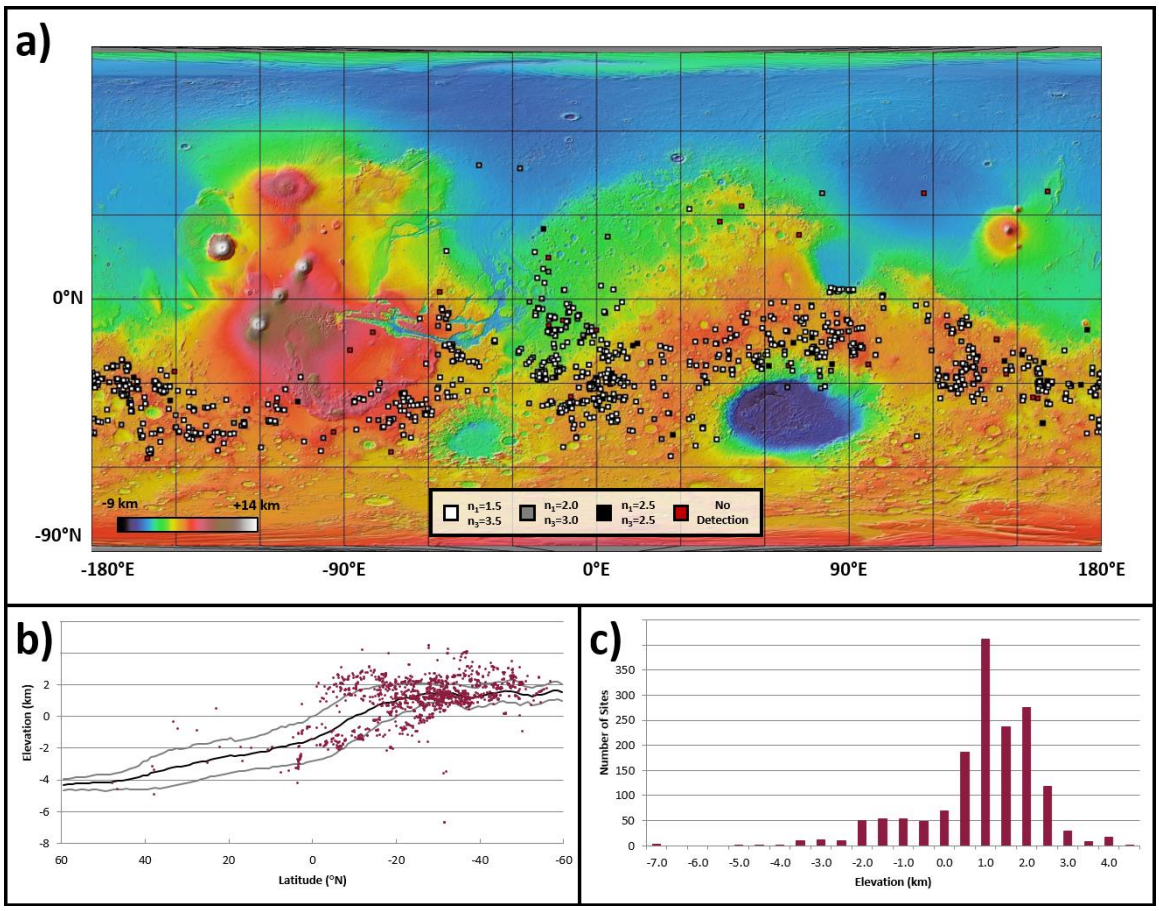

Figure 3.13. Distribution of chloride sites versus elevation: a) chloride sites plotted on the colorized MOLA elevation map; b) scatter plot of chloride sites versus elevation; with average elevation line (black) and average ±1 standard deviation elevation lines (gray); c) histogram of chloride sites in 0.5km elevation bins.

3.4.3 Global Chloride Site Shapefile

All 1,605 chloride sites identified by this survey were outlined with polygons at the resolution of CTX images (~6m/pix), according to the procedure in Section 3.4. The resulting shapefile is included in the supplementary material.

This shapefile enabled the entire chloride site population to be studied as a whole relative to various global properties. For example, Figure 3.13b shows the chloride sites plotted against elevation and latitude, while Figure 3.13c shows a histogram of the chloride site distribution across different elevations.

3.5 Discussion

3.5.1 Chloride Sites versus Elevation

This survey identified many new chloride sites, but the overall assessment made by Osterloo et al. (2010) was confirmed: chloride salts are mainly constrained to the Martian southern highlands. The only potential exception is a cluster in Margaritifer Terra, south of Meridiani Planum, which might not qualify as part of the southern highlands depending on the definition being used.

Figure 3.13b shows the chloride site elevations plotted against latitude. For comparison purposes, the average elevation profile between 60°N and 60°S is plotted in black, with gray lines representing one standard deviation above and below the average. These average lines exclude major impact basins and volcanic provinces between 40°E-110°E (Hellas Planitia), 140°E-155°E (Elysium Mons), and 220°E-340°E (Olympus Mons, Tharsis, Valles Marineris, and Argyre Planitia) in order to more accurately estimate the overall global dichotomy. The point distribution confirms that the vast

majority of chloride sites are located in the southern highlands, although there are numerous interesting outliers that should be investigated in more detail in the future.

Figure 3.13c shows a histogram of chlorides sites across elevation using 0.5km bins. This confirms the results of Osterloo et al. (2010), which concluded that chloride sites are typically located between 1,000m and 3,000m above the datum. However, this work identifies a significant subset of sites occurring between 1.0km and 1.5km above the datum, roughly corresponding to the lower elevations within the southern highlands.

For comparison purposes, Figure 3.13 mirrors a similar summary presented in Figure 9 of Osterloo et al. (2010).

3.5.2 Chloride Sites versus Terrain Age

The results of this study can provide a more accurate estimate of the chloride sites' ages based on their surrounding terrain. This is possible primarily due to the publication of the updated Geological Map of Mars by Tanaka et al. (2014), which was not available to Osterloo et al. (2010) at the time of their analysis. The increased number of chloride sites identified by this study also adds statistical significance to the observed age distributions.

Osterloo et al. (2010) determined that the chloride sites were primarily located in terrains from the Middle Noachian to the Early Hesperian. However, as shown in Figure 3.14, this work has determined that the vast majority of chloride salts occur in terrains from the Early to Late Noachian, with very few occurring in Early Hesperian and younger terrains.

The distribution of chloride sites across different-aged units can be considered in terms of both raw area and normalized area (the area of the chloride site divided by the total area of the geologic unit where it is located). Figure 3.14b shows that in terms of raw area, the chloride sites are mostly located in Middle Noachian-aged terrains. Figure 3.14c shows that in terms of normalized area, the chloride sites are primarily located in Late Noachian-aged terrains. In both cases, the analysis was performed with and without the non-detected sites, which ultimately did not significantly affect the observed distributions.

These results are interpreted as indicating that most of the chloride salts currently exposed on the Martian surface are found in Middle Noachian-aged terrains, but they are much more common in Late Noachian-aged terrains, which cover a smaller percentage of the planet.

Overall, these results show that the precipitation of chloride salts occurred as early as the Early Noachian period, indicating water-rock interactions occurred on large scales during these earliest periods of Martian history. These interactions, and the subsequent precipitation of chloride salts, then came to a relatively abrupt end at the Noachian-Hesperian boundary, with only a small number of sites remaining active into the Early Hesperian.

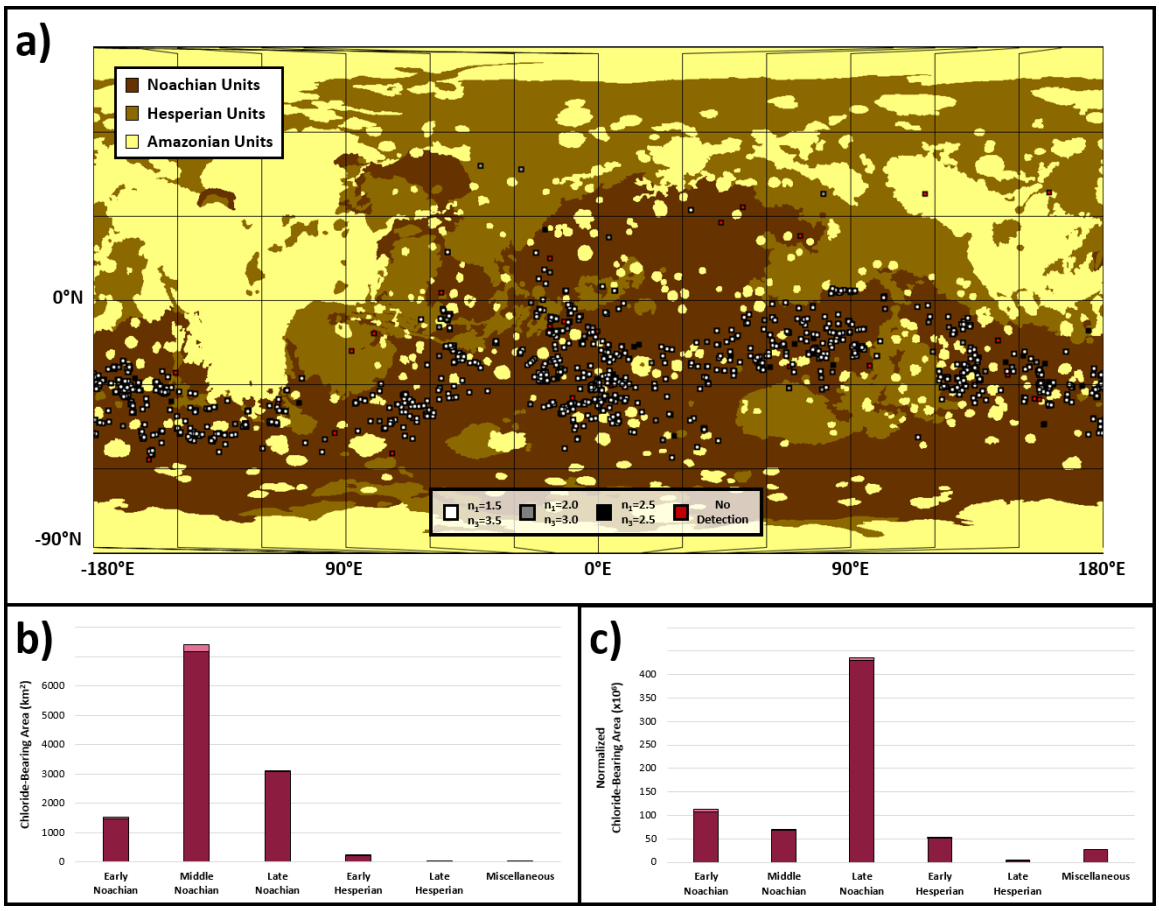

Figure 3.14. Distribution of chloride sites versus geologic period units from the Geologic Map of Mars (Tanaka et al., 2014): a) chloride sites plotted on a geologic map, with units combined by geologic period; b) histogram of chloride site raw area versus geologic period, with THEMIS PC Chloride Index detected sites in dark maroon and non-detected sites in light maroon; c) histogram of chloride site normalized area versus geologic period, with detected sites in dark maroon and non-detected sites in light maroon.

3.5.3 Chloride Sites versus Thermal Inertia

The improved survey of chloride sites has also enabled a more statistically-significant study of their thermophysical characteristics.

Figure 3.15a shows the chloride sites plotted on a colorized map of median nighttime thermal inertia (Putzig and Mellon, 2007). The average thermal inertia of the terrain surrounding the chloride sites is 257 tiu, lower than the average of ~300 tiu calculated by Osterloo et al. (2010), but still consistent with their interpretation of indurated materials with dust cover.

The vast majority of chloride sites fall within the bounds of the "Unit 4" described by Putzig et al. (2005), which is characterized by high thermal inertia and high elevation. This is demonstrated graphically in Figure 3.15b, where nearly all the sites occur above the datum in the southern highlands and have relatively high thermal inertia values between 200-350tiu. Figure 3.15c shows that the chloride site thermal inertias have a Gaussian distribution centered at a median value of 251 tiu, which is consistent with "Unit 4" materials.

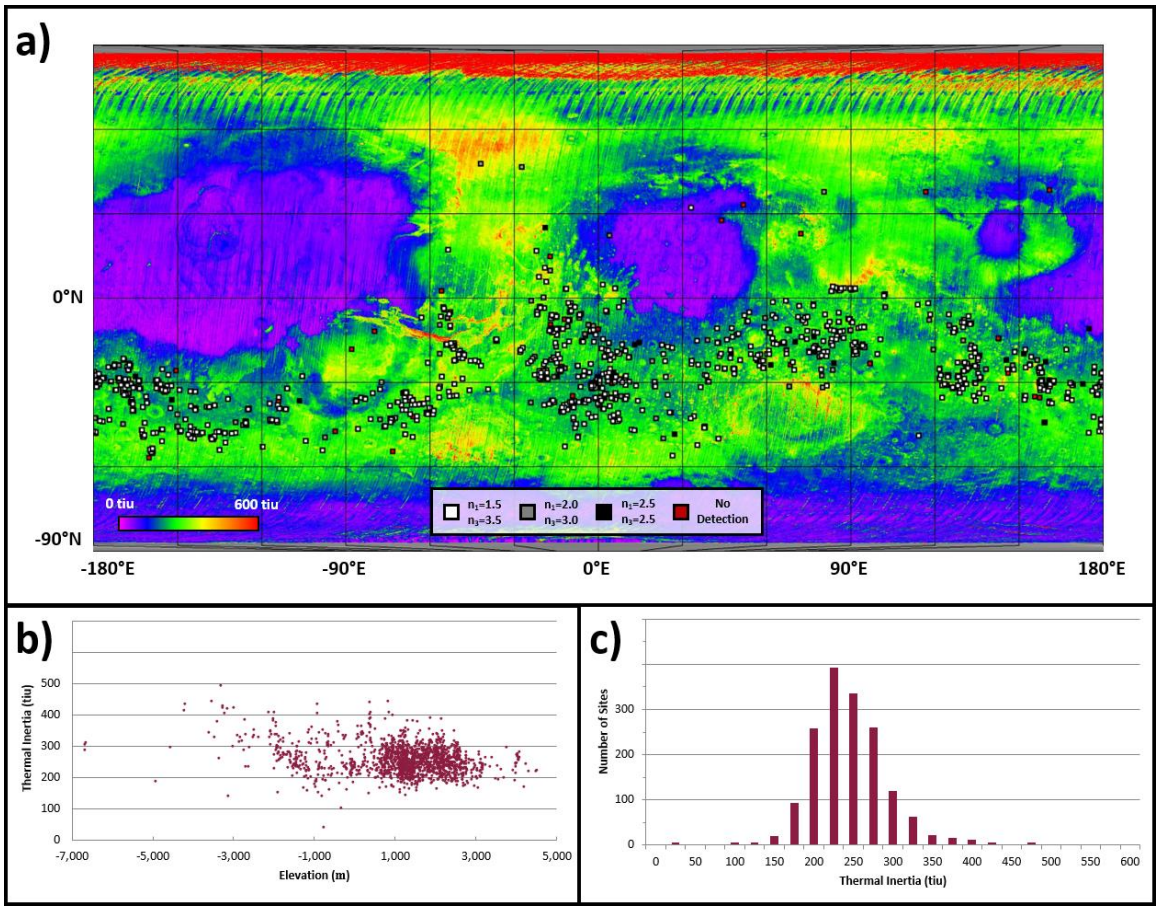

Figure 3.15. Distribution of chloride sites versus median nighttime thermal inertia (Putzig and Mellon, 2007): a) chloride sites plotted on the median nighttime thermal inertia map; b) scatter plot of chloride site thermal inertia versus elevation; c) histogram of chloride site thermal inertias in 25 tiu bins.

3.5.4 Chloride Sites versus Albedo

Osterloo et al. (2010) concluded that nearly all chloride sites are located in low albedo terrains, which is consistent with the results of this updated global survey.

Figure 3.16a shows the chloride sites plotted on the TES Lambert Albedo map, with an obvious correlation between the chloride sites and the low albedo southern highlands. This relationship is quantified in the scatter plot in Figure 3.16b, which shows low albedos with a sharp cutoff at ~0.10 and a less distinct, but still fairly abrupt, cutoff at ~0.19. Similarly, Figure 3.16c shows a histogram of chloride side albedo values with a tight Gaussian distribution centered around a median value of ~0.14 with distinct cutoffs on either side.

Also, Figure 3.16 demonstrates that the chloride sites can also be primarily classified as the "Unit B" materials described by Putzig et al. (2005), due to their relatively high thermal inertias (160-355 tiu) and relatively low albedos (0.10-0.19).

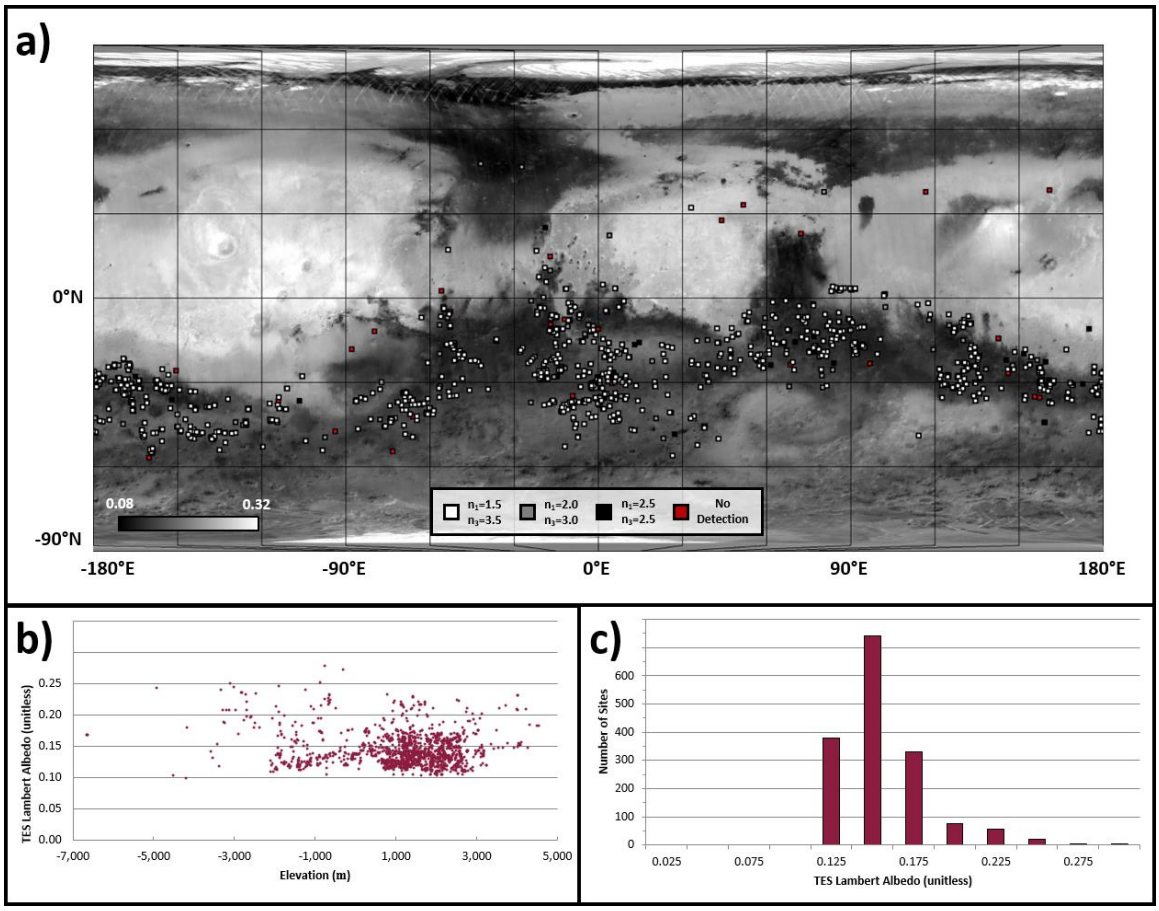

Figure 3.16. Distribution of chloride sites versus TES lambert albedo: a) chloride sites plotted on the TES lambert albedo map; b) scatter plot of chloride site albedo versus elevation; c) histogram of chloride site albedos in 0.025 (unitless) bins.

3.5.5 Chloride Sites versus Dust Cover Index

Osterloo et al. (2010) did not assess the spectral properties of the chloride salt sites, presumably because chloride salts do not have diagnostic features in the spectral ranges of the instruments that have studied Mars to date. However, as demonstrated in this study, chloride salts contain nearly-diagnostic characteristics in THEMIS principal component images, which may behave much like spectral features and become muted by dust cover. Therefore, the TES Dust Cover Index (DCI) (Ruff and Christensen, 2002) was used to assess how spectrally clean the chloride sites are in the thermal infrared wavelengths.

Figure 3.17a shows the chloride sites plotted on the TES DCI map, showing a noticeable correlation with the southern hemisphere's high dust cover index values. Note that the DCI values are colorized in reverse, with high DCI values indicating less dust and low DCI values indicating more dust.

Figure 3.17b plots the chloride site DCI values versus thermal inertia, demonstrating that these two parameters are not equivalent. Thermal inertia is a thermophysical measurement, while DCI is a spectral measurement. The two values may be well-correlated in some situations, but can just as easily be uncorrelated in other situations. Except for a few outliers, the chloride sites are clustered very close to the top of the scale, with an average value of 0.9717 and a median value of 0.9726. This indicates that nearly all chloride sites occur in terrains with spectrally-thin dust covers, which presumably make the principal component features more distinct, similar to the spectral features in the surrounding terrain.

Figure 3.17c shows a histogram of chloride site DCI values, which is roughly Gaussian with a relatively tight distribution around the median value of 0.9726.

These results suggest that additional chloride sites in Noachian-aged terrains with high dust cover (ex: Arabia Terra) might have been missed by this survey because the dust muted the THEMIS principal component features below the detection threshold of the THEMIS PC Chloride Index. Some of the outliers in Figures 3.17b and 3.17c may be due to chloride sites that are dust-free enough to be detected at THEMIS resolution, but are in relatively dust-covered terrains at TES resolution. Therefore, even this survey should not be considered a definitive inventory of the planet's chloride sites.

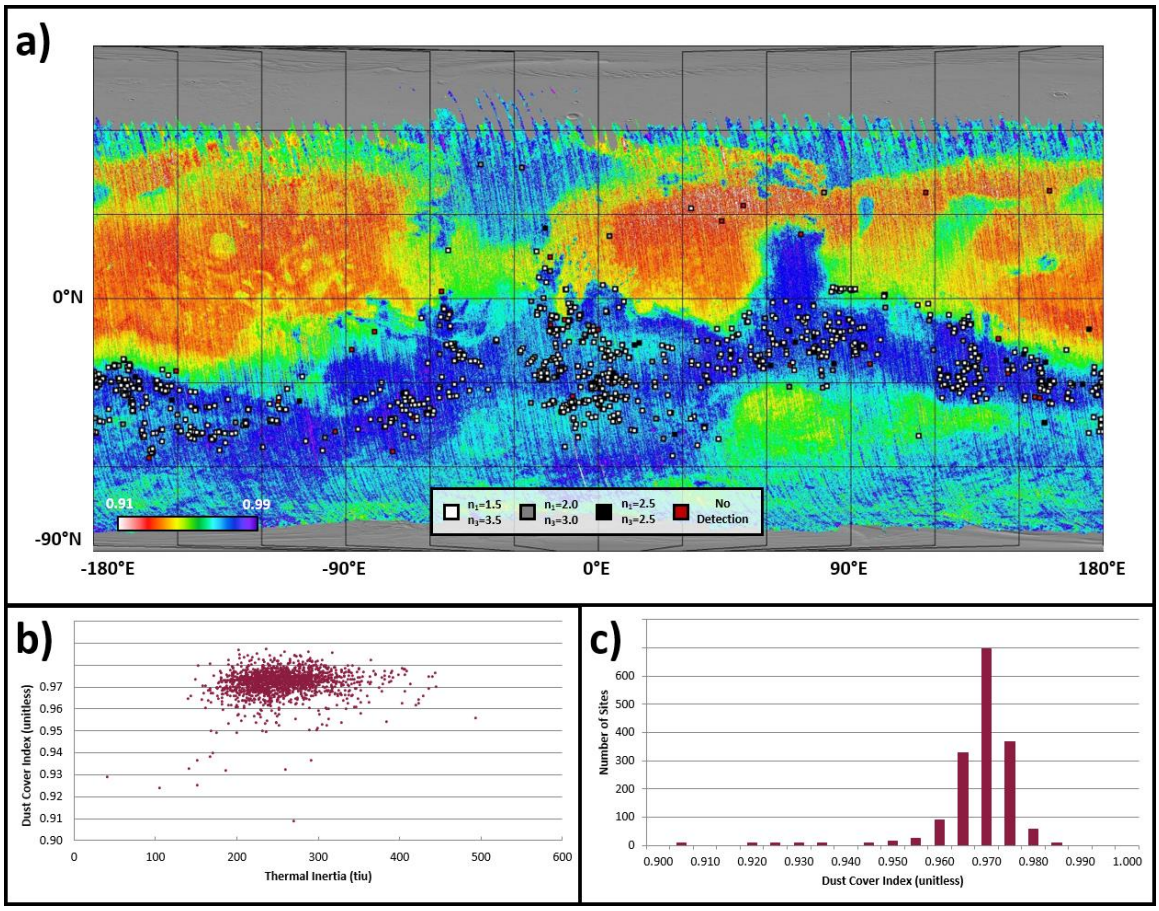

Figure 3.17. Distribution of chloride sites versus TES Dust Cover Index (Ruff and Christensen, 2002): a) chloride sites plotted on the TES Dust Cover Index map; b) scatter plot of chloride site Dust Cover Index values versus thermal inertia; c) histogram of chloride site Dust Cover Index values in 0.005 bins.

3.5.6 Chloride Sites versus Magnetic Field

Osterloo et al. (2010) also did not assess the remnant magnetic field strength of the regions containing chloride salt sites. This relationship was investigated because it could help constrain the time period of chloride salt precipitation relative to the end of the global dynamo. Therefore, the MAG/ER Filtered Radial Magnetic Field map (Connerney et al., 2005) was used to determine the remnant magnetic field strength in the region surrounding each chloride salt deposit.

Figure 3.18a shows the chloride salt sites plotted on the MAG/ER Filtered Radial Magnetic Field map. It appears to show that chloride salt sites preferentially occur in regions with relatively strong magnetic fields, but this is primarily a misconception due to the unusual color scale of the map produced by Connerney et al. (2005).

Figure 3.18b shows that the individual chloride salt sites are clustered around low magnetic field strengths, with only a few outliers in the truly highly magnetized regions of the surface. Figure 3.18c displays this same data as a histogram, showing a Gaussian distribution centered at low negative values. In the future, it would be interesting to examine the outlier deposits, since they might be located in particularly old sections of the Martian crust if they correspond to relatively high remnant magnetic field strengths.

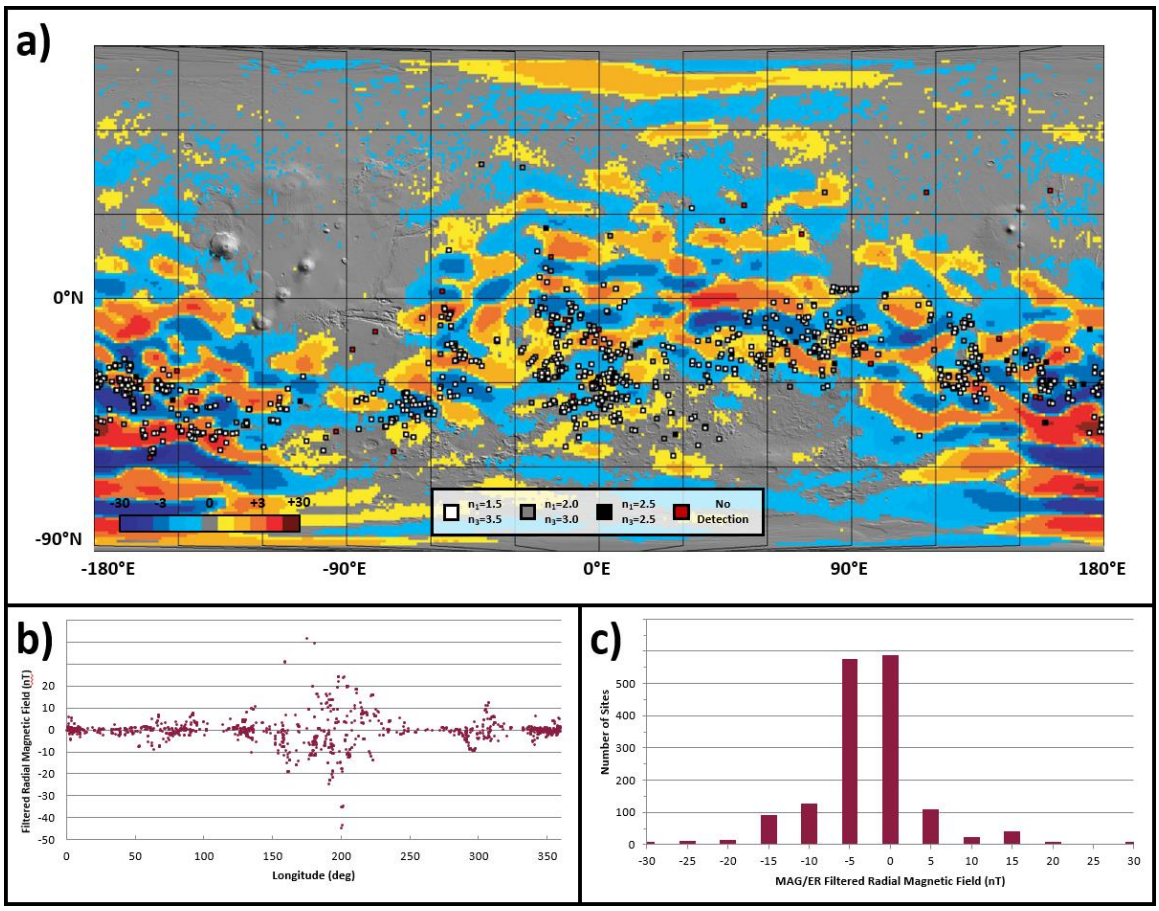

Figure 3.18. Distribution of chloride sites versus MAG/ER Filtered Radial Magnetic Field (Connerney et al., 2005): a) chloride sites plotted on the MAG/ER Filtered Radial Magnetic Field map; b) scatter plot of chloride site magnetic field values versus longitude; c) histogram of chloride site magnetic field values in 5 nT bins.

3.5.7 Chloride Sites versus Elemental Concentrations

Osterloo et al. (2010) did not find any correlation between the chloride sites identified by their survey and the GRS global elemental concentration maps. However, because this updated survey has a larger sample size and the potential for a more statistically-significant analysis, the relationship between the chloride sites and global elemental concentrations was revisited

The primary element of interest is chlorine, since this study is concerned with chloride minerals. Figure 3.19a shows the chloride sites plotted on the GRS chlorine concentration map. There is no apparent global correlation between the chloride site locations and elevated chlorine concentrations. Clusters of chloride sites are seen in regions with relatively high chlorine concentrations, such as in eastern Terra Cimmeria, but can just as easily be found in regions with relatively low chlorine concentrations, such as in southeastern Terra Sirenum.

Unfortunately, GRS is not sensitive to sodium. However, a secondary element of interest is potassium, since it also commonly acts as the cation in chloride salts, at least in terrestrial settings. Figure 3.19b shows the chloride sites plotted on the GRS potassium concentration map. Interestingly, very few chloride sites are located in the relatively potassium-poor regions of the southern hemisphere. There are also some notable clusters of chloride sites in regions with relatively high potassium concentrations, like Terra Cimmeria and Tyrrhna Terra.

Possible correlations between the chloride sites and the various elements detectable by GRS can be more quantitatively assessed using histograms of the elemental concentrations across the entire population of chloride sites, rather than by viewing the locations plotted

on a map. Figure 3.20 presents histograms for the elements detectable by GRS, along with H_2O. The chlorine and potassium histograms, correlating to Figures 3.19a and 3.19b, are shown in Figures 3.20a and 3.20b, respectively.

The histogram of chlorine concentrations appears roughly Gaussian, although the distribution skews towards higher chlorine concentrations. This skewed distribution is encouraging, because it is consistent with the most basic assumption of this study: that the features being studied contain chloride salts. However, it is not particularly surprising that the chloride sites are not always associated with higher chlorine concentrations at the GRS scale (5°x5° bins), since the sites themselves are so small that they would be unable to affect the GRS measurements themselves. Instead, the GRS concentration values represent regional concentration trends, which may or may not be representative of the chloride sites themselves.

The potassium concentration histogram in Figure 3.20b shows an even more noticeable skew towards higher potassium concentrations. These concentrations are roughly comparable to the chlorine concentrations, which is interesting because potassium chloride (sylvite) contains equal parts potassium and chlorine. This skewed distribution is likely due to the clusters of chloride sites in regions with high potassium concentrations seen in Figure 3.19b.

The remaining elements that GRS can detect are not common cations in chloride salts, but it is still informative to quantify their distributions across the chloride site population. For example, Figure 3.20c shows a definite distribution skew towards higher silicon concentrations. This could be interpreted as evidence that chloride sites are more common

in felsic terrains. This would be consistent with the increased concentrations of light elements, such as sodium and potassium, expected in felsic terrains.

On the other hand, Figure 3.20d shows a histogram that skews noticeably towards lower thorium concentrations. Future work should be performed to determine if a potential relationship between chloride salts and lower radioactive element concentrations would provide any valuable insights.

Figure 3.20e is interesting because it shows that chloride sites are associated with a wide variety of regional iron concentrations. Figure 3.20f is interesting because it shows a relatively Gaussian distribution of H_2O abundance, without chloride sites preferentially occurring in either relatively wet or dry terrains. This could be interpreted as evidence that the chloride sites developed in a hydrological regime completely different from the current one.

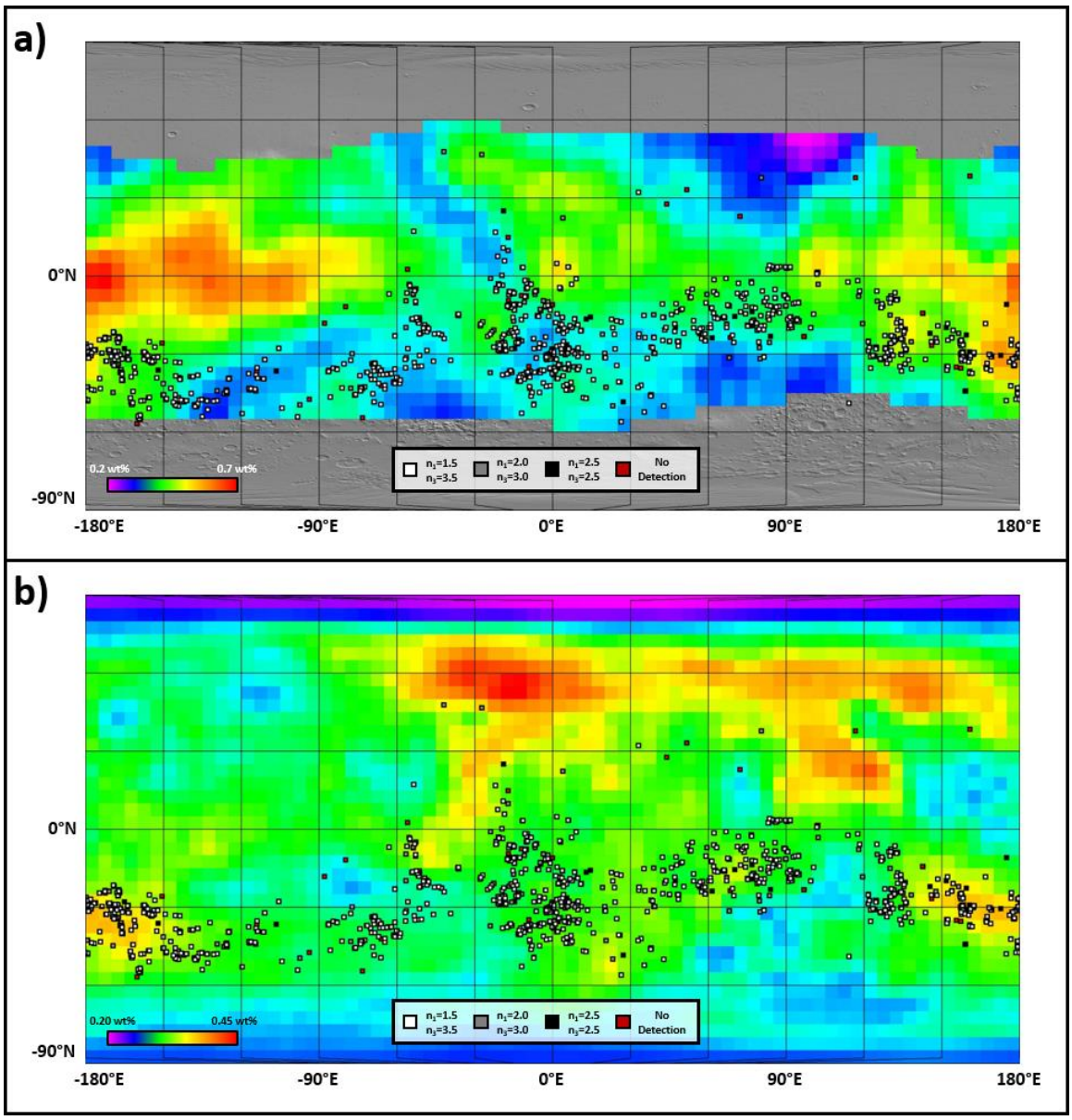

Figure 3.19. Chloride salt site locations relative to chloride mineral cation concentrations: a) chloride sites plotted on the GRS chlorine concentration map; b) chloride sites plotted on the GRS potassium concentration map.

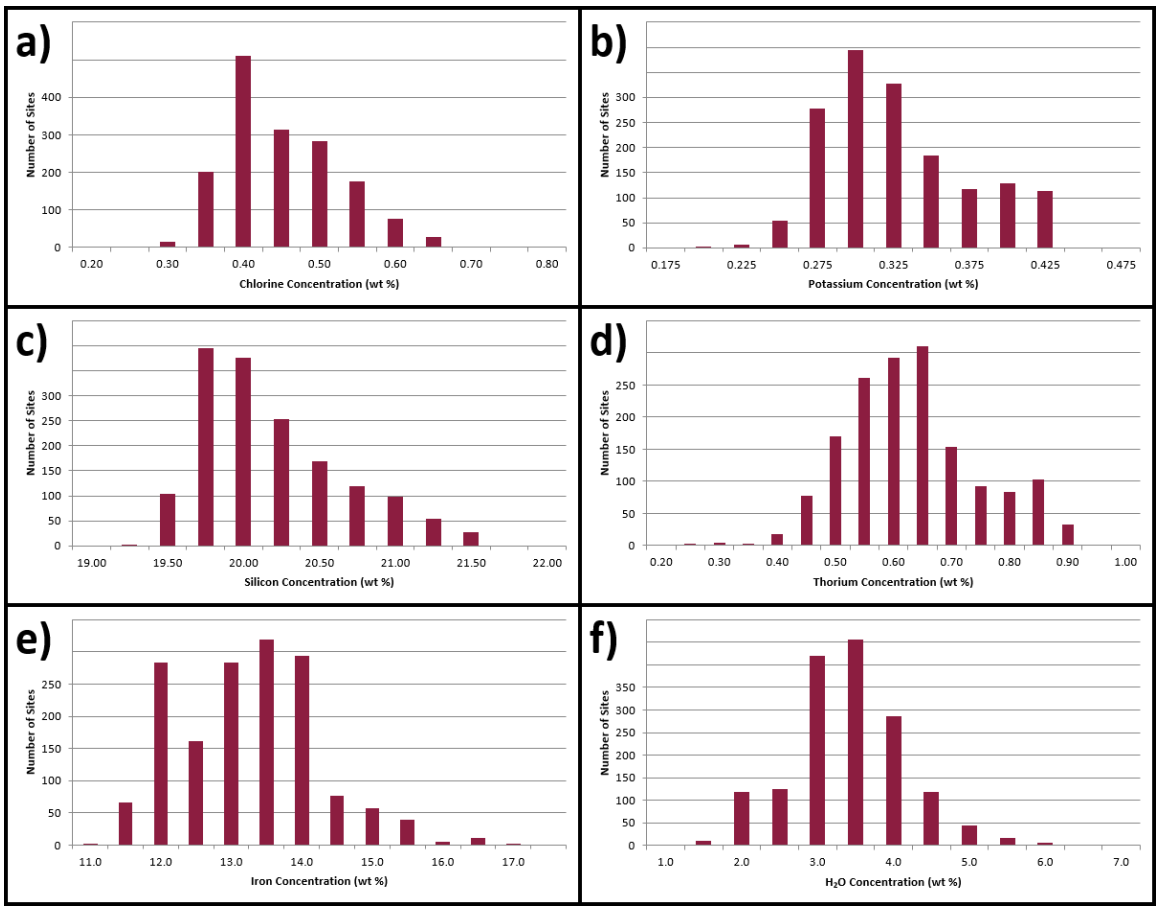

Figure 3.20. GRS elemental concentrations of terrains surrounding chloride salt sites: a) histogram of chlorine concentrations with 0.05 wt% bins; b) histogram of potassium concentrations with 0.025 wt% bins; c) histogram of silicon concentrations with 0.25 wt% bins; d) histogram of thorium concentrations with 0.05 wt% bins; e) histogram of iron concentrations with 0.5 wt% bins; f) histogram of H_2O concentrations with 0.5 wt% bins.

3.6 Conclusions

Expanded global datasets and improved data analysis techniques enabled a more thorough global survey of Martian chloride salts, identifying 1,605 distinct sites. The results of this improved survey confirm the conclusion of Osterloo et al. (2010) that the vast majority of chloride salt sites occur in the Martian southern highlands, although numerous interesting outliers that deserve further investigation were also identified.

Comparing the improved survey results with the Geologic Map of Mars by Tanaka et al. (2014) allowed the terrains surrounding the chloride sites to be dated. These results suggest the timeframe of chloride salt precipitation occurred earlier in Martian history than previously thought. In particular, the Early Noachian terrains contain a much higher percentage of chloride sites than previously reported, while the Early Hesperian terrains contain a much smaller percentage than previously reported. This indicates that the water-rock interactions that led to the formation of chloride salt sites occurred in the earliest periods of Martian history, when the planet was similar to the Earth of the same time period.

A re-analysis of chloride salt distributions compared to global properties did not identify any significant new correlations with thermophysical properties, but did reveal a correlation with spectrally dust-free terrains. This suggests that additional chloride salt sites might exist in dusty terrains, like Arabia Terra, but are obscured from our currently-available remote sensing instruments.

Comparison with global elemental concentrations found chloride sites preferentially occur in terrains with increased chlorine and potassium concentrations. This raises the possibility that potassium chloride could be a significant component of the chloride salt sites. Additionally, the chloride sites were found to preferentially occur in more felsic

terrains, which is not surprising due to the increased concentrations of light elements like silicon, chlorine, and potassium. The current H_2O concentrations of the chloride site terrains have a Gaussian distribution, indicating that the chloride sites are not correlated with the current distribution of water on Mars.

This work will provide future investigators with a more accurate tool for studying Martian chloride salts and new avenues of research relating to their formation.

CHAPTER 4

EVIDENCE FOR CHLORIDE SALT DEPOSITION IN THE EARLY NOACHIAN PERIOD

4.1 Introduction

Chloride salts were discovered on the Martian surface by Osterloo et al. (2008), based on their featureless sloping thermal infrared emissivity spectra, their resulting distinctive colors in decorrelation stretched infrared images, their relatively high thermal inertias, and their light-toned, polygonally-fractured surfaces in visible wavelength images.

Osterloo et al. (2010) conducted a global survey of chloride salts and identified 642 deposits, primarily in the Noachian terrains of the Martian southern highlands. They concluded that most deposits occur in local lows, suggesting that they were either formed by ponded water and/or were exposed in erosional windows that reveal subsurface materials older than the surrounding terrain. Although the individual deposits were small, their prevalence throughout the southern highlands suggested they resulted from a globally ubiquitous process that was active throughout the Noachian period.

The newly-developed THEMIS Principal Component (PC) Chloride Index has enabled the identification of 1,605 chloride salt sites on the Martian surface, of which ~16% (257 sites) are found in Early Noachian terrains, based on the geologic mapping of Tanaka et al. (2014). Their existence in such ancient terrains poses a critical question about their age: were they formed in the Early Noachian contemporaneously with their surrounding terrain, or during later geologic eras and were superimposed on the Early Noachian terrains. Three categories of chloride salt deposits have been identified in Early Noachian terrains as

having characteristics consistent with an Early Noachian origin: circular deposits, regional high deposits, and ejecta deposits.

In this paper, we briefly review our methods, describe and provide examples for each of the three key categories of chloride salt deposits in Early Noachian terrains, and present our interpretation of their most likely formation and modification histories. Then, we discuss what they can tell us about Martian surface conditions during the Early Noachian period, which approximately corresponds to the Hadean-Archean transition on Earth, during which terrestrial life first arose.

4.2 Datasets and Methods

4.2.1 Instrument Descriptions

The Thermal Emission Imaging System (THEMIS), onboard Mars Odyssey spacecraft, consists of two multispectral imaging subsystems: a ten-band thermal infrared (IR) imager and a five-band visible/near-infrared (VIS) imager. The thermal infrared subsystem is a pushbroom imager that acquires data at a nominal spatial resolution of 100 meters/pixel using an uncooled 320×240 pixel microbolometer array covered by ten ~1-μm-bandwidth strip filters centered at nine different wavelengths between 6.8μm and 14.9μm (Christensen et al., 2004). THEMIS IR images were used in this study to identify chloride salt deposits and map their extents via the THEMIS PC Chloride Index.

The Context Camera (CTX), onboard the Mars Reconnaissance Orbiter (MRO), is a pushbroom imager that acquires data at a nominal spatial resolution of ~6m/pixel using a 5056-pixel linear charge-coupled device (CCD) centered at a wavelength of 0.611μm with a full-width half-maximum (FWHM) bandpass of ±0.189μm (Malin et al., 2007;

Bell et al., 2013). CTX images were used in this study to investigate the chloride salt deposits' morphology and qualitatively assess their tone in visible wavelengths, since color images at this resolution are not available for most chloride salt deposits.

The High Resolution Imaging Science Experiment (HiRISE), also onboard MRO, is a pushbroom imager that acquires data at a nominal spatial resolution of 0.25m/pixel using an array of 14 CCD detectors, with ten detectors centered at 0.694μm (red), two detectors centered at 0.536μm (blue-green) and two detectors centered at 0.874μm (near-infrared) (McEwen et al., 2007). The two blue-green and two near-IR detectors are aligned with the center two red detectors, allowing multi-band approximate true color images to be acquired along the center of the HiRISE field-of-view (FOV). HiRISE images were used in this study to qualitatively assess the visible wavelength color of the few chloride salt deposits with HiRISE color coverage and investigate the deposits' morphology at a higher spatial resolution than is possible with CTX images.

The High Resolution Stereo Camera (HRSC), onboard the Mars Express spacecraft, consists of two imaging subsystems: a four-band visible/near-infrared pushbroom scanning imager capable of acquiring along-track stereo image triplets and a panchromatic visible framing imager. The stereo triplet images permit a robust stereo reconstruction process, which yields Digital Terrain Models (DTMs) with a spatial resolution of up to 10m/pixel and a vertical resolution of up to ~ ±10m (Neukum and Jaumann, 2007; Jaumann et al., 2007). HRSC DTMs were used in this study to assess the topographic context of the chloride salt deposits.

The Mars Orbiter Laser Altimeter (MOLA), onboard the Mars Global Surveyor spacecraft, consisted of a co-aligned 1.064μm laser and 0.5m diameter telescope, which

measured the elevation of the surface relative to the planet's center of mass by pulsing the laser at 10 Hz and recording the return time of each pulse's surface reflection. The resulting point measurements were then converted into both gridded and spherical harmonic models of the topography and overall shape of Mars (Smith et al., 2001). MOLA global gridded elevations were used in this study to assess the topographic context of chloride salt deposits that were not covered by HRSC DTM products.

4.2.2 Dataset Descriptions

The HRSC-MOLA Blended 200m Digital Elevation Model (DEM) version 2.0 (Fergason et al., 2018) is a global digital elevation model that uses HRSC topographic data where it is available and MOLA topographic data where HRSC data is not available. The spatial resolution is 200 m/pixel and the vertical accuracy is ±10m. The HRSC-MOLA DEM was used in this study to ensure topographic assessments were always conducted using the highest resolution data available.

The global Geologic Map of Mars (Tanaka et al., 2014) is based on multiple remote sensing datasets acquired since the end of the Viking orbiter missions and identifies the major geologic units on the planet's surface along with their ages based on crater size-frequency distribution statistics. The THEMIS Day IR Global Mosaic (Edwards et al., 2011a,b) was used as the standard basemap for constructing the map because it is mostly unaffected by atmospheric haze and thus allowed reliable analysis of surface morphology and texture at a higher resolution than other available global products could provide at the time. The relative age of each map unit was determined using the scheme of three chronostratigraphic periods and eight epoch divisions of the periods established by Scott

and Carr (1978) and refined by Tanaka (1986) and Werner and Tanaka (2011). The Geologic Map of Mars was used in this study to determine the relative ages, and proposed absolute ages, of the terrains where chloride salt deposits occur, which obviously includes all of the caveats associated with terrain ages calculated using crater size-frequency distribution statistics.

The THEMIS Day IR Global Mosaic version 13.4 (Hill and Christensen, 2017) is composed of over 24,000 daytime, band 9 (12.75 μm) images acquired over the instrument's first 16 years at Mars. The images were blended together using the algorithms of Edwards et al. (2011a/b), creating a seamless image mosaic covering 100% of the Martian surface. The THEMIS Day IR Global Mosaic was used in this study to show the regional context of chloride salt deposits at scales larger than a single CTX image.

4.2.3 Analytical Tool Descriptions

The Java Mission-planning and Analysis for Remote Sensing (JMARS) geospatial information system (http://jmars.asu.edu) (Christensen et al., 2009) was used to conduct image reconnaissance and identify appropriate example images.

Image data were map-projected and analyzed using the Integrated Software for Imagers and Spectrometers (ISIS) maintained by the United States Geologic Survey's Astrogeology Science Center (http://isis.astrogeology.usgs.gov) [e.g., Anderson et al., 2004; Becker et al., 2013], as well as the DaVinci generic array processing tool maintained by Arizona State University's Mars Space Flight Facility (http://davinci.asu.edu) [e.g., Edwards et al., 2011a,b].

4.2.4 THEMIS Principal Component Chloride Index

The THEMIS Principal Component (PC) Chloride Index is a principal component-based index calculated from THEMIS IR multiband radiance images that have been rotated into principal component axes using a globally-applicable covariance matrix. The global covariance matrix is described by Hill and Christensen (2022a), and the calculation of the THEMIS PC Chloride Index is described by Hill and Christensen (2022b).

4.2.5 Colorization of THEMIS PC Chloride Index Values

For consistency, this paper will present THEMIS PC Chloride Index figures colorized using the same color scale used by Hill and Christensen (2022b). However, it is often helpful to only consider pixels with multiple positive THEMIS PC Chloride Index detections, as this helps to significantly reduce false positive detections without significantly affecting true positive detections. Therefore, the THEMIS PC Chloride Index figures presented in this paper will only show pixels with multiple detections. As a result, the low end of the color spectrum (violet) will not be seen in this paper's figures.

4.2.6 THEMIS PC Chloride Index Sensitivity Parameters

As described by Hill and Christensen (2022b), the values of the two sensitivity parameters in the THEMIS PC Chloride Index calculation can be varied, depending on the goal of the analysis being performed. For the figures presented in this paper, only the recommended parameter combination of n1=2.0 and n3=3.0 was used, because it represents a balance between reducing false positive detections and increasing true positive detections.

4.2.7 Colorization of HRSC/MOLA Elevation Values

The colorized elevation figures in this paper are intended to show the relationship between the chloride salt deposits and their surrounding topography. For consistency, except where otherwise noted, these figures have been colorized using the same color spectrum assigned across an elevation range of 250m, although the actual elevation values vary from figure to figure. For example, the transition from green to red will always represent an elevation change of 125m, although the actual elevation values associated with the green and red colors will vary from figure to figure.

4.3 Results

4.3.1 Circular Deposits

Circular deposits are one of the most common chloride salt morphologies identified by the updated survey conducted by Hill and Christensen (2022a), representing ~16% (255 deposits) of the currently identified sites. Of these, 55 circular deposits are located in Early Noachian terrains. They are characterized by their roughly circular shapes, light-toned textured appearance in visible images, and high confidence THEMIS PC Chloride Index detections. Notably, they are almost always topographically indistinct, meaning that they are not raised or lowered relative to the local topography at the vertical resolution of the MOLA-HRSC Blended Global DEM. Figure 4.1 shows an example of three topographically indistinct circular deposits within Middle Noachian terrain in Terra Cimmeria. This particular example from Middle Noachian terrain, rather than an example from Early Noachian terrain, was chosen because it clearly illustrates the characteristics of multiple circular deposits within a single figure.

At higher resolutions, circular deposits are associated with rough textures that appear whitish in the approximate true color HiRISE images. Figure 4.2 shows an example of an eroded circular deposit in Late Noachian terrain with the whitish portions corresponding to the highest confidence THEMIS PC Chloride Index detections. This particular example from Late Noachian terrain was chosen because none of the Early Noachian circular deposits currently have sufficient HiRISE Color coverage to clearly demonstrate the relationship between the whitish material and THEMIS PC Chloride Index detections.

Circular deposits across the planet are remarkably similar, although they can range in size. Figure 4.3 shows a sampling of circular deposits in Early Noachian terrains with diameters between 1km and 5km.

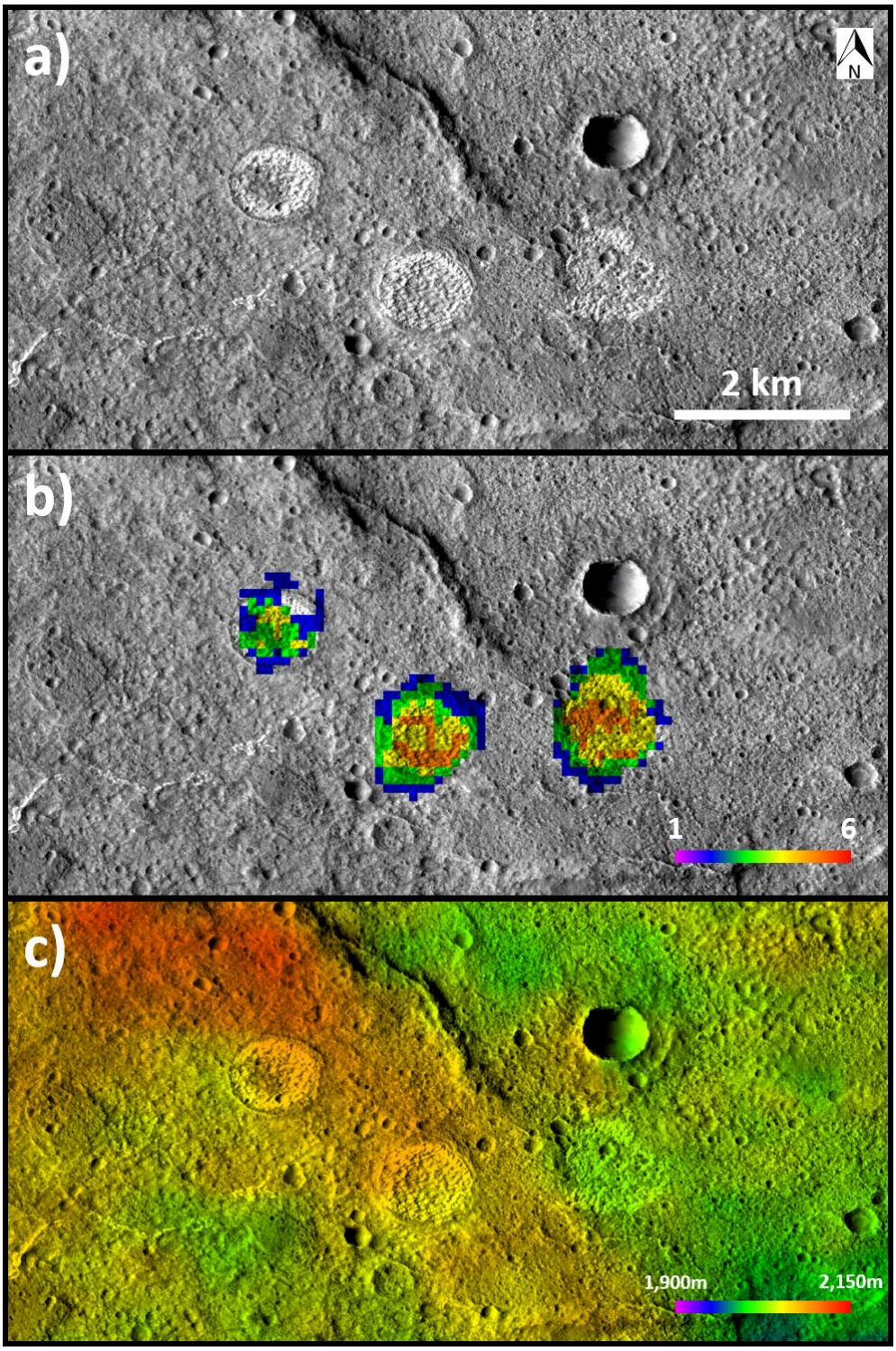

Figure 4.1. Three circular deposits located in Middle Noachian terrain in Terra Cimmeria at -33.875°N, 135.905°E, shown in: (a) CTX image J07_047403_1476_XN_32S224W; (b) CTX image overlaid with colorized THEMIS PC Chloride Index detections; and (c) CTX overlaid with colorized HRSC-MOLA Blended DEM elevation data.

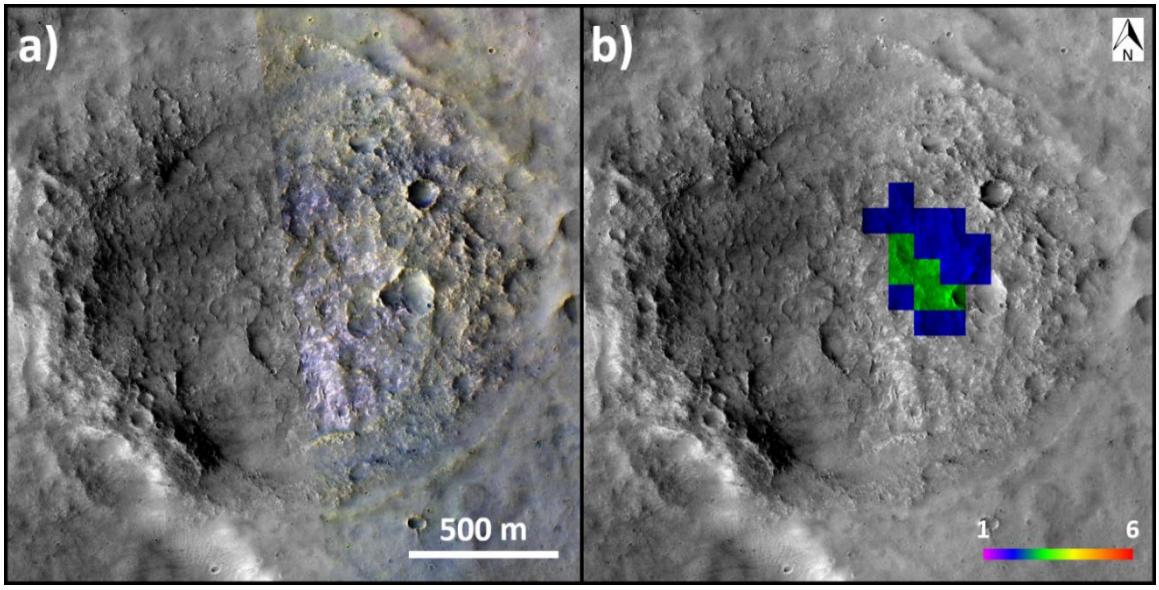

Figure 4.2. Eroded circular deposit located in Late Noachian terrain in Noachis Terra at -32.135°N, 357.760°E, shown in: (a) HiRISE image ESP_030160_1475 with color bands where available; and (b) HiRISE Red image overlaid with colorized THEMIS PC Chloride Index detections.

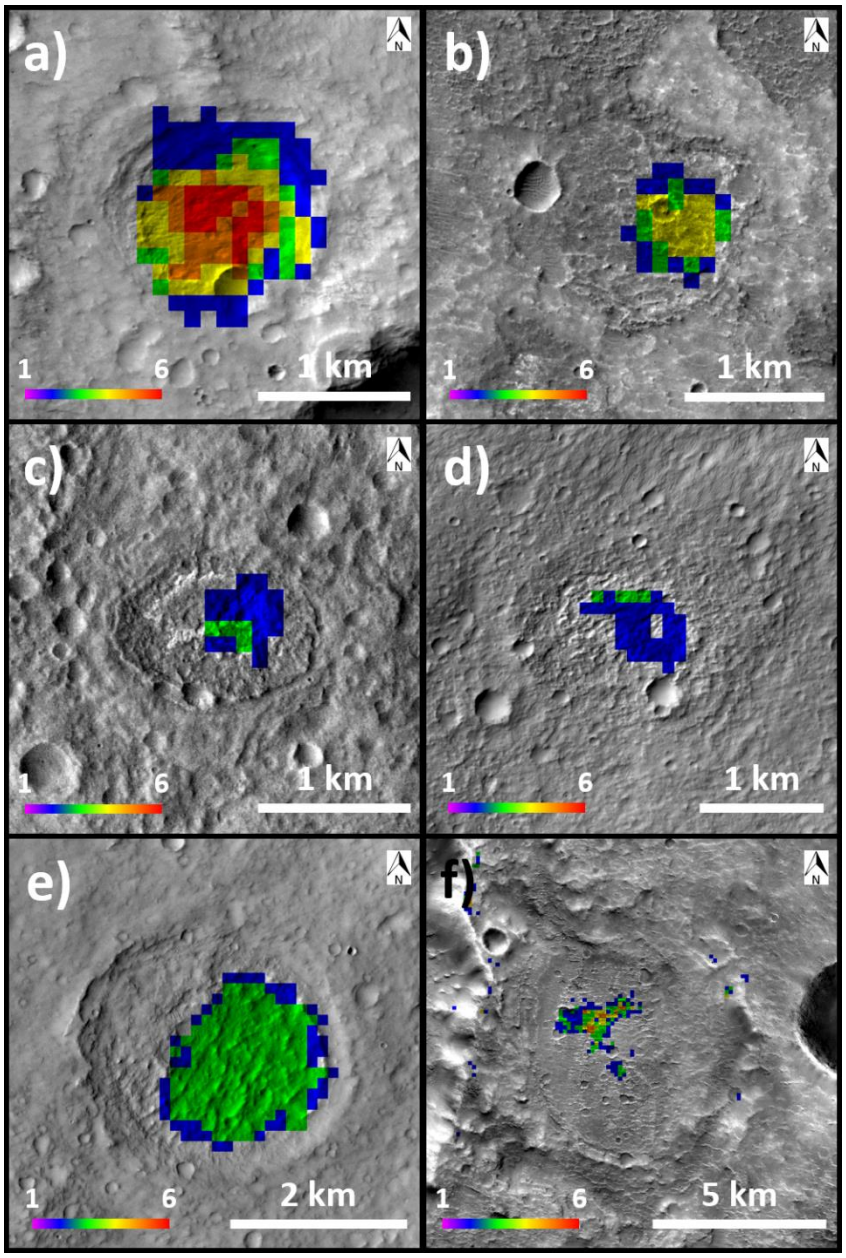

Figure 4.3. Diversity of circular deposits located in Early Noachian terrains with overlaid colorized THEMIS PC Chloride Index detections: (a) deposit at -27.340°N, 181.355°E in CTX image F17_042509_1520_XN_28S178W; (b) deposit at -11.900°N, 85.835°E in CTX image D20_035075_1661_XN_13S274W; (c) deposit at -32.175°N, 129.050°E in CTX image F07_038489_1493_XN_30S231W; (d) deposit at -32.185°N, 129.920°E in CTX image B19_016982_1477_XI_32S230W; (e) deposit at -22.090°N, 4.120°E in CTX image J05_046643_1579_XN_22S355W; and (f) deposit at -2.725°N, 76.650°E in a mosaic of CTX images D18_034060_1795_XN_00S283W and J08_048117_1791_XN_00S283W.

4.3.2 Regional High Deposits

Another distinct category of chloride salt deposits identified by the updated survey of Hill and Christensen (2022a) were those located on regional highs, which represent ~3% (51 deposits) of all chloride salt sites. The regional high deposits are characterized by their topographic context, which does not provide a sufficient uphill source of chloride-rich water, either from surface runoff or subsurface groundwater flow. Therefore, their size, morphology, and other physical characteristics can vary significantly. Coincidently, many of the best examples are also classified as circular deposits.

Figure 4.4 shows an example of a chloride salt deposit on a regional high between two large craters. In this case, the chloride salt appears to be associated with the textured terrain on the ridge, in particular the small eroded crater where the THEMIS PC Chloride Index detections are mostly located. There are additional THEMIS PC Chloride Index detections in the vicinity, including locations on the textured surface of the ridge and directly below the ridge on the crater floor.

It is always important to consider the entire geologic context of a chloride salt deposits before classifying it as a “regional high deposits”. Some deposits technically occur on regional highs, but are entirely consistent with the inferred geologic history of the location. For example, Figure 4.5 shows a relatively large and mostly continuous chloride salt deposit on a distinct regional high in Late Noachian terrain. However, given the geologic context, the most likely explanation is that the chloride salts precipitated near the bottom of the broad regional low and were subsequently lifted above the surrounding terrain by the wrinkle ridge forming underneath them. Therefore, although this deposit is currently on a regional high, it was not classified as a “regional high deposit”.

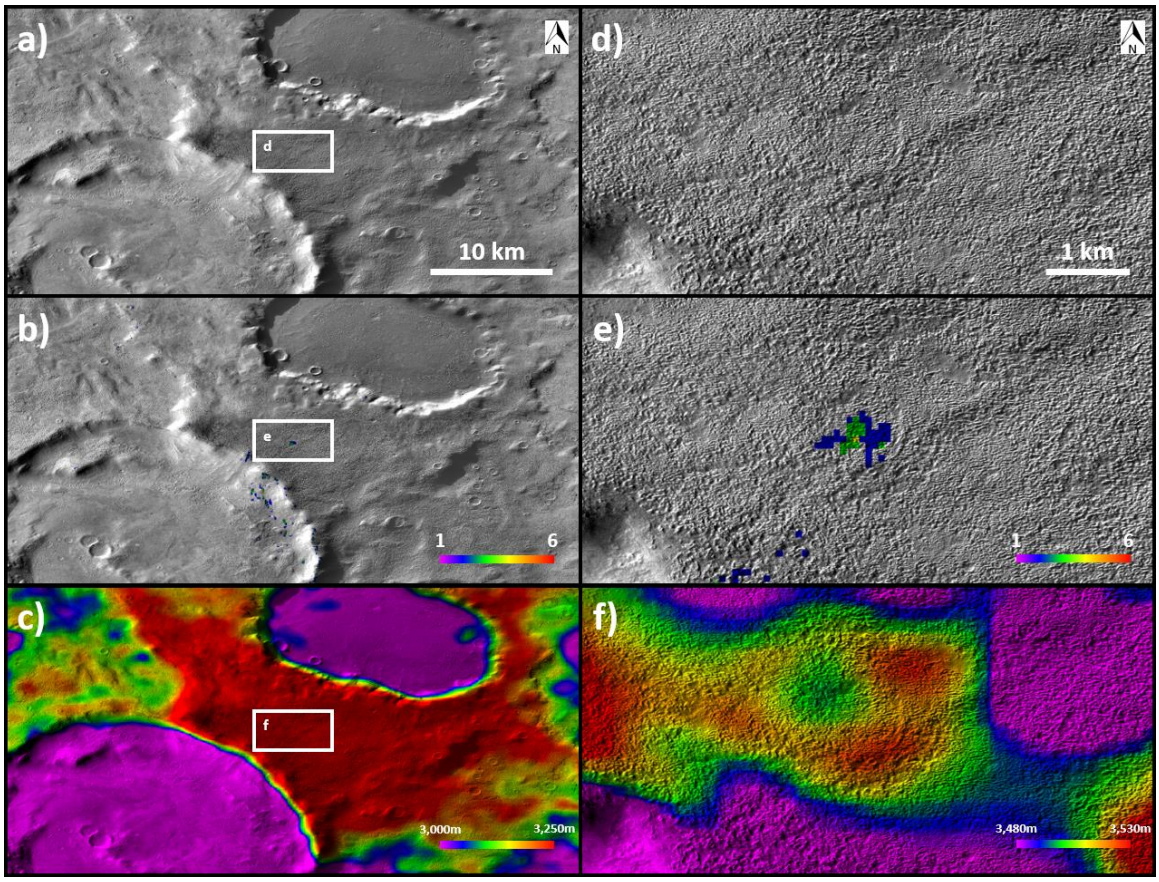

Figure 4.4. Heavily eroded circular deposit on a regional high between two large craters located in Early Noachian terrain in Terra Sirenum at -47.520°N, 215.565°E, shown in: (a) a regional CTX mosaic; (b) CTX mosaic overlaid with colorized THEMIS PC Chloride Index detections barely visible; (c) CTX mosaic overlaid with colorized HRSC-MOLA Blended DEM elevation data; (d) a closer view of the chloride deposit in (a); (e) a closer view of the chloride deposit in (b) with colorized THEMIS PC Chloride Index detections more easily visible; and (f) a closer view of the chloride deposit's location in (c).

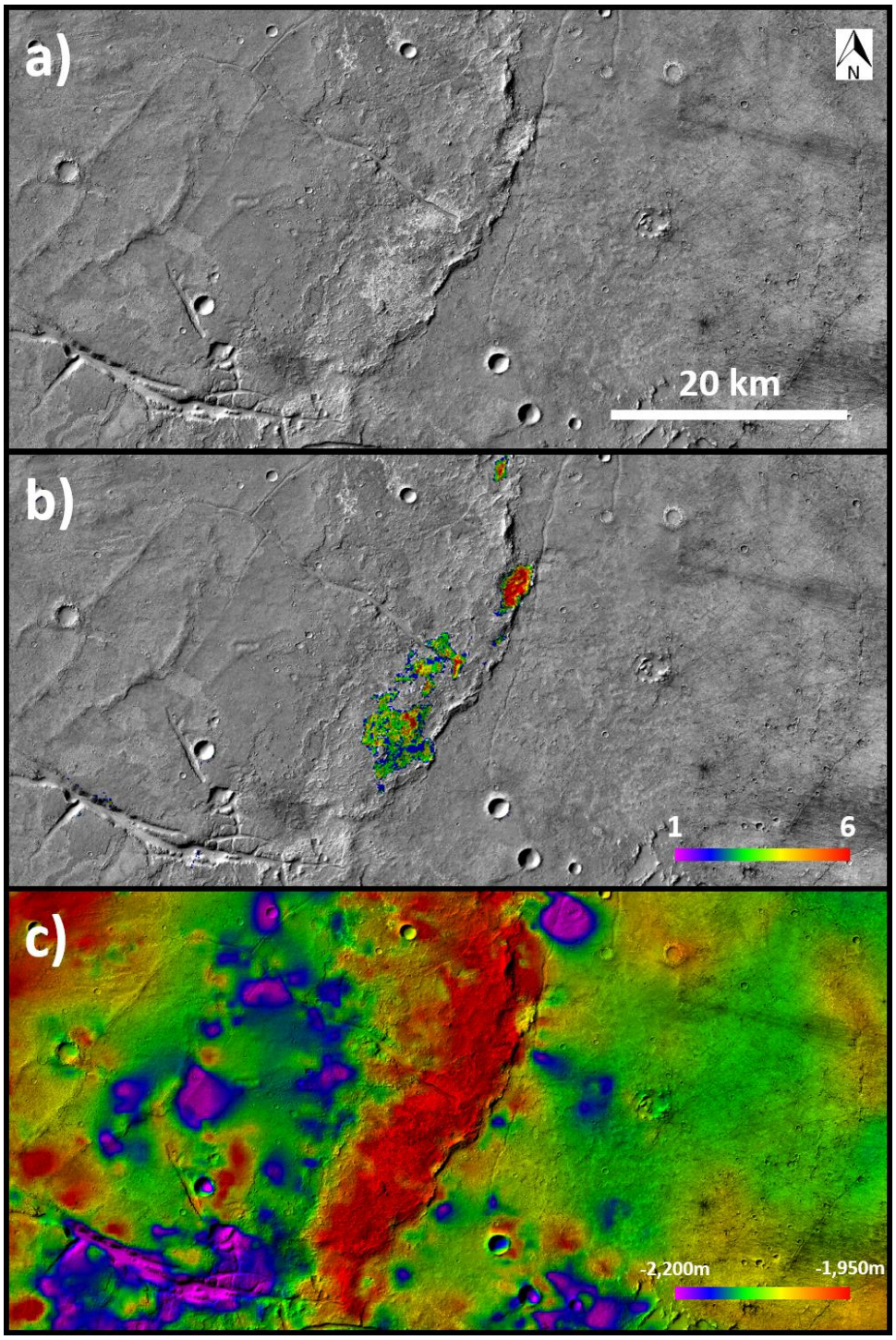

Figure 4.5. Chloride deposits on a raised wrinkle ridge located in Late Noachian terrain in the plain separating Ladon Valles and Morava Valles at -18.845°N, 332.200°E, shown in: (a) a CTX regional mosaic; (b) CTX mosaic overlaid with colorized THEMIS PC Chloride Index detections; and (c) CTX mosaic overlaid with colorized HRSC-MOLA Blended DEM elevation data.

4.3.3 Ejecta Deposits

The ejecta deposits are a rare form of Martian chloride salts, representing only ~1% (19 sites) of the sites identified in the Hill and Christensen (2022a) survey. They most often occur surrounding small (~100m diameter) impact craters, but cover larger areas than the craters themselves, allowing the THEMIS PC Chloride Index (100m/pix resolution) to resolve and detect them.

Figure 4.6 shows an ejecta deposit in Early Noachian terrain in Terra Sirenum, located in a local depression with surface roughness and morphology typically associated with chloride salt deposits, but without significant THEMIS PC Chloride Index detections. Instead, the high-confidence detections only occur over the heavily-eroded ejecta deposit.

Ejecta deposits have also been found in nearby Middle Noachian terrains, which are of interest because they are excavating materials that are below, and potentially older, than the surface terrain age. Figure 4.7 shows an example of an ejecta deposit in Middle Noachian terrain in Margaritifer Terra, demonstrating how the THEMIS PC Chloride Index detections are very well-correlated with the small ejecta deposit.

The examples in Figures 4.6 & 4.7 can only provide evidence of subsurface chloride salt in a single discrete location. The true extent of any subsurface chloride salt layers cannot be assessed. However, in the case of Figure 4.8, multiple ejecta deposits in close proximity imply the existence of a continuous subsurface chloride salt layer between the two, and possibly beyond.

The updated chloride survey also identified a single example of chloride salt within a large crater's regolith dominated ejecta deposit. Figure 4.9 shows an area of light-toned material <1km across within the ejecta deposit of an ~20km diameter impact crater. The

light-toned material has multiple high-confidence THEMIS PC Chloride Index detections, while there is a noticeable lack of other detections in the vicinity.

Examples of the opposite case have also been identified: an impact crater in a chloride salt deposit excavating non-chloride salt material from underneath it. These examples place constraints, albeit fairly wide, on the thicknesses of the chloride salt deposits. Figure 4.10 shows an example of an impact crater penetrating a chloride salt deposit.

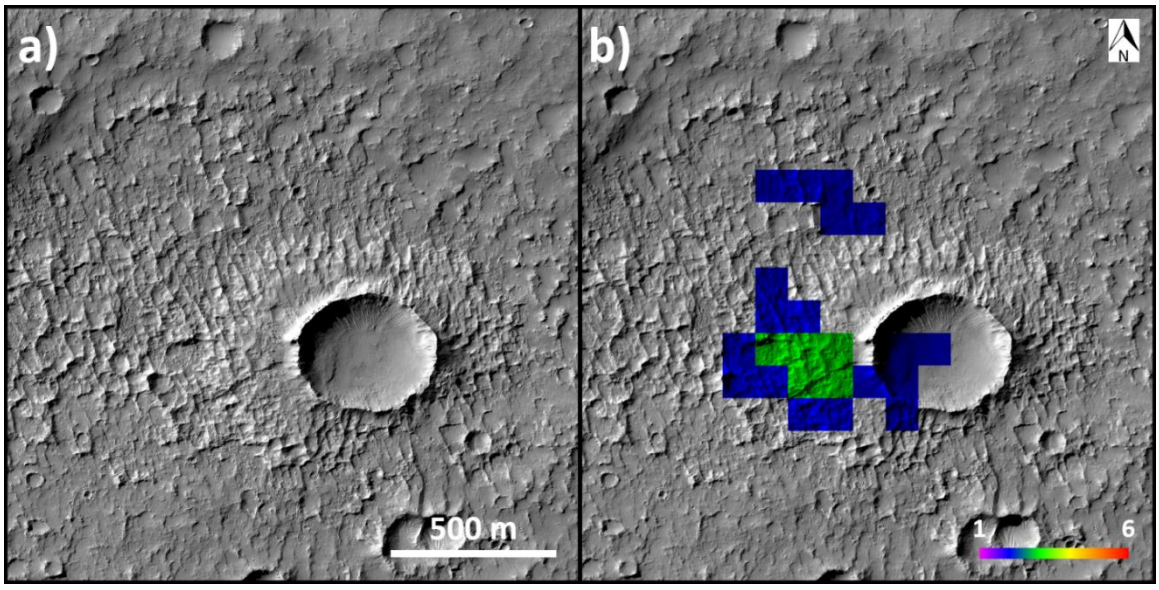

Figure 4.6. Impact crater ejecta deposit located in Early Noachian terrain in Terra Sirenum at -32.285°N, 190.555°E, shown in: (a) HiRISE image PSP_009846_1475; and (b) HiRISE image overlaid with colorized THEMIS PC Chloride Index detections.

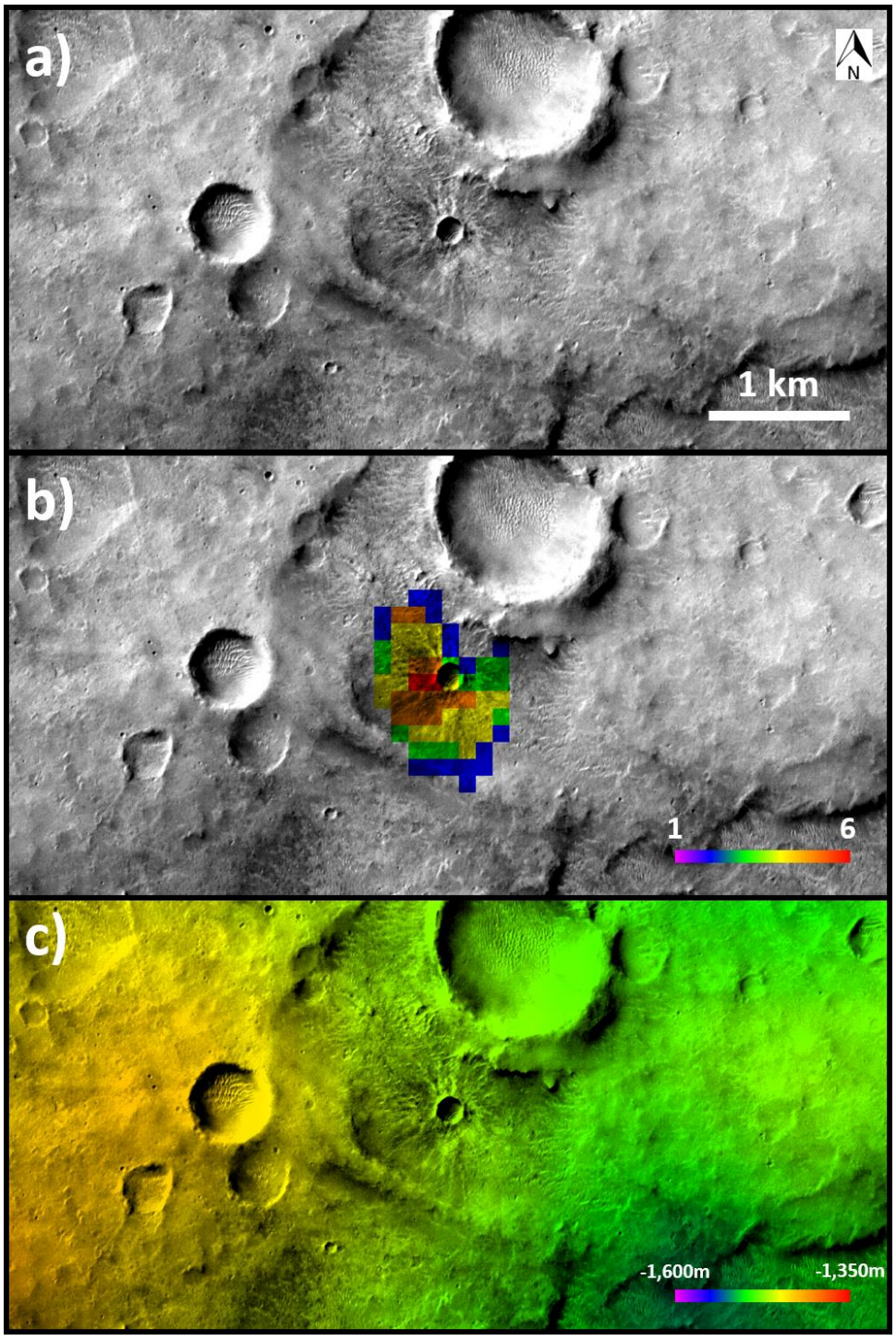

Figure 4.7. Impact crater ejecta deposit located in Middle Noachian terrain in Margaritifer Terra at -7.825°N, 349.710°E, shown in: (a) CTX image B18_016842_1722_XN_07S010W; (b) CTX image overlaid with colorized THEMIS PC Chloride Index detections; and (c) CTX image overlaid with colorized HRSC-MOLA Blended DEM elevation data.

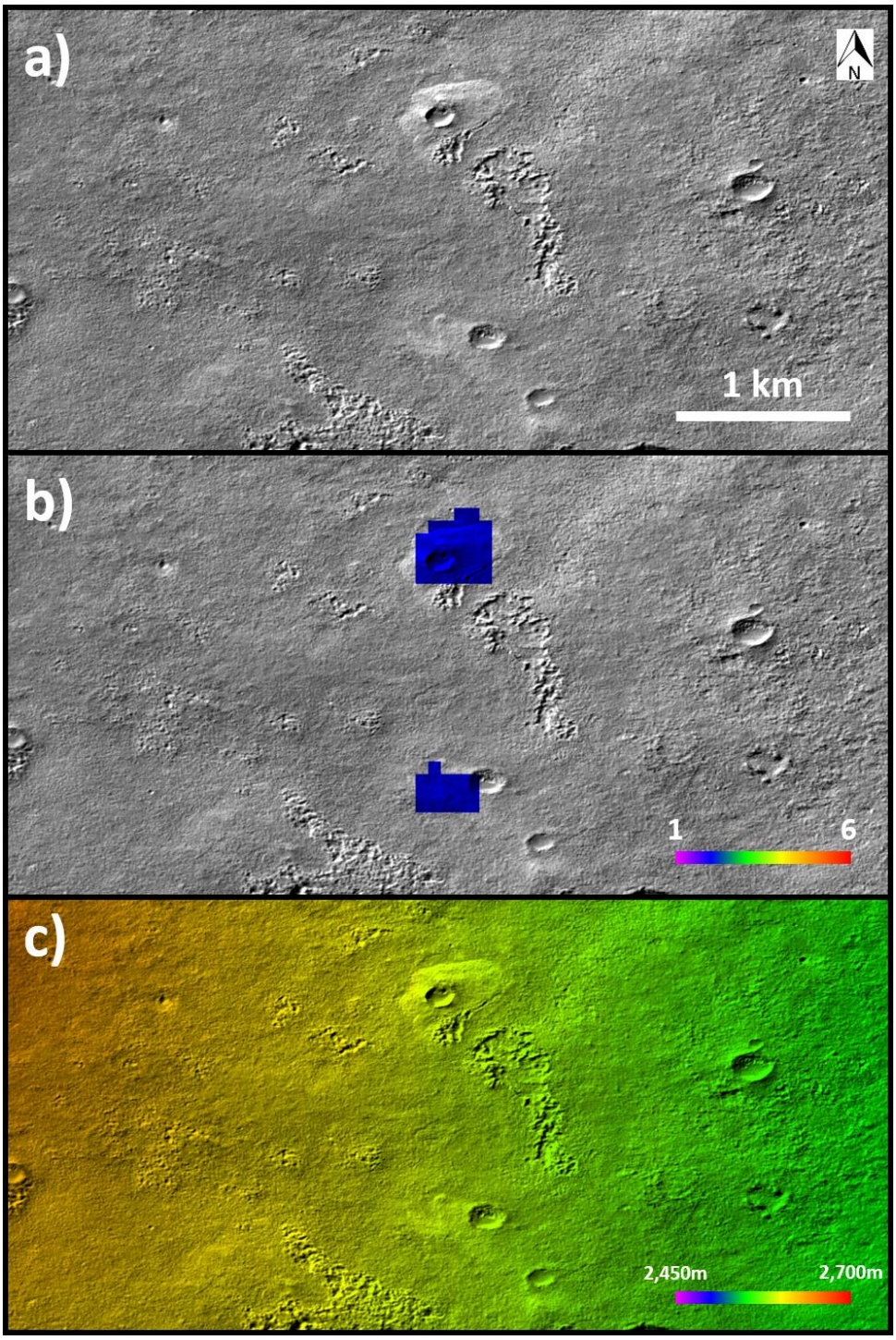

Figure 4.8. Pair of ejecta deposits located at the boundary between Early and Middle Noachian terrain in Terra Sirenum at -47.285°N, 210.890°E, shown in: (a) CTX image G19_025471_1338_XN_46S149W; (b) CTX image overlaid with colorized THEMIS PC Chloride Index detections; and (c) CTX image overlaid with colorized HRSC-MOLA Blended DEM elevation data.

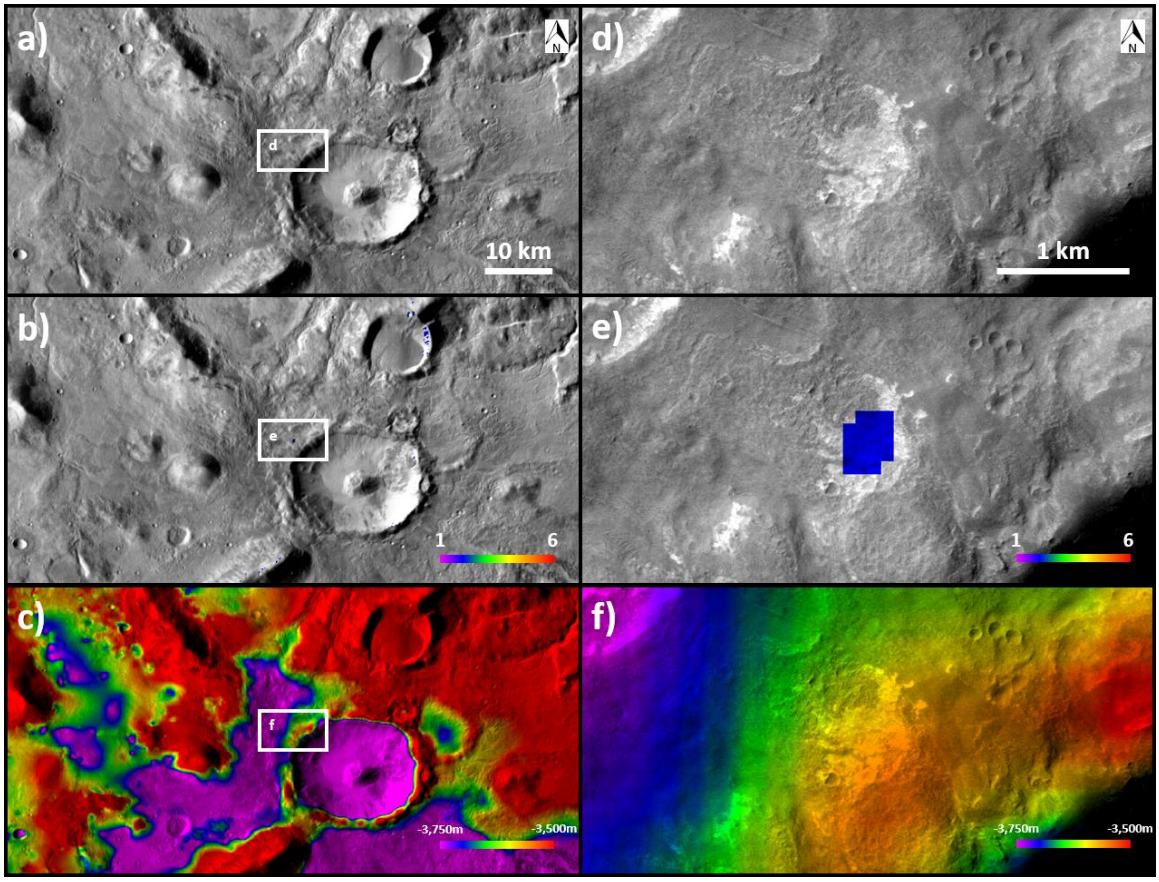

Figure 4.9. Chloride salt within a large crater's impact ejecta located in Early Noachian terrain surrounding Hellas Planitia at -31.190°N, 81.410°E, shown in: (a) a subsection of the THEMIS Day IR Global Mosaic v13.4; (b) THEMIS global mosaic overlaid with colorized THEMIS PC Chloride Index detections, showing only a very small detection at the center of the image; (c) THEMIS global mosaic overlaid with colorized HRSC-MOLA Blended DEM elevation data; (d) a closer view of (a) in CTX image B16_016008_1495_XN_30S278W; (e) a closer view of (b) in CTX image overlaid with colorized THEMIS PC Chloride Index detections; and (f) a closer view of (c) in CTX image overlaid with colorized HRSC-MOLA Blended DEM elevation data.

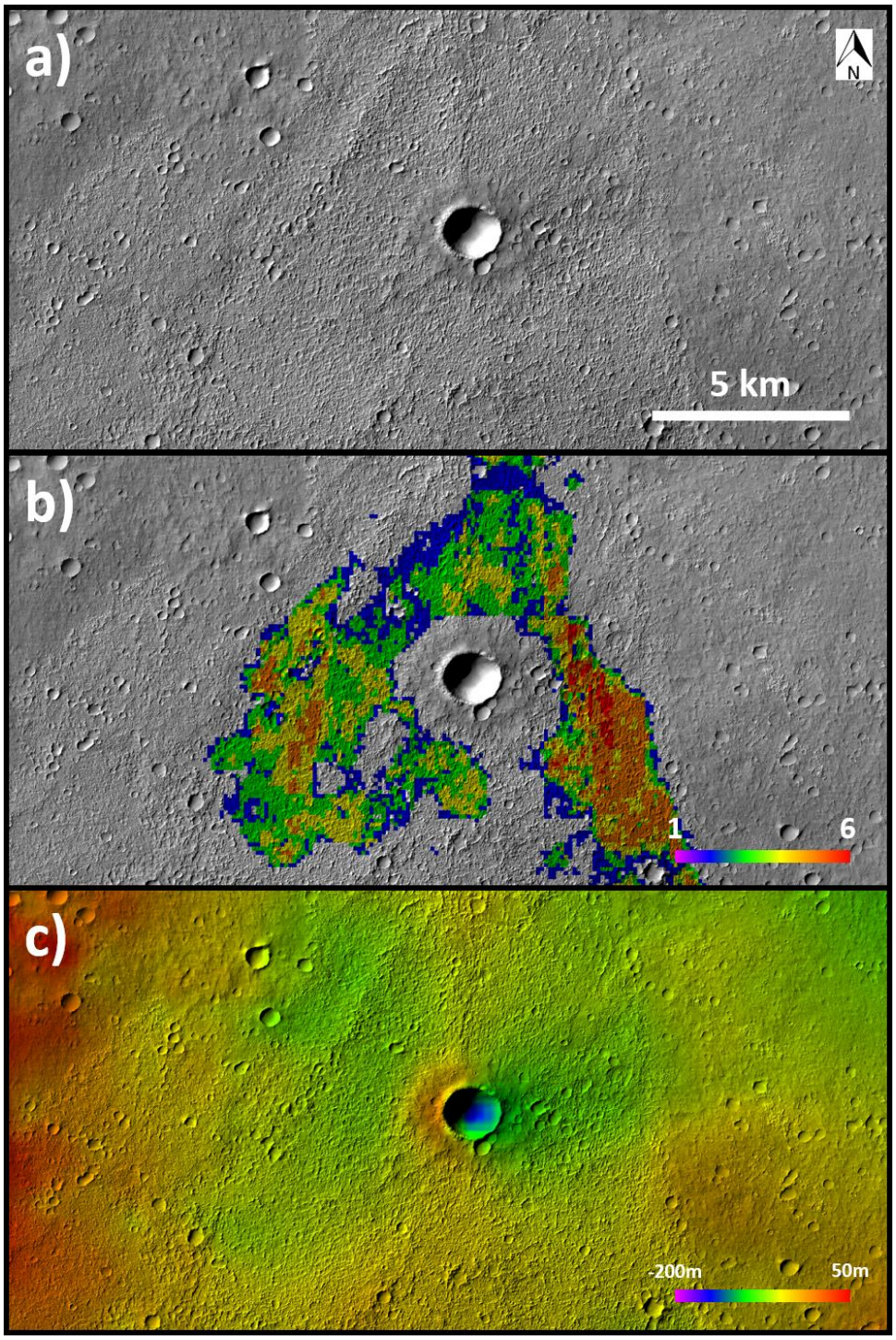

Figure 4.10. Impact crater ejecta on top of a pre-existing chloride salt deposit located in Late Noachian terrain in Noachis Terra at -25.295°N, 346.605°E, shown in: (a) CTX image B01_009893_1546_XN_25S013W; (b) CTX image overlaid with colorized THEMIS PC Chloride Index detections; and (c) CTX image overlaid with colorized HRSC-MOLA Blended DEM elevation data.

4.4 Discussion

4.4.1 Formation of Circular Deposits

The circular deposits are interpreted as chloride salts deposited in impact craters via chloride-rich groundwater, with a proposed life-cycle illustrated in Figure 4.11.

The groundwater would have entered and pooled in these topographic lows that extended below the regional groundwater level (Figure 4.11a-4.11b). The exposed water would have then evaporated and precipitated chloride salts (Figure 4.11c). This cycle likely repeated numerous times, leading to chloride salt deposits thick enough and durable enough to be detected by orbital remote sensing instruments. Over time, these deposits were likely buried by younger material (ex: crater ejecta, aeolian deposits, etc.) that both filled the remaining portion of the crater above the chloride salts and draped the surrounding terrain (Figure 4.11d). Then, when the dominant surface mechanisms changed from depositional to erosional, the entire surface eroded down relatively evenly to expose the circular casts of chloride salt level with the surrounding terrain (Figures 4.11e-4.11f).

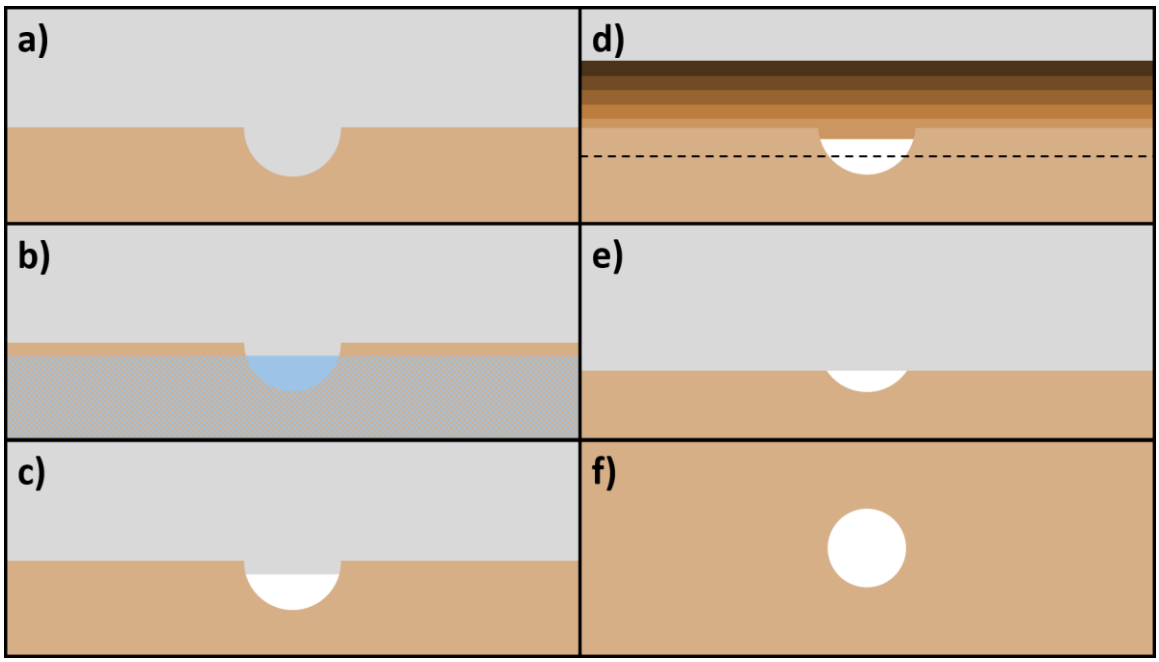

Figure 4.11. Proposed formation and evolution of a circular chloride deposit: (a) a preexisting impact crater; (b) chloride-rich groundwater fills the crater; (c) as the water evaporates, chloride salts precipitate out; (d) over time, regolith layers are emplaced on top of the chloride salt deposit by various mechanisms; (e) erosion during later geologic periods eventually strips away the overlying regolith and some of the pre-existing terrain to reveal the circular cast of the chloride salt deposit level with the surrounding terrain; (f) viewed from above, the now-exposed chloride salt deposit appears circular.

4.4.2 Formation of Regional High Deposits

The regional high deposits are noteworthy because they appear to lack an uphill source of chloride-rich water that could have led to their formation.

One possible formation mechanism involves sub-glacial channelized flow, which can flow against topography for short distances because it is primarily driven by the sub-glacial pressure gradient and not the gravitational gradient (Schoof, 2010; Grau Galofre et al., 2020). However, in the cases of the regional high deposits described in this work, this is unlikely. Any sub-glacial flow carrying chloride-rich water to these locations would have been forced to relatively extreme elevations. It is unlikely that sufficiently thick glaciers ever formed in these regions to provide a sufficient pressure gradient.

Instead, the regional high deposits are interpreted as being very old chloride salt deposits that formed when the regional topography was considerably different and did have an uphill source of chloride-rich water. Subsequently, the terrain underwent significant modification, most likely due to large impacts, which left the chloride salts stranded on a regional high.

Figure 4.12 illustrates a proposed timeline of the formation and evolution of a regional high chloride salt deposit like the one shown in Figure 4.4.

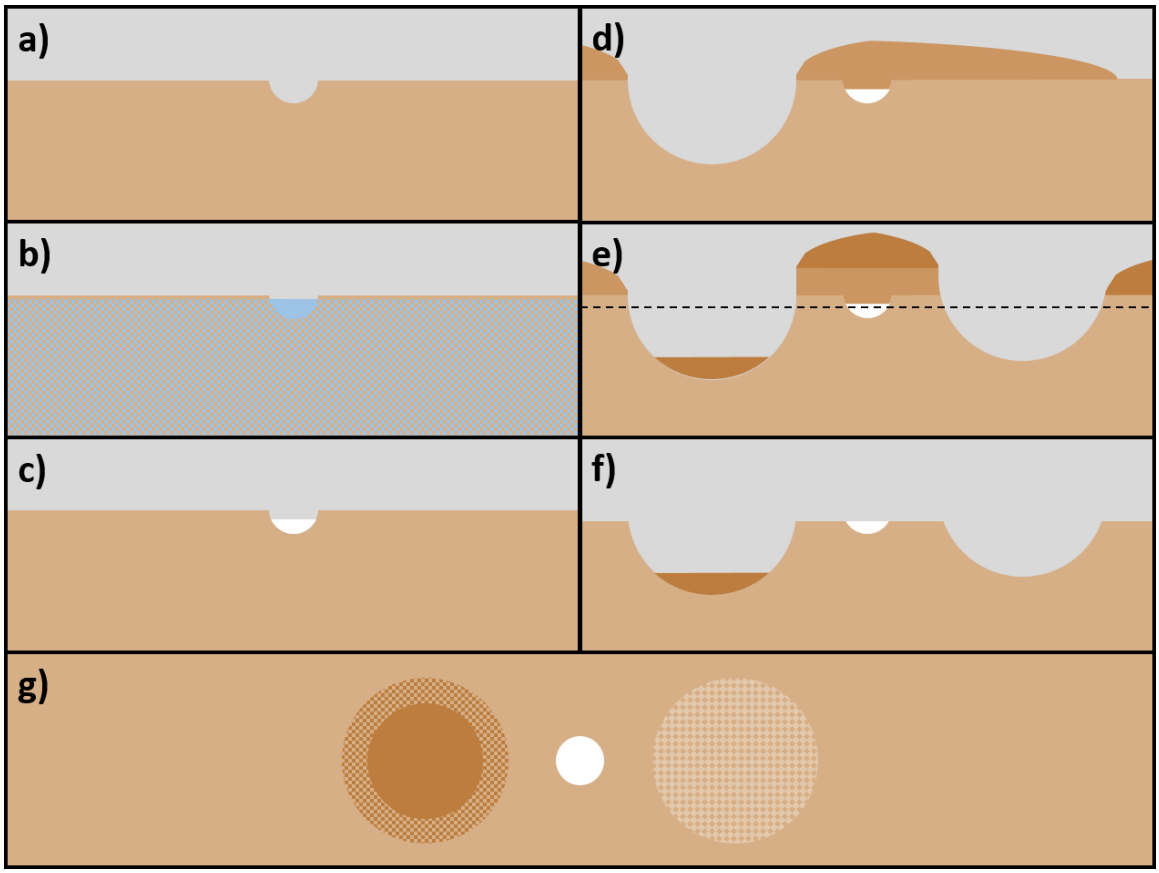

Figure 4.12. Proposed formation and evolution of a regional high deposit between large impact craters: (a) a preexisting surface with a topographic low, such as an impact crater; (b) chloride-rich groundwater fills the topographic low; (c) as the water evaporates, chloride salts precipitate out; (d) a nearby large impact covers the chloride deposit with ejecta material; (e) another nearby large impact covers the chloride deposit with additional ejecta material; (f) erosion over geologic timescales removes the ejecta deposits above the chloride deposit and possibly some of the preexisting terrain, revealing the circular cast of the chloride salt deposit level with the surrounding terrain; (g) viewed from above, the chloride salt deposit appears as a circular deposit in an area that has now become a regional high.

4.4.3 Formation of Ejecta Deposits

The ejecta deposits are interpreted as forming via an impact into a pre-existing chloride salt deposit that is covered by a thin layer of regolith, which obscures it from the THEMIS PC Chloride Index. The chloride salt is only detectable when the impact process excavates the subsurface material and re-deposits it as an ejecta blanket. Figure 4.13 illustrates this proposed timeline for the formation of a chloride salt ejecta deposit.

In the case of two ejecta deposits occurring in close proximity to each other, as seen in Figure 4.8, they imply the existence of a continuous chloride salt layer that extends between the two of them, and possibly beyond.

The case of chloride salts representing only a small fraction of an ejecta blanket, as seen in Figure 4.9, also implies the existence of subsurface chloride salts. It is unreasonable to assume this patch of chloride salt was deposited in its current location post-impact. Instead, it is interpreted as having been a discrete subsurface chloride salt deposit, rather than a subsurface layer, that was re-exhumed by the large impact. The chloride salt deposit is relatively close to the crater rim, indicating the material was originally in the shallow subsurface (Shoemaker, 1960). As noted by Shoemaker (1960) at Meteor Crater, inverted stratigraphy can be found surrounding impact crater rims, demonstrating that such pre-existing subsurface structures can be preserved in the ejecta deposit in an altered, but still recognizable, form. Figure 4.14 illustrates a proposed timeline of the formation and evolution of this particular deposit.

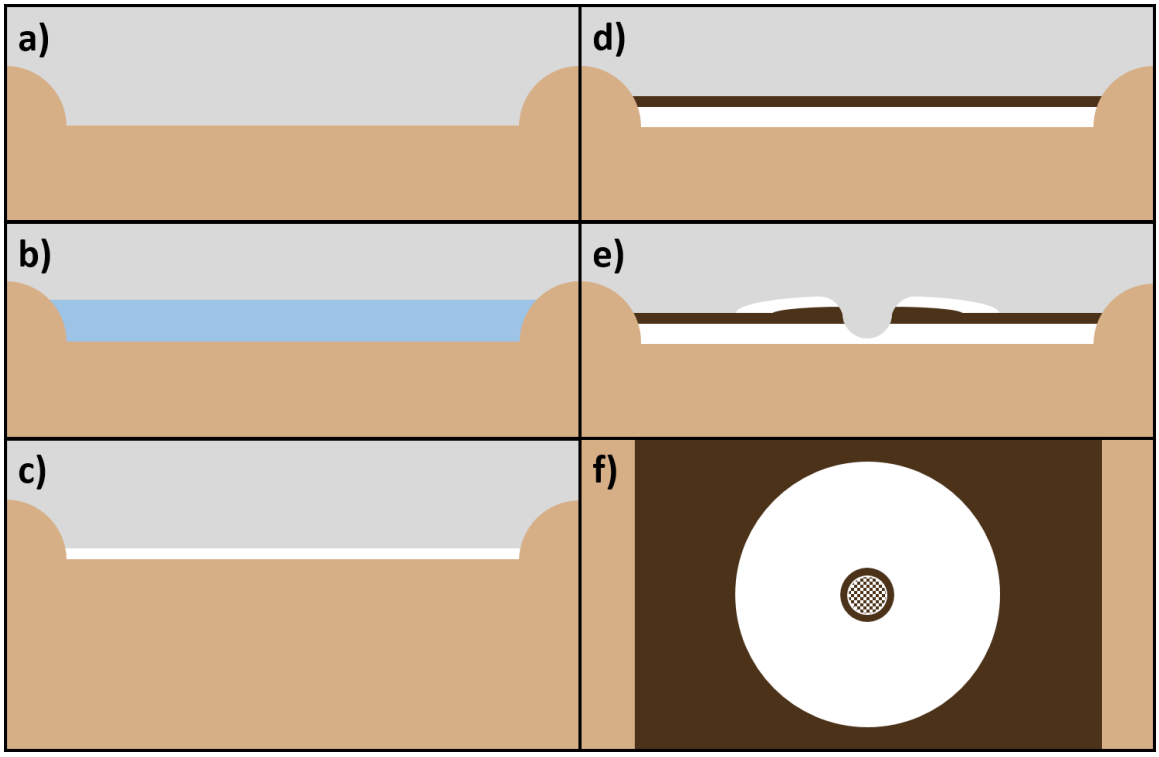

Figure 4.13. Proposed formation and evolution of a chloride ejecta deposit: (a) a relatively flat preexisting surface; (b) chloride-rich water covers the terrain; (c) as the water evaporates, chloride salts precipitate out and create a continuous chloride salt layer; (d) over time, regolith is emplaced on top of the chloride salt layer by various mechanisms; (e) an impact crater penetrates through the top layer of regolith and into the chloride salt layer, which creates an ejecta deposit primarily composed of chloride salt; (f) viewed from above, the chloride salt is visible as the top layer of the ejecta deposit, while the walls of the impact crater are composed of the previous regolith layer, and the center of the crater contains a mixture of both as material collapsed back into the crater post-impact.

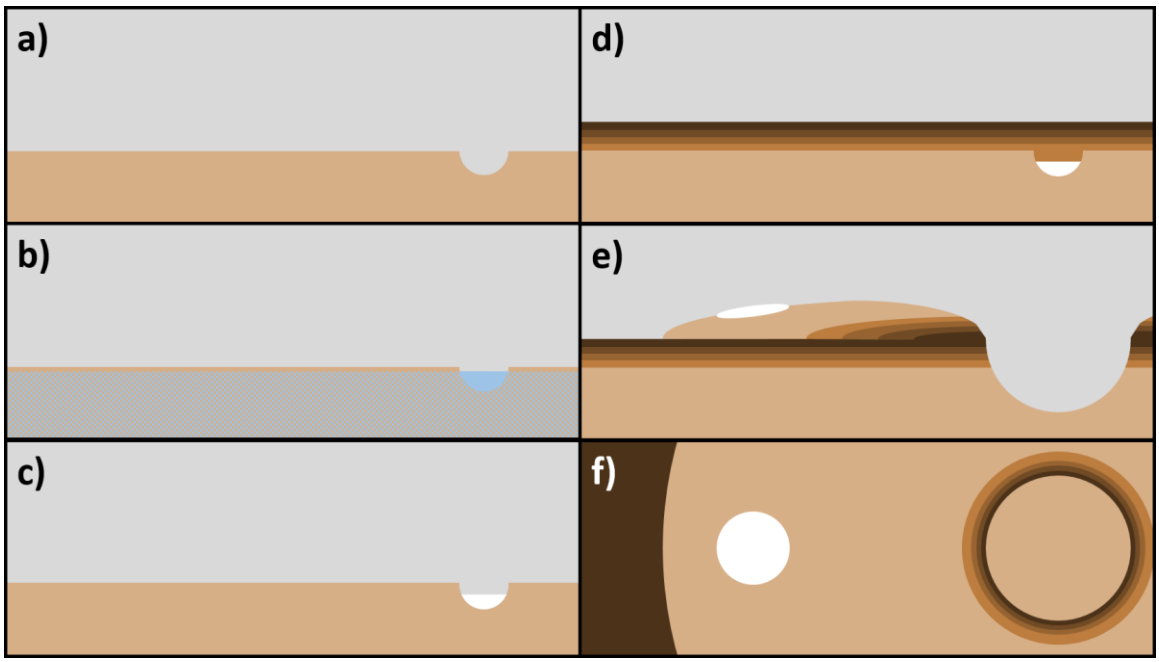

Figure 4.14. Proposed formation and evolution of a discrete chloride salt deposit in impact crater ejecta: (a) a preexisting surface with a topographic low, such as an impact crater; (b) chloride-rich groundwater flows into the topographic low; (c) as the water evaporates, chloride salts precipitate out; (d) over time, regolith is emplaced on top of the chloride salt deposit by various mechanisms and completely covers it; (e) a large impact crater penetrates the surface at least down to the depth of the chloride deposit, which then becomes incorporated into the crater's overall ejecta deposit; (f) viewed from above, the chloride salt is visible as a distinct patch within the larger regolith-dominated ejecta deposit.

4.4.4 Chlorides Salts in Early Noachian Terrains

One of the most important open questions regarding the Martian chloride salt deposits is their ages, because this would put constraints on when the Martian surface had sufficient water-rock interaction to generate chloride salts, as well as the conditions that would lead to their precipitation. Hill and Christensen (2022a) showed that ~16% (257 deposits) of the currently identified chloride deposits occur in terrains classified as "Early Noachian" by Tanaka et al. (2014). However, did the chloride salt deposits found in Early Noachian terrains form contemporaneously with the surrounding terrain, or were they superimposed on these terrains during later geologic eras.

Each chloride deposit likely has a unique age and formation history, but when the three categories discussed in this paper (circular deposits, regional high deposits, and ejecta deposits) are considered as a whole, they indicate that chloride salt deposition was occurring during the Early Noachian period.

First, the regional-high deposits are inconsistent with their current topographic locations, because they do not have sufficient uphill sources of water (surface runoff or subsurface groundwater flow) to have transported and precipitated chloride salts in abundances that are identifiable using orbital remote sensing instruments. This indicates they formed during a time when the local topography was significantly different than it is currently. Erosion over billions of years would have significantly altered the terrain, but is unlikely to be the sole explanation for the current topographic isolation of these sites. Kite and Mayer (2017) estimated the regional erosion rates in the equatorial portions of the southern highlands at ~0.1m/My. Erosion rates of this magnitude could have theoretically eroded Early Noachian terrains by 200m-300m, which is approximately the topographic

relief between the regional high deposit in Figure 4.4 and its surrounding terrains. However, that erosion would have had to act almost exclusively on the terrain surrounding the deposits and barely at all on the deposits themselves, and there is no obvious evidence that would support this degree of differential erosion.

A more reasonable explanation for these sites' current topographic isolation is to invoke the ability of large impacts to significantly reshape the terrain. Notably, the deposit in Figure 4.4 is surrounded by two ~20km diameter impact craters. Calculating crater size-frequency values for such large craters in such a small area includes many caveats, but it is still helpful to put general constraints on the ages of the features. The crater size-frequency isochrones of Michael and Neukum (2010) show that two ~20km diameter craters occurring in a roughly 3,500 km^2 area corresponds to a point slightly older than the 4 Ga isochron. This means that for such a small patch of Mars to record two such large impacts, the terrain must be from approximately ~4 Ga, which is consistent with the dating of this terrain by Tanaka et al. (2014). If the topography requires the chloride salt site in Figure 4.4 to have formed with different surrounding terrain, and 4 Ga would have been needed for the surrounding terrain to record two impact craters of this size, then we can infer that the chloride salt site must be at least 4Gyr, which would place its formation in the Early Noachian.

A second indication that the chloride salt sites in Early Noachian terrains formed contemporaneously with those terrains is the ejecta deposits, which demonstrate the existence of subsurface chloride salt deposits. If the terrain above the subsurface deposits is dated to the Early Noachian, as in Figure 4.6, then it implies that the subsurface chloride salts are at least as old and likely older. In cases such as Figures 4.7 and 4.8, where the

surface terrain has been dated to the Middle Noachian, the chloride salts must be older than the surface terrain. Since these regions show no major elevation differences between adjacent Early and Middle Noachian terrains, it is very likely that the chloride salts being excavated by the impacts are from the Early Noachian.

And third, the chloride salts within the circular deposits sometimes occur in erosional windows within the barely-distinguishable outlines of the original impact craters, as seen in Figures 4.2 and 4.3. In Figure 4.2, which shows one of the few circular deposits covered by high-resolution HiRISE images, it's possible to identify the chloride salts as a distinct layer within the crater, with nearby material above and below it that does not register in the THEMIS PC Chloride Index. This pattern likely occurs in other circular deposits, but cannot be verified until HiRISE coverage expands to include more examples. Because the chloride salts can be observed as part of the local stratigraphy in heavily eroded craters within Early Noachian terrains, it is reasonable to date the original formation of the chloride salts to the Early Noachian as well.

When considered individually, each of these three classes of deposits points to chloride salt deposition occurring very early in Mars' history, particularly in the Early Noachian. When considered together, it is difficult to construct an alternate scenario where chloride salt deposition occurred significantly later and all three types of deposits still developed their current expressions by the present day.

4.4.5 What Does "Early Noachian" Actually Mean?

As early as 1971, with only Mariner 4, 6, and 7 data available, it was clear that the Noachis Terra region (then referred to by the corresponding albedo features, Noachis-

Hellespontis) represented some of the oldest terrains on the planet (McGill and Wise, 1972). Scott and Carr (1978) formally established the Noachian-Hesperian-Amazonian geologic timescale for Mars in their global geologic map based on Mariner 9 images and subsequent crater counts.

The most recent global geologic map of Mars produced by Tanaka et al. (2014) meticulously describes the characteristics of the Early Noachian terrains, but does not attempt to assign a date or bounding event as the official start of the Early Noachian period. Based on their analysis of the crater size-frequency distribution statistics, they classify the Hellas Basin impact as "Early Noachian". Their stratigraphy shows the massif units created by the Hellas Basin impact as being older than Middle Noachian, but they do not go so far as to define the Hellas Basin impact as the start of the Noachian period, as some researchers assume. Instead, the results of their statistical analysis show that the Hellas Basin impact could conceivably be associated with either the start or end of the Early Noachian period, or fall somewhere in-between and merely represent one of the many basin-forming impacts that occurred during that period.

Although they do not list a definitive age for the start of the Early Noachian period, the crater statistics of their individual Early Noachian reference units result in model ages between a minimum of 3.94 Ga and a maximum of 4.17 Ga, which is roughly equivalent to the current estimates for the transition between the Hadean and Archean Eons on Earth (Watson and Harrison, 2005).

In their description of the Early Noachian terrain, Tanaka et al. (2014) also point out that Pre-Noachian features are identifiable in Early Noachian terrains, in the form of buried (ghost) craters and circular topographic lows that are likely the eroded remains of Pre-

Noachian impact craters. These "ghost craters" bear a remarkable resemblance to the heavily eroded circular chloride salt deposits in Early Noachian terrains, possibly indicating that the impact craters that filled with chloride salts during the Early Noachian actually formed during the far-less understood Pre-Noachian period.

4.4.6 Early Noachian Surface Conditions and Astrobiological Preservation Potential

Studies of terrestrial zircons from the Hadean and Early Archean, primarily from the Early Archean sediments of the Jack Hills in Western Australia, have demonstrated the existence of wet, low temperature melting conditions during the Hadean, from approximately 4.35 Ga to 4.0 Ga (Watson and Harrison, 2005). This contradicts previous assumptions of a hellish Pre-Archean world where the formation of a hydrosphere and tectonic plates was constantly reset by large impacts during the Late Heavy Bombardment.

A relatively temperate Early Noachian period on Mars could have started much earlier than the equivalent period on Earth, given the lack of a late-stage Moon-forming impact (Benz et al., 1986). This idea is also supported by Mars' modeled rapid accretion over only ~1-10 Myr (Nimmo and Kleine, 2005) and its early isolation from other large planetesimals after being scattered out of the terrestrial planet-forming disk created by the migration of Jupiter, as described by the "Grand Tack" model for the formation of the inner solar system (Pierens and Raymond, 2011).

The possibility of a prolonged Martian hydrosphere in a relatively temperate Early Noachian period has significant astrobiological implications. A small percentage of the terrestrial Jack Hills zircons with ages >3.8 Ga have been found to include carbonaceous inclusions, at least one of which has been dated to 4.10 ± 0.01 Ga and has $^{13}C/^{12}C$ ratios

consistent with biologic isotope fractionation (Bell et al., 2005). This could indicate that life established itself on the Earth's surface shortly after the planet's formation and was resilient enough to survive the effects of the Late Heavy Bombardment, assuming an increase in impact activity actually occurred. If similar conditions existed on the Martian surface even earlier than on Earth, the proposition that life could have independently developed on Mars becomes increasingly reasonable.

If chloride salts were being precipitated and deposited during the Early Noachian under such conditions, and have survived mostly intact until the present, they would represent invaluable opportunities to explore the conditions under which life formed on Earth and potentially formed on Mars.

Halite crystals formed by precipitation in ephemeral and perennial lakes have been shown to host fluid inclusions within the crystal structure that can preserve microorganisms for long periods of time. Schubert et al. (2009) documented the presence of microorganisms within fluid inclusions in recently crystalized halite samples from Saline Valley, California (1980-present), as well as in fluid inclusions in halite samples from Death Valley, California that crystalized between 10-35 Ka. The same team successfully cultured three genera of halophilic Archaea from halite fluid inclusions up to an age of 35 Ka, while older samples contained preserved halophilic Archaea that were no longer viable (Schubert et al., 2010).

The astrobiology community has long recognized the preservation potential of chloride salts on Mars (Farmer and Des Marais, 1999, and references therein). Still, because such minerals have a reputation for being very easily re-mobilized in terrestrial settings, the field has concentrated on more stable preservation media such as amorphous silica. However, it

is possible that the mobility of chloride salts in the Martian environment is low enough that they also represent a geologically-stable preservation medium.

This concern over the long-term stability of chloride salt preservation is partially supported by the results of Hill and Christensen (2022a), which show that chloride salt deposits can be found in terrains from throughout the Noachian period. This demonstrates that the Martian hydrosphere was likely at least regionally active for hundreds of millions of years, which is more than enough time for Early Noachian deposits to be re-dissolved, re-mobilized, and re-precipitated during the later Noachian periods, destroying any previously preserved Early Noachian fluid inclusions and any biological material they may have hosted.

However, it is possible that all three chloride salt deposit types discussed in this paper were protected from subsequent modification by the Martian hydrosphere due to their burial and still retain fluid inclusions from their initial crystallization in the Early Noachian.

The inferred history of the chloride salt circular deposits (Figure 11) suggests that they were buried by material that lithified and was later eroded down along with the surrounding terrain. Given the higher impact rates in the Early Noachian period, it would be expected that some chloride deposits were buried by crater ejecta shortly after their formation, protecting them from the Martian hydrological cycle until after it had shut down.

The chloride salt ejecta deposits demonstrate that buried chloride salt exists, both as discrete deposits and as larger (>1 km diameter) basin-filling deposits. Again, burial could have sufficiently protected the original chloride salts from the Martian hydrologic cycle, allowing them to retain any original fluid inclusions. Although the chloride salts in the ejecta deposits themselves are unlikely to have retained any of the original fluid inclusions

due to the temperatures and pressures they were subjected to during the impact process, the sub-surface chloride salt layer itself could still contain well-preserved fluid inclusions within crystal structures. This becomes increasingly likely the more extensive the subsurface layers are, since the effects of an impact would decrease with distance from the impact site.

However, the regional high chloride deposits may represent the most likely candidates for containing unaltered chloride salt crystals from the Early Noachian. Nearby large impacts would have buried them under thick ejecta layers, offering significant protection from the Martian hydrosphere. Also, by significantly changing the regional topography and leaving these deposits stranded on regional highs, these deposits may have been out of the Martian hydrologic cycle's reach, even while it was still active.

Although some chloride salt deposits found within these Early Noachian terrains may show evidence of being re-worked in later geologic eras, the three deposit types discussed here were likely protected to varying degrees while the Martian hydrologic cycle was active, possibly allowing them to maintain their crystal structures and retain fluid inclusions from their original formation in the Early Noachian until the present day.

4.5 Conclusions

Among the many chloride salt deposits identified in Early Noachian terrains, the circular deposits, the regional high deposits, and the ejecta deposits likely represent the oldest exposed chloride salt deposits on Mars and likely formed contemporaneously with their surrounding terrain. The geologic context of each deposit type provides a

straightforward mechanism for protecting them from re-mobilization in subsequent geologic periods regardless of the hydrosphere's level of activity.

Although chloride salts are considered unstable preservation mediums in terrestrial settings, this is primarily due to their short crustal residence times, which are driven by the very active and pervasive terrestrial hydrosphere. A less active and less pervasive Martian hydrosphere may not have had an opportunity to re-dissolve or otherwise alter these three types of deposits after their initial formation, in which case the stability of their biological preservation potential could be as high as other materials, such as amorphous silica and microcrystalline quartz.

Of all the 1,605 currently identified chloride salt deposits on Mars, these three categories may represent the most scientifically valuable deposits, as they could preserve evidence of the earliest water-rock interactions on Mars. Such evidence would be invaluable not only for the study of Mars, but also for the study of the emergence of life on Earth, since so little geologic evidence from that period has survived on our own planet. Therefore, they should be considered as possible sites of future exploration by either robotic or crewed missions.

CHAPTER 5

EXPOSED CHLORIDE SALT DIAPIR IN ARES VALLES

5.1 Introduction

The global survey of Martian chloride salt sites by Hill and Christensen (2022b) using the THEMIS Principal Component (PC) Chloride Index confirmed the results of the previous survey by Osterloo et al. (2010), which found that chloride salt sites are almost exclusively limited to the Noachian-aged southern highlands. However, the improved survey did identify two previously unknown chloride salt formations within Ares Vallis, which appear inconsistent with the hypothesized formation process for the chloride salt sites in the southern highlands: water-rock interactions during the brief existence of a surface hydrological cycle concentrated chloride ions within fluids and then precipitated chloride salts as surficial deposits until the hydrological cycle eventually shut down.

The larger of the two formations, the Northern Ares Vallis Chloride (AVC) Formation, is located ~1km below the surrounding Early and Middle Noachian highlands terrain and appears to have formed during the Pre-Noachian rather than during the erosion of Ares Vallis. Unlike the relatively two-dimensional structures of other chloride salt sites, this formation has a three-dimensional structure and contains meter-scale layers exposed in cliff faces. After considering the available information, it has been interpreted as an erosionally exposed chloride salt diapir, which indicates that a wide-spread chloride salt layer from the Pre-Noachian is located under the Noachian-aged terrains in this region of Mars.

5.2 Methods

The THEMIS instrument onboard the 2001 Mars Odyssey spacecraft consists of two multispectral imaging subsystems: a ten-band thermal infrared imager and a five-band visible/near-infrared imager. The thermal infrared (IR) subsystem is a pushbroom imager consisting of a 320 × 240 pixel uncooled microbolometer array with ten strip filters centered at nine different wavelengths that acquire data at a nominal spatial resolution of 100 meters/pixel. The visible/near-infrared (VIS) subsystem is a pushframe imager that consists of a 1024 × 1024 pixel charge-coupled device (CCD) with five strip filters and acquires data at a nominal spatial resolution of 18 meters/pixel. The IR and VIS imagers are co-boresighted through a germanium beamsplitter (Christensen et al., 2004). Over its first twenty years at Mars, THEMIS has acquired over 300,000 IR images and 265,000 VIS images of the Martian surface.

The Context Camera (CTX), onboard the Mars Reconnaissance Orbiter (MRO), is a pushbroom imager that acquires data at a nominal spatial resolution of ~6m/pixel using a 5056-pixel linear CCD centered at a wavelength of 0.611μm with a full-width half-maximum (FWHM) bandpass of ±0.189μm (Malin et al., 2007; Bell et al., 2013).

The High Resolution Imaging Science Experiment (HiRISE) onboard the Mars Reconnaissance Orbiter (MRO) spacecraft is a pushbroom imager that acquires data at a nominal spatial resolution of 0.25m/pixel using an array of 14 CCD detectors, with ten detectors centered at 0.694μm (red), two detectors centered at 0.536μm (blue-green) and two detectors centered at 0.874μm (near-infrared) (McEwen et al., 2007). The two blue-green and two near-IR detectors are in line with the center two red detectors, enabling the

acquisition of multiband approximate true color images along the center of the HiRISE field-of-view (FOV).

PlanetScope, operated by Planet Labs PBC, is a constellation of approximately 130 satellites, able to image the entire land surface of the Earth every day at a resolution of ~3m/pixel with 4-band (blue, green, red, and infrared) images (Planet, 2021). PlanetScope data was accessed through NASA's Commercial SmallSat Data Acquisition (CSDA) Program.

The HRSC-MOLA Blended 200m Digital Elevation Model (DEM) version 2.0 (Fergason et al., 2018) is a global digital elevation model that uses topographic data from the High Resolution Stereo Camera (HRSC) (Neukum and Jaumann, 2007; Jaumann et al., 2007) where it is available and topographic data from the Mars Orbital Laser Altimeter (MOLA) (Smith et al., 2001) where HRSC topographic data is not available. The spatial resolution of the blended product is 200 meters/pixel with a vertical accuracy of ±10 meters.

The Geologic Map of Mars (Tanaka et al., 2014) is based on multiple remote sensing datasets and identifies the major geologic units on the planet's surface, along with their ages based on crater size-frequency distribution statistics. These remote sensing datasets provided morphologic, topographic, spectral, and thermophysical observations for analysis and interpretation during the geologic mapping effort. The THEMIS Day IR Global Mosaic (Edwards et al., 2011a,b) was used as the standard basemap for constructing this global geologic interpretation because it is mostly unaffected by atmospheric haze and thus allowed reliable analysis of surface morphology and texture at a higher resolution than other available global products could provide at the time.

THEMIS Thermal Inertia images were derived from THEMIS nighttime IR images using the techniques of Fergason et al. (2006) during the generation of the THEMIS Thermal Inertia Global Mosaic (Christensen et al., 2013). The absolute accuracy of these thermal inertia values is ~20% and their precision is 10%–15%, which are due to instrument calibration limitations, uncertainties in model input parameters at THEMIS spatial resolutions, and thermal model limitations.

An updated, semi-automated global survey of chloride sites was conducted using all available high-quality late-afternoon THEMIS daytime IR images collected throughout the mission to date. The survey was first performed using the qualitative Quasi-Spectral Chloride Index (Hill and Christensen, 2019) and then using the quantitative Principal Component (PC) Chloride Index (Hill and Christensen, 2022b). Both methods detected two chloride salt locations within Ares Vallis, which was unexpected because the global survey conducted by Osterloo et al. (2010) established that the Martian chloride salt sites occur almost exclusively within the Noachian-aged southern highlands.

Investigation of the AVC Formations using the previously described datasets was conducted using the Java Mission-planning and Analysis for Remote Sensing (JMARS) geospatial information system (http://jmars.asu.edu) (Christensen et al., 2009). The data was then analyzed using the Integrated Software for Imagers and Spectrometers (ISIS) maintained by the United States Geologic Survey's Astrogeology Science Center (http://isis.astrogeology.usgs.gov) [e.g., Anderson et al., 2004; Becker et al., 2013], as well as the DaVinci generic array processing tool maintained by Arizona State University's Mars Space Flight Facility (http://davinci.asu.edu) [e.g., Edwards et al., 2011a,b].

5.3 Results

5.3.1 Identification of Chloride Salts in Ares Vallis

Two chloride salt formations were identified within Ares Vallis and have been designated the Ares Vallis Chloride (AVC) Formations. Their locations are shown in Figure 5.1.

The Northern AVC Formation, which is the larger of the two, is located at 7.572°N, 338.863°E and is shown in Figure 5.2. Multiple datasets and analysis methods have been used to confirm that this formation contains chloride salts.

Osterloo et al. (2008) and Osterloo et al. (2010) described a qualitative method for identifying Martian chloride salts using decorrelation-stretched (DCS) THEMIS IR images: chloride salts regularly appear light blue in DCS 875 images, teal in DCS 964 image, and yellow/orange in DCS 642 images. Individually, these DCS colors are not diagnostic of chloride salts. However, when considered together, chloride salts are the only surface material that always appears with this particular combination of colors across these three standard THEMIS DCS products. This can be seen in Figures 5.2a-5.2c, particularly in the center of the Northern AVC Formation.

Osterloo et al. (2008) and Osterloo et al. (2010) also determined that chloride salt sites often have elevated thermal inertia values relative to their surrounding terrain due to the cemented nature of the material. This can be seen in Figure 5.2d, where the Northern AVC Formation has thermal inertia values of 550-650 tiu (J m−2 K−1 s–1/2), which is significantly higher than the 500 tiu of the surrounding terrain.

Visible datasets can also be used to corroborate the identification of chloride salts on the Martian surface. Osterloo et al. (2010) established that chloride salt sites are nearly

always relatively white in approximate true color images. Figure 5.2e shows an approximate true color THEMIS Color VIS image of the Northern AVC Formation, which appears relatively white. This is also true of the approximate true color strip within the HiRISE image shown in Figure 5.2f.

These qualitative identification methods are further supported using the quantitative THEMIS PC Chloride Index (Hill and Christensen, 2022b). Figure 5.2g shows the index detections over the Northern AVC Formation, which are colorized by their confidence level. The confidence level quantifies how many independent THEMIS IR images yielded chloride index detections for each particular pixel location on the surface.

The Southern AVC Formation, which is smaller and located within the eroded wall of Ares Vallis, is located at 5.803°N, 341.379°E and is shown in Figure 5.3. However, there is less confidence in this identification due to the lack of THEMIS Color VIS and HiRISE coverage, as well as the low confidence level of the THEMIS PC Chloride Index detections. At the time of writing, additional image data have been requested from the appropriate instrument teams to help increase the confidence level of this detection.

Similar to Figure 5.2, Figures 5.3a-5.3c show the standard THEMIS IR DCS images, with the crescent-shaped Southern AVC Formation appearing as light blue in DCS 875, teal in DCS 964, and (only slightly) yellow/orange in DCS 642. Similarly, Figure 5.3d shows a THEMIS thermal inertia image highlighting the formation as an area of higher thermal inertia relative to the surrounding terrain. Figure 5.3e shows the formation highlighted by THEMIS PC Chloride Index detections, which match the shape of the surface feature despite their low confidence level.

The remainder of this work will focus on the Northern AVC Formation because the lack of high-resolution visible images makes a similar analysis of the Southern AVC Formation impossible at this time.

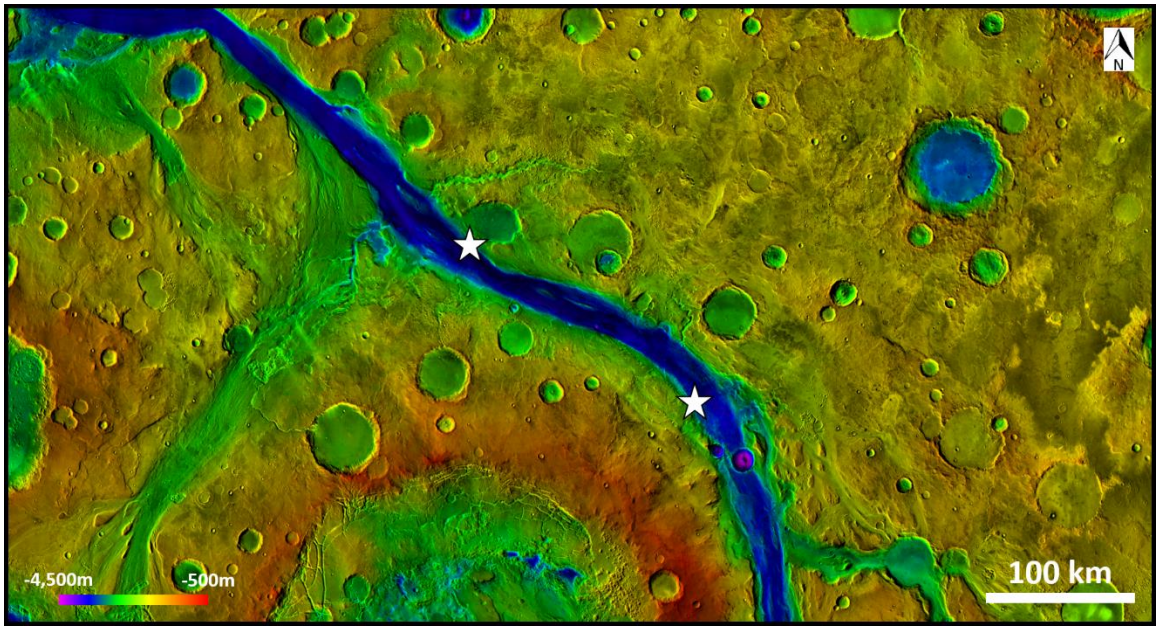

Figure 5.1. Context image for the Ares Vallis Chloride (AVC) Formations (marked with stars) in a subsection of the THEMIS Day IR Global Mosaic overlaid with locally-colorized HRSC/MOLA elevation data.

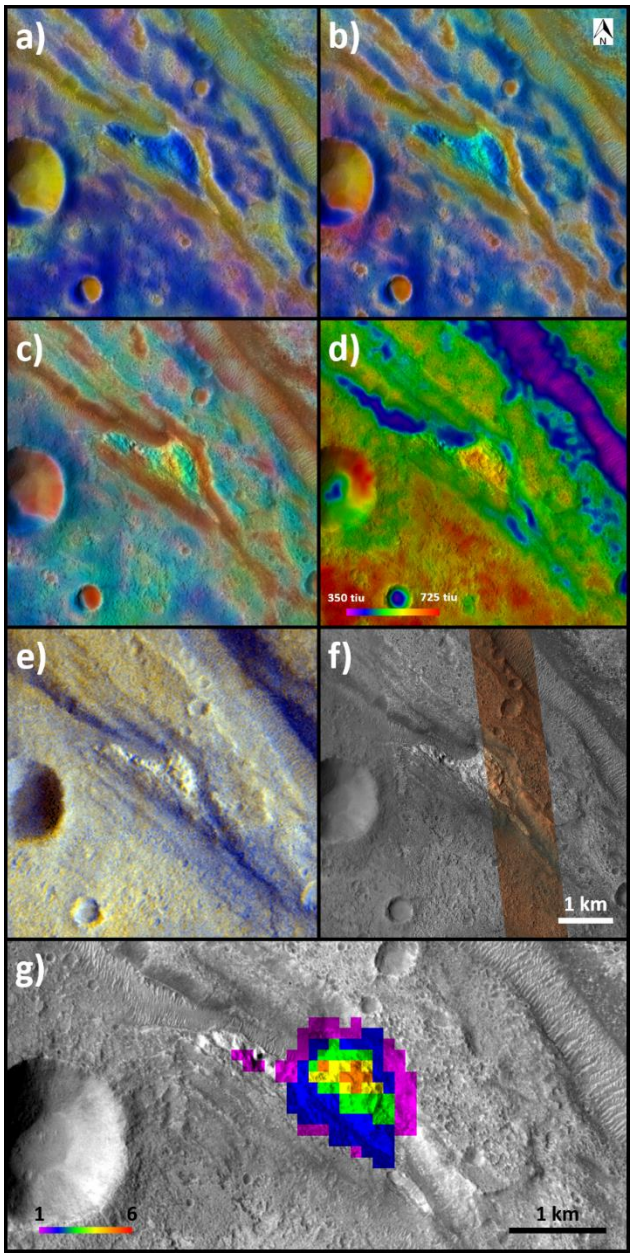

Figure 5.2. Northern Ares Vallis Chloride (AVC) Formation located at 7.572°N, 338.863°E: a) DCS 875 of THEMIS image I40023012 overlaid on CTX image N03_063483_1876 _XN_07N021W, showing chloride salts in light blue; b) DCS 964 of THEMIS image overlaid on CTX image, showing chloride salts in teal; c) DCS 642 of THEMIS image overlaid on CTX image, showing chloride salts in yellow/orange; d) Derived Thermal Inertia from THEMIS image I07622011 overlaid on CTX image, with chloride salts highlighted by elevated thermal inertia; e) THEMIS Color VIS image V81560007 showing chloride formation in white; f) HiRISE Merged Color image ESP_063483_1875 showing chloride salts in white; g) THEMIS PC Chloride Index Detections overlaid on CTX image with chloride salts highlighted by high-confidence detections.

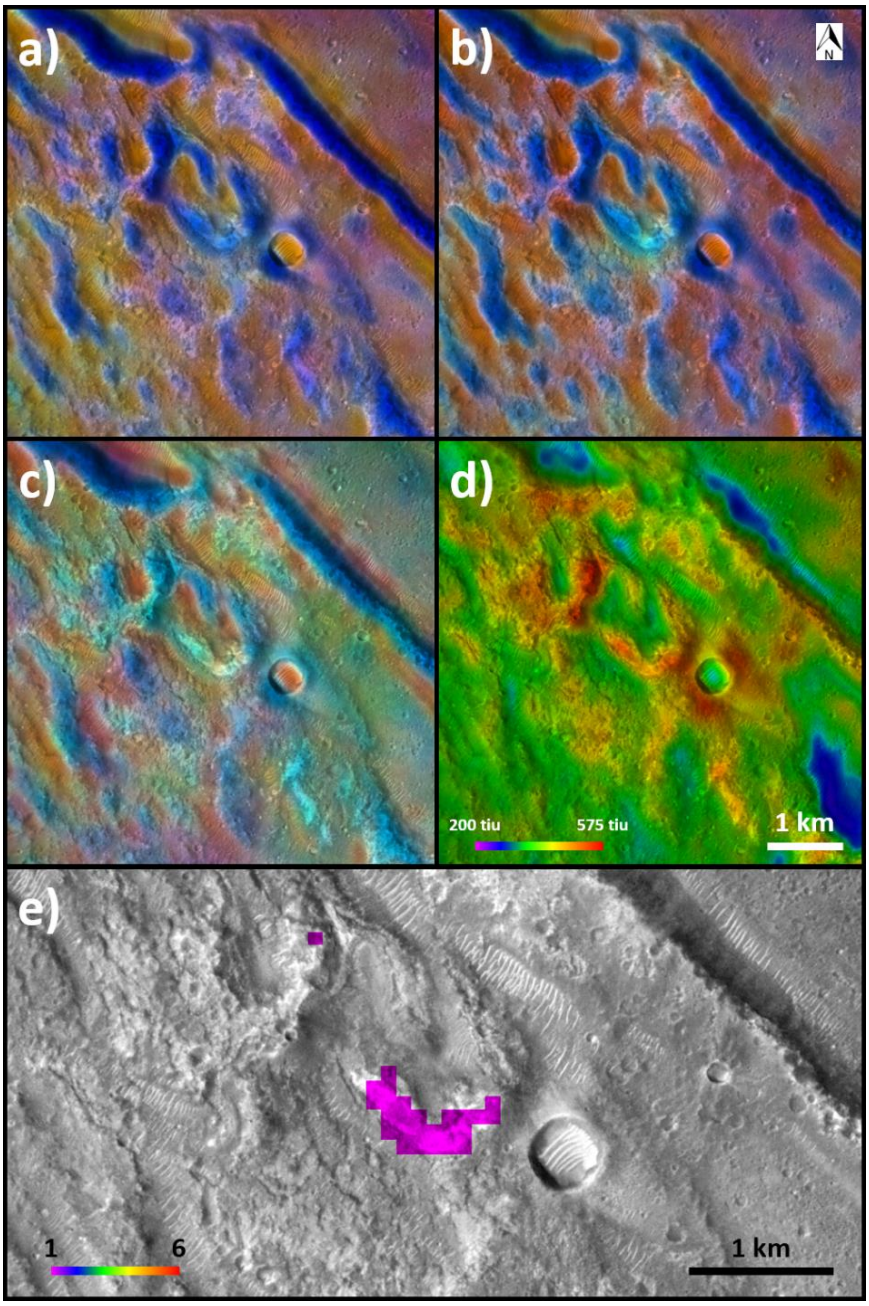

Figure 5.3. Southern Ares Vallis Chloride (AVC) Formation located at 5.803°N, 341.379°E: a) DCS 875 of THEMIS image I08539014 overlaid on CTX image J10_048661_1861_XN_06N018W, showing chloride salts in light blue; b) DCS 964 of THEMIS image overlaid on CTX image, showing chloride salts in teal; c) DCS 642 of THEMIS image overlaid on CTX image, showing only a small part of the chloride salts in yellow/orange; d) Derived Thermal Inertia from THEMIS image I17868017 overlaid on CTX image, with chloride salts highlighted by elevated thermal inertia; e) THEMIS PC Chloride Index Detections overlaid on CTX image, with chloride salts highlighted by a crescent-shaped cluster of low-confidence detections.

5.3.2 Geologic Context

One characteristic that makes the AVC Formations unique among the Martian chloride sites is their location in the eroded terrain of Ares Vallis rather than the heavily cratered southern highlands.

Figures 5.4a and 5.4d show the locations of the Northern and Southern AVC Formations, respectively, relative to the geologic units identified by Tanaka et al. (2014). Both formations are located in the Noachian highlands undivided (Nhu) terrains of the floor and walls of Ares Vallis, which lie topographically below the Middle Noachian highlands (mNh) terrains that surround them. Nearby portions of Ares Vallis are surrounded by Early Noachian highlands (eNh) terrains, which are essentially at the same elevation as the Middle Noachian highlands (mNh) terrains.

Figures 5.4b and 5.4e display elevation maps with profile lines drawn through the Northern and Southern AVC Formations, respectively. The elevation profiles are plotted in Figures 5.4c and 5.4f, respectively, with dotted lines indicating the locations of the AVC Formations. Both AVC Formations are located ~1km below the surrounding Middle Noachian highlands terrain.

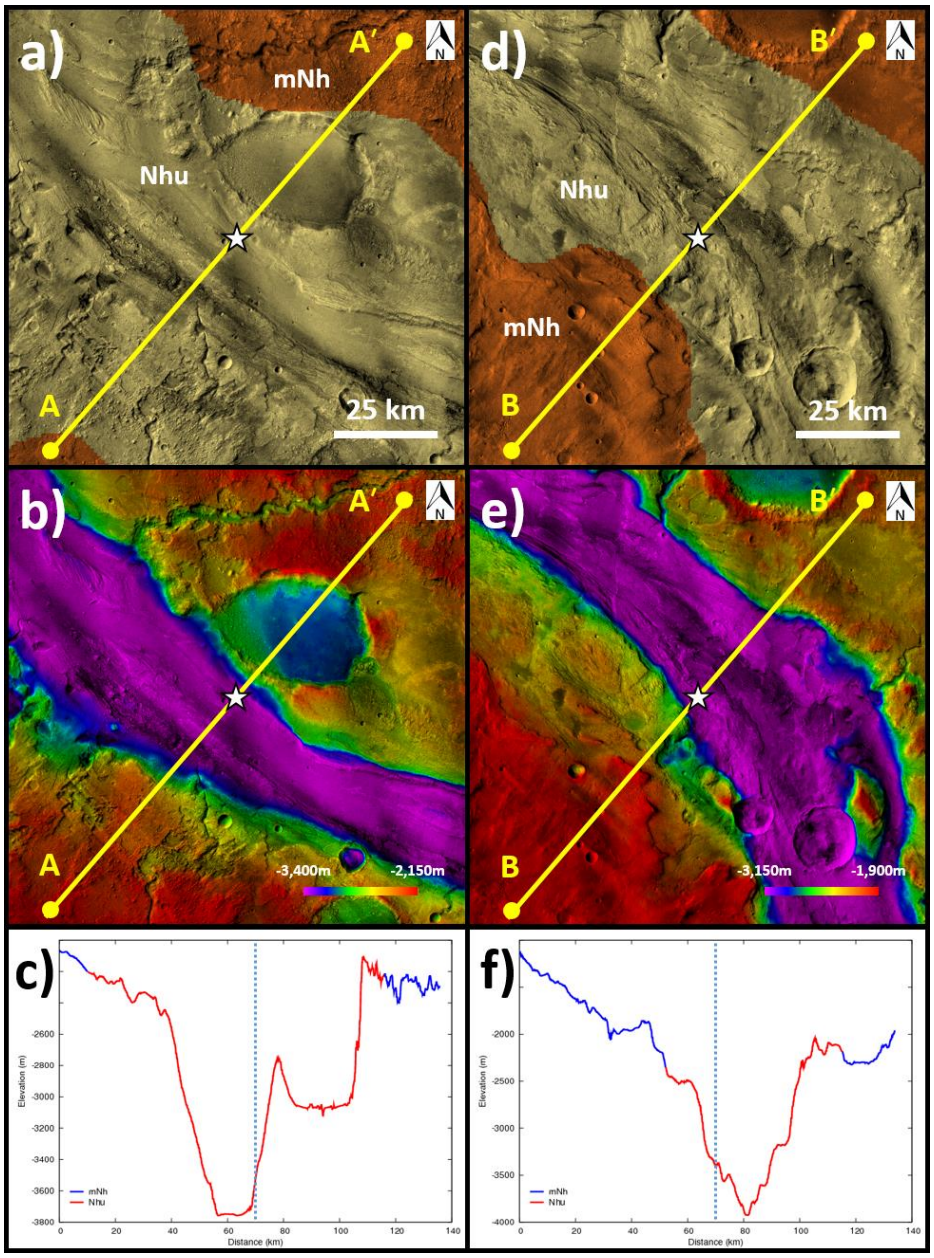

Figure 5.4. Geologic context of the AVC Formations: a) Geologic Map of Mars (Tanaka et al., 2014) overlaid on a CTX mosaic centered on the Northern AVC Formation with profile line; b) Colorized HRSC-MOLA elevation map overlaid on a CTX mosaic centered on the Northern AVC Formation with profile line; c) Elevation plot along the A-A′ profile line with the Northern AVC Formation indicated by a dashed blue line; d) Geologic Map of Mars (Tanaka et al., 2014) overlaid on a CTX mosaic centered on the Southern AVC Formation with profile line; e) Colorized HRSC-MOLA elevation map overlaid on a CTX mosaic centered on the Southern AVC Formation with profile line; f) Elevation plot along the B-B′ profile line with the Southern AVC Formation indicated by a dashed blue line.

5.3.3 Three-Dimensional Structure

Another unique aspect of the Northern AVC Formation is its three-dimensional structure, shown in Figure 5.5. Shadow measurements of Figure 5.5 are difficult due to the complex terrain and relatively high solar incidence angle (~53°) of the image. Still, where possible, they indicate vertical reliefs of a few 10s of meters, which is far more than is typically seen in the relatively surficial southern highland chloride salt sites.

The Northern AVC Formation has light-toned material on all hillsides, suggesting that the chloride salt is continuous through the hills rather than superimposed on top of them. This interpretation is supported by the highly-confident THEMIS PC Chloride Index detections across the entire formation. This suggests that the Northern AVC Formation is a three-dimensional chloride formation that contains a large volume of chloride salts.

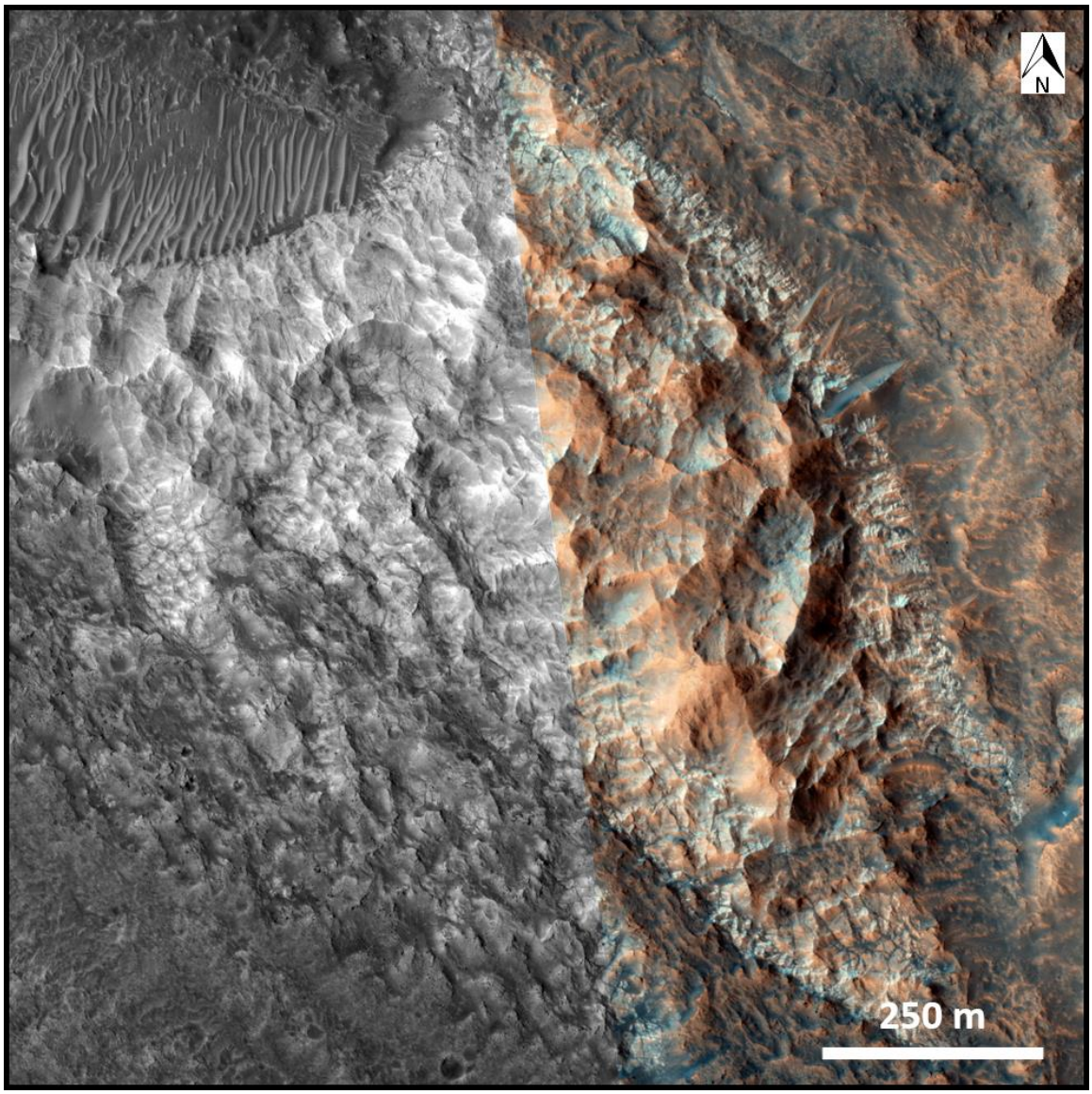

Figure 5.5. Northern AVC Formation in HiRISE Merged Color Image ESP_063483_1875 centered at 7.568°N, 338.868°E.

5.3.4 Three-Dimensional Polygonal Fracturing

The Northern AVC Formation also displays evidence of polygonal fracturing in three dimensions, unlike the relatively two-dimensional surficial polygonal fracturing of other chloride salt sites identified by Osterloo et al. (2010), further indicating that it is likely a solid formation of chloride salt.

Figure 5.6a is centered on a prominent ridge within the Northern AVC Formation, which is cut by multiple dark fractures. The fractures likely appear darker than the surrounding terrain because they are local traps for darker, non-chloride-bearing materials. Figure 5.6b shows a similar, but smaller, group of hills that are also crossed by three-dimensional fractures, which appear to penetrate much deeper than the top-most surface layer.

In contrast, other examples of polygonal fracturing within the formation appear only to be fracturing in two dimensions, most likely within the top-most surface layer. This two-dimensional fracturing can be seen in Figures 5.6c and 5.6d. However, unlike typical surficial chloride salt sites, these two-dimensional fractures occur on relatively steep slopes that lie well above the surrounding terrain.

5.3.5 Meter-Scale Layering

Finally, distinct layers are identifiable within the Northern AVC Formation, which are most easily visible in heavily-stretched HiRISE Color images.

Figure 5.7a shows a band of layered material generally running north-south along the eastern edge of the Northern AVC Formation. The individual layers are best seen when the images are more heavily stretched, as shown in Figures 5.7b and 5.7c. In these images,

meter-scale layering appears as alternating bands of white and red, most likely due to varying amounts of chloride salt and Martian dust within each layer.

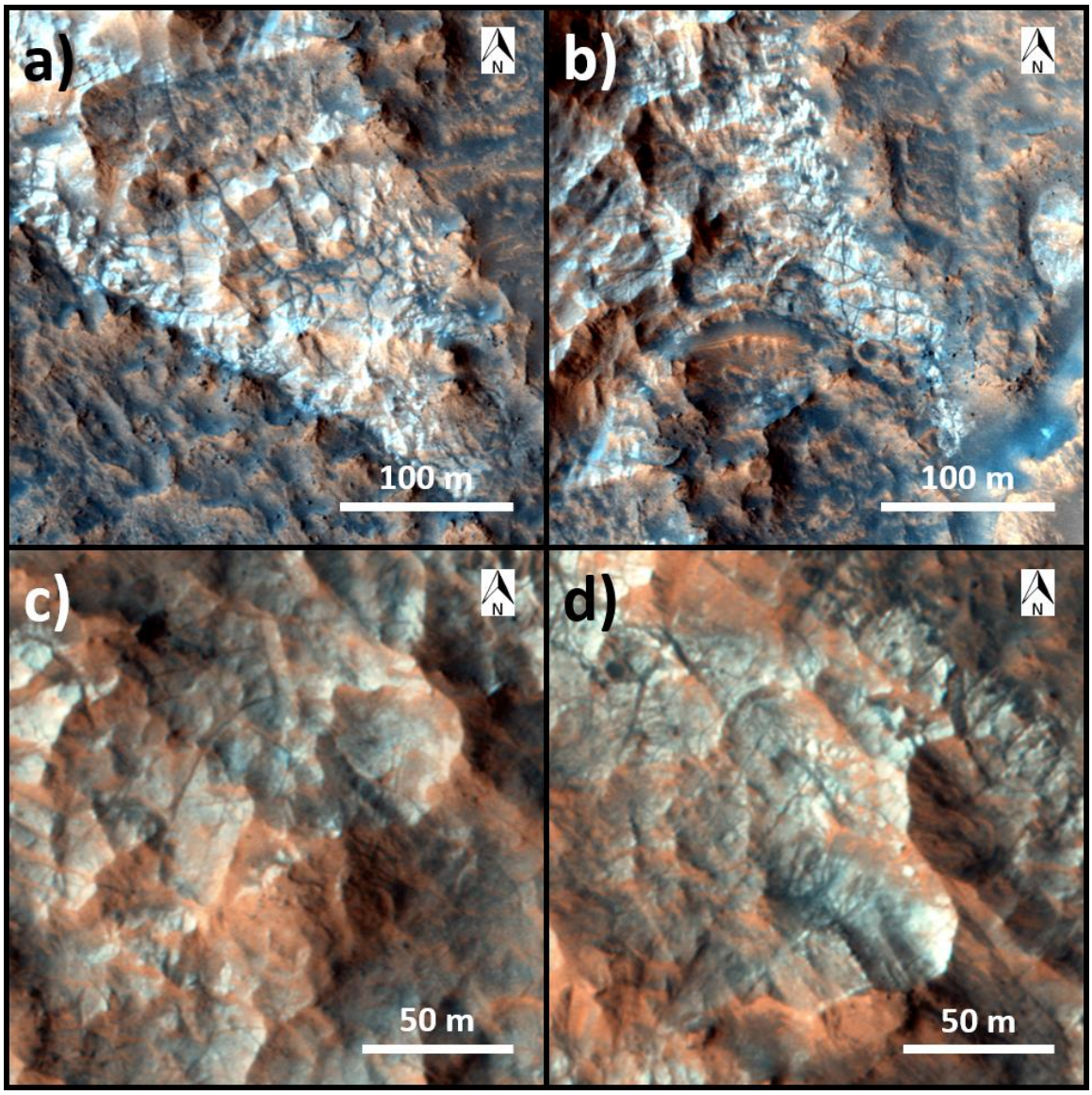

Figure 5.6. Examples of 3D and 2D fracturing within the Northern AVC Formation in HiRISE Merged Color Image ESP_063483_1875: a) Apparent 3D fracturing within the formation at 7.559°N, 338.874°E; b) Apparent 3D fracturing within the formation at 7.562°N, 338.876°E; c) Superficial 2D fracturing on steep slopes within the formation at 7.569°N, 338.871°E; d) Superficial 2D fracturing on steep slopes within the formation at 7.568°N, 338.869°E.

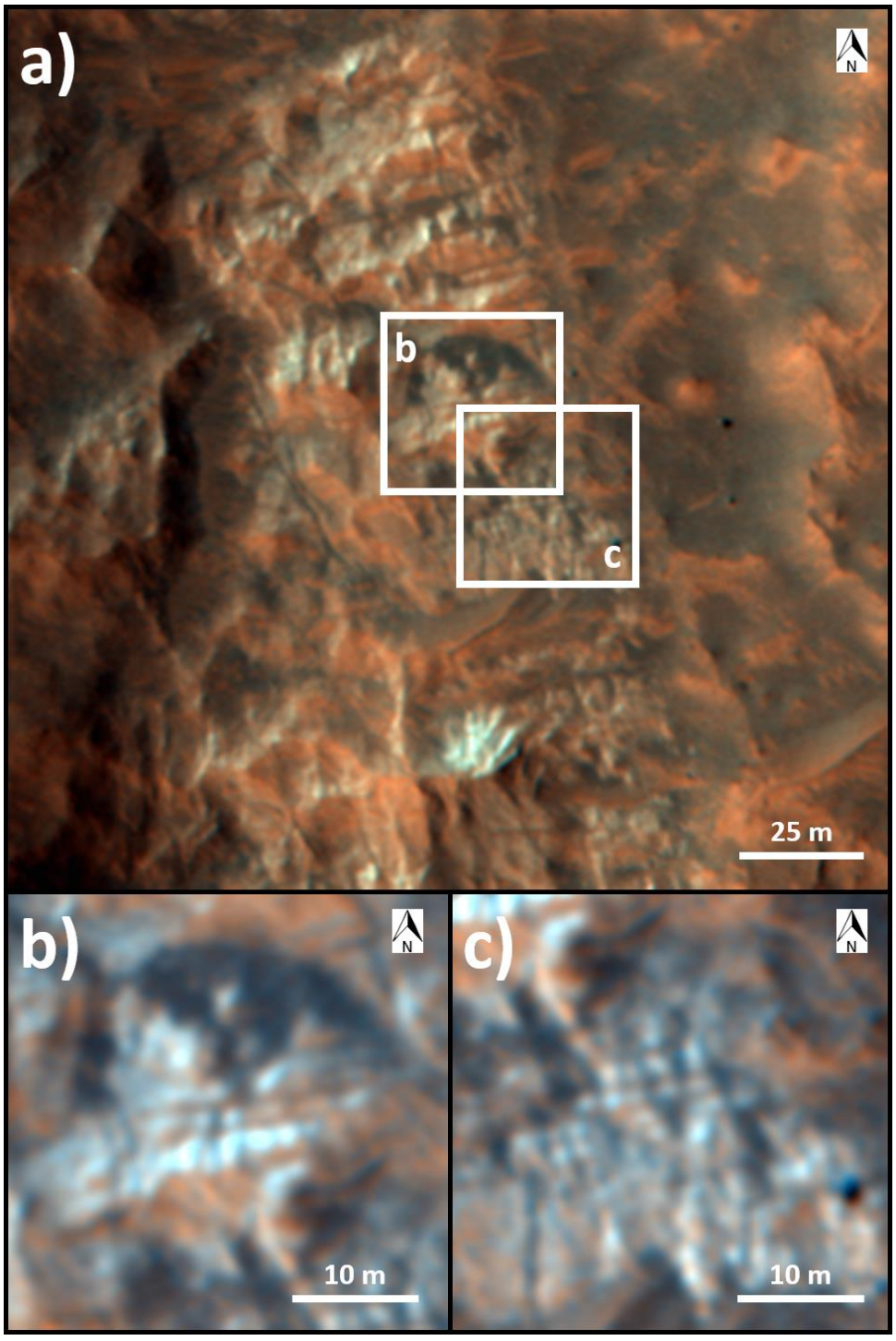

Figure 5.7. Meter-scale layering within the Northern AVC Formation in HiRISE Merged Color Image ESP_063483_1875: a) Band of exposed layering on the eastern side of the formation at 7.566°N, 338.875°E; b) Locally-stretched subsection in Box B showing meter-scale layering; c) Locally-stretched subsection in Box C showing meter-scale layering.

5.4 Discussion

5.4.1 Geologic Context of the AVC Formations

The location of the two AVC Formations ~1km below the surrounding Early and Middle Noachian terrain has three potential explanations: 1) the AVC Formations are indeed stratigraphically lower than the Early and Middle Noachian highlands terrains, indicating that they were emplaced during the Pre-Noachian period; 2) the AVC formations were emplaced in the Noachian highland undivided (Nhu) terrains of Ares Vallis by chloride-rich fluids or brines during the catastrophic outflow events that carved the channel; or 3) the AVC Formations were emplaced by deep sub-surface chloride salt precipitation from chloride-rich groundwater. All three hypotheses are intriguing and potentially problematic for current models of the geologic evolution of early Mars.

The Pre-Noachian origin hypothesis requires that water-rock interactions were occurring and resulting in significant chloride salt precipitation relatively soon after the planet's accretion, during a period roughly equivalent to the Hadean period on Earth. The terrestrial Hadean period has long been viewed as a hellish environment with frequent devastating impacts from the Late Heavy Bombardment (Hartmann et al., 2000) that would have frustrated any early attempts at abiogenesis (Maher and Stevenson, 1988). A similar environment has been assumed for Pre-Noachian Mars, with many basin-forming impacts occurring early in the planet's history when a core dynamo-driven magnetic field was still present, which were then subsequently modified or buried by the late-stage basin-forming impacts of the Early Noachian, such as Hellas and Argyre (Frey, 2006). However, recent work has shown that the Hadean period on Earth might have been much more geologically quiet and conducive to abiogenesis than previously thought (Harrison, 2009; Abramov and

Mojzsis, 2009; Kadoya et al., 2019), raising the possibility that Mars might have also been unexpectedly quiescent during the Pre-Noachian and had intermittent conditions conducive to the orderly precipitation of large-scale chloride salt layers.

The outflow origin hypothesis is consistent with the widely-held view that Ares Vallis was formed due to the catastrophic melting and outflow of subsurface brines from aquafers at the locations of present-day chaos terrains along the Uzboi-Ladon-Morava outflow system, as well as Aram and Hydaspis Chaos (Lucchitta et al., 1987; Warner et al., 2009). As the individual brine outflows receded, chloride salts would have been left behind within Ares Vallis. However, this process would have been expected to leave behind widespread chloride salts within Ares Vallis and where the brines disgorged onto Chryse Planitia, not just two discrete formations. The updated chloride survey by Hill and Christensen (2022b) has verified the earlier findings of Osterloo et al. (2010) that such widespread chloride salt sites do not exist in either Ares Vallis, Chryse Planitia, or any of the other outflow channels hypothesized to have formed through brine outflow processes. Also, because the melting brines would have originated from significantly below Noachian highlands terrains, it merely delays an explanation for how such extensive inventories of chloride salts came to be located so far below the Noachian highland terrains, and is thus an unsatisfying explanation.

The subsurface precipitation origin hypothesis is based on the existence of chloride salt horizons, designated conjelo, in the somewhat Mars-like environment of the Atacama Desert. Conjelo consists of an ~2m thick salt-cemented regolith layer at a depth of ~10m. Sodium chloride and other salts are transported to that depth by small volumes of intermittent rainwater dissolving the chloride salts on the surface and transporting them

into the subsurface via small cracks (Ericksen, 1983; Rech et al., 2003). The key to conjelo formation is the very low volumes of precipitation involved. Slightly larger amounts of precipitation would result in surface runoff, transporting any dissolved chloride salts downstream. Conjelo layers do not form in most terrestrial environments simply because the precipitation volume is too high. This would not be the case in a cold and dry Martian environment. However, the small amounts of water involved also inherently limit the depth that the dissolved chloride salts can be transported to only a few meters. Any additional water, particularly groundwater, would transport the dissolved chlorides to other locations. So although conjelo layers very possibly exist on Mars, they would be orders of magnitude shallower than the ~1km deep AVC Formations.

Ultimately, we favor the Pre-Noachian origin hypothesis, with the chloride salts precipitating during the Pre-Noachian period and then being erosionally re-exposed during the formation of Ares Vallis because: 1) it addresses the ultimate source of the chloride salts, 2) it is consistent with the lack of widespread chloride salts within Ares Vallis and Chryse Planitia, 3) it is consistent with the depth of the AVC Formations, and 4) it is consistent with the hypothesized global environment on Earth during the equivalent Hadean period.

It should be noted that this is not the first time that extensive subsurface chloride salts have been suggested in this region of Mars. Andrews-Hanna (2009) and Montgomery et al. (2009) both hypothesized that the presence of a low shear strength chloride salt layer under Thaumasia Planum would have permitted the Thaumasia mega-slide to occur despite the relatively low regional slope.

5.4.2 Chloride Salt Structures

The structure of the Northern AVC Formation is distinctly different from the structures of typical Martian chloride salt sites, examples of which are shown in Figure 5.8 at the same scale as Figure 5.5. Figure 5.9 shows higher-resolution views of the sites in Figure 5.8, at similar scales to Figures 5.6 & 5.7.

Typical chloride salt sites, like those in Figures 5.9a-5.9d, are characterized by relatively two-dimensional structures with relatively two-dimensional polygonal fracturing. This superficial nature is demonstrated by the chloride salt site shown in Figures 5.8e and 5.9e, which has been cut by a landslide. The exposed cross-section shows that the relatively white chloride-bearing material does not extend significantly into the sub-surface. In contrast, Figures 5.5-5.7 show that the Northern AVC Formation is characterized by a relatively three-dimensional structure with three-dimensional polygonal fracturing.

The only other potentially three-dimensional chloride salt formation identified by this study is located at -31.565°N, 206.370°E and is shown in Figures 5.8f and 5.9f. In addition to the main chloride salt deposit in the channel, there are relatively white polygonally-fractured deposits located on the nearby hills. A close inspection of Figure 5.9f shows that this material preferentially occurs on the northern slopes of the hills and almost never on the southern slopes, indicating it is not continuous through the hills. This implies these chloride deposits are a superficial layer, possibly formed by wind-blown chloride salts from the main deposit being preferentially re-deposited on the northern slopes of the nearby hills. Although these hillside deposits have an atypical three-dimensional aspect to them, the deposits themselves are still relatively superficial and two-dimensional.

The three-dimensional structure of the Northern AVC Formation is more similar to terrestrial surface-piercing salt domes in desert environments, particularly the Ghaba salt domes of the Arabian Peninsula (Peters et al., 2003). The similarly-sized Jebel Majayiz salt dome in northern Oman is shown in Figure 5.10. The jumbled surface expression is a combination of exposed halite (white material in Figure 5.10a and blue material in Figure 5.10b) and blocks of subsurface material carried to the surface by the rising salt dome (dark brown material in Figure 5.10a and green material in Figure 5.10b), which is typical of terrestrial salt domes (Ellison et al., 2022). The Northern AVC Formation does not include any obvious subsurface regolith blocks, but unlike Jebel Majayiz and other terrestrial salt domes, it was subjected to catastrophic erosion events that likely removed such blocks and exposed the central column of the salt diapir. Much smaller cobble-sized blocks of subsurface regolith would still be expected to be mixed within the chloride salt, but are certainly below the resolution of currently available remote sensing systems at Mars.

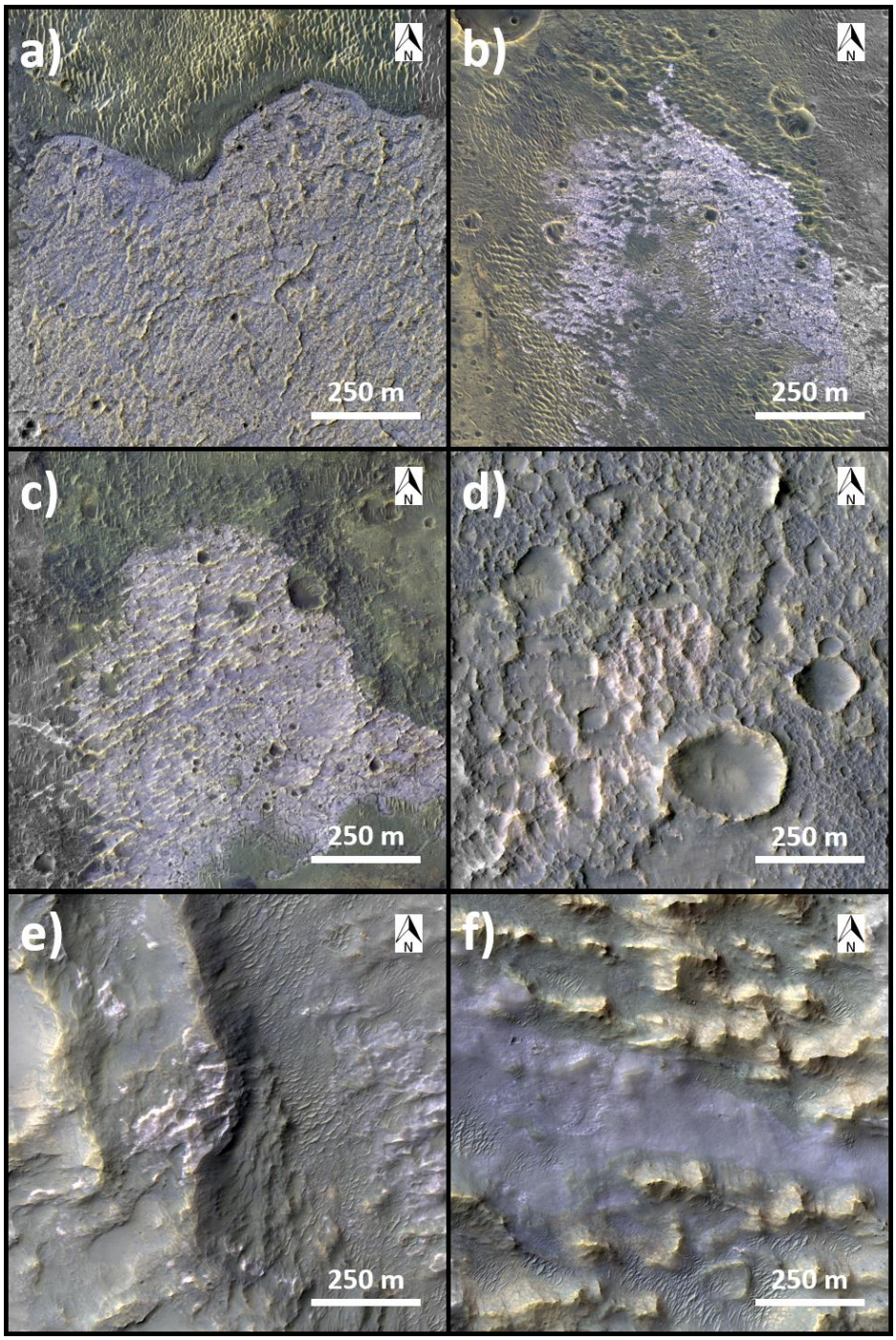

Figure 5.8. HiRISE Merged Color images of comparable chloride salt sites: a) HiRISE image PSP_007770_1770 centered at -3.120°N, 351.500°E; b) HiRISE image ESP_056904_1580 centered at -21.965°N, 309.140°E; c) HiRISE image ESP_028209_1770 centered at -3.095°N, 339.245°E; d) HiRISE image ESP_011547_1475 centered at -32.088°N, 191.060°E; e) HiRISE image ESP_016017_1495 centered at -29.985°N, 196.112°E; f) HiRISE image ESP_016043_1480 centered at -31.570°N, 206.377°E.

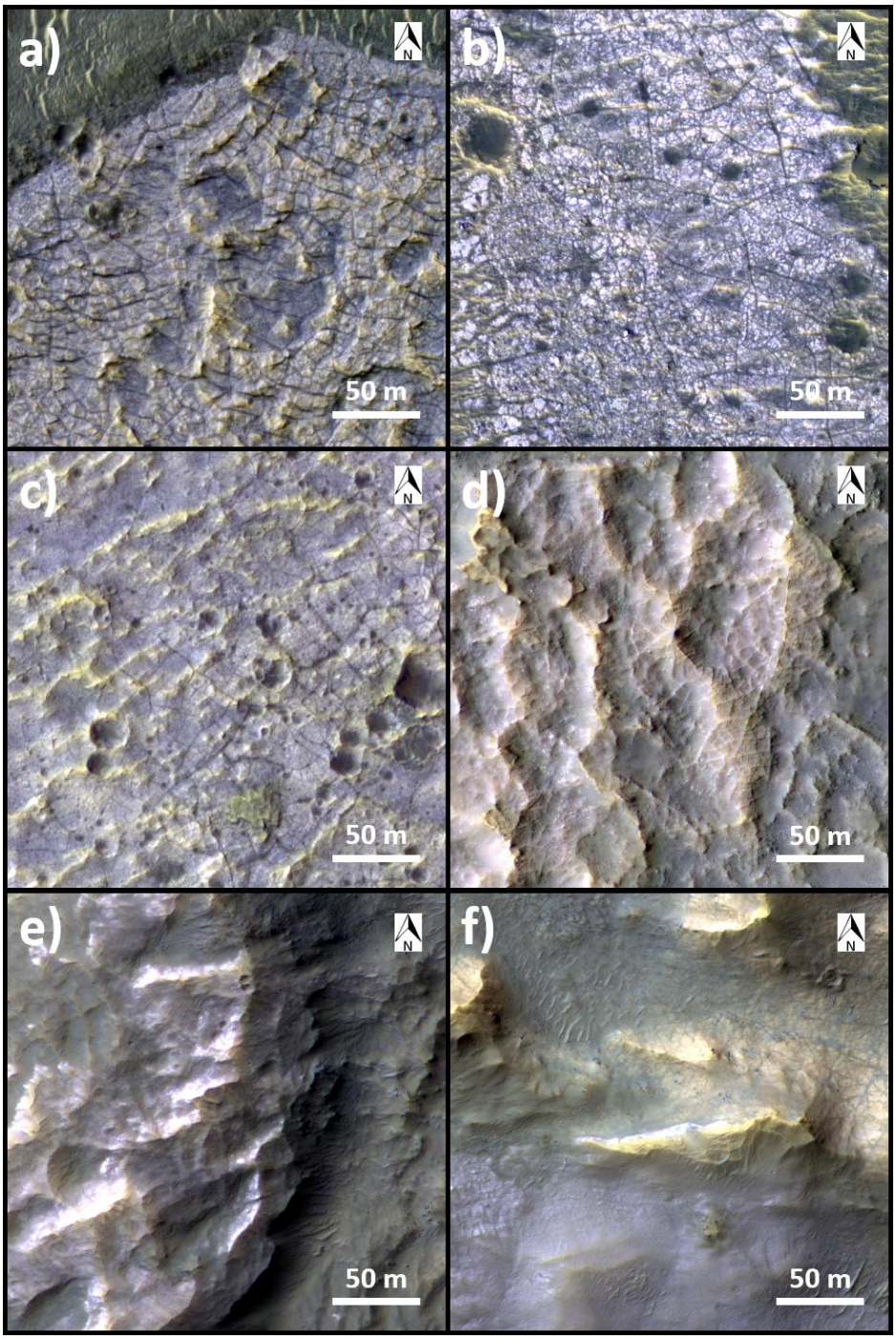

Figure 5.9. Higher resolution views of the comparable chloride salt sites in Figure 5.8, with more easily visible surface textures: a) HiRISE image PSP_007770_1770 centered at -3.120°N, 351.500°E; b) HiRISE image ESP_056904_1580 centered at -21.965°N, 309.140°E; c) HiRISE image ESP_028209_1770 centered at -3.095°N, 339.245°E; d) HiRISE image ESP_011547_1475 centered at -32.088°N, 191.060°E; e) HiRISE image ESP_016017_1495 centered at -29.985°N, 196.112°E; f) HiRISE image ESP_016043_1480 centered at -31.570°N, 206.377°E.

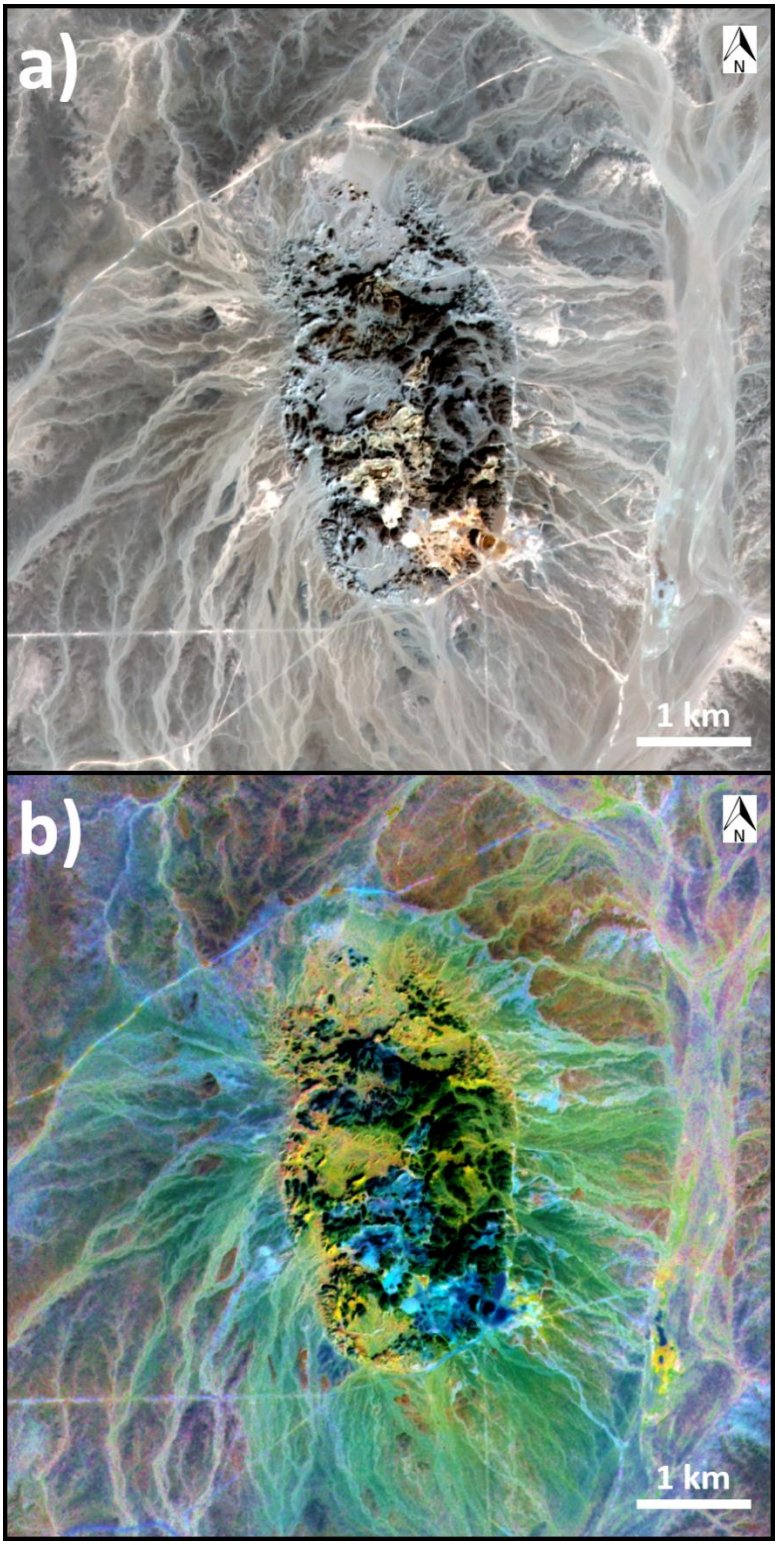

Figure 5.10. Jebel Majayiz salt dome in northern Oman located at 21.498°N, 57.374°E: a) PlanetScope RGB image; b) PlanetScope DCS 321 image, with exposed halite shown in blue.

5.4.3 Salt Dome Layering

The meter-scale layering seen in the Northern AVC Formation is very similar to the layering in terrestrial salt domes and salt glaciers located in desert environments, such as those in the Jashak Salt Dome in southwest Iran. HiRISE-resolution remote sensing images of the Jashak salt dome, comparable to Figure 5.7, are not currently available. However, Figure 5.11 shows surface-level images with visible layering at multiple scales. The most noticeable layering is centimeter-scale, and even millimeter-scale, layering caused by varying amounts of contaminants within the individual salt layers. When viewed as a whole, these formations also include larger meter-scale layers caused by the average concentration of contaminants within the individual layers changing over time. These meter-scale layers are likely equivalent to the meter-scale layers seen in the Northern AVC Formation in Figure 5.7.

This study did not identify similar layering in any other Martian chloride salt sites with high-resolution HiRISE Color image coverage, making this another unique feature of the Northern AVC Formation.

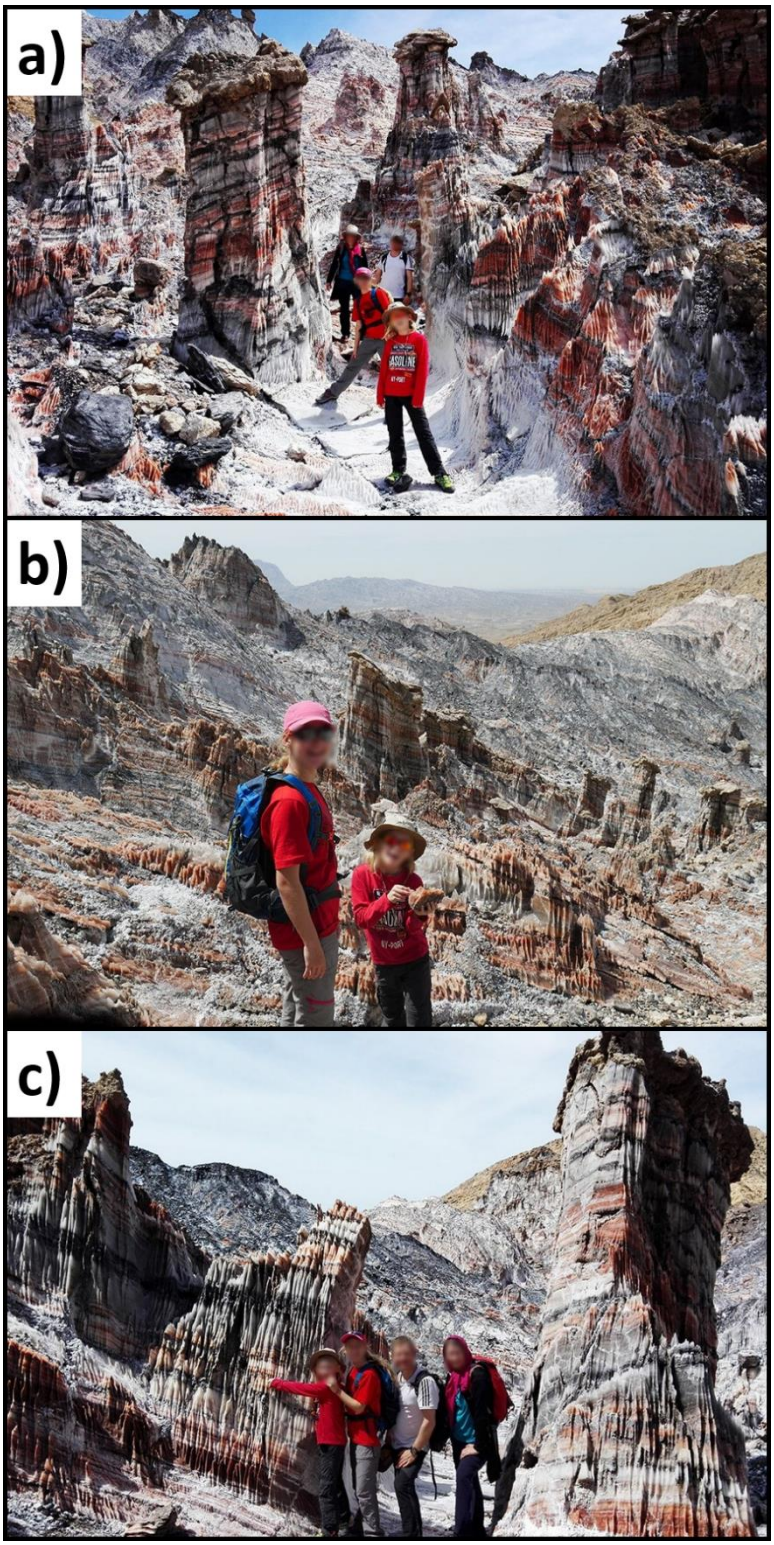

Figure 5.11. Meter-scale, centimeter-scale, and millimeter-scale layering within the Jashak salt dome of southwestern Iran (Cheraghsahar, 2021).

5.4.4 AVC Formation Hypothesis

Given the previously-discussed evidence, we propose the following formation hypothesis, which is illustrated in Figure 12. A pre-existing Pre-Noachian terrain was covered with chloride-rich water, which precipitated a significantly thick layer of chloride salts. This layer was subsequently buried under ~1km of regolith, mostly from the ejecta of Pre-Noachian basin-forming impacts. This created a density inversion, with less dense chloride salts underneath denser Martian regolith. Rayleigh-Taylor instabilities initiated the formation of chloride salt diapirs, which began buoyantly rising towards the surface. However, before this particular diapir could reach the surface and form a salt dome, catastrophic outflow events carved Ares Vallis, which revealed a horizontal cross-section of the chloride salt diapir along the floor of Ares Vallis. The underlying chloride salt layer was not exposed because Ares Vallis did not erode deep enough to reach it. Over time, the buoyancy of the chloride salt continued causing the diapir to rise, leading to a positive relief feature on the eroded surface of Ares Vallis.

The existence of an erosionally exposed chloride salt diapir necessarily requires the presence of a substantial subsurface chloride salt layer. This would imply that the Pre-Noachian period on Mars was not simply a hellish landscape punctuated by basin-forming impacts, but included periods stable enough to result in significant water-rock interactions that led to large volumes of chloride-rich fluids, which then had time to precipitate in an orderly fashion and form a coherent regional-scale layer.

Such subsurface layers cannot be interrogated using short-wavelength remote sensing methods (visible, near-infrared, or thermal infrared). Therefore, longer wavelength radar observations should be used in the future to constrain the possible depth and thickness of

the original chloride salt layer, which would shed significant light on the otherwise invisible Pre-Noachian period on Mars.

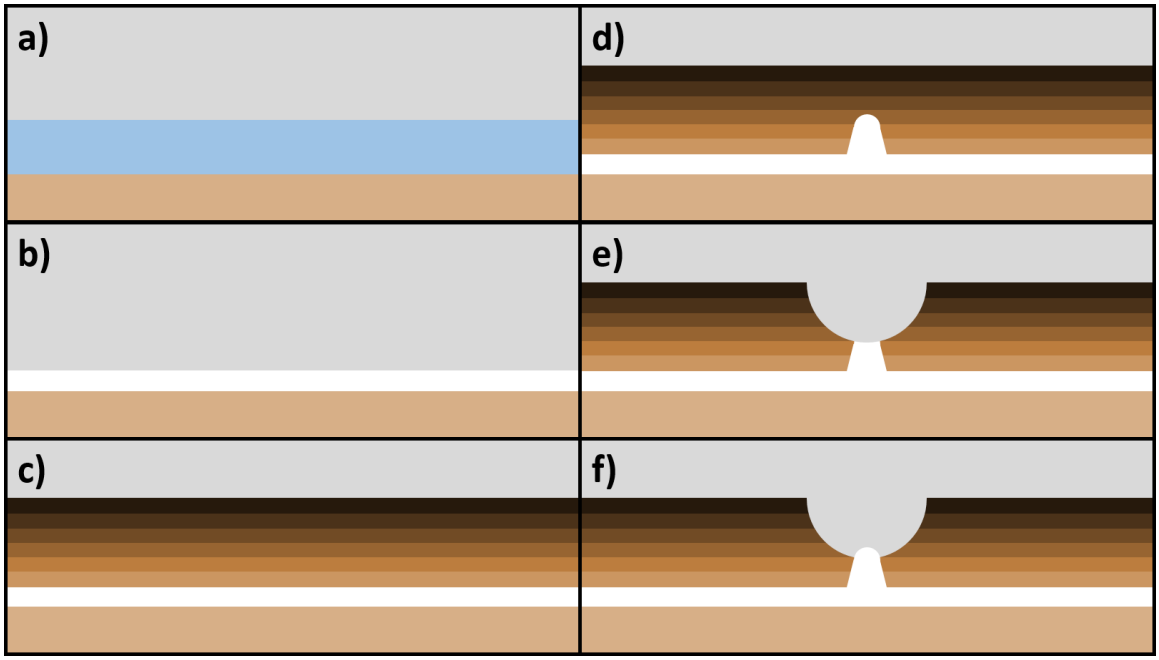

Figure 12. Proposed formation hypothesis for the Northern AVC Formation: a) a pre-existing regional surface is covered by chloride-rich fluids; b) chloride salts precipitate from the fluids and form a distinct layer; c) subsequent processes bury the chloride layer; d) Rayleigh-Taylor instabilities cause the less-dense chloride salts to begin forming diapirs; e) Ares Vallis forms before the chloride salt diaper can reach the surface, eroding into the diapir as well; f) the buoyancy of the chloride salt continues causing the diapir to rise, leading to a positive relief feature on the eroded surface of Ares Valles.

5.5 Conclusions

The two chloride salt formations within Ares Vallis were identified using multiple methods and are significantly different from the typical chloride salt sites of the Martian southern highlands in several important ways.

First, they are located within the erosionally exposed terrain of Ares Vallis, which is located significantly below the surrounding Noachian highland terrain, where most of the previously-identified chloride salt sites are located. Second, the Northern AVC Formation has a three-dimensional structure along with three-dimensional polygonal fracturing, which is significantly different from the relatively two-dimensional structure and polygonal fracturing of other chloride salt sites. And third, the Northern AVC Formation is the only currently-identified chloride salt site with meter-scale layering, similar to the layering observed in terrestrial salt domes and salt glaciers.

When considered together, these three lines of evidence indicate that the Northern AVC Formation, and possibly the Southern AVC Formation, are not chloride salts superficially deposited by local hydrologic activity in the Noachian period. Instead, the evidence indicates that these chloride salt formations are portions of much more significant subsurface chloride salt layers formed during the Pre-Noachian period and exposed during the erosion of the Ares Vallis outflow channel.

In particular, the Northern AVC Formation appears to share more characteristics with terrestrial salt domes and salt glaciers than with terrestrial lacustrine basin chloride salt deposits. The Northern AVC Formation is likely a subsurface chloride salt diapir that would have remained subsurface if not for the erosion of Ares Vallis. The diapir hypothesis also explains why the erosion of Ares Vallis only exposed these two small chloride salt

formations rather than an entire chloride salt layer: the erosion only reached deep enough to expose diapirs that had already begun to buoyantly rise through overlying geologic layers.

The Ares Vallis Chloride Formations imply that a much more significant and widespread chloride salt layer from the Pre-Noachian lies within the Martian subsurface stratigraphically below the oldest terrains currently exposed on the surface.

CHAPTER 6

WALK ON MARS: PHYSICALLY EXPLORING THE THEMIS INFRARED GLOBAL MOSAIC

6.1 Introduction

The 2001 Mars Odyssey spacecraft was launched on April 7, 2001 and arrived in orbit around Mars on October 24, 2001. The Thermal Emission Imaging System (THEMIS) (Christensen et al., 2004), one of Odyssey's three science instruments, has acquired over 300,000 infrared (IR) images of the Martian surface at a resolution of 100 meters/pixel, including global coverage at late-afternoon local times. Over 24,000 high-quality late-afternoon images were previously used to create a global IR mosaic of the entire planet (Hill and Christensen, 2017), as well as a version that was colorized according to elevation using data from the Mars Orbiter Laser Altimeter (MOLA) (Smith et al., 2001) onboard NASA's Mars Global Surveyor spacecraft.

However, the THEMIS team found it challenging to communicate the importance of this global map to the public, who could only interact with it one section at a time on a computer screen. To better convey the scientific value of this map to the public, the THEMIS team wanted to make interacting with it a more physical experience.

Inspired by the National Geographic Society's Giant Maps Program (National Geographic Society, 2021) and the Arizona Geographic Alliance's Giant Traveling Map Program (AZ Geographic Alliance, 2021), the THEMIS Day IR Global Mosaic with Colorized MOLA Elevation was printed at approximately one-third resolution, making it the size of a standard basketball court. The team was also inspired to develop educational

content related to the map by Dr. Buzz Aldrin's ShareSpace Foundation and their Giant Mars Map program (ShareSpace Foundation, 2019), which was developed independently from this effort.

Buchanan et al. (2016) first proposed large floor maps as a novel tool for teaching United States geography, world geography and spatial thinking, which are core parts of elementary school curricula. Anthamatten et al. (2018) conducted a pilot study using the National Geographic Society's U.S. state floor maps with students between eight and twelve years old, which found statistically-significant improvements in spatial thinking skills. Similarly, Kranitz (2018) conducted a pilot study using a single state floor map with 4th grade students and saw significant improvements in scores on the National Assessment of Education Progress (NAEP) Standardized Geography Assessment. They also reported an increase in positive student attitudes towards geography in general, due to the floor map's appeal to visual, auditory, and kinesthetic learners.

There have been no studies regarding the effectiveness of floor map programs with middle school students or with alternative education topics (i.e.: Mars and planetary science). Therefore, an assessment study was performed to quantify the effectiveness of the "Walk on Mars" map and the associated instructional material in teaching junior high school students about Mars geography and the history of Mars exploration. The study participants consisted of 158 students in 6th, 7th, and 8th grades, with 140 students completing all of the study components.

The results show statistically-significant increases in student knowledge about Mars and the history of Mars exploration after a lesson based around the "Walk on Mars" map. However, the results also reveal that future improvements will be needed regarding

teaching students how to interpret the colorized elevation scale used on the map, which can likely be accomplished using an augmented reality sandbox activity.

6.2 Data, Materials, and Methods

6.2.1 Instruments

The THEMIS instrument consists of two subsystems: a ten-color thermal infrared (IR) imager and a five-color visible/near-infrared imager. The thermal infrared subsystem takes images with a resolution of 100 meters/pixel (Christensen et al., 2004). THEMIS is one of three science instruments on NASA's 2001 Mars Odyssey spacecraft.

The THEMIS IR Global Mosaic was created using daytime images blended together using the algorithms of Edwards et al. (2011a,b). Elevation data from the Mars Orbital Laser Altimeter (MOLA), onboard NASA's Mars Global Surveyor spacecraft, was colorized using the standard MOLA color scheme (Smith et al., 2001) and then overlaid onto the THEMIS Day IR Global Mosaic.

The Context Camera (CTX), onboard NASA's Mars Reconnaissance Orbiter (MRO), is a black-and-white camera that takes visible-light images with a resolution of ~6 meters/pixel (Malin et al., 2007; Bell et al., 2013). CTX images were used to provide higher-resolution views of the scavenger hunt sites.

6.2.2 Map Production

The "Walk on Mars" map is actually composed of three maps: 1) a rectangular global map (-180°E to 180°E, 90°S to 90°N) in a Simple Cylindrical projection; 2) a circular north pole map (0°E - 360°E, 65°N - 90°N) in a polar stereographic projection centered at 90°N; and 3) a circular south pole map (0°E - 360°E, 65°S - 90°S) in a polar stereographic

projection centered at 90°S. Although both polar maps are circular, they were printed on square sheets with a black background to make them easier to fold and transport.

All three maps were printed on reinforced 7 ounce/square-yard (33.9 g/m^2) vinyl sheeting. The standard vinyl sheets are 16ft (4.88m) wide, which allowed the two polar maps to be printed as single pieces, while the global map had to be printed in six strips (Figure 6.1) and then carefully bonded together into a single map. The printing was performed by the Kubin-Nicholson Corporation's facility in Milwaukee, WI, then shipped via standard freight to Arizona State University's (ASU) Mars Space Flight Facility.

The dimensions of the maps were chosen to fit on a standard-size basketball court, because many public schools in the Phoenix metropolitan area have indoor basketball courts, which provide an ideal surface on which to display the maps (Figures 6.2 & 6.3). The global map is 47.5ft × 90ft (14.48m × 28.96m), while each of the polar maps are 15ft × 15ft (4.57m × 4.57m).

Given the dimensions and the density of the vinyl material used, the polar maps each weigh ~11 lbs (~5 kg), while the global map weighs ~220 lbs (~100 kg).

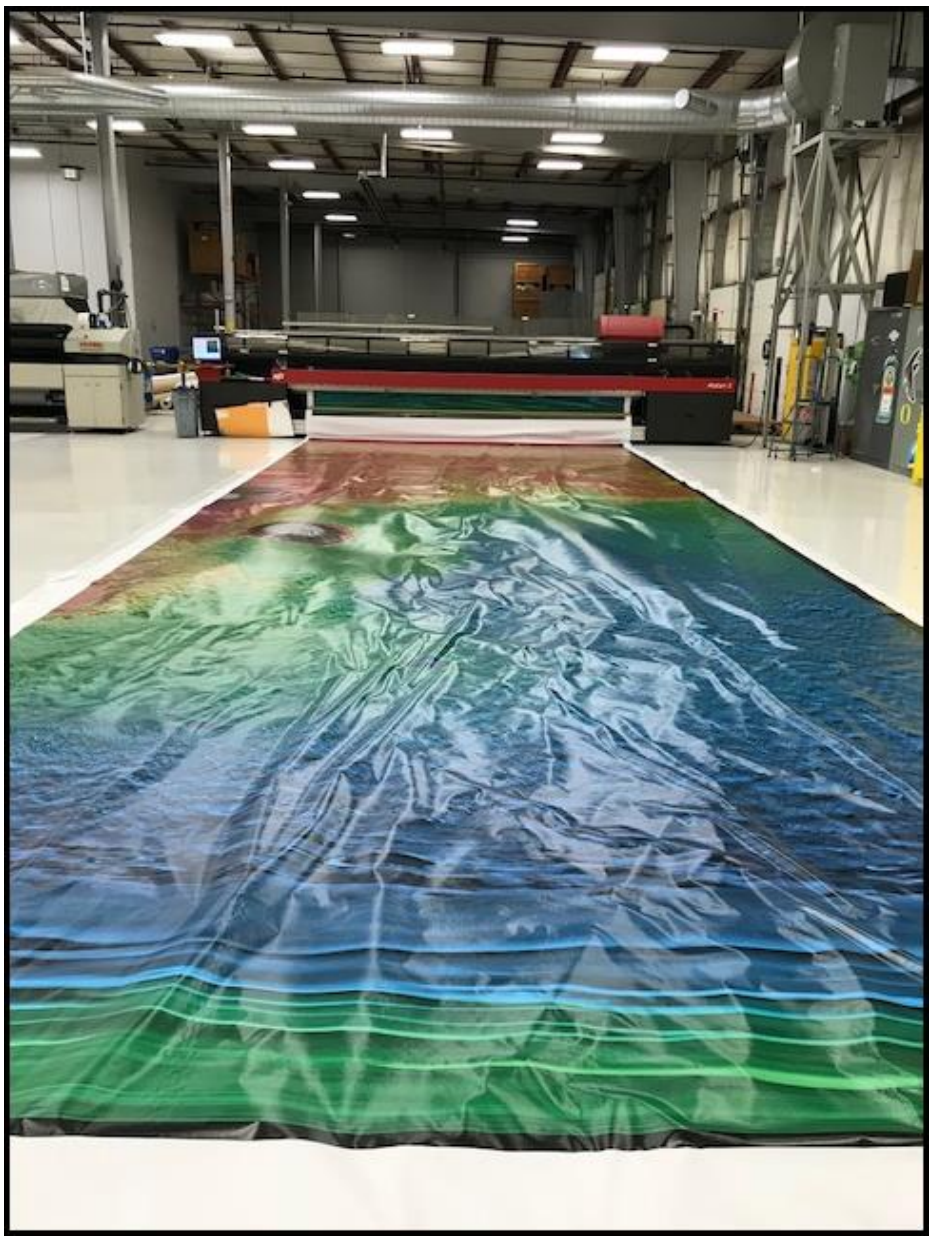

Figure 6.1. “Walk on Mars” map strip being printed by the Kubin-Nicholson facility in Milwaukee, WI (Swanson, 2018).

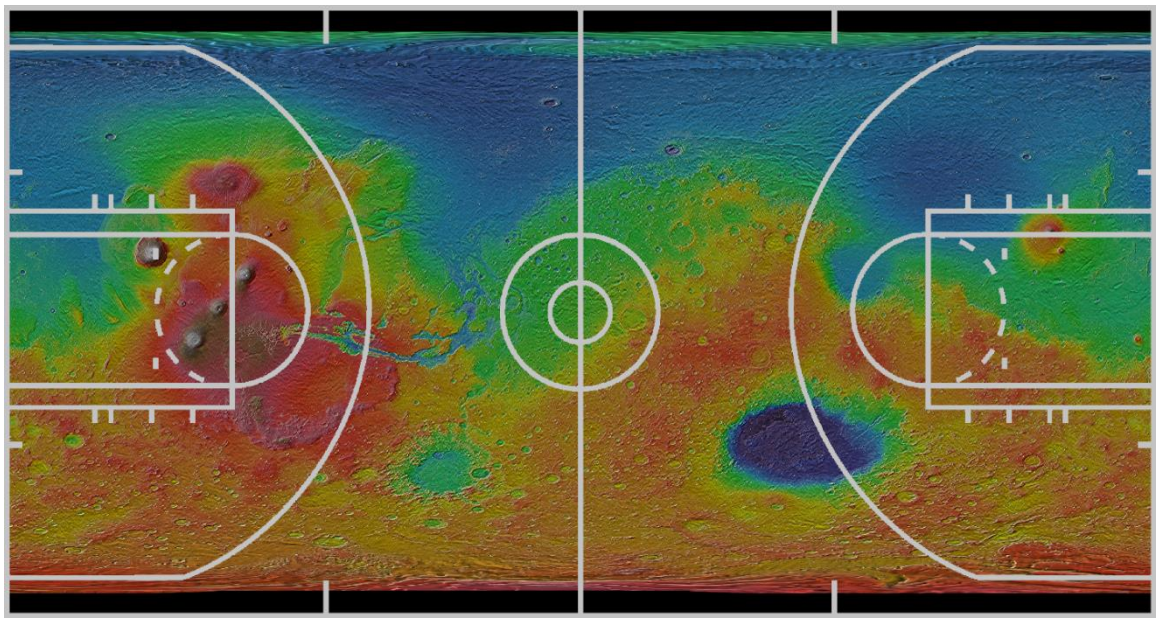

Figure 6.2. “Walk on Mars” global map with basketball court markings for scale.

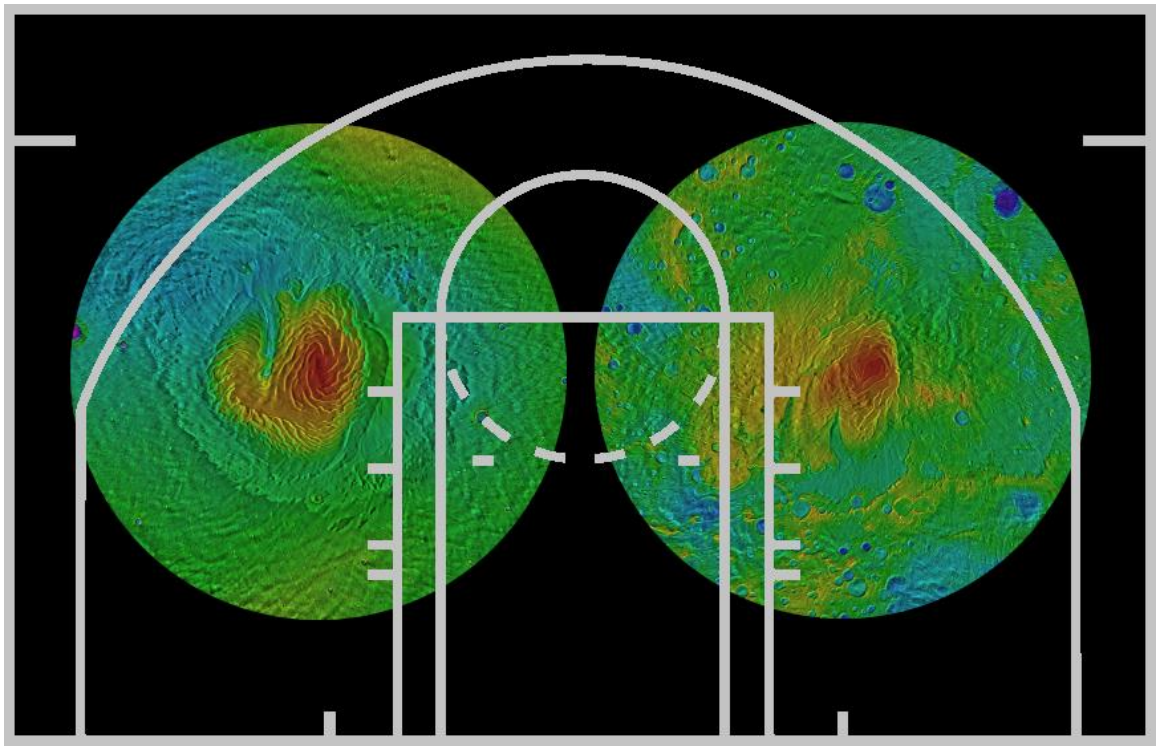

Figure 6.3. “Walk on Mars” polar maps with basketball court markings for scale.

6.2.3 Storage, Transportation, and Set-up

When folded, all three maps fit into a single 40in ×30in × 20in (50.8cm × 76.2cm × 101.6cm) (L×W×H) triple-wall cardboard box with a total weight of ~250lbs (~113kg). Although multiple people are required to lift the box, a single person can move it once placed on a cart.

The box is sized to be easily transported using a medium-sized sport utility vehicle (SUV) or a small pickup truck. A motorcycle scissor jack cart was purchased to help transport the map and lift the box high enough to easily load and unload it from a vehicle (Figure 6.4). The map can be loaded and unloaded by a single person with this cart.

Once the box has been carted from the transporting vehicle to the display location, four people are required to move the box off the cart safely. The polar maps are then removed before tipping the box on its side and rolling out the global map. A team of 4-6 people is then needed to unfold and straighten the global map. Six people are ideal and can have the map ready for participants within 5 minutes. Each of the polar maps can be unfolded and straightened in under a minute by a team of two people.

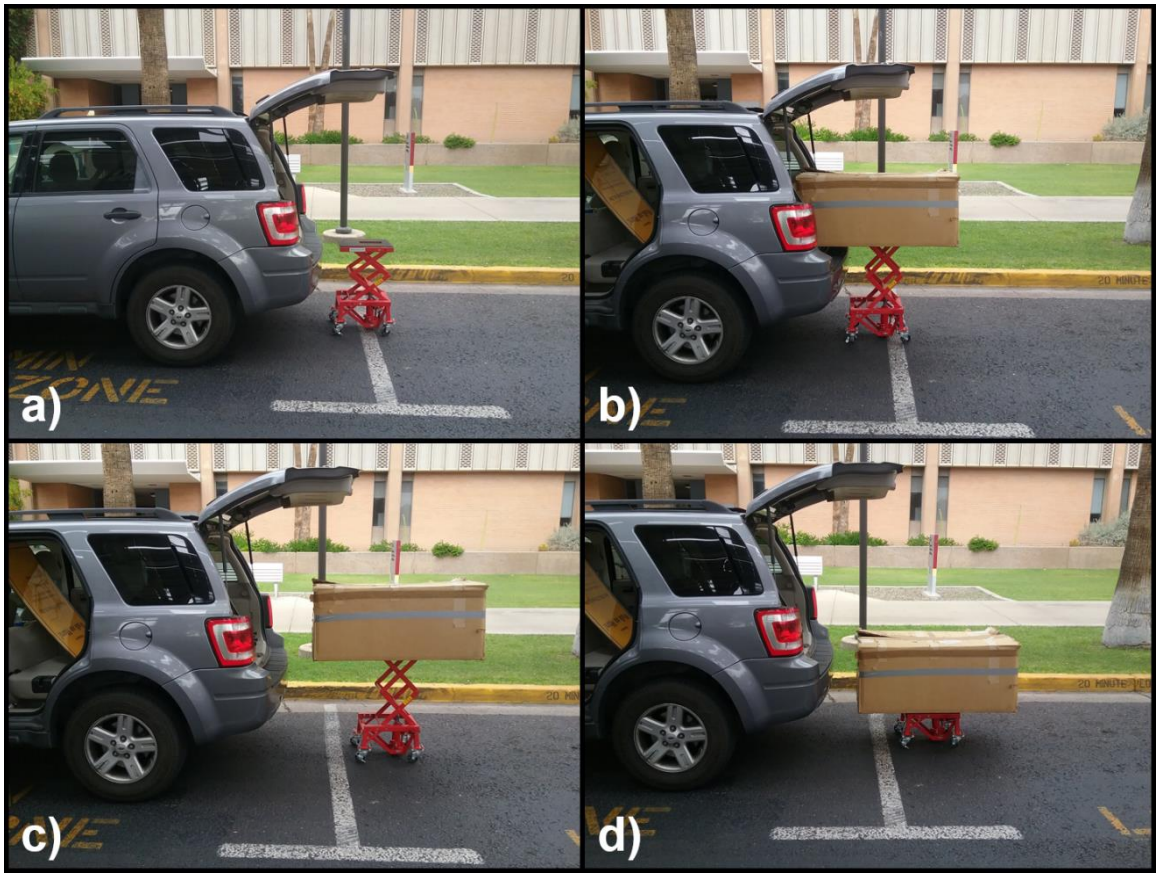

Figure 6.4. Unloading the "Walk on Mars" maps from a mid-sized SUV using the scissor jack cart

6.2.4 Outdoor Foam Mat

Although most public elementary and high schools in the Phoenix metropolitan area have large indoor basketball courts to display the map, many charter schools and rural schools do not have such facilities. Therefore, the team learned that having the capability to display the map outdoors was very helpful, since almost every school in the Phoenix metropolitan area has a large enough outdoor space (ex: basketball court, parking lot, or field) to accommodate the map.

This capability is particularly valuable at large public events, such as science-technology-engineering-mathematics (STEM) festivals, where most attractions are outdoors. The nearest indoor surfaces large enough for the map are often far from the center of activity, so this capability allows the map to be displayed in locations with a higher density of participants.

A giant foam mat composed of 2ft × 2ft (0.61m × 0.61m) puzzle pieces was purchased to protect the map from these uneven and rough outdoor surfaces. For events with only the global map, 1,152 pieces are used to construct a 48ft × 96ft (14.63m × 29.26m) mat. For larger events that also include the polar maps, an additional 192 pieces can be used to add a 16ft × 48ft (4.88m × 14.63m) extension (Figure 6.5).

The logistics of transporting the foam mat can be challenging, because a small box truck is required. However, once at the display location, the individual pieces are extremely light and can be handled by volunteers of nearly any age. With ten volunteers, the entire 48ft × 112ft (14.63m × 34.14m) mat can be assembled in ~60 minutes and disassembled in ~30 minutes.

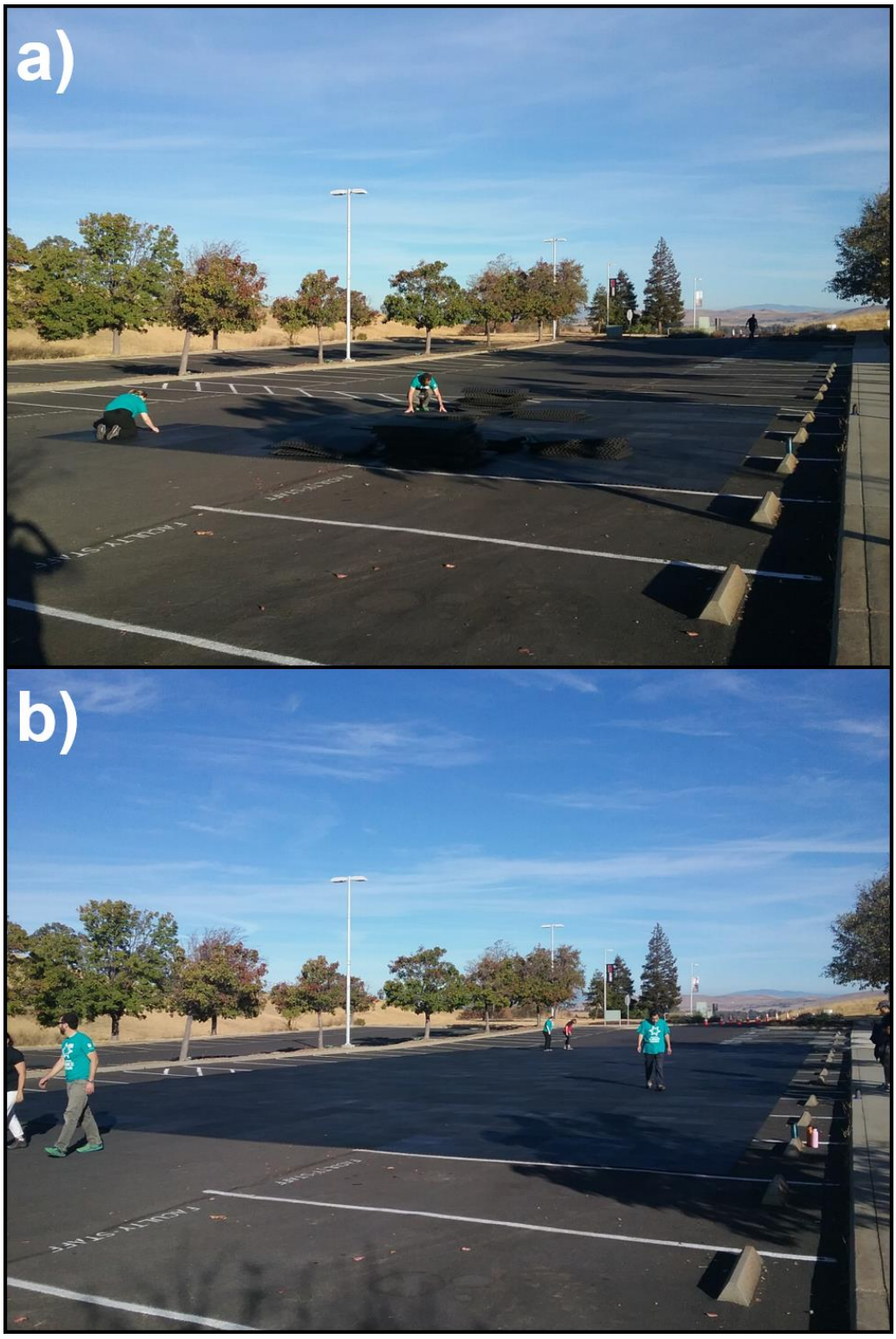

Figure 6.5. Foam mat assembly at an outdoor science festival in Concord, CA: a) volunteers starting to assemble the foam mat; b) volunteers walking on the fully assembled foam mat.

6.2.5 Scavenger Hunt Activities

Three scavenger hunt activities were developed to serve as self-guided tours of the "Walk on Mars" map, allowing participants to explore the map at their own pace and focus on topics that catch their interest. These activities have been particularly useful at public outreach events, where participants arrive unevenly and cannot be easily organized into small groups for guided tours of the map. The scavenger hunts are also an easy way for participants to begin interacting with the map, since they give participants enough information and time to formulate their own questions about Mars, which the event volunteers can then answer.

The covers of the three scavenger hunt activities are shown in Figure 6.6: Mars Geography Scavenger Hunt, Mars Landing Site Scavenger Hunt, and "The Martian" Scavenger Hunt.

The Mars Geography Scavenger Hunt activity takes participants to 15 important and distinctive geographic sites around the map. This activity replicates the guided tours given by volunteer Mars experts during school events and addresses the sites that often generate the most questions from participants. The 15 geography scavenger hunt sites are listed in Table 6.1. The scavenger hunt is organized as a booklet with a subsection of the THEMIS Day IR Global Mosaic with Colorized MOLA Elevation map showing each site on the left side and the right side containing the name, description, and a higher-resolution CTX image mosaic of each location. For example, the entry for Olympus Mons is shown in Figure 6.7. The entire Mars Geography Scavenger Hunt is documented in Appendix A.

Figure 6.6. Cover pages for the three scavenger hunt activities.

Table 6.1. Mars Geography Scavenger Hunt locations.

Site	Importance
Olympus Mons	Highest Elevation
Valles Marineris	Largest Canyon
Hellas Planitia	Lowest Elevation
Ares Vallis	Large Outflow Channel
Tharsis Montes	Large Volcanoes
Kasei Vallis	Large Outflow Channel
Elysium Mons	Large Volcano
Argyre Planitia	Large Impact Crater
Alba Mons	Large Shield Volcano
Gusev Crater & Ma'adim Vallis	Evidence of Flowing Water
Gale Crater & Dichotomy Boundary	Paleo-lake and Global Topographic Change
Deuteronilus Mensae	Subsurface Ice
Aurorae Chaos	Past Subsurface Ice
North Polar Cap	H_2O & CO_2 Ice
South Polar Cap	H_2O & CO_2 Ice

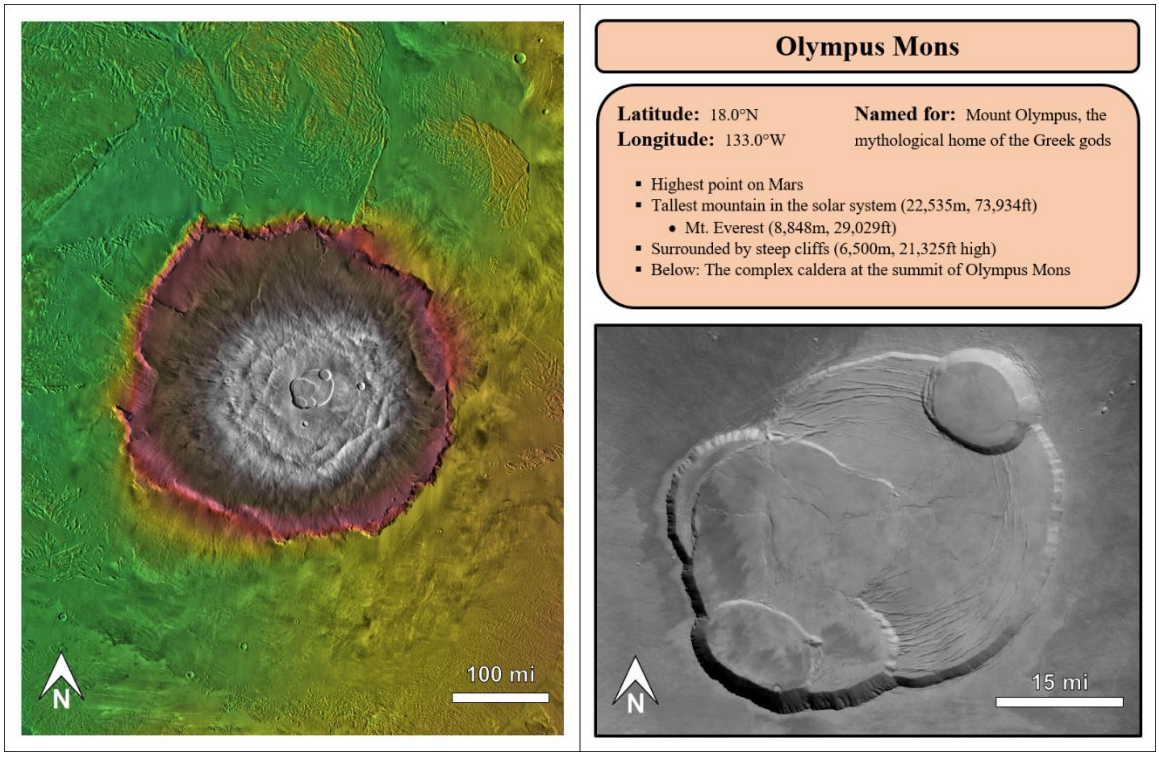

Figure 6.7. Mars Geography Scavenger Hunt entry for Olympus Mons.

The Mars Landing Site Scavenger Hunt activity is designed as a follow-on activity for participants who have finished the Mars Geography Scavenger Hunt and are interested in further exploring the "Walk on Mars" map. This activity is also structured as a self-guided tour booklet and takes participants to all 17 surface mission landing sites (successful, unsuccessful, and planned). Many of the landing sites are in geographic locations that are much less distinct on the map than the prominent features in the Mars Geography Scavenger Hunt, so this activity is typically used with more advanced participants. Small star stickers are usually added to the "Walk on Mars" map at each landing site to give participants confirmation when they find each location.

The entry for each mission includes a subsection of the THEMIS Day IR Global Mosaic with Colorized MOLA Elevation map showing each landing site on the left side, and the right side containing the mission name, mission description, a flag from the country or organization of origin, and either a surface image (for successful missions) or an image of the spacecraft (for unsuccessful and planned missions). All 17 surface missions and their general locations on Mars are listed in Table 6.2. An example entry for the Perseverance rover mission is shown in Figure 6.8. The entire Mars Landing Site Scavenger Hunt is documented in Appendix B.

Table 6.2. Mars Landing Site Scavenger Hunt locations.

Mission/Site	Location
Mars 2	Hellas Planitia
Mars 3	Terra Sirenum
Mars 6	Margaritifer Terra
Viking 1	Chryse Planitia
Viking 2	Utopia Planitia
Mars Pathfinder & Sojourner	Ares Vallis
Mars Polar Lander	Ultimi Scopuli
Beagle 2	Isidis Planitia
MER-A / Spirit	Gusev Crater
MER-B / Opportunity	Meridiani Planum
Phoenix	Vastitas Borealis
MSL / Curiosity	Gale Crater
Schiaparelli	Meridiani Planum
InSIGHT	Elysium Planitia
Mars 2020 Rover	Jezero Crater
Rosalind Franklin & Kazachok	Oxia Planum

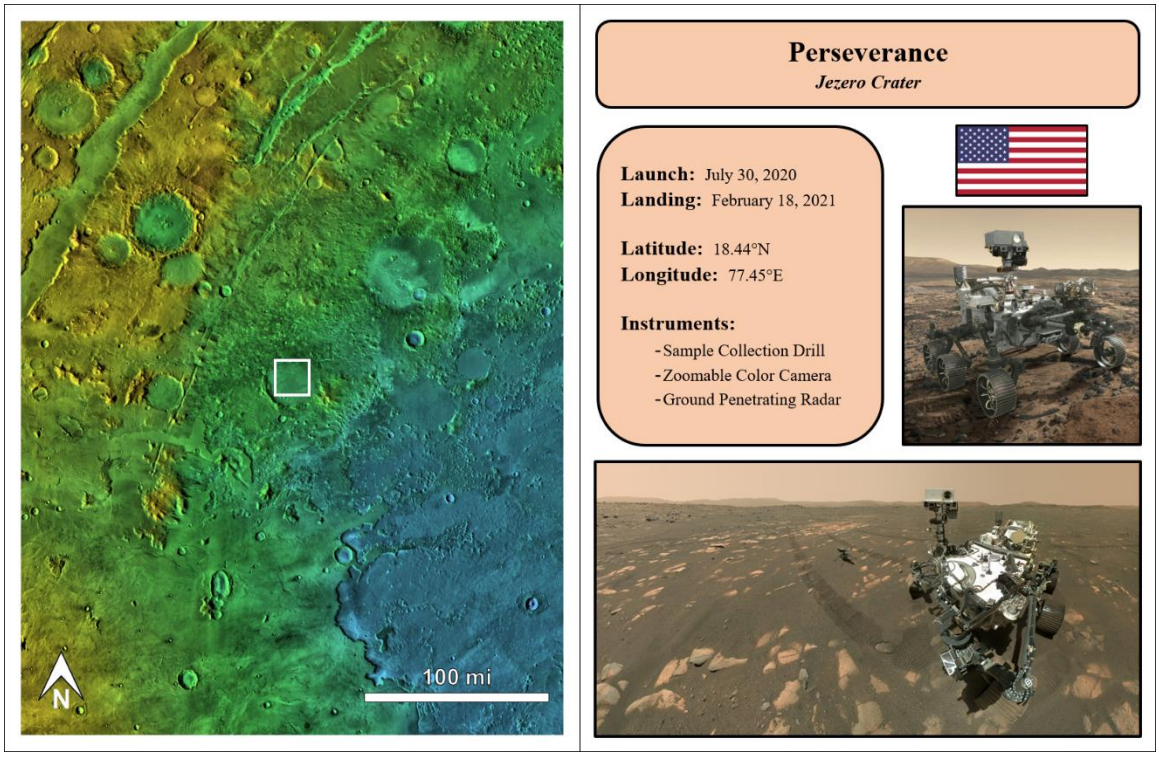

Figure 6.8. Mars Landing Site Scavenger Hunt entry for the Perseverance rover mission.

Finally, "The Martian" Scavenger Hunt activity was primarily designed for adult participants and was created in response to the overwhelming number of questions that participants regularly ask regarding the movie.

"The Martian" was written by Andy Weir (Weir, 2014) and was later adapted into a movie directed by Ridley Scott (Scott et al., 2015) and starring Matt Damon as American astronaut Mark Watney, who becomes marooned on Mars and must survive for over 18 months until his crew can return to rescue him. The book describes his time on Mars in great detail, giving the real geographic names of the places where Watney travels along with the associated dates (in Martian sols). This high degree of realism in both the book

and movie often leads participants to ask questions about it while exploring the "Walk on Mars" map.

The scavenger hunt begins in the plains of Acidalia Planitia, at the fictional location of the Ares III habitat where Mark Watney's story begins. Participants then follow Watney's journey, first to the mouth of Ares Vallis, where he retrieves a radio from the Mars Pathfinder lander, then back to his habitat in Acidalia Planitia, and finally on his trek across Arabia Terra to the Ares IV ascent vehicle located in Schiaparelli Crater.

In all, participants are taken to nine real sites specifically mentioned in the book and movie, which are listed in Table 6.3. The entry for each site includes a subsection of the THEMIS Day IR Global Mosaic with Colorized MOLA Elevation map showing Watney's path on the left side. On the right side, the entry gives the actual place name, the fictional date (sol) when Watney arrived there, a short description of his activities at that location, and two movie scenes from the site. An example entry for Mawrth Crater (sol 474) is shown in Figure 6.9. The entire "The Martian" Scavenger Hunt is documented in Appendix C.

Table 6.3. "The Martian" Scavenger Hunt locations.

Sol	Location
018-019	Acidalia Planitia – Ares III Habitat
076	Acidalia Planitia – Lewis Valley
082	Ares Vallis – MPF Landing Site
109-461	Acidalia Planitia – Ares III Habitat
461-474	Mawrth Vallis
474	Mawrth Crater
486	Coimba & Vernal Craters
500-549	Schiaparelli Crater – Ares IV Ascent Vehicle
549	Mars Orbit

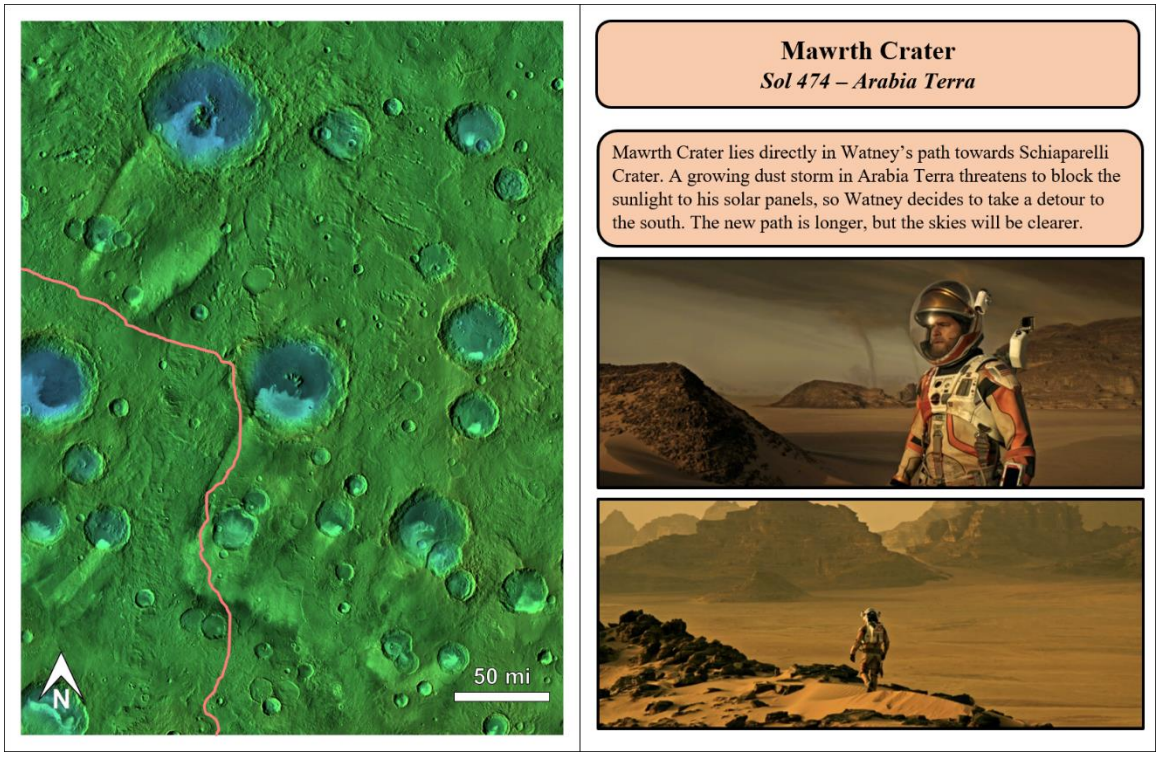

Figure 6.9. "The Martian" Scavenger Hunt entry for Sol 474 at Mawrth Crater.

6.2.6 Program Operations

The "Walk on Mars" program has educated over 8,000 participants (Table D.1) from various audiences and age groups about Martian geography, Mars exploration, and planetary science during its first four years in operation.

The "Walk on Mars" program was initially funded by an education and public outreach (EPO) grant from Arizona State University's School of Earth and Space Exploration (SESE) in 2017, which provided the funds required to print the "Walk on Mars" map and purchase associated materials. Most events have been held in the Phoenix metropolitan area on a volunteer basis, while a handful of out-of-state events were made possible by donations and grants. Over half of the events were organized by volunteers in

the NASA/JPL Solar System Ambassador program, which provides resources and support for volunteers to hold space-related EPO events across the country (Jet Propulsion Laboratory, 2021).

Most events have been held at elementary and middle schools, because the Solar System Ambassador volunteers often work with these age groups. However, the program has reached a wide variety of ages and audience types. A breakdown of the events by the target audience(s) is provided in Table 6.4. Some events targeted multiple groups, so they have been counted more than once in Table 6.4.

These audiences have ranged from kindergarten classes, who were captivated by the idea of giant volcanoes and canyons on Mars (Figure 6.10), to professional planetary scientists, who were excited to find their study regions on the map (Figure 6.11), to families visiting the National Mall in Washington, D.C., who saw the map from a distance and were interested enough to come over and talk with the volunteer Mars experts (Figure 6.12).

Table 6.4. Walk on Mars - target audiences

Audience	Number of Events
Kindergarten	1
Elementary School	13
Middle School	8
High School	5
College	1
Public	10
Professional	3

Figure 6.10. Kindergarten students walking along Valles Marineris behind NASA/JPL Solar System Ambassador Suzan Balowek.

Figure 6.11. Planetary volcanologist Dr. Brent Garry on the "Walk on Mars" map next to Arsia Mons, his recent study area (Garry, 2018).

Figure 6.12. A family explores the "Walk on Mars" map with a volunteer Mars expert at the "Mars on the Nation Mall" event in Washington, D.C., sponsored by the American Geophysical Union's Celebrate 100 grants program (American Geophysical Union, 2019).

6.2.7 Instructional Methods

In a formal education setting, the "Walk on Mars" map lesson has four components, which are described in detail in Appendix G.

First, before walking on the map, students are introduced to the concept of colorized elevation. A common misconception is that the map colors represent temperatures on Mars, similar to a weather map of the Earth. It can be helpful to build on this connection by relating the "high temperature" colors with "high elevation", and "low temperature" colors with "low elevation". Once the students show that they understand the connection between color and elevation, they are invited to walk on the map.

The second component of the lesson focuses on the major geographic features on Mars, such as Olympus Mons (the largest volcano in the solar system), Valles Marineris (the largest canyon in the solar system) and Hellas Basin (the largest recognizable impact crater on Mars). The instructor leads the students as a group to the major geographic features, stopping briefly at each feature to explain its significance, point out interesting details, and compare it to similar geographic structures on the Earth (Figure 6.13).

The third component focuses on the five currently-operating robotic surface missions and their locations on the Martian surface: Curiosity (USA), InSIGHT (USA), Perseverance (USA), Ingenuity (USA), and Zhurong (China). The instructor guides the student groups to each landing site and tells them the name of the mission, its scientific reasons for landing at that particular location, some of the mission's major accomplishments, and when the mission landed relative to the students' ages (ie: Eighth-grade students in 2022 would have been seventh-grade students when the Perseverance rover landed, but would have been in pre-school when the Curiosity rover landed).

And finally, the lesson concludes with a general question and answer session. Students are encouraged to ask questions throughout the lesson, but it is helpful to have a dedicated period at the end when they can ask general questions about Mars that are not particularly related to any of the locations visited during the lesson.

Figure 6.13. Students gathered around Olympus Mons on the "Walk on Mars" map while an instructor describes how big the volcano is compared to Mount Everest on Earth.

6.2.8 Study Setting and Participants

The assessment study was conducted at Ss. Simon and Jude Cathedral School in Phoenix, Arizona. The study participants consisted of 158 students from the 6th, 7th, and 8th grades, who completed the study components during their regular science classes. Each grade level was unevenly divided into two classes based on their math level placements, so the instructor-to-student ratio varied by class.

Due to various student absences during the three days of the study, 141 matched test pairs were collected. These matched pairs represent ~89% of the student participants, which is reasonably representative of the entire dataset, so the analysis will be focused on only the matched data. However, a single matched test pair was removed from the analysis because the student was not fluent in English and responded to some questions in their native language. The study team was unable to locate a translator or interpreter for the language in question, so the responses within this test pair could not be interpreted.

The following analysis is performed using the final set of 140 matched pairs and is based on the procedure used by Simon et al. (2019). A breakdown of study participants is given in Table 6.5.

Table 6.5. Assessment study participants

Test	6th Grade Students	7th Grade Students	8th Grade Students
Pre-Test	46	59	45
Post-Test	47	58	43
Matched Pairs	44	56	40

6.2.9 Study Structure

Because the study included human subjects, a study protocol was developed consistent with the Collaborative Institutional Training Initiative (CITI) best practices. The process included all study investigators completing the CITI Social and Behavioral Research certification training course, obtaining permission from the elementary school to perform a human research study on their premises, developing a privacy plan to ensure that the study investigators did not collect personally identifiable information (PII) during the study, and performing a safety assessment that demonstrated that the participants would not be exposed to any risks beyond what they usually experience in their everyday lives. The study protocol was reviewed and approved by the Arizona State University (ASU) Institutional Review Board (Study ID: 00014374). The study protocol is contained in Appendix E.

The assessment consisted of three parts. First, the participating students were given a pre-test (see Figures F.1 and F.2) to assess their pre-existing knowledge of Mars and Mars exploration before any relevant material was taught in their classes that school year. This included general questions that would later be specifically addressed by the "Walk on Mars" map, as well as a free-form response section designed to assess any related pre-existing knowledge they might have on these subjects.

Second, a week after the pre-test, the students participated in a 45-minute lesson during their science class, which included a 30-minute guided tour of the "Walk on Mars" map and a 15-minute question-and-answer session. The lesson is documented in Appendix G.

And third, one week after the "Walk on Mars" lesson, the students were given a post-test to re-assess their knowledge about Mars and Mars exploration (see Figures F.3 and

F.4). The first post-test section was identical to the general question section in the pre-test, so that a quantitative before-and-after comparison could be made. The second section of the post-test consisted of questions about the map itself, which the students could not reasonably be expected to know before the lesson. The third section of the post-test consisted of free-response questions to assess what information stood out most to the students and their general opinions about the map lesson.

Regardless of grade level, all students received the same pre-test and post-test. Both tests included a section for the students' names, which the school staff used to collate and staple both tests together as matched pairs. To prevent the collection of PII by the study investigators, the school staff cut these sections off of both tests before delivering them to the study investigators, who assigned each test pair a unique identifier for later reference. The tests were then graded using the rubrics in Appendices H and I.

6.2.10 Assessment Test Validity

Crocker & Algina (1986) define validity as the ability of a scientific test, and the test items within it, to measure the intended concept domain(s). Following the procedure of Bardar et al. (2006), the assessment test was evaluated for both content validity and face validity.

Content validity assesses the extent to which the test questions are scientifically accurate and representative of the concept domain(s) being evaluated. To evaluate the content validity, the same assessment tests were administered to five planetary science graduate students, who are subject-matter experts. All five graduate students had perfect

scores and were in agreement that the questions were fair measures of general Mars knowledge, indicating a satisfactory level of content validity.

Face validity assesses whether a test covers topics appropriate for assessing student knowledge in the concept domain being evaluated. To evaluate the face validity, we compared the assessment test questions to the Mars section of the school's junior high astronomy textbook (Pasachoff et al., 2005). The school's curriculum covers astronomy in 6th grade, although the 6th grade students had not yet covered it at the time of the assessment study. The textbook includes all the facts needed to correctly answer the assessment test questions, demonstrating that the test addresses Mars-related content commonly taught in junior high science classes and that the level of knowledge being assessed is age-appropriate.

6.3. Results

6.3.1 Internal Consistency – Cronbach's Alpha

The internal consistency, or reliability, of the pre-test and post-test were quantitatively assessed by calculating Cronbach's alpha, which is defined in Equation 6.1.

$$\alpha = \frac{K}{K-1}\left(1 - \frac{\Sigma\sigma_i^2}{\sigma_x^2}\right) \qquad \text{Eq. 6.1}$$

where: K = number of test items/questions

σ_i^2 = variance of each item/question

σ_x^2 = variance of the entire test

The value of Cronbach's alpha can vary between 0 and 1, and is a measure of unidimensionality. In other words, it indicates whether or not the assessment test is measuring a single concept. The entire set of matched pairs (N=140 students) was used in both the pre-test and post-test calculations. For the pre-test, α=0.456, and for the post-test, α=0.570. Both of these values are below the 0.70 typically considered acceptable (Nunnally, 1978), however the increase after instruction does show that the test was able to measure the expected post-instruction improvement.

A factor analysis was performed on the test scores in order to determine if the low Cronbach's alpha values were primarily due to non-unidimensionality in the tests' concept domain. The resulting eigenvalues are plotted in Figure 6.14, showing that both tests had only one strong factor, verifying that the test's concept domain was unidimensional. Therefore, the low Cronbach's alpha scores were likely caused by the low number of test questions and possibly the use of multiple test question formats (see Appendix F).

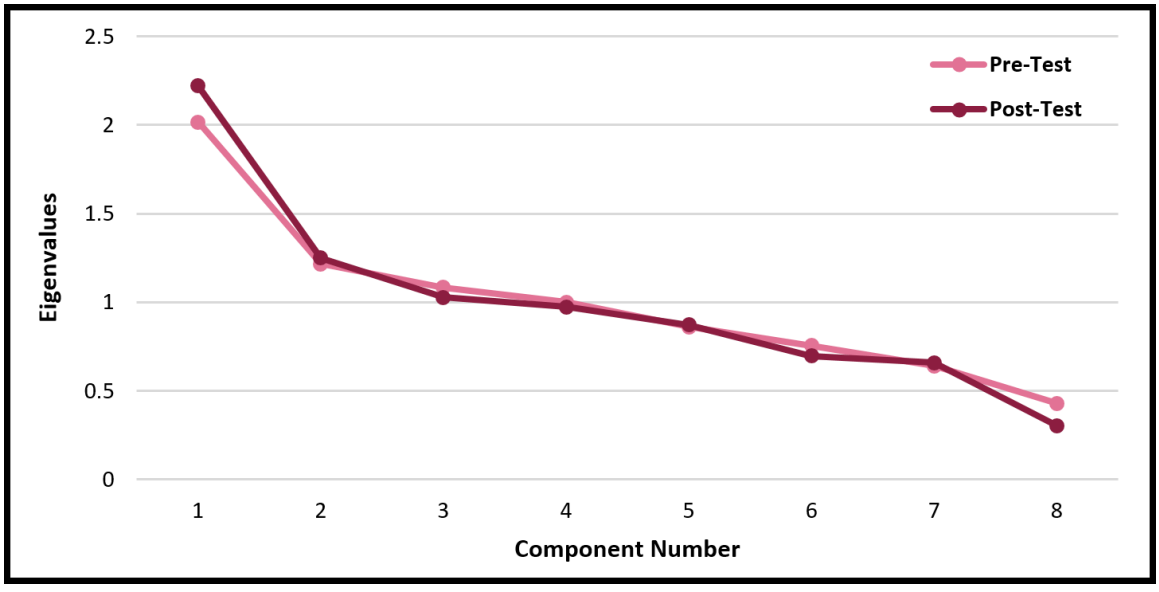

Figure 6.14. Eigenvalues from a Factor Analysis of the Pre-Test and Post-Test Scores

6.3.2 General Mars Questions – Item Difficulty

The "General Mars Questions" section of the pre-test and post-test consisted of eight increasingly difficult questions about Mars and Mars exploration. The students could have learned the answers from prior coursework, media coverage, or individual research, but they were explicitly covered during the map lesson. The rubric for scoring the tests is provided in Appendices H and I.

The item difficulty, *p*, of a particular question is defined as the proportion of students who answer the question correctly (Crocker & Algina, 1986). An assessment test will ideally have questions with a wide variety of item difficulties between $0.2 < p < 0.8$ (Bardar et al., 2006). The goal of the pre-test/lesson/post-test assessment structure is for the *p*-values to increase significantly after the students have received the lesson.

Overall, this study's pre-test *p*-values varied between $0.02 < p < 0.87$ and the post-test varied between $0.34 < p < 0.97$, although these ranges are sometimes slightly larger when only a single grade level is considered. The item difficulties per grade level are given in Table 6.6, while the item difficulties for the entire study population are given in Table 6.7.

Table 6.6. Item difficulty statistics – per grade level

	6th Grade		7th Grade		8th Grade	
Question	Pre-*p*	Post-*p*	Pre-*p*	Post-*p*	Pre-*p*	Post-*p*
1	0.34	0.70	0.32	0.52	0.65	0.65
2	0.61	0.68	0.68	0.79	0.58	0.58
3	0.86	0.98	0.80	0.95	0.98	1.00
4	0.00	0.52	0.13	0.52	0.05	0.55
5	0.00	0.30	0.05	0.36	0.00	0.35
6	0.09	0.61	0.09	0.48	0.14	0.68
7	0.02	0.50	0.13	0.57	0.13	0.55
8	0.75	0.93	0.88	0.96	0.88	1.00

Table 6.7. Item difficulty statistics – all students

Question	Pre-*p*	Post-*p*
1	0.42	0.61
2	0.63	0.69
3	0.87	0.97
4	0.06	0.53
5	0.02	0.34
6	0.10	0.58
7	0.08	0.54
8	0.84	0.96

The pre-test and post-test item difficulties for each question are plotted in Figure 6.15, first by grade level (Figures 6.15a-c) and then combined (Figure 6.15d). All items plot above the diagonal, indicating higher test scores after the "Walk on Mars" map lesson. The only exceptions occur in the 8th grade plot (Figure 6.15c), where two questions happen to lie exactly on the diagonal, indicating no overall change in knowledge post-lesson. In both cases, some matched test pairs had different answers between the pre-test and post-test, but the overall totals were the same, resulting in no net change for the grade level.

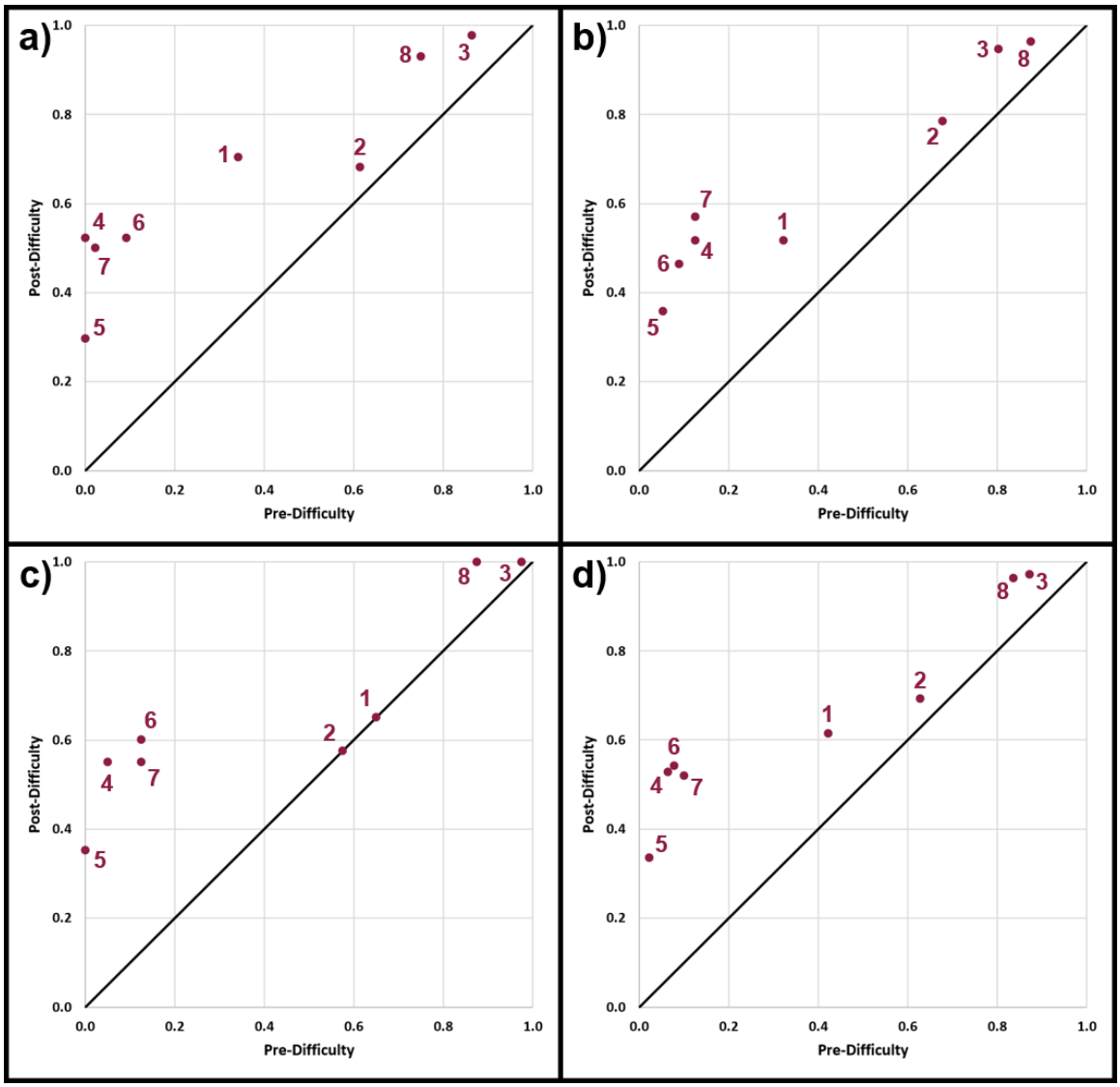

Figure 6.15. General Mars questions: pre-instruction versus post-instruction item difficulty: a) 6th grade students; b) 7th grade students; c) 8th grade students; d) all students.

6.3.3 General Mars Questions – Student Learning Gains

Gain is defined as the change in a student's test score percentage after instruction (Equation 6.2). The normalized gain for an individual student is defined as the ratio between the actual gain and the maximum possible gain (Equation 6.3). The average normalized gain for a group is defined as the ratio between the average actual gain and the average maximum possible gain. (Equation 6.4) (Hake, 1998). The gain statistics for the assessment test are given in Table 6.8.

$$\text{gain} = \text{post\%} - \text{pre\%} \quad \text{Eq. 6.2}$$

$$g_{student} = \frac{\text{post\%} - \text{pre\%}}{100 - \text{pre\%}} \quad \text{Eq. 6.3}$$

$$g_{group} = \frac{\langle \text{post\%} \rangle - \langle \text{pre\%} \rangle}{100 - \langle \text{pre\%} \rangle} \quad \text{Eq. 6.4}$$

Table 6.8. General Mars questions: gain statistics

Grade	Pre-test ⟨M⟩ (%)	Pre-test ⟨SD⟩ (%)	Post-test ⟨M⟩ (%)	Post-test ⟨SD⟩ (%)	g_{group}
6	33.52	13.14	64.20	22.16	0.46
7	38.39	19.49	64.06	22.87	0.42
8	42.19	12.24	65.94	19.40	0.41
All	**37.95**	**16.04**	**64.64**	**21.57**	**0.43**

We conducted a series of paired-sample *t*-tests comparing individual students' pre-test and post-test scores for the matched pairs dataset, which showed significant improvement following the "Walk on Mars" lesson: $t(140)=15.781$, $p<0.001$. Table 6.9 shows the *t*-test parameters for each grade level and the entire study population.

Table 6.9. General Mars questions: paired sample two-tailed *t*-test parameters

Grade	Mean	Std. Dev.	SE Mean	95% Conf.	*t*	df	Sig (2-tailed)
6	-2.4546	1.4379	0.2168	±0.4372	-11.323	43	<0.001
7	-2.0536	1.8032	0.2410	±0.4829	-8.5220	55	<0.001
8	-1.9000	1.4465	0.2287	±0.4626	-8.3080	39	<0.001
All	**-2.1357**	**1.6013**	**0.1353**	**±0.2676**	**-15.7810**	**139**	**<0.001**

6.3.4 General Mars Questions – Mars Missions

Question 7 asked students to list the names of all robotic Mars missions that they knew. Students received full credit for listing at least one mission name, although they could answer with multiple mission names. Therefore, it is possible to explore the diversity of their answers in more depth.

Five active missions were presented during the "Walk on Mars" map lesson: Perseverance, Ingenuity, Curiosity, InSIGHT, and Zhurong. Each of these missions can be treated as a sub-question, with the pre-test and post-test item difficulties for each plotted in Figure 6.16. Again, points plotted above the diagonal indicate that more students answered the question correctly in the post-test than on the pre-test, which was true for all missions across the entire matched pairs dataset.

Because the diversity of answers to a single question is being explored, it is not meaningful to calculate the gain or perform a *t*-test on this data subset.

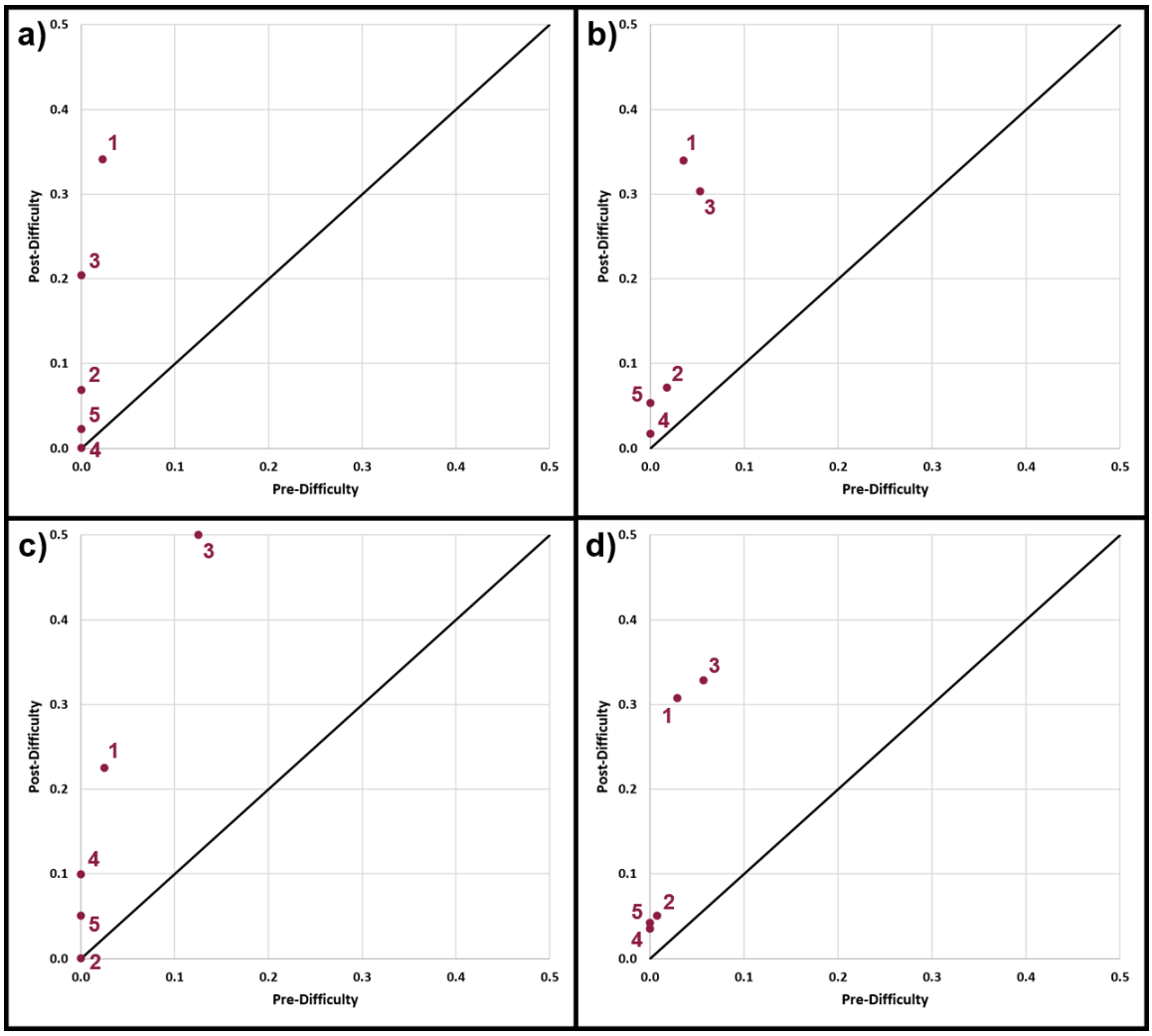

Figure 6.16. Mars mission question: pre-instruction versus post-instruction item difficulty for the five missions discussed during the map lesson; (1) Perseverance, (2) Ingenuity, (3) Curiosity, (4) InSIGHT, and (5) Zhurong: a) 6th grade students; b) 7th grade students; c) 8th grade students; d) all students. Note the atypical maximum values on both axes, which were chosen to better visualize the tightly-spaced datapoints.

6.3.5 General Mars Questions – Mars Exploration Countries

Question 8 asked students to list all the countries/organizations that have sent robotic missions to Mars. Although they could list multiple countries/organizations, students received full credit for listing at least one. Therefore, it is possible to explore the diversity of their answers in more depth.

The four countries/organizations that have attempted to land missions on the Martian surface were discussed during the "Walk on Mars" map lesson: the United States, China, Russia, and the European Space Agency (ESA). For this question, "Europe" or any specific ESA countries were accepted as correct answers. The pre-test and post-test item difficulties for each country/organization are plotted in Figure 6.17. Points plotted above the diagonal indicate that more students answered the question correctly in the post-test than on the pre-test, while points plotted below the diagonal indicate that fewer students answered the question correctly in the post-test. Clearly, the students remembered the American and Chinese missions following the "Walk on Mars" lesson, but perhaps at the expense of forgetting about the unsuccessful Russian and European missions, which were only briefly mentioned.

Because the diversity of answers to a single question is being explored, it is not meaningful to calculate the gain or perform a *t*-test on this data subset.

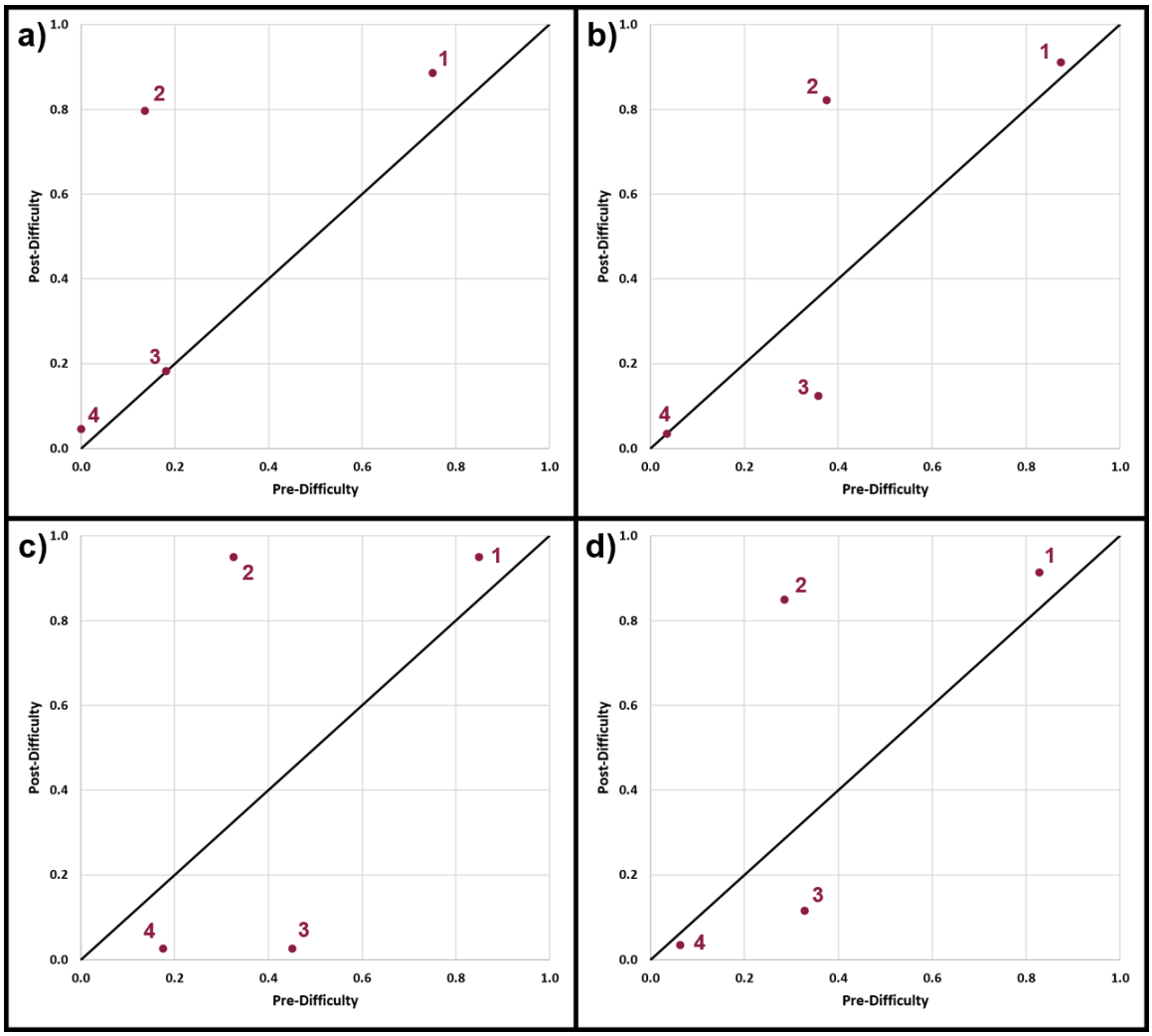

Figure 6.17. Mars exploration countries question: pre-instruction versus post-instruction item difficulty for the four countries discussed during the map lesson; (1) the United States, (2) China, (3) Soviet Union / Russia, and (4) European Space Agency: a) 6th grade students; b) 7th grade students; c) 8th grade students; d) all students.

6.3.6 Topography Comprehension Questions

The topography comprehension section of the post-test was designed to evaluate whether or not the students understood the "Walk on Mars" map colors, which indicate elevation using a temperature color scale.

This information is critical for understanding the geography of Mars, so it must be effectively communicated to the students. The colorized elevation scale is always discussed with students at the beginning of the guided map tour. Then, the students are directed to the initial tour stops by asking them to find the highest point (Olympus Mons) and the lowest point (Hellas Basin) based on their expected color.

The proportions of students per grade level who answered each topography question correctly are shown in Figure 6.18.

6.3.7 Free Response Questions

The goal of the free-response test sections was to capture any additional student knowledge about Mars that was not covered by the other questions. However, many students either left it blank or simply re-stated facts that were covered by the other questions. This left us with very little additional insight into their level of knowledge or what aspects stood out to them the most.

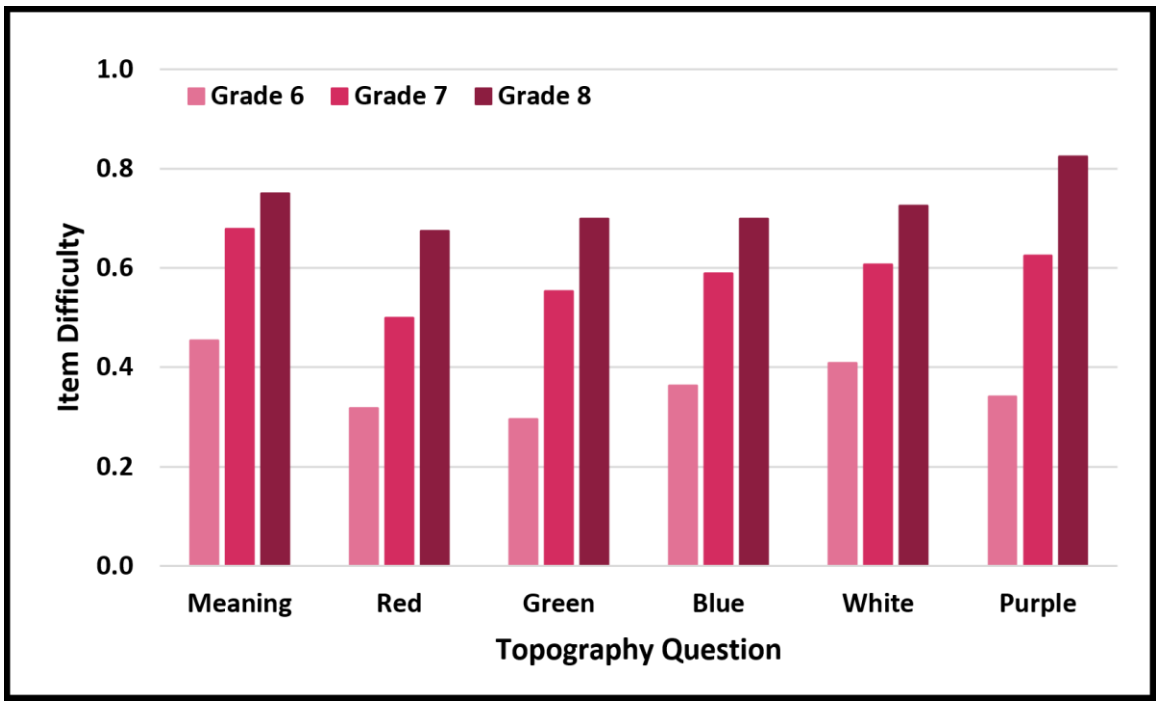

Figure 6.18. Topography comprehension questions: post-instruction item difficulty by grade level.

6.4. Discussion

6.4.1 General Mars Questions

The student gains summarized in Table 6.8 show that 6th grade students had the highest mean gain, while the 7th and 8th grade students showed slightly lower, but nearly identical, gains. This is likely a result of the school's science curriculum, which covers the planets in 6th grade, but after the time of year when the assessment study was conducted. This means the 7th and 8th grade students had previously covered this material, which explains their higher pre-test mean scores. Since all three grade levels ended with nearly the same mean scores, this meant that the 7th and 8th grade students had less room for improvement than the 6th grade students.

The 8th grade pre-test mean score was also higher than the 7th grade pre-test mean score, even though much more time had passed since the 8th grade students covered this material in their regular science classes. This suggests that as the students' general level of education increases, they are more likely to reinforce previously-learned material with material learned through other sources (ie: other classes, news, social media, etc).

6.4.2 General Mars Questions – Mars Missions

Question 7 asked students to list the names of any robotic Mars missions that they knew. In the pre-test, this was intended to assess whether they had learned about any missions through news coverage, social media, or other sources. This was specifically relevant for the two newest Mars surface missions, which landed only a few months before the assessment study was conducted. In the post-test, this question was intended to assess

how well students retained information about the five active missions presented during the "Walk on Mars" map lesson.

The expectation was that the students would be most familiar with the Perseverance rover mission, because it is an American mission and landed on Mars only seven months before the assessment study was conducted. However, as shown in Figure 6.16, very few students in any grade level were previously aware of the mission. After the lesson, approximately one-third of the 6^{th} and 7^{th} grade students and about one-quarter of the 8^{th} grade students recalled the mission. These numbers are surprisingly low, given that Perseverance's Jezero Crater landing site is one of the main stops on the guided tour and the mission had very recently been in the news.

Figure 6.16 shows that only a single student was previously aware of the Ingenuity mission and only a few students recalled the mission after the lesson. This is discouraging because the Ingenuity mission, which is a sub-mission under the Perseverance mission, was specifically described during the Jezero Crater stop on the guided map tour, focusing on how it was the first vehicle to fly on another planet.

The students were most familiar with the Curiosity mission in both the pre-test and post-test, even though it has been on Mars for most of their lives and did not have significant news coverage immediately before the assessment study. This was unexpected because we had assumed that the mission would have been relatively unremarkable from the students' perspective, leading to fewer answers in both the pre-test and post-test. Curiosity's landing site in Gale Crater was one of the stops during the guided map tour, but was not emphasized as much as the recent Perseverance rover's landing site. We are currently unable to explain why the Curiosity mission stood out so much to the students,

but it may be related to the mission name being easier for the young students to remember and spell.

As the only active lander (rather than rover) mission, the InSIGHT landing site in Elysium Planum was one of the guided map tour stops. Not a single student in the study was aware of the mission before the map lesson and only a small number of students recalled it afterward. This is surprising because the students tended to be very intrigued by the idea of Marsquakes, which InSIGHT discovered. It might be tempting to attribute this to the less "memorable" mission name, but the students did not even describe it, which was considered an acceptable answer if they could not remember or spell the actual mission name.

The final stop on the guided map tour was the landing site for China's Zhurong rover in southern Utopia Planitia. Again, not a single student knew about the mission beforehand, but a disappointingly low number of students recalled it afterward. This was despite the emphasis placed on the mission during the guided map tour, as Zhurong is China's first Mars mission and is the first non-U.S. mission to land on the surface successfully.

6.4.3 General Mars Questions – Mars Exploration Countries

Question 8 asked students to list countries that have sent robotic missions to Mars. In the pre-test, this was primarily intended to assess if the students were aware of any countries, other than the United States, who have participated in Mars exploration. In the post-test, it was intended to assess how well students retained information about the non-American (Chinese, Soviet/Russian, and European) surface missions discussed during the

guided map tour. The students were given a point for providing at least one country, but it is still informative to look at the full diversity of answers in more detail.

Figure 6.17 shows that most students were already aware that the United States has sent robotic missions to Mars before the map lesson, although it was not 100%. The post-test showed a slight improvement in this number, although it still did not reach 100%. This demonstrates that the students are mostly aware of U.S. participation in Mars exploration, even though their detailed knowledge of that participation varies, as shown in Figure 6.16.

The People's Republic of China is the only other country to successfully land a mission on the Martian surface, with the landing of the Zhurong rover occurring only four months before the assessment study. Figure 6.17 shows that a small percentage of students were aware of China's Mars exploration activities before the map lesson, likely from recent news coverage. After the map lesson, this increased to levels comparable with the United States, possibly due to the emphasis placed on the Zhurong landing site during the guided map tour. Interestingly, the vast majority of students knew of Chinese involvement in Mars exploration, but did not provide the name (or a description) of the Zhurong rover in their Mars mission answers.

The Mars exploration efforts of both the Soviet Union/Russia and the European Space Agency (ESA) are briefly mentioned during the guided map tour as countries/organizations that have tried to land on the surface but have so far been unsuccessful. Figure 6.17 shows that the overall proportion of students who identified the Soviet Union/Russia and Europe/ESA as participants in Mars exploration actually decreased after the lesson. This can likely be attributed to the relative lack of emphasis on their unsuccessful missions during the guided map tour. This may have led the students to focus only on the successful

missions, or possibly gave them the incorrect impression that these countries have not participated in Mars surface exploration. Either way, the attempted surface landings by the Soviet Union/Russia and the ESA should be emphasized more during future lessons.

6.4.4 Topography Comprehension Questions

Figure 6.18 shows that student understanding of the colorized elevation scale increased with increasing grade level. This suggests that the school's curriculum, likely related to graphing in their math and science classes, plays a role in the students' ability to understand and interpret the colorized elevation scale. However, even amongst the 8th grade students, nearly 20% were still unable to connect the colors with elevation.

This suggests that even though the students could locate high and low points on the map based on color during the map lesson, it may have been due to a portion of the students understanding the colorization and the rest merely tagging along. This is particularly disappointing since the colorization scheme is essential to understanding and interpreting the map. Future work should focus on increasing student comprehension of the colorized elevation scale before starting the guided map tour.

6.5 Future Work

The assessment study demonstrated that the primary weakness of the "Walk on Mars" program is a consistent lack of student understanding regarding the colorized elevation scale. Although student understanding did increase with grade level, all three grade levels still had many students who were unable to connect the colors with different surface elevations. Because this relationship is essential to understanding the "Walk on Mars" map,

the program will need to specifically address this shortcoming in the future. A possible solution is to incorporate an augmented reality sandbox into the program.

The augmented reality (AR) sandbox was developed by Reed et al. (2014) and Reed et al. (2016) as a novel hands-on approach to teaching watershed development. After releasing the designs under a GNU General Public License, other researchers began evaluating the AR sandbox as a tool for teaching students to interpret topographic maps in general, since it provides them with real-time feedback in the form of dynamic colorization. Woods et al. (2016) and Richardson et al. (2018) found that the AR sandbox improved student learning outcomes related to interpreting topographic maps.

A follow-on study with the "Walk on Mars" map should be conducted with the addition of a pre-lesson on reading colorized topographic maps that uses an AR sandbox. Based on the results of the previous AR sandbox studies, this should lead to increased student understanding of the colorized topography, although it will come at the expense of increasing the amount of material that needs to be transported to events. However, the additional logistical challenges will likely be worth the increased student learning outcomes.

We also intend to conduct a similar study with high school students in order to determine how student gains change with increasing levels of education and development. In particular, whether the deficiencies noted in the Mars missions and Mars exploration countries questions are primarily the result of grade level or the instructional material. This should allow us to confidently identify the ideal grade levels for "Walk on Mars" participants, which will guide the more widespread implementation of the program in the future.

6.6 Conclusions

The “Walk on Mars” program was started to communicate to students and the general public the true scale of the THEMIS Day IR Global Mosaic, as well as to bring awareness to the many accomplishments of the 2001 Mars Odyssey mission over its first twenty years at Mars. The program has educated over 8,000 participants of all ages across the United States and taught them about Martian geography, the history of Mars exploration, and what the future of the international Mars exploration program will look like.

The assessment study verified that the “Walk on Mars” map effectively teaches junior high students about Martian geography and the history of Mars exploration. Specifically, the map reinforced basic Mars information that students cover as part of their school curriculum and successfully introduced them to Martian geography. The map also reinforced students’ understanding of the United States’ leadership in Mars exploration and increased their awareness of international contributions, although future lessons should further emphasize the other countries involved to improve retention of that information. Finally, the study demonstrated that many students had difficulty fully understanding the colorized elevation on the map, so future lessons should be preceded by a more thorough explanation of colorized topography, perhaps with the assistance of an augmented reality sandbox.

These assessment study results will help the “Walk on Mars” program ensure that the next 8,000 participants will have a more rewarding experience when they interact with the map.

CHAPTER 7

WELL-PRESERVED LOW THERMAL INERTIA EJECTA DEPOSITS SURROUNDING YOUNG SECONDARY IMPACT CRATERS ON MARS

7.1 Introduction

Impact cratering remains an active process shaping the Martian surface, not only in the geologically recent past, but over the timescales observed by the instruments that have been sent to study the planet.

Hundreds of new primary impact craters <50m in diameter have been documented over the last two decades, many with formation dates constrained by before-and-after visible image pairs (Malin et al., 2006; Byrne et al., 2009; Daubar et al., 2013). These new impact craters are commonly identified by their "blast zones" or "scour zones", which are low albedo surface features created by the removal of high-albedo dust from otherwise low-albedo surfaces by either aerodynamic shockwaves (Daubar et al., 2016) or high-speed winds generated by expanding impact-generated vapor (Schultz and Quintana, 2017). This removal is the result of either: a) the interaction of the aerodynamic shockwave(s) from the descent and/or impact of the bolide, or b) the mechanical disruptions caused by the emplacement of the subsequent ejecta. This removal results in diffuse low-albedo halos around the new impact craters, sometimes associated with extended linear and arcuate rays (Daubar et al., 2016).

Large rayed craters >1km in diameter, which could be as young as 20Myr, have previously been identified using a combination of visible and thermal infrared (IR) images (Tornabene et al., 2006; Tornabene and McEwen, 2008). These young large

impact craters produced thousands of smaller secondary impact craters with dimensions and ejecta morphologies that differ from similarly-sized primary impact craters. While the large primary craters are associated with distal ray systems >100 crater radii in length, the secondary craters are associated with ray systems 10s of crater radii in length and continuous ejecta blankets, both of which are consistent with low velocity (~1 km/s) impacts (Calef et al., 2009).

These previous studies have demonstrated that the impact cratering process is currently actively altering the Martian surface.

The focus of this study is a previously unidentified population of small (vast majority <500m diameter) young impact craters with well-preserved low thermal inertia (low-TI) ejecta deposits that were identified using Thermal Emission Imaging System (THEMIS) (Christensen et al., 2004) infrared images during the systematic assembly and validation of the THEMIS Day IR with Colorized Night IR global map.

Compared to the confirmed recent impact craters, they are an order of magnitude larger, have well-defined low-TI ejecta deposits surrounding them and occur in different regions of the planet. Compared to the rayed craters, they are at least an order of magnitude smaller, occur in a wider range of terrains and often have continuous ejecta deposits rather than discrete ejecta rays. The low-TI ejecta deposits also occur in much larger numbers than either the confirmed recent impact craters or the rayed craters. These differences indicate that the low-TI ejecta deposits belong to a distinct population of impact features.

The goals of this study were to: 1) determine the global distribution of these low-TI ejecta deposits, 2) categorize them based on their apparent state of degradation, 3)

identify the ejecta properties that cause their characteristic appearance in thermal infrared images, and 4) compare and contrast them with previously-identified populations of young impact features on the Martian surface in order to determine their origin.

The results of this study indicate that the low-TI ejecta deposits were created by secondary impacts, many of which originated from the primary impacts associated with the young rayed craters identified by Tornabene et al. (2006) and Tornabene and McEwen (2008). Therefore, it is not only possible to identify young secondary impact craters by their thermophysical properties, but also to assess the effects of secondary impact craters on the ages calculated for many important surface units across the planet using crater size-frequency distribution techniques.

7.2 Datasets and Methods

7.2.1 Instrument Descriptions

THEMIS consists of two multispectral imaging subsystems; a ten-band thermal infrared imager and a five-band visible/near-infrared imager. The thermal infrared subsystem is a pushbroom imager that acquires data at a nominal spatial resolution of 100m/pixel using an uncooled microbolometer array covered by ten ~1-µm-bandwidth strip filters centered at nine different wavelengths between 6.8µm and 14.9µm (Christensen et al., 2004). Daytime infrared images are typically acquired with all ten bands, while nighttime infrared images are commonly acquired with only bands 4 (8.56µm), 9 (12.57µm) and 10 (14.88µm). THEMIS infrared images were used in this study to identify the low-TI ejecta deposits through the THEMIS Day IR with Colorized

Night IR global map and to quantify the thermal inertia variations associated with the deposits.

The Context Camera (CTX), onboard the Mars Reconnaissance Orbiter (MRO), is a pushbroom imager that acquires data at a nominal spatial resolution of ~6m/pixel using a 5056-pixel linear CCD centered at a wavelength of 0.611μm with a full-width half-maximum (FWHM) bandpass of ±0.189μm (Malin et al., 2007; Bell et al., 2013). CTX images were used in this study to qualitatively assess the visible wavelength appearance of the ejecta deposits and to provide morphologic information at a higher spatial resolution than THEMIS IR images.

The High Resolution Imaging Science Experiment (HiRISE), also onboard MRO, is a pushbroom imager that acquires data at a nominal spatial resolution of 0.25m/pixel using an array of 14 CCD detectors, with ten detectors centered at 0.694μm (red), two detectors centered at 0.536μm (blue-green) and two detectors centered at 0.874μm (near-infrared) (McEwen et al., 2007). The two blue-green detectors and two near-IR detectors are in-line with the center two red detectors, allowing the acquisition of multi-band images along the center of the HiRISE image swath. HiRISE images were used in this study to qualitatively assess the visible wavelength color of the ejecta deposits and to provide morphologic information at a higher spatial resolution than CTX images.

7.2.2 THEMIS Global Mosaics

Edwards et al. (2007a,b) used THEMIS IR band 9 (12.57μm) radiance images acquired during the first 7.5 years of the Mars Odyssey mission to generate global daytime and nighttime infrared mosaics. However, they were unable to achieve full

global coverage in both mosaics due to incomplete high quality data coverage in most regions. Hill et al. (2014) expanded on this work by using THEMIS IR band 9 images from the first twelve years of the mission, which allowed them to complete the daytime global mosaic between 87.3°N and 87.3°S and significantly improve the coverage of the nighttime global mosaic between 60°N and 60°S. This updated version of the THEMIS Day IR global mosaic was designated version 12.0 and this updated version of the THEMIS Night IR global mosaic was designated version 14.0.

Hill et al. (2014) also produced two global overlay maps, which used different datasets to colorize the THEMIS Day IR global mosaic. The first was the THEMIS Day IR with MOLA Color global map, which overlaid colorized global elevation data from the Mars Orbital Laser Altimeter (MOLA) (Smith et al., 2001) onto the THEMIS Day IR global mosaic. The second was the THEMIS Day IR with Colorized Night IR global map, which emphasizes the relationship between the thermophysical properties of the surface materials, expressed as variations in nighttime surface temperatures, and the surface morphology, expressed primarily as variations in the daytime surface temperatures.

The updated THEMIS Day IR and Night IR global mosaics, which were used as the inputs to this combination map, were produced by first running a high pass filter with a size of 1,000 pixels over the individual band 9 radiance images. Next, a running sigma stretch was applied to the images, which stretched the radiance data according to the equation:

$$L_{stretch} = \left[\left(L - L_{avg}\right) \cdot \left(\frac{\sigma^2}{\sigma}\right)\right] + 127 \quad (7.1)$$

where L is the spectral radiance from the band 9 image, Lavg is the average spectral radiance of the specified subsection of the band 9 image, σ is the standard deviation of the spectral radiance values within the specified image subsection, σ2 is the variance of the spectral radiance values within the specified image subsection, and Ls is the resulting stretched spectral radiance value. A standardized variance value of 40 was used for all images and the image subsection was defined as ±500 rows from the row being operated on, with the missing rows ignored at the beginning and end of the image. The two-dimensional linear ramp blending algorithm of Edwards et al. (2007a,b) was then used to blend the images one at a time into the final mosaic, which resulted in seamless qualitative global mosaics.

The THEMIS Night IR global mosaic was then colorized using an algorithm that bins the data (which, after the mosaicking process, is in the form of digital numbers, DNs, ranging from 1 to 255, with 0 reserved for the ignore value) into six equally-sized DN bins. The algorithm then assigns each bin a visible wavelength color varying from violet, for low values, to red, for high values. Finally, the overlay product was created by dividing the red, green and blue bands of the resulting color image by 255, and then multiplying each band by the corresponding DN values from the THEMIS Day IR global mosaic. The resulting bands were then recombined into a single RGB image. This overlay method was chosen over a hue-saturation-value (HSV) overlay because it produced more vivid colors in the final product, which enhances the contrast between thermally-distinct units.

The resulting THEMIS Day IR with Colorized Night IR global map motivated and enabled this study.

7.2.3 THEMIS Thermal Inertia

The thermal inertia values from selected low-TI ejecta deposits were obtained from individual THEMIS nighttime infrared images that were processed into derived thermal inertia images using the techniques of Fergason et al. (2006) during the generation of the THEMIS Thermal Inertia Global Mosaic (Christensen et al., 2013). The absolute accuracy of these THEMIS thermal inertia values are ~20% and their precision is 10%-15%, which are due to instrument calibration limitations, uncertainties in model input parameters at THEMIS spatial resolutions and thermal model limitations. The differences in thermal inertia between the concentric facies of the low-TI ejecta deposits are on the order of 100-150 tiu (thermal inertia units of J m-2 K-1 s-1/2 abbreviated as "tiu" for simplicity), which in most cases represents ~35% of the thermal inertia variation within the THEMIS scenes. This makes the low-TI ejecta deposits easily and reliably identifiable in the THEMIS thermal inertia images.

7.2.4 Ejecta Deposit Facies

This study was motivated by the observation of craters in the THEMIS Day IR with Colorized Night IR global map that are surrounded by well-preserved relatively low-TI ejecta deposits. The type example chosen for this study is a 520m diameter crater with a well-formed ejecta deposit in Terra Sirenum at -23.09°N, 182.94°E, which is shown in Figure 7.1.

Similar craters in the Cerberus Plains were reported by McEwen et al. (2005), who described them as having three facies, each of which have a distinct signature in the

thermal infrared. This study will use the same facies descriptions with minor modifications to describe and characterize the low-TI ejecta deposits.

The inner facies of the ejecta deposits have relatively high thermal inertia values on the order of 350-450 tiu and correspond to the crater interior, crater rim and the blocky ejecta within ~1km of the crater rim. The middle facies have intermediate thermal inertia values on the order of 250-350 tiu, which correspond to areas with a mixture of blocky and fine-grained ejecta, and only extend between ~1km and ~2km of the crater rim since they are a transitional facies. The outer facies have relatively low thermal inertias on the order of 200-250 tiu, which corresponds to fine-grained material (Piqueux and Christensen, 2011), and most often occur as continuous deposits out to ~3km from the crater rim with some short rays of low thermal inertia material extending further.

These facies are easily distinguishable in Figure 7.1a, which shows the type example of the low-TI ejecta deposits in a colorized thermal inertia image overlaid on a CTX image. The high-TI facies appears as red and orange, the intermediate-TI facies as green and the low-TI facies as blue and purple. Figure 7.1b shows the same crater and ejecta deposit, but from the THEMIS Day IR with Colorized Night IR global map overlaid on the same CTX image. All three facies appear as the same basic colors as in Figure 7.1a, with the boundaries and colors varying slightly due to the different image processing methods, which were previously described.

The similarity between these two figures demonstrates that the nighttime temperature data is a very good proxy for thermal inertia; therefore this study refers to the ejecta deposits as “low-TI” even though most examples were primarily characterized using the THEMIS Day IR with Colorized Night IR global map.

To further characterize these three facies, Figure 7.2 shows north-to-south and west-to-east thermal inertia cross-sections through the center of the low-TI ejecta deposit in Figure 7.1a. In both cases, the high-TI and intermediate-TI facies both stand out from the surrounding terrain, with a noticeable step representing the boundary between the two. The low-TI facies is also distinguishable in both cross-sections as troughs between the intermediate-TI facies and the baseline thermal inertia of the surrounding terrain. It should be noted that the descriptions of these facies (ie: the “high-TI” facies) are defined relative to the surrounding terrain. For example, the highest thermal inertia values shown in Figure 7.2 are significantly lower than the thermal inertias of typical high-TI materials, such as bedrock (Piqueux and Christensen, 2011), but are still high relative to the other terrain in the scene.

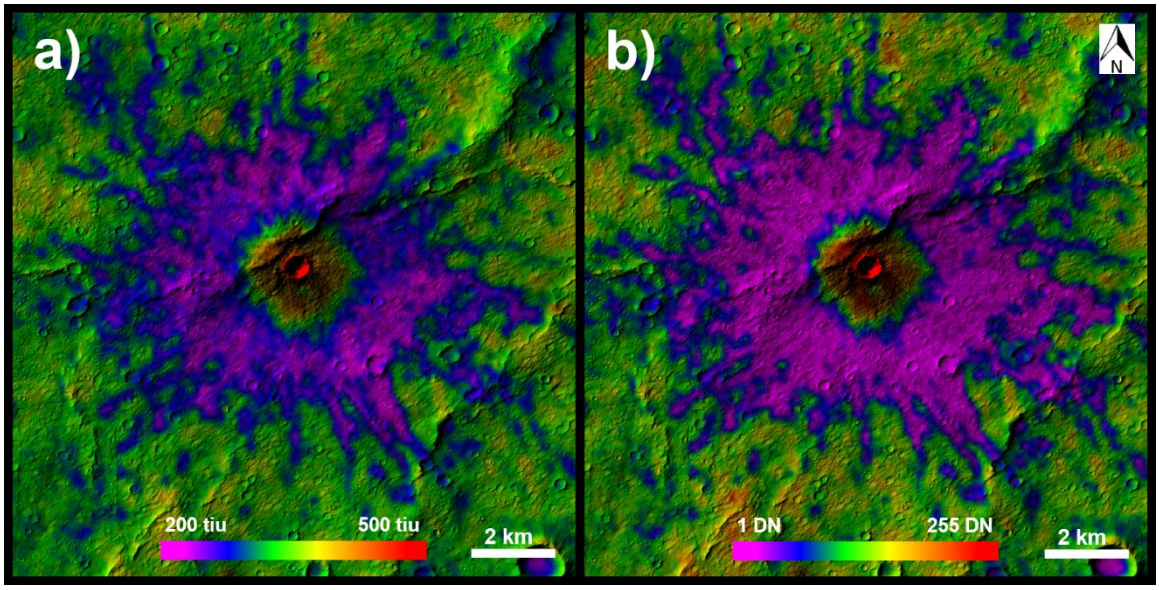

Figure 7.1. Low-TI ejecta deposit in Terra Sirenum (-23.09°N, 182.94°E), shown in: (a) a colorized THEMIS thermal inertia image (I08027013) overlaid on a CTX image (P17_007829_1571_XN_22S177W), and (b) a section of the THEMIS Day IR with Colorized Night IR global map overlaid on the same CTX image. The structure of the ejecta deposit is clearly visible in both images, the boundaries between the three main facies occur in approximately the same locations and the shapes of the short ejecta rays are also effectively identical between the two images. Therefore, the THEMIS Day IR with Colorized Night IR global map can be reliably used as a proxy for thermal inertia images for the purposes of this survey.

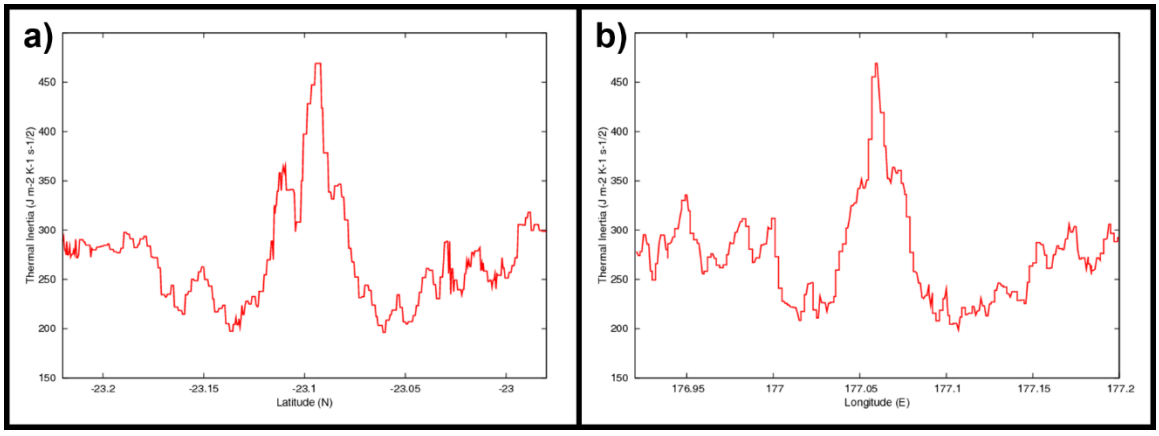

Figure 7.2. Thermal inertia cross-sections for the low-TI ejecta deposit in Figure 7.1a: (a) North-to-South TI cross-section, (b) West-to-East TI cross-section.

7.2.5 Ejecta Deposit Classification

The initial survey of these low-TI ejecta deposits by Hill and Christensen (2014) revealed that they have a broad range of forms that were interpreted as indicative of degradation, most likely due to aeolian erosion of the fine-grained component of the ejecta. This interpretation was based on HiRISE images of low-TI ejecta deposits that show obvious evidence of aeolian modification, which is discussed in Section 3.3. A classification scheme was developed in order to capture this variation during the global survey of the ejecta deposits, which included six broad categories defined by the apparent state of degradation relative to the low-TI ejecta deposit type example in Figure 7.1.

Type 1: Below Data Resolution. These ejecta deposits are sufficiently small, usually <3km diameter, that it is difficult to assess their state of degradation using the 100m/pixel THEMIS nighttime temperature and thermal inertia images. As a result, these deposits were not included in the subsequent analysis. (Figure 7.3a)

Type 2: Heavily Degraded. Ejecta deposits in this category are degraded to the point that they are nearly unrecognizable as distinct ejecta deposits. This category may include some low-TI aeolian deposits surrounding impact craters that have been misidentified as low-TI ejecta deposits, so this category was not included in most of the subsequent analysis. (Figure 7.3b)

Type 3: Degraded. While the concentric nature of the different thermal inertia facies within the deposits is more apparent in this category, the contrast between them is either not as high or is more inconsistent than in Types 4-6. (Figure 7.3c)

Type 4: Modified. The concentric thermal inertia facies in these deposits have much greater contrast and are mostly continuous around the crater. (Figure 7.3d)

Type 5: Preserved. These ejecta deposits are similar to the type example in Terra Sirenum (Figure 7.1) that motivated this study. There is a large thermal inertia contrast between the concentric facies of the deposits and the outer facies contain low-TI material that is effectively continuous around the entire crater. (Figure 7.3e)

Type 6: Well-Preserved. These features are similar to the preserved ejecta deposits, but also have low-TI material covering the central crater. (Figure 7.3f)

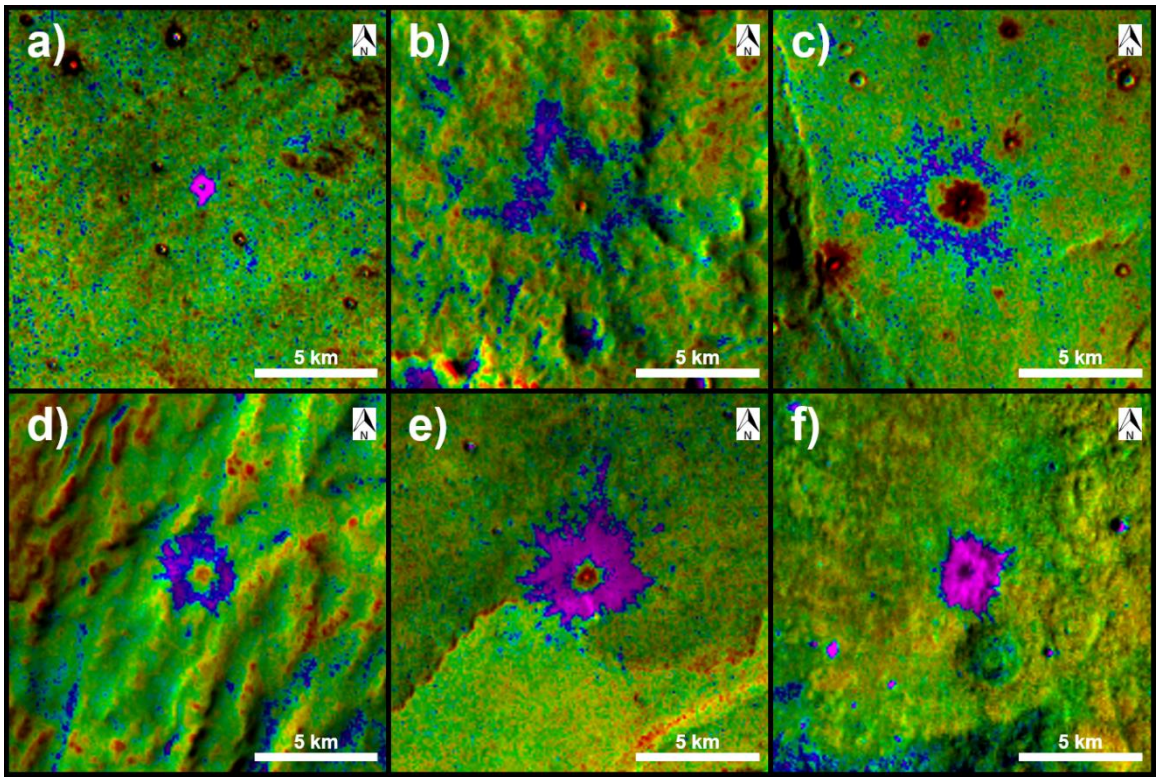

Figure 7.3. Examples of the low-TI ejecta deposit categories from the THEMIS Day IR with Colorized Night IR global map: (a) Type 1 - Below Data Resolution, (b) Type 2 - Heavily Degraded, (c) Type 3 - Degraded, (d) Type 4 - Modified, (e) Type 5 - Preserved, and (f) Type 6 - Well Preserved.

7.2.6 Near-Global Survey

The near-global survey of the low-TI ejecta deposits was conducted between 60°N-60°S by using the Java Mission-planning and Analysis for Remote Sensing (JMARS) geospatial information system (http://jmars.asu.edu) (Christensen et al., 2009) to systematically search the THEMIS Day IR with Colorized Night IR global map for low-TI ejecta deposits. The location, approximate size and classification of each of the 4,024 deposits identified by the survey were recorded using the JMARS Shape Layer, which produced a comma-delimited shapefile that includes the low-TI ejecta deposit survey results.

7.3 Results

7.3.1 Global Distribution

The near-global survey conducted between 60°N and 60°S using the THEMIS Day IR with Colorized Night IR global map identified 4,024 low-TI ejecta deposits, which were classified according to the scheme described above.

The locations of the Type 3-6 deposits are plotted in Figure 7.4, which reveals a clearly non-random distribution with concentrations in the mid-latitude portion of the southern highlands, Elysium Planitia, Utopia Planitia, Solis Planum and Syrtis Major. If only the preserved and well-preserved examples are considered (Types 5-6), there are clear concentrations in northern Terra Sirenum, Solis Planum and southwestern Daedalia Planum.

In order to better understand their regional context, the locations of the Type 3-6 low-TI ejecta deposits were plotted on a global Thermal Emission Spectrometer (TES)

(Christensen et al., 2001) thermal inertia map, where regions of low thermal inertia correspond to dust cover at least one diurnal skin depth (~1cm) thick (Putzig and Mellon, 2007). As shown in Figure 7.5, the global distribution of the low-TI ejecta deposits is very well correlated with the regions of the Martian surface without significant dust cover. Figure 7.6 shows the same low-TI ejecta deposit locations plotted on a TES Dust Cover Index (DCI) map, where regions with high dust cover index values correspond to dust thicknesses that are at least tens of microns thick, making them spectrally significant (Ruff and Christensen, 2002).

After retrieving the TES TI and DCI values from the respective numerical maps, which had already been binned and averaged at 20ppd resolution, at the location of each low-TI ejecta deposit, histograms were generated to give more insight into the relationship between the low-TI ejecta deposits and their surrounding terrains.

Figure 7.7a shows a roughly Gaussian distribution of low-TI ejecta deposit locations across a limited range of regional thermal inertia values with an average value of 184 tiu, which approximately corresponds to an unconsolidated regolith composed of sand-sized grains (Piqueux and Christensen, 2011). They also almost never occur in regions with average thermal inertias below 50 tiu, which corresponds to unconsolidated dust. The low-TI ejecta deposits are located almost exclusively in regions of intermediate-to-high thermal inertia, and the boundaries of the low-TI ejecta deposit concentrations correlate very well with the boundaries of the dusty, low thermal inertia regions. Figure 7.7b, however, shows that the low-TI ejecta deposits occur in terrains with a wide range of DCI values. This indicates that if the thickness of the regional dust cover is influencing the formation and/or preservation of the low-TI ejecta deposits, it needs to be present in

thermophysically-significant thicknesses (a few to several centimeters), and not just spectrally-significant thicknesses (a few tens of microns).

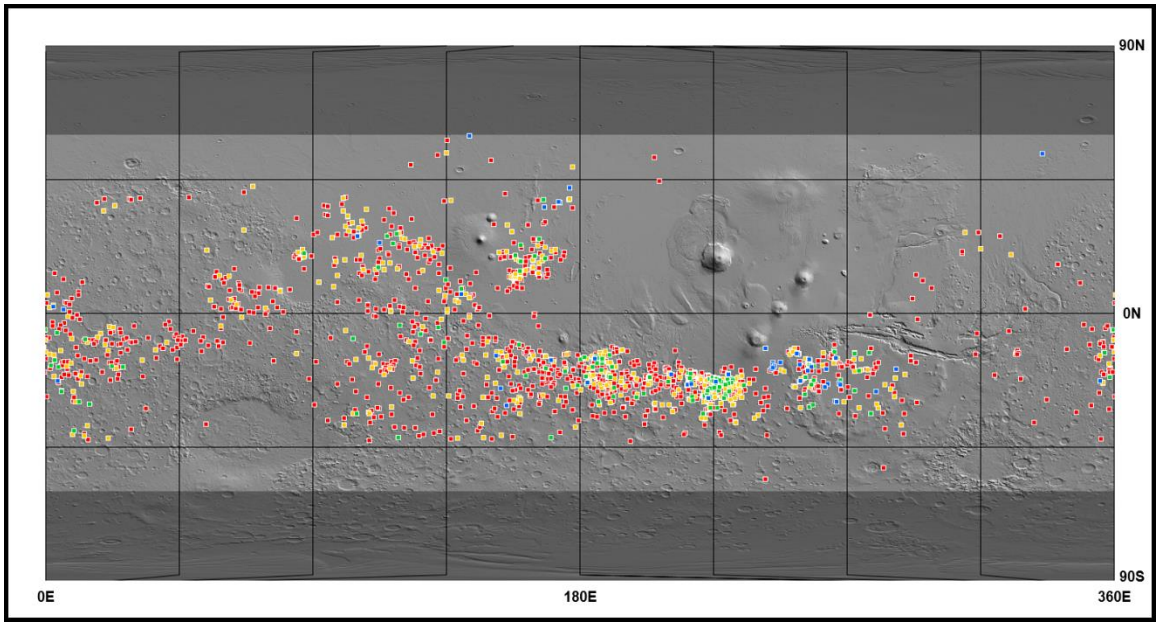

Figure 7.4. Global distribution of low-TI ejecta deposits plotted on a MOLA Shaded Relief map (*Smith et al.*, 2001) and color-coded by type: Type 3 - Degraded (red), Type 4 - Modified (yellow), Type 5 - Preserved (green) and Type 6 Well-Preserved (blue). The regions poleward of 60° have been shaded to indicate that they were not included in the survey.

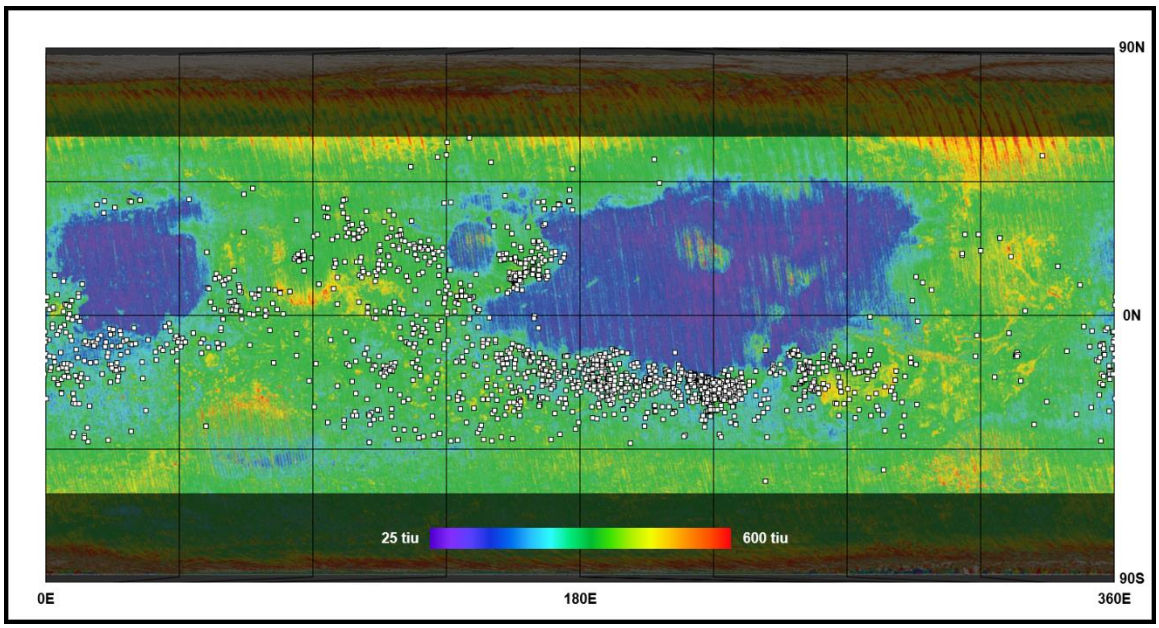

Figure 7.5. Global distribution of low-TI ejecta deposits (Types 3, 4, 5 & 6), collectively plotted in white, on a TES Daytime Thermal Inertia map (*Putzig and Mellon*, 2007), showing that they are located in intermediate-to-high thermal inertia regions. The regions poleward of 60° have been shaded to indicate that they were not included in the survey.

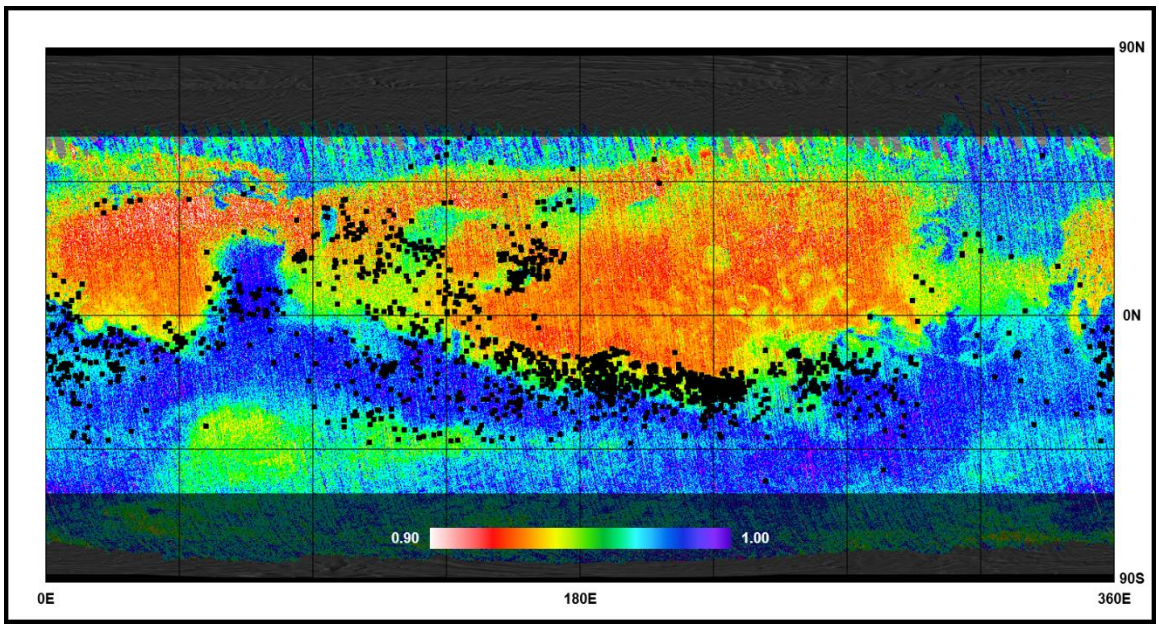

Figure 7.6. Global distribution of low-TI ejecta deposits (Types 3, 4, 5 & 6), collectively plotted in black, on the TES Dust Cover Index (DCI) map (*Ruff and Christensen*, 2002), where high DCI values (blue) indicate the least dust and low DCI values (red/pink) indicate the most dust. The low-TI ejecta deposits are located in regions with a variety of DCI values. The regions poleward of 60° have been shaded to indicate that they were not included in the survey.

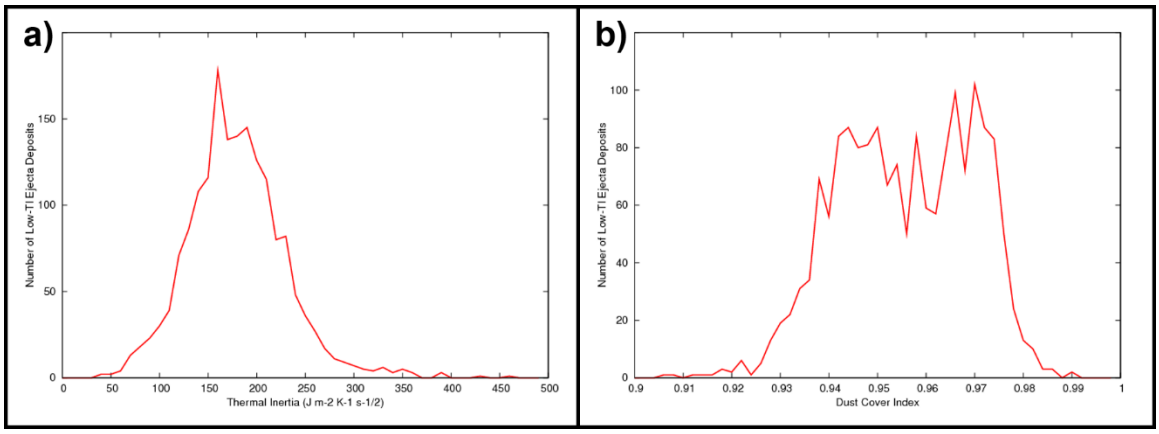

Figure 7.7. Histograms of: (a) the regional thermal inertia values surrounding each of the low-TI ejecta deposits shown in Figure 7.5; the distribution is unimodal and centered about an average thermal inertia of 184 tiu, and (b) the regional Dust Cover Index values surrounding each of the low-TI ejecta deposits shown in Figure 7.6; the distribution is relatively broad, centered about a regional DCI value of 0.9568 and indicates that the low-TI ejecta deposits are present in terrains with a relatively wide range of DCI values.

7.3.2 Ejecta Grain Size and Thermal Inertia

The distinctive nighttime temperature patterns of the low-TI ejecta deposits are caused by a decrease in the average particle size of the ejecta material with radial distance from the crater, which causes the thermal inertia of the ejecta deposit to similarly decrease with radial distance. Although this effect is present in all of the low-TI ejecta deposits, it is best observed in the preserved (Type 5) deposits. These average particle size variations can be observed in the HiRISE approximate true color images in Figure 7.8, which cover the different facies of the type example in Figure 7.1.

The inner high-TI facies is located at the center of the ejecta deposit and includes the crater interior, crater rim and the blocky ejecta immediately surrounding it. As shown in Figure 7.8a, bedrock is exposed in the walls and rim of the crater and blocky ejecta extends approximately one crater diameter from the rim, both of which contribute to the elevated thermal inertia in this facies. However, as shown in Figure 7.1a, the thermal inertia values in this high-TI facies are only approximately 350-500 tiu, which is lower than would be expected for exposed bedrock. So despite their rocky appearance in Figure 7.8a, the inner facies must still contain a significant fraction of low-TI material in order to reduce the average thermal inertia over each 100m pixel to the observed values.

The intermediate-TI facies is relatively thin and is mostly a transitional facies. Although this facies often appears to have the same thermal inertia as the terrain surrounding the ejecta deposit, as seen in Figure 7.1, HiRISE images show that it is composed of both blocky and fine-grained ejecta material. As shown in Figure 7.8b, this region has distinct rays of blocky ejecta surrounded by muted terrain that appears mantled in fine-grained material. This mixing of the high-TI blocky ejecta and low-TI

fine-grained ejecta results in average thermal inertia values between approximately 300-350 tiu.

The low-TI facies is usually the most extensive and is dominated by fine-grained ejecta material. This is not unexpected since impact experiments by Gault et al. (1963) demonstrated that the vast majority of the mass ejected by impacts into solid basalt targets is in the form of fine-grained particles, and the modeling work of Schultz and Gault (1979) predicted that the distal facies of craters would be dominated by fine-grained deposits due to the effects of atmospheric entrainment. As shown in Figure 7.8c, this region appears to have a mantling unit deposited on the surface, indicated by muted crater rims, ridges and other pre-existing topographic features. There is also a distinct absence of blocky ejecta and exposed bedrock, which allows the fine-grain ejecta material to dominate and lower the average thermal inertia to 200-300 tiu. Also, as seen in Figure 7.1, this facies often has fine-scale spatial variations in infrared images. In many cases, the lowest thermal inertia material appears to be concentrated along discreet rays within the continuous ejecta deposit. This structure tends to become increasingly pronounced as the size of the crater, and therefore the size of the ejecta deposit, increases.

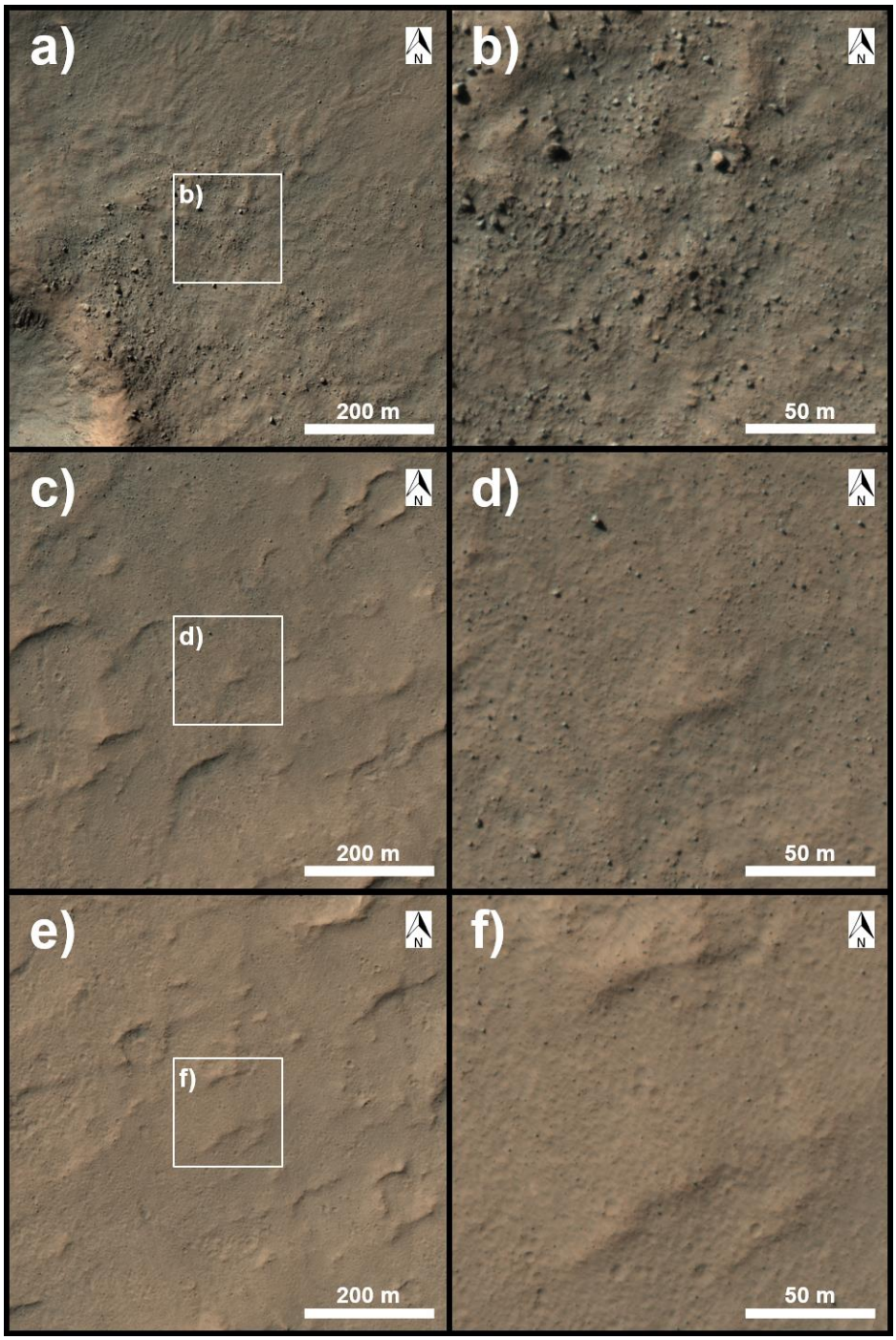

Figure 7.8. Low-TI ejecta deposit facies from Figure 7.1 in an approximate true color HiRISE image (PSP_007829_1565_RGB), showing: (a) the crater rim and blocky ejecta of the high-TI facies, (b) a closer view of the blocky ejecta, (c) the mixing of blocky ejecta rays and mantled terrain in the intermediate-TI facies, (d) a closer view of the mixed blocky and fine-grained ejecta, (e) the fine-grained mantling ejecta deposit of the low-TI facies, and (f) a closer view of the fine-grained ejecta deposit.

7.3.3 Ejecta Deposit Morphologies

Although the low-TI ejecta deposits are very distinct relative to the surrounding terrain in infrared images, their appearance in visible images is much more subtle. They can appear either slightly lighter (Figure 7.9a), slightly darker (Figure 7.9b) or essentially the same tone (Figure 7.9c) as the surrounding terrain. The difference in tone is almost always subtle regardless of the low-TI ejecta deposit type, which makes the deposits difficult to identify or classify using only visible images. However, at very high spatial resolutions, the ejecta deposits and the craters at their centers have morphologies that are more diagnostic.

The low-TI facies have a range of morphologies that are consistent with being composed of fine-grained material. Most of the deposits appear to be smoothly mantled terrains that have been pockmarked by secondary craters to varying degrees, often with dense rays of secondaries radiating from the central craters, as shown in Figure 7.9d. Some ejecta deposits correspond to slightly raised terrains that have more secondary craters than the terrain that surrounds and presumably underlies them, as shown in Figure 7.9e. Others are composed of aeolian forms (dunes, ripples, etc) that are presumably reworked forms of the fine-grained ejecta material, as shown in Figure 7.9f. While these figures show portions of different low-TI ejecta deposits with clear examples of each morphology, most of the deposits contain combinations of these morphologies.

The appearances of the central craters, however, are not diagnostic and are seemingly independent of the low-TI ejecta deposit type. Figure 7.10 shows HiRISE images of representative central craters from each of the low-TI ejecta deposit types. In all cases, the craters have a mixture of fine-grained and blocky material in their interiors, exposed

bedrock along the crater rims, and blocky ejecta immediately surrounding the craters. Although there appears to be a slight correlation between the density of the blocky ejecta and the apparent degradation state of the ejecta deposit, the correlation is not strong enough to positively identify the low-TI ejecta deposit type by only examining the central crater.

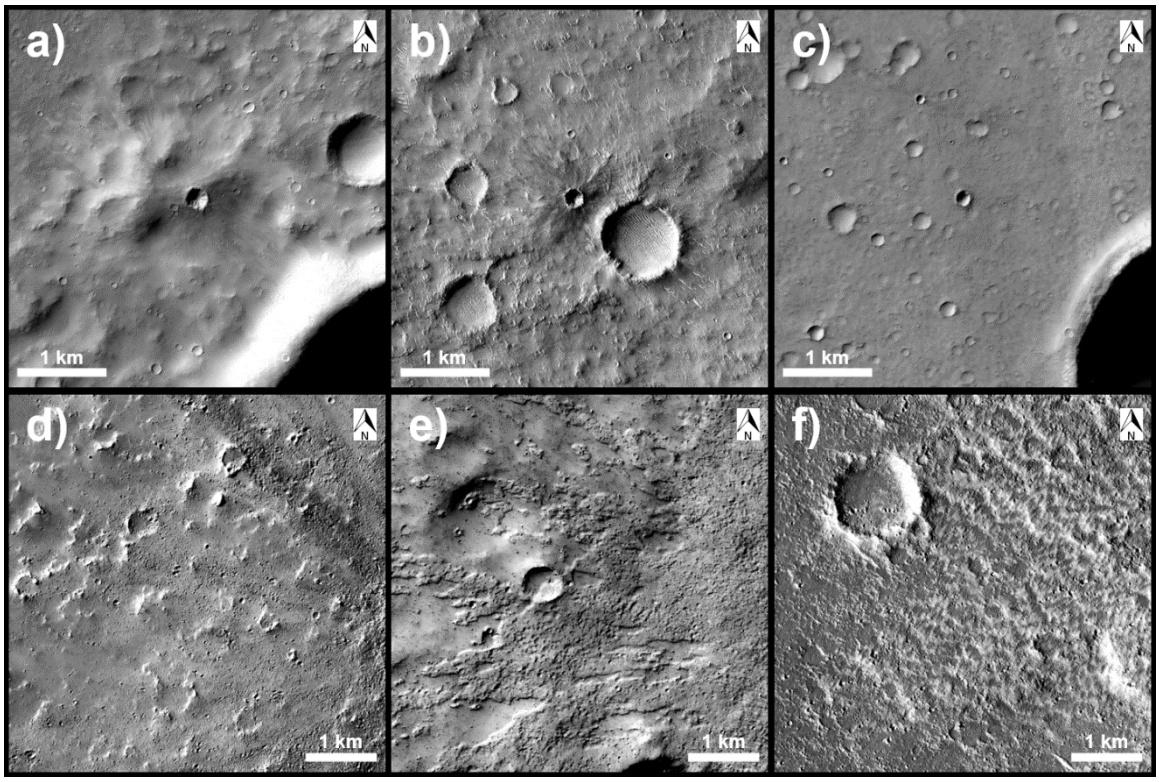

Figure 7.9. Compared to the surrounding terrain in HiRISE visible images, the low-TI ejecta deposits can appear: (a) slightly lighter (PSP_008541_1640_RED), (b) slightly darker (ESP_036432_1755_RED), or (c) essentially the same tone (mosaic of ESP_044697_1565_RED and CTX image F04_037510_1557_XN_24S150W) as the surrounding terrain. The lowest thermal inertia portion of the ejecta deposits have a wide range of morphologies, such as: (d) smoothly mantled terrain pockmarked to varying degrees by secondary craters (ESP_027369_1575_RED), (e) a layer of pockmarked ejecta that appears distinct from the underlying terrain (ESP_044697_1565_RED), and (f) aeolian dunes and ripples (ESP_019552_1995_RED).

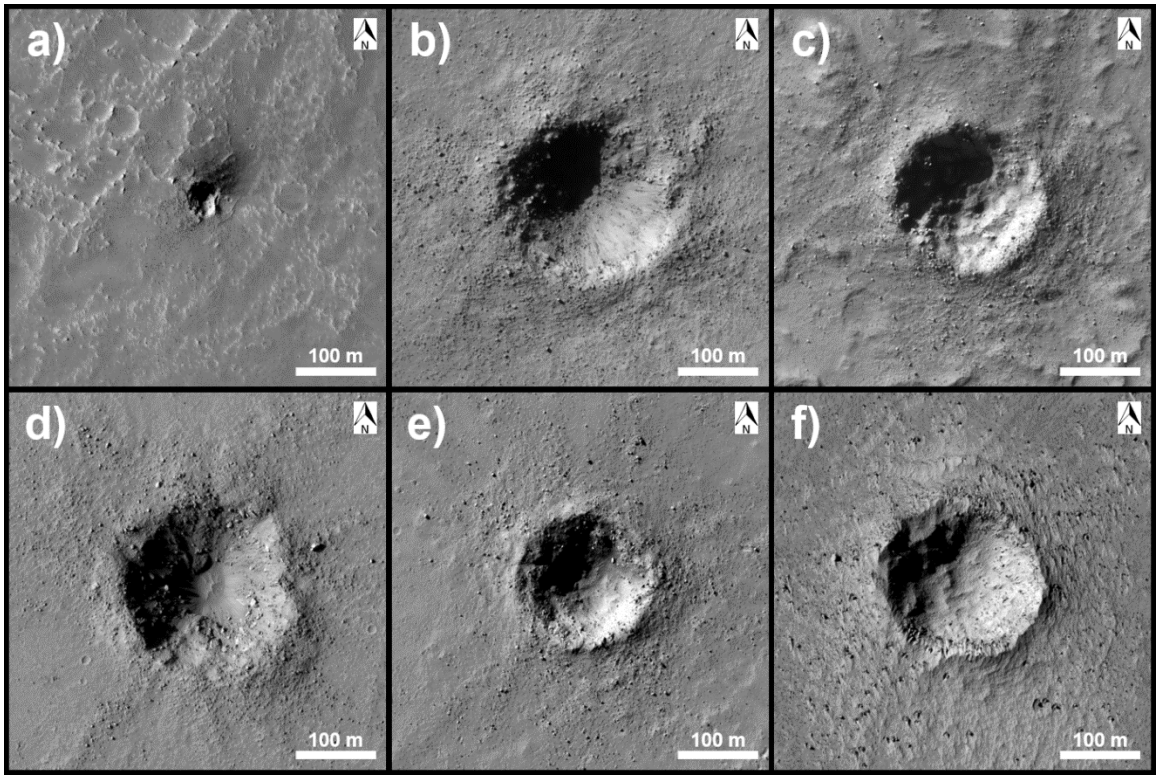

Figure 7.10. HiRISE images of the low-TI ejecta deposit central craters show that they all have exposed bedrock in their rims and are surrounded by blocky ejecta extending approximately one crater diameter from the rim regardless of the low-TI ejecta deposit type: (a) Type 1 - Below Data Resolution (ESP_026855_1510_RED), (b) Type 2 - Heavily Degraded (ESP_017606_1620_RED), (c) Type 3 - Degraded (ESP_026855_1510_RED), (d) Type 4 - Modified (ESP_037133_1755_RED), (e) Type 5 - Preserved (ESP_027369_1575_RED), and (f) Type 6 - Well Preserved (ESP_036704_1660_RED).

7.4 Discussion

7.4.1 Comparison with Lunar Cold Spot Craters

Bandfield et al. (2014) identified a previously unrecognized class of small fresh lunar impact craters using nighttime temperature maps compiled from Diviner radiometer data (Paige et al., 2010). These lunar cold spots are characterized by increased nighttime temperatures near the central craters and decreased nighttime temperatures in the surrounding material, much like the Martian low-TI ejecta deposits identified by this study. They conducted a near-global (50°N - 50°S) survey using the Diviner nighttime rock-free regolith relative temperature map (Bandfield et al., 2011) and identified 2,060 lunar cold spots, which were randomly distributed across the lunar surface.

Figure 7.11a shows an example of a lunar cold spot crater in the Diviner rock-free nighttime regolith relative temperature map overlaid on the Lunar Reconnaissance Orbiter Camera (LROC) Wide Angle Camera (WAC) equatorial shaded relief map (Robinson et al., 2010). The lunar cold spot craters share many characteristics with the Type 5 (Preserved) low-TI ejecta deposits, particularly the continuous region of low nighttime temperature material that transitions into discrete rays with increasing radial distance from the crater. Figure 7.11b shows the crater at the center of Figure 7.11a in a mosaic of images from the LROC Narrow Angle Camera (NAC) (Robinson et al., 2010). It shares many similarities with visible images of the Martian craters with low-TI ejecta deposits, particularly the lighter-toned ejecta immediately surrounding the crater, which is comparable to the ejecta deposit in Figure 7.9a.

However, despite their many similarities, the lunar cold spots and the Martian low-TI ejecta deposits appear to have been formed by different mechanisms. Since the cold spots

themselves do not have any significant albedo, spectral or morphological characteristics that distinguish them from the surrounding terrain, Bandfield et al. (2014) concluded that they are the result of the upper few centimeters of existing regolith being mechanically disturbed by either cascades of secondary impacts or gas flows originating from the primary impact. This mechanical disturbance would have lowered the thermal inertia of the already very low thermal inertia lunar regolith by "fluffing" it, which would have resulted in increased pore space sizes and decreased contact between the regolith grains. This conclusion was further supported by the observation that the low temperature areas showed no evidence for either the deposition or erosion of material.

While the existing Martian regolith surrounding the craters with low-TI ejecta deposits was likely altered by the same mechanisms, it does not appear that these were the dominant mechanisms leading to the formation of the low-TI ejecta deposits. Unlike the lunar cold spots, the low-TI ejecta deposits do have morphologies indicating the deposition of material in the low-TI facies, specifically the apparent mantling of the pre-existing surface by relatively fine-grained material that mutes the relief of pre-existing topographic features (Figure 7.8).

Bandfield et al. (2014) also concluded that the delicate "fluffing" of the regolith in the lunar cold spots was being preserved on geologic timescales due to the relatively quiet environment on the lunar surface, and hypothesized that similar features might not occur on planetary surfaces with active aeolian processes, such as Mars. This conclusion is supported by the absence of similar relatively low nighttime temperature features surrounding recent Martian impact craters (Figure 7.15), which would likely retain even

delicate modifications to the existing regolith over the timescales necessary to be observed by THEMIS routine mapping observations.

Although it is likely not a dominant factor, additional work on the relative contribution of the mechanical "fluffing" processes to the decreased thermal inertia of the Martian low-TI ejecta deposits could provide further insight into the formation of the lunar cold spots.

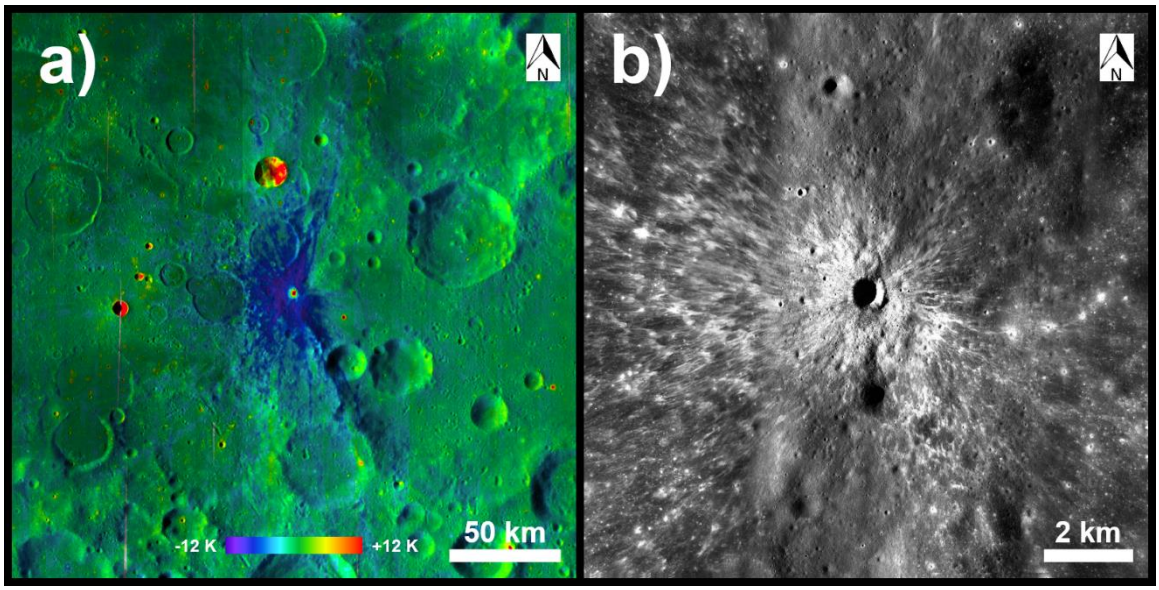

Figure 7.11. Example of a lunar cold spot crater in: (a) the Diviner rock-free nighttime regolith relative temperature map (*Bandfield et al.*, 2011) overlaid on the LROC-WAC equatorial shaded relief map (*Robinson et al.*, 2010), (b) a mosaic of LROC-NAC images M1181876866LE, M187649349RE and M1172461385RE.

7.4.2 Comparison with Low Nighttime Temperature Halos

Ghent et al. (2010) identified 88 Martian craters surrounded by low nighttime temperature (low-nT) halos, which they attributed to preserved deposits of fine-grained ejecta material. However, when their catalog of low-nT ejecta halos was compared with the catalog of low-TI ejecta deposits identified by this study, there were no features identified as belonging to both populations. This was unexpected given that both types of features were independently identified using nearly the same criteria, but a closer inspection of the low-nT halos reveals a few reasons for this result.

The low-nT halos can be roughly divided into two groups based on their sizes. Figures 7.12a and 7.12b show examples of the smaller low-nT halos, which have central craters slightly larger than the craters with low-TI ejecta deposits, while Figures 7.12c and 7.12d show examples of the larger low-nT halos. Figure 7.13 shows the global distribution of the low-nT halos (red) in relation to the low-TI ejecta deposits (white).

While conducting the low-TI ejecta deposit survey, many craters similar to those in Figures 7.12a and 7.12b were encountered. They were not categorized as low-TI ejecta deposits, though, because their forms differed from the type example being used (Figure 7.1b). Specifically, the low-TI material was usually located around and below rampart ejecta deposits surrounding the craters. In some cases the low-TI material surrounds the entire rampart, as in Figure 7.12a, but in many cases it only surrounds a portion of the rampart, as in Figure 7.12b.

Since these craters were often found in close proximity to other deposits of low-TI material that appeared unrelated to the craters (ex: southeastern corner of Figure 7.12a, southwestern corner of Figure 7.12b), the working hypothesis was that regional low-TI

material was being deposited against the much older rampart ejecta by aeolian processes and trapped in those areas due to surface roughness. While it is still possible that these craters might have begun as craters with low-TI ejecta deposits, they appeared to have been modified to an extent that they were no longer relevant to this study. However, in hindsight, these craters share as many similarities as differences with the low-TI ejecta deposits and could indicate that there is a higher degree of variability in the population than initially thought.

The low-TI ejecta deposit survey also encountered craters similar to those in Figures 7.12c and 7.12d. These types of craters were not identified as low-TI ejecta deposits because they were also judged to be sufficiently different from the type example used for the survey, primarily due to the presence of rampart ejecta and their much larger size. Instead, they appear to be degraded versions of the rayed craters identified by Tornabene et al. (2006) and Tornabene and McEwen (2008). Since we did not initially suspect a connection between the rayed craters and the low-TI ejecta deposits, these large low-nT halos also did not appear relevant to the survey and were not cataloged. However, in hindsight, a more thorough global survey of these potentially degraded rayed craters could provide additional insights into their relationship with the low-TI ejecta deposits.

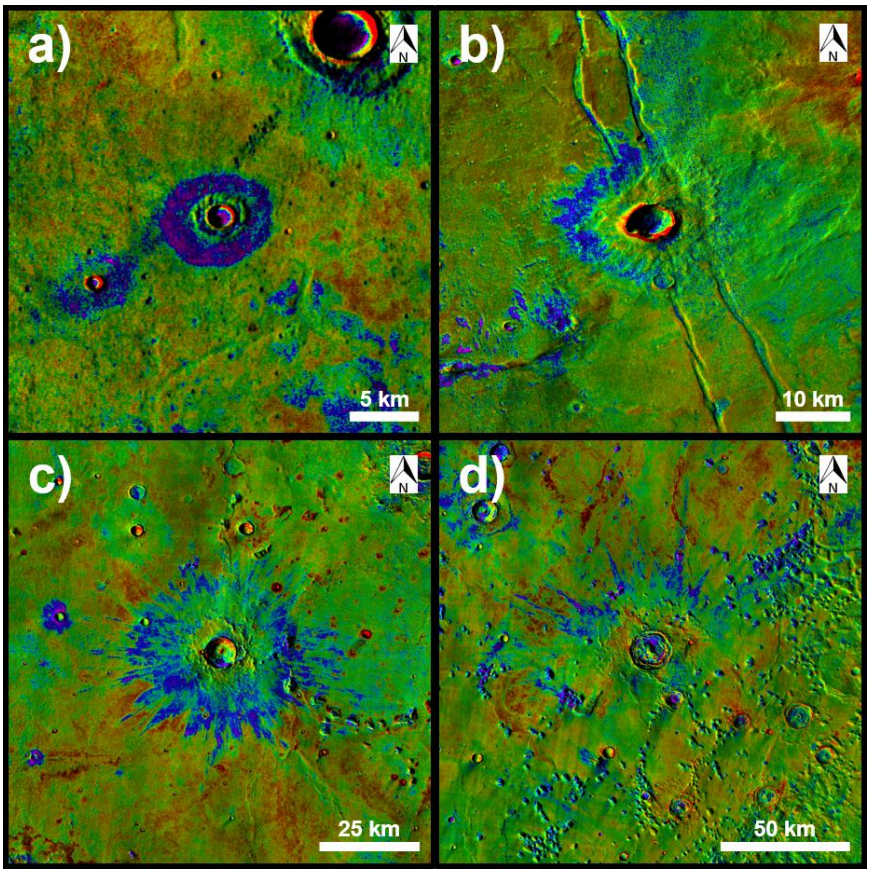

Figure 7.12. Examples of the low-nT halos identified by *Ghent et al.* (2010) in sections of the THEMIS Day IR with Colorized Night IR global map: **(a)** a small low-nT halo at 31.885°N, 115.110°E, **(b)** a small low-nT halo at -45.582°N, 273.432°E, **(c)** a large low-nT halo at 25.785°N, 333.190°E, and **(d)** a large low-nT halo at 22.555°N, 334.375°E. The small low-nT halos share many characteristics with the low-TI ejecta deposits, while the large low-nT halos share many characteristics with rayed craters.

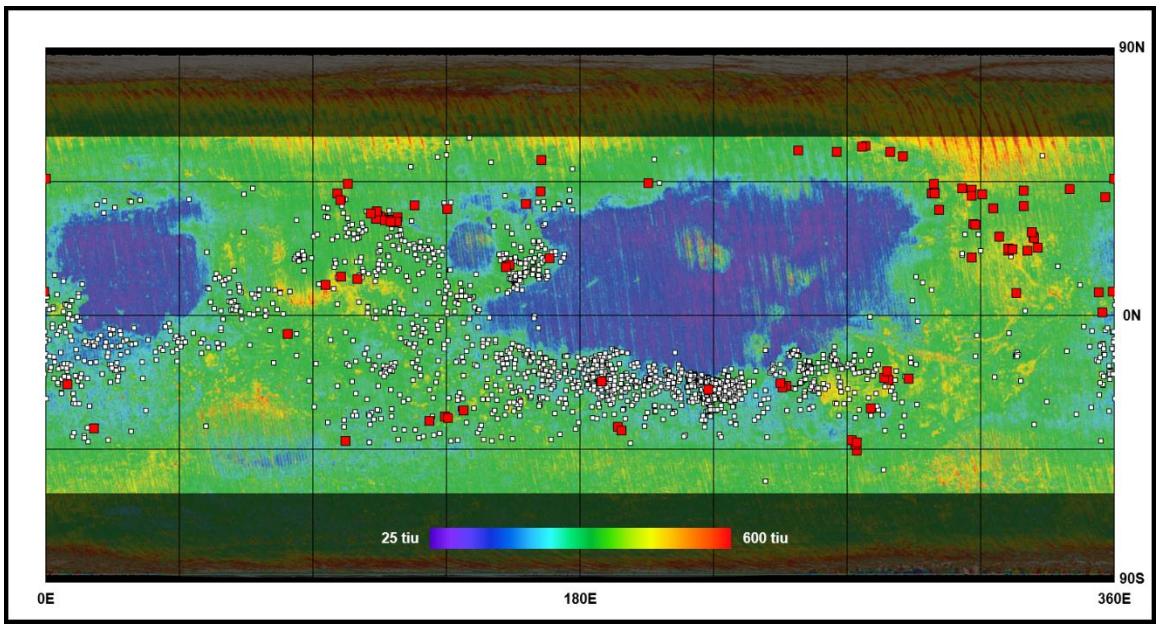

Figure 7.13. Global distribution of low-TI ejecta deposits (Types 3, 4, 5 & 6), collectively plotted in white, on a TES Daytime Thermal Inertia map (*Putzig and Mellon*, 2007), along with the low-nT halos (red) identified by *Ghent et al.* (2010). The regions poleward of 60° have been shaded to indicate that they were not included in the low-TI ejecta deposit survey.

7.4.3 Low-TI Ejecta Deposit Equivalents in Dusty Terrains

As seen in Figure 7.5, the distribution of low-TI ejecta deposits across the Martian surface is well-correlated with the absence of regional dust cover at thicknesses on the order of centimeters. However, since similarly-sized impacts are expected to occur in the dusty regions at the same frequency as in the non-dusty regions, it raises the question of how similar craters and their associated ejecta deposits would be expressed if they formed in a region with thick dust cover.

To address this question, a limited visual search of CTX images was carried out in southwestern Daedalia Planum for impact craters with distinguishable ejecta deposits that did not appear fresh enough to be recent impacts. This search area was chosen because it lies just north of a large cluster of Type 5-6 low-TI ejecta deposits and is an area of low regional thermal inertia. Of the many craters located in the search area that are similar in size to the craters with low-TI ejecta deposits, only one was identified with an ejecta deposit that is distinguishable from the surrounding terrain in both visible and thermal infrared imagery, but is not associated with a low albedo "blast zone" that would be indicative of a recent impact.

Figure 7.14a shows the crater at -18.719°N, 223.729°E in a CTX image and Figure 7.14b shows the same crater in the THEMIS Day IR with Colorized Night IR global map, which has been overlaid on the same CTX image. Similar to the craters with low-TI ejecta deposits in Figures 7.9a-7.9c, the ejecta in Figure 7.14a only has a slightly darker tone than the surrounding terrain. The crater also has an area of higher nighttime temperatures immediately surrounding it, which is reminiscent of the high-TI facies of the low-TI ejecta deposits. However, there is no evidence of a low-TI facies.

In order to rule out the possibility that the low-TI facies is simply being obscured by the colorization algorithm that was used for the THEMIS Day IR with Colorized Night IR global map, modified versions of the algorithm were created to emphasize both the low and high ends of the temperature range within the nighttime infrared images.

In its original form, the colorization algorithm bins the nighttime temperature data (which, after the mosaicking process, has been stretched into DNs ranging from 1 to 255, with 0 reserved for the ignore value) into six equally-sized DN bins and then assigns each bin a color from red (high values) to purple (low values). In the modified versions, the algorithm still uses six equally-sized DN bins, but the bin sizes are smaller (~35 DN wide, instead of ~43 DN wide) and biased towards either end of the total DN range of the data. A variety of smaller bin sizes were tested, but due to the relatively high noise levels in the nighttime images of this region, which are a result of the low nighttime surface temperatures, bins smaller than 35 DN were found to only further exaggerate the noise without emphasizing any additional thermophysical structure on the surface.

Figure 7.14c shows the nighttime infrared images colorized using 35 DN-wide bins, but only for values between 1 DN and 210 DN. Any values higher than 210 DN oversaturate the scale and are colored as if they are 210 DN. The resulting colorized image shows slightly more detail in the high-TI facies surrounding the crater, but there is still no indication of a low-TI facies.

Figure 7.14d also shows the nighttime infrared images colorized using 35 DN-wide bins, but instead shifted to the high end of the data range and only covering values between 45 DN and 255 DN. Any values lower than 45 DN will undersaturate the scale

and be colored as if they are 45 DN. The resulting colorized image shows slightly less detail in the high-TI facies, but again, does not show any evidence of a low-TI facies.

Although a complete survey and analysis of comparable craters will be needed before any definitive conclusions can be drawn, this example demonstrates that craters similar to those at the center of the low-TI ejecta deposits do occur within the dusty, low thermal inertia regions of the planet. It also demonstrates that the absence of identifiable low-TI ejecta deposits in those regions is likely not due to the colorization algorithm used for the THEMIS Day IR with Colorized Night IR global map.

However, this single example does not provide much insight into the reason for the absence of a low-TI facies surrounding similar craters in the dusty regions. One possible explanation is that the rate of dust deposition in these regions is high enough that despite the relatively young ages of these craters, the low-TI component of the ejecta has been covered by enough dust to thermally mask it. However, since the high-TI facies is still easily distinguishable, that does not appear to be the case. Another possible explanation is that the aeolian erosion rate is higher in these regions and the fine-grained component of the ejecta has either been stripped away or reworked sufficiently to blend it into the surrounding regolith. Higher resolution visible images of this crater and others like it would help to determine whether there is evidence for aeolian reworking of the ejecta deposits, as seen in Figure 7.9f. A third possibility is that the absence of a distinguishable low-TI facies is due to low thermal inertia contrast between the ejecta and the surrounding terrain. The deposition of low-TI material on an already low-TI surface would not be easily identifiable in thermal inertia images. Again, further investigation of these comparable craters will be required before any definitive conclusions can be drawn.

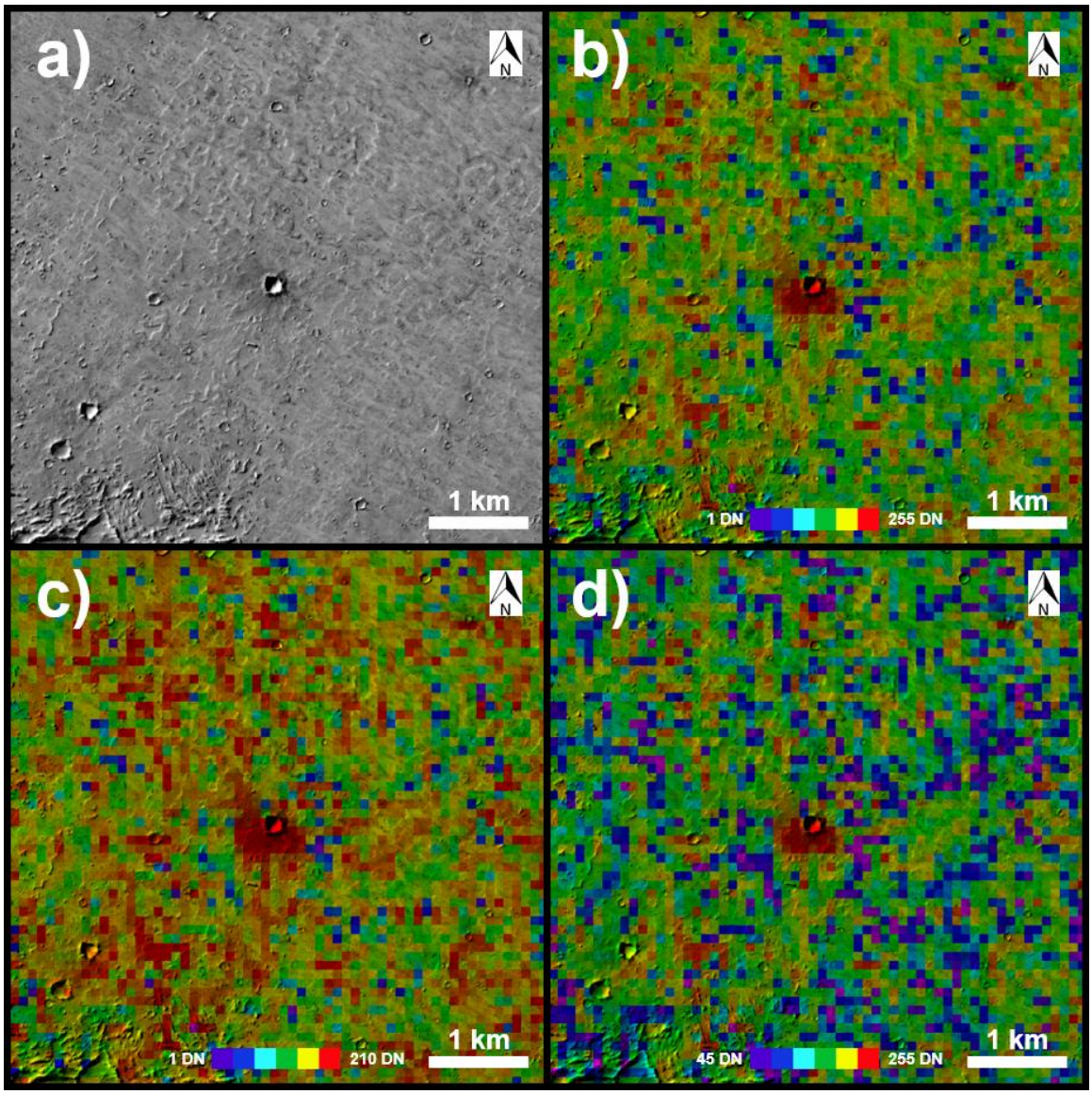

Figure 7.14. Potential equivalent of the craters with low-TI ejecta deposits located in a dust-covered low thermal inertia region in southwestern Daedalia Planum (-18.719°N, 223.729°E), shown in: **(a)** a CTX image (P22_009581_1610_XN_19S136W) and **(b)** a section of the THEMIS Day IR with Colorized Night IR global map overlaid on the same CTX image. Also shown are sections of the THEMIS Day IR with Colorized Night IR global map overlaid on the same CTX image that have been colorized using algorithms that preferentially emphasize differences in **(c)** the cold end of the nighttime temperature range, and **(d)** the warm end of the nighttime temperature range.

7.4.4 Comparison with Recent Primary Impact Craters

The craters with low-TI ejecta deposits can also be compared to recent primary impact craters to further investigate their origins. Using visible images acquired by multiple instruments over the last twenty years, investigators have identified recent impact craters with formation dates that can be constrained by before-and-after image pairs. These recent impact craters have also been identified as primary impact craters since there have been no corresponding recent impact craters large enough to generate secondary impact craters of these sizes. Following the work of Malin et al. (2006) and Byrne et al. (2009), Daubar et al. (2013) compiled a catalog of 226 confirmed recent primary impact craters.

The locations of these craters were examined in the THEMIS Day IR with Colorized Night IR global map to determine whether any of them correspond to the locations of low-TI ejecta deposits. While none of them had low-TI ejecta deposits and the majority were not distinguishable from the surrounding terrain in the nighttime infrared images, there were 21 recent craters with subtle infrared features and 13 with distinct infrared features. The locations of three recent impact craters that are distinguishable in infrared images are shown in Figure 7.15.

All 34 recent impact craters that are distinguishable in infrared images have essentially the same appearance, which differs significantly from the low-TI ejecta deposits. In the THEMIS Day IR with Colorized Night IR global map, they appear as diffuse bright spots with little color difference between them and the surrounding terrain. The increased brightness is due to daytime temperatures that are higher than the surrounding terrain, which are caused by the lower albedos of the “blast zones” around

the craters, as seen in Figures 7.15a, 7.15c and 7.15e. The color similarity with the surrounding terrain is due to nighttime temperatures that are not significantly different from the adjacent surfaces, as seen in Figures 7.15d and 7.15f. However, there are eight recent craters that do exhibit elevated nighttime temperatures near the impact crater itself, such as the one in Figure 7.15b.

This indicates that either: 1) the mechanical vibrations from the impact and the subsequent ejecta deposition are not significantly changing the average grain size and/or porosity on the surface, except possibly in the immediate vicinity of the crater where bedrock is being exposed and large ejecta blocks are present, or 2) the finest fraction of the ejecta material has been mobilized and removed on timescales short enough that their initial presence was not observed by THEMIS. This is in contrast to the low-TI ejecta deposits, where the average grain size and/or porosity of the surface has been significantly changed and those changes have persisted on timescales long enough to be observed by THEMIS.

However, the appearance of the recent craters in the nighttime infrared images is consistent with the infrared signature that would be expected for primary impact craters based on the conclusions of Hartmann (1985). The higher ejecta velocities of primary impacts would be expected to spread the ejecta material over a much larger area, causing the average thickness of the ejecta deposit to be thinner than for a similarly-sized secondary impact. Since a layer of lower thermal inertia material will significantly decrease the apparent thermal inertia of a surface even if it is only a fraction of a thermal skin depth thick (Kieffer et al., 1977), the average thickness of the recent crater ejecta deposits would have to be exceedingly thin for there to be no recognizable low-TI facies.

A comparison of the locations of the low-TI ejecta deposits identified by this study and the recent impact craters cataloged by Daubar et al. (2013) further emphasizes the differences between these two populations. Figure 7.16 shows the locations of the Type 3-6 low-TI ejecta deposits (white) in relation to the recent impact craters (red).

The concentration of the recent impact craters in the low-TI dusty regions of the planet is not surprising, since the vast majority of them are located by the low albedo "blast zones" that are created when the atmospheric shockwaves generated by the impacts remove high albedo dust from the lower albedo underlying surface (Daubar et al., 2013), as seen in Figures 7.15a, 7.15c and 7.15e. There are almost certainly equivalent numbers of recent impacts in the less-dusty regions, as discussed in Section 4.3, but different methods would be required to locate and identify them.

While it would be tempting, based on Figure 7.16, to suspect that the low-TI ejecta deposits are merely the expression of recent impacts in less-dusty regions, the evidence does not indicate that is the case. First, HiRISE images of the recent impact craters (Daubar et al., 2013, Figure 7.2) do not indicate the presence of thick fine-grained ejecta deposits that appear to mantle the pre-existing terrain like those in Figures 7.8c and 7.9d-7.9f. Second, the low-TI facies of the low-TI ejecta deposits often show signs of aeolian modification, which would not be expected on that spatial scale given the very young ages of the recent impact craters. Third, the recent impact craters are significantly smaller than the craters at the centers of the low-TI ejecta deposits. All but one of the recent craters are <25m in diameter (Daubar et al. (2013), Table 1), but the craters with low-TI ejecta deposits are typically in the 200m-300m diameter range. Finally, fourth, the infrared signature of the recent impact craters in Figure 7.15 are significantly different

from the appearance of the crater in Figure 7.14, which is suspected of being an equivalent to a low-TI ejecta deposit crater in a dusty, low thermal inertia region.

These results indicate that the craters with low-TI ejecta deposits are not primary impact craters. They also indicate that the low-TI ejecta deposits are not simply very young features that have yet to lose the fine-grained component of their ejecta deposits due to the pervasive aeolian erosional environment on Mars (Greeley et al., 2004), since the recent impact craters are clearly younger and do not possess distinguishable low-TI ejecta facies.

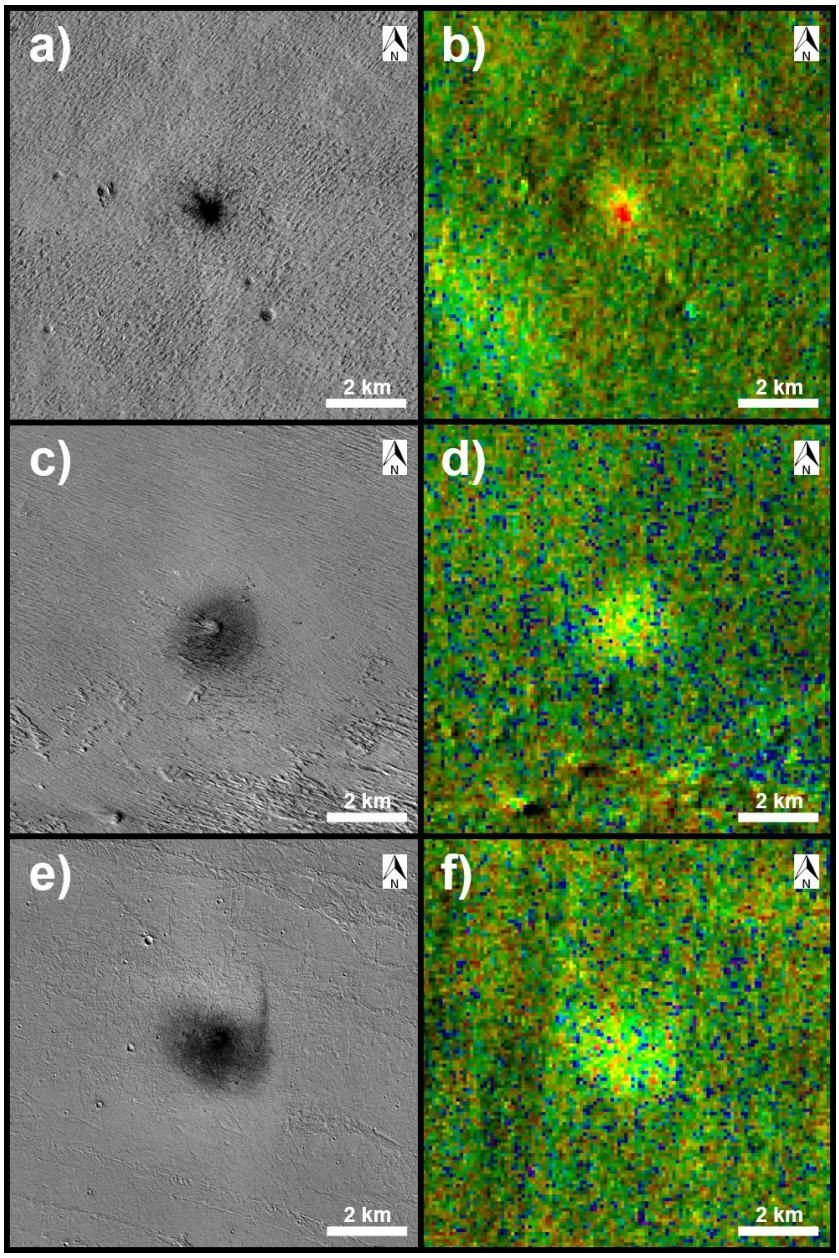

Figure 7.15. Examples of recent primary impact craters in visible and infrared data: Site 45 (-8.786°N, 182.673°E) crater in (a) a CTX image (P06_003425_1720_XN_08S177W) and (b) a section of the THEMIS Day IR with Colorized Night IR global map; Site 53 (5.469°N, 224.353°E) crater in (c) a CTX image (D15_032881_1855_XN_05N135W) and (d) a section of the THEMIS Day IR with Colorized Night IR global map; and Site 76 (13.851°N, 208.582°E) crater in (e) a CTX image D09_030574_1939_XN_13N151W) and (f) a section of the THEMIS Day IR with Colorized Night IR global map, where the asymmetrical shape of the "blast zone" is apparent even in the infrared images.

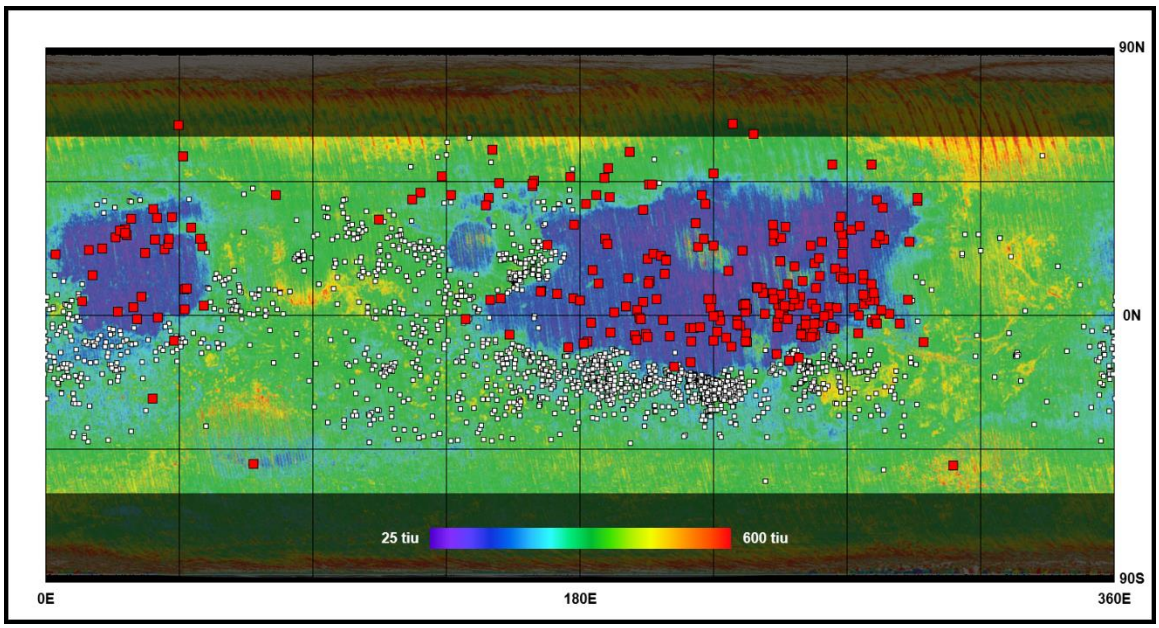

Figure 7.16. Global distribution of low-TI ejecta deposits (Types 3, 4, 5 & 6), collectively plotted in white, on a TES Daytime Thermal Inertia map (*Putzig and Mellon*, 2007), along with the recent impact craters (red) catalogued by *Daubar et al.* (2013). The regions poleward of 60° have been shaded to indicate that they were not included in the low-TI ejecta deposit survey.

7.4.5 Comparison with Secondary Impact Craters

While the low-TI ejecta deposits are not the result of primary impacts, there is evidence that they are instead the result of secondary impacts.

McEwen et al. (2005) examined secondary impact craters created by the Zunil impact ejecta, many of which appear similar to the low-TI ejecta deposits in thermal infrared images. Figure 7.17 shows one of the Zunil secondary craters described in their study (McEwen et al. (2005), Figure 3a). When both visible (CTX) and thermal infrared (THEMIS) images are considered, this Zunil secondary crater could easily be classified as a Type 1 (Below Data Resolution) low-TI ejecta deposit. However, since only infrared images were used in the current survey, the small size of this feature prevented a clear identification and it was not included in the survey results.

This example further demonstrates the likely incompleteness of the Type 1 category in this survey due to resolution limitations. This also likely explains why there was no dual identifications between the craters identified as Zunil secondaries by the McEwen et al. (2005) study (only the secondary craters with published coordinates were included in the comparison) and the low-TI ejecta deposits identified by this study. If this survey were repeated in the vicinity of Zunil Crater using both visible and infrared images, it would likely result in many dual identifications.

However, it is still possible to further investigate the potential secondary impact origin of the low-TI ejecta deposits without re-conducting the survey using additional datasets. Calef et al. (2009) compared recent primary impact craters with the Zunil Crater secondaries identified by McEwen et al. (2005) and developed a list of criteria for determining whether a crater is either primary or secondary. While their study was

primarily based on numerical measurements of the craters in visible images, two of their criteria can still be applied to the craters with low-TI ejecta deposits examined in this study.

First, they observed that primary craters typically have thin ejecta deposits with diffuse boundaries, while secondary craters have relatively thick ejecta deposits with well-defined rampart-like boundaries. Based on the experimental work of Hartmann (1985), they attributed this difference to the lower impact velocity of secondary craters, which results in lower ejecta velocities, which causes the ejecta material to fall closer to the crater. The low-TI ejecta deposits appear to clearly fall into the latter category based on the typical morphologies summarized in Figures 7.9d-7.9f.

Second, they found that the lengths of the ejecta rays from primary craters were tens to hundreds of crater radii long, while the ejecta rays from secondary craters were only a few to tens of crater radii long. This difference was also attributed to impact velocities, with higher impact velocities resulting in higher ejecta velocities and ejecta rays that radiate farther from the crater. Again, the low-TI ejecta deposits appear to clearly fall into the secondary impact category. Their ejecta rays are often very short and barely extend past the continuous portion of the low-TI ejecta deposits, as seen in Figure 7.1. However, they should be assessed in terms of both their rayed and continuous ejecta, since the already short rays could be shortened further over time by aeolian erosion.

Although more detailed shape measurements will be needed before fully evaluating the craters with low-TI ejecta deposits according to the quantitative criteria developed by Calef et al. (2009), they are consistent with enough of the qualitative criteria that they appear to be secondary impact craters.

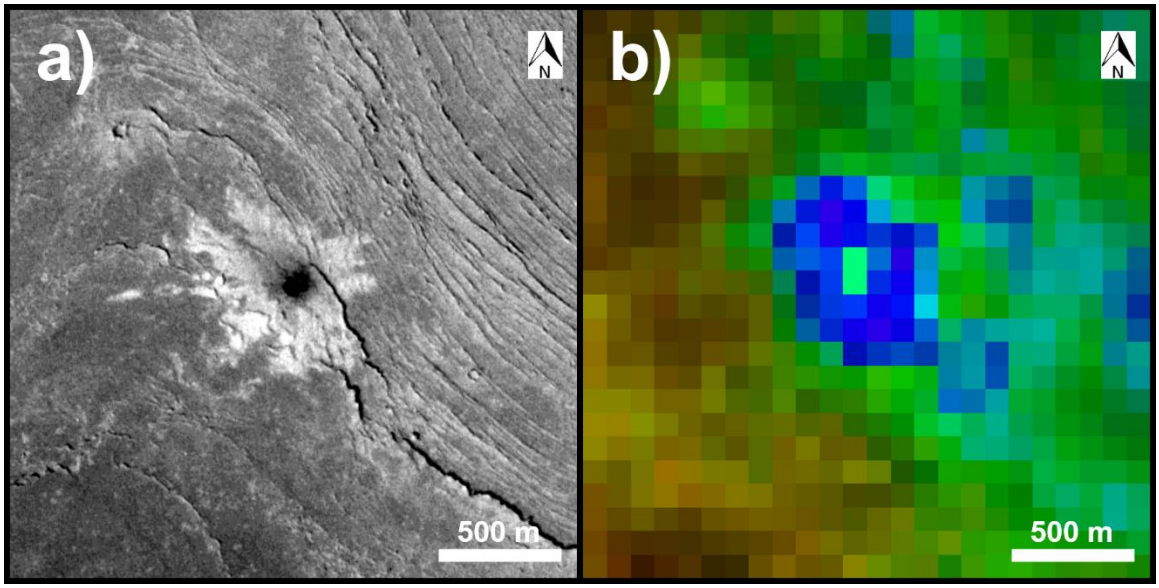

Figure 7.17. Zunil Crater secondary crater at 8.8785°N, 155.7575°E in: (a) a CTX image (D10_031288_1886_XN_08N204W), and (b) a section of the THEMIS Day IR with Colorized Night IR global map. While the visible image is sufficient for identifying this as a secondary crater, both visible and thermal infrared images are required to also identify it as a Type 1 (Below Data Resolution) low-TI ejecta deposit.

7.4.6 Relationship with Rayed Craters

Tornabene et al. (2006) and Tornabene and McEwen (2008) identified a total of six definitive and three probable rayed craters on the Martian surface using THEMIS nighttime infrared images. Like their lunar counterparts, the Martian rayed craters are associated with secondary crater chains and ejecta rays hundreds of kilometers in length. The fact that these features are so easily distinguishable in the nighttime infrared and visible images suggests the rayed craters are relatively young features that have not yet been significantly modified by the erosional processes currently active on the Martian surface.

In the global survey of low-TI ejecta deposits, the largest identified deposit is located around Dilly Crater, which is described by Tornabene et al. (2006) as the smallest definitively identified rayed crater on Mars. A comparison of the rayed craters and the low-TI ejecta deposits using the THEMIS Day IR with Colorized Night IR global map, summarized in Figure 7.18, suggests that they are closely related features that perhaps represent endmembers of a spectrum, with the variations in size and form being controlled by the size and/or velocity of the impactor.

Figure 7.18a shows Gratteri Crater, the best rayed crater example identified by Tornabene et al. (2006). The crater is surrounded by multiple thin ejecta rays of low thermal inertia material, which led to it being identified as a rayed crater. There are also diffuse regions immediately surrounding the crater with high and intermediate thermal inertia values, but they are not nearly as distinct as the high-TI and intermediate-TI facies immediately surrounding the craters with low-TI ejecta deposits.

Figure 7.18b shows Dilly Crater, which exemplifies the similarities between the rayed craters and the craters with low-TI ejecta deposits. Like the larger rayed craters, it has numerous distinct rays of low-TI ejecta material radiating out from the rim and extending at least tens of crater diameters. However, like the smaller low-TI ejecta deposits, there is a distinct high-TI facies immediately surrounding the crater, followed by an intermediate-TI facies and finally a low-TI facies that includes both rays and locally continuous deposits.

Figures 7.18c and 7.18d show progressively smaller low-TI ejecta deposits surrounding unnamed craters, demonstrating how the rays shorten and the ejecta deposits become more continuous as the size of the impact crater decreases. Figure 7.18e shows the same low-TI ejecta deposit from Figure 7.1, but at a similar scale to the others for comparison. At this size, the low thermal inertia ejecta material has formed a continuous deposit around the crater with some short ejecta rays still emanating from the outer edge.

Figure 7.18f shows an example of a Type 1 (Below Data Resolution) ejecta deposit. Although the small size of these ejecta deposits prevents them from being fully analyzed with THEMIS images due to resolution limitations, they appear to simply be smaller versions of the low-TI ejecta deposits. These deposits appear to be continuous around the craters and, although they are not observable in the nighttime temperature images, there are distinct streaks and rays in the low-TI facies that are observable in higher resolution visible images.

The rayed craters and the craters with low-TI ejecta deposits both show trends of decreasing ejecta ray length with decreasing crater size, and increasingly continuous low-TI ejecta deposits with decreasing crater size. Both populations are also located in the

same intermediate-to-high thermal inertia regions, as shown in Figure 7.19. The overlap between these two populations is most apparent in the case of Dilly Crater, which has been characterized as belonging to both populations. This suggests that these two populations are closely related, if not endmembers on a spectrum of impact features.

However, beyond merely representing similar types of impact features, it is possible that there is a more direct relationship between these two populations. The locations of the rayed craters correlate well with concentrations of low-TI ejecta deposits. Figure 7.19 shows the locations of the definitive rayed craters (Corinto, Dilly, Gratteri, Tomini, Zumba and Zunil, shown in black) and the probable rayed craters (Naryn, Thila and Wiltz, shown in gray) identified by Tornabene et al. (2006) and Tornabene and McEwen (2008) in relation to the locations of the low-TI ejecta deposits (Types 3-6) identified by this study (white).

In particular, there are significant concentrations of low-TI ejecta deposits surrounding Zumba (-28.65°N, 226.90°E) and Dilly (13.28°N, 157.22°E) Craters. To better understand the relationship between these two populations, a point density map was generated using the Point Density function within the Spatial Analyst Toolbox of ArcGIS 10.4, which is shown in Figure 7.20. The densest concentration of low-TI ejecta deposits is centered north of Zumba Crater, while another significant concentration is located southeast of Dilly Crater. In both cases, the rayed crater is offset from the center of the concentration.

Figures 7.21a and 7.21c show closer views of the spatial relationship between Zumba and Dilly craters, respectively, and the nearby low-TI ejecta deposit concentrations. The location of the concentration north of Zumba Crater can possibly be explained by the

shape of the crater's proximal ejecta, as seen in Figure 7.21b. The Zumba Crater butterfly pattern indicates that the impact occurred at an oblique angle with the impactor moving generally south to north, which would cause the ejecta to be preferentially ejected towards the north (Gault and Wedekind, 1978). This would result in secondary craters being preferentially located toward the north as well, which is consistent with the concentration of low-TI ejecta deposits in that region.

The location of the concentration southeast of Dilly Crater is not as easily explained. Dilly Crater's ejecta also forms a butterfly pattern, indicating an oblique impact. The orientation of the pattern suggests the impactor was travelling northeast to southwest, which would have resulted in a concentration of ejecta and secondary craters towards the southwest, but this is not consistent with the observed concentration. However, this region is complicated by the presence of nearby Wiltz and Thila Craters, which are classified as probable rayed craters. If they are, then each impact should have created a secondary crater field and the current low-TI ejecta deposit concentration should be a combination of all three. Since the relative ages of these impacts are not well-constrained and the proximal ejecta of Wiltz and Thila are not well-preserved, it is not possible to assess whether this low-TI ejecta deposit concentration is the result of secondaries from some or all of these rayed crater impacts.

However, this correlation between rayed craters and concentrations of low-TI ejecta deposits suggests that the surface materials and environmental variables that have allowed the low-TI ejecta deposits to preferentially persist in certain regions are likely the same variables that have allowed the low-TI rays surrounding the rayed craters to persist

as well. It further suggests that the low-TI ejecta deposits are likely the result of secondary impacts originating from the rayed crater primary impact events.

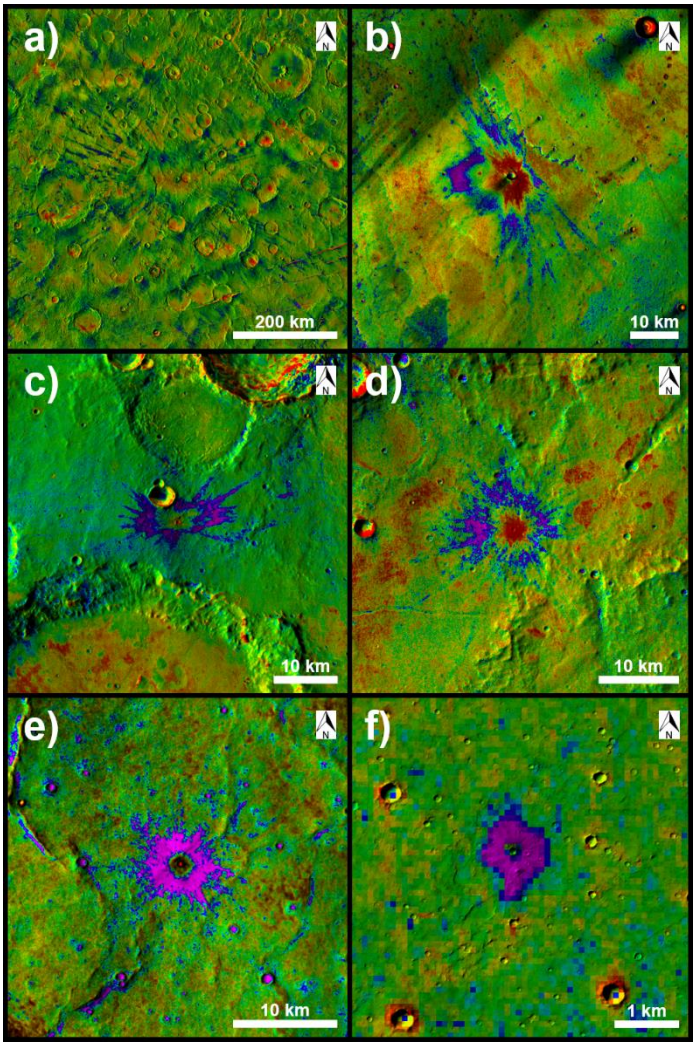

Figure 7.18. Transition from rayed craters to low-TI ejecta deposit craters with decreasing crater size from the THEMIS Day IR with Colorized Night IR global map: (a) Gratteri Crater was identified as a rayed crater by *Tornabene et al.* (2006), (b) Dilly Crater is the smallest rayed crater identified by *Tornabene et al.* (2006) and the largest low-TI ejecta deposit identified by this study, (c) a large low-TI ejecta deposit surrounding an unnamed crater in Terra Cimmeria (-30.14°N, 158.75°E) that also has distinct rays, (d) a smaller low-TI ejecta deposit surrounding an unnamed crater in Terra Sirenum (-23.31°N, 194.04°E) with less distinct rays and a more continuous ejecta *deposit, (e) the type example for the low-TI ejecta deposits, also surrounding an unnamed* crater in Terra Sirenum (-23.09°N, 182.94°E), with only a few distinct rays and a wide continuous ejecta deposit, and (f) a Type 1 (Below Data Resolution) low-TI ejecta deposit in Daedalia Planum (-24.37°N, 225.65°E) with similar features, shown overlaid in a mosaic of CTX images (D21_035505_1577_XI_22S134W and P13_006008_1577_XN_22S134W).

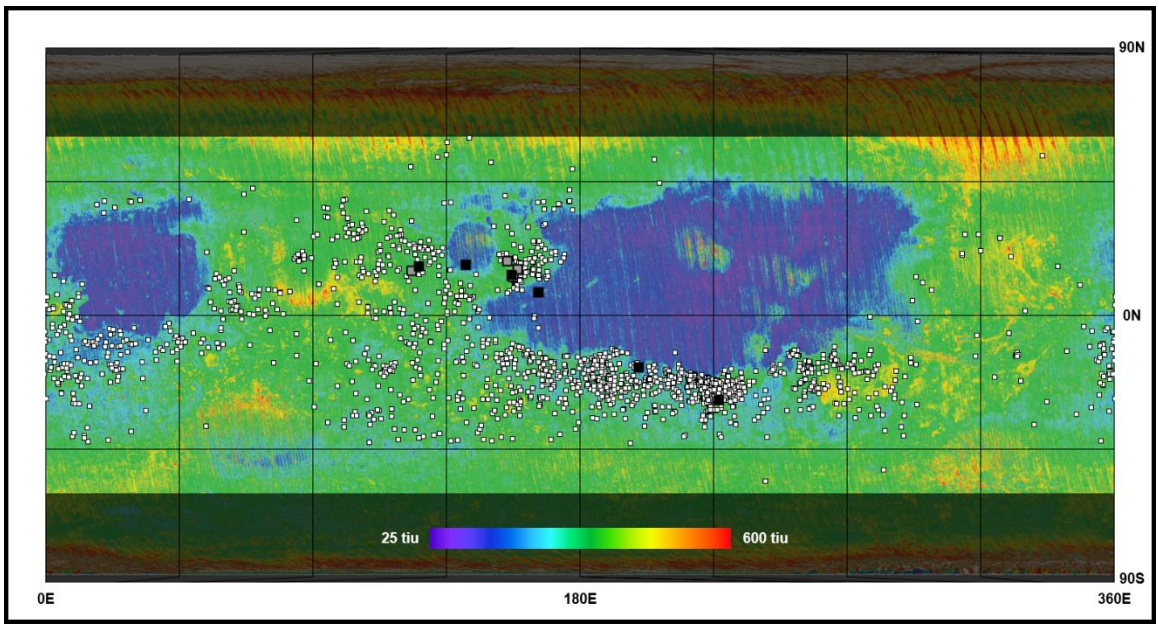

Figure 7.19. Global distribution of low-TI ejecta deposits (Types 3, 4, 5 & 6), collectively plotted in white, on a TES Daytime Thermal Inertia map (*Putzig and Mellon*, 2007), along with the probable (grey) and definitive (black) rayed craters identified by *Tornabene et al.* (2006) and *Tornabene and McEwen* (2008). The regions poleward of 60° have been shaded to indicate that they were not included in the low-TI ejecta deposit survey.

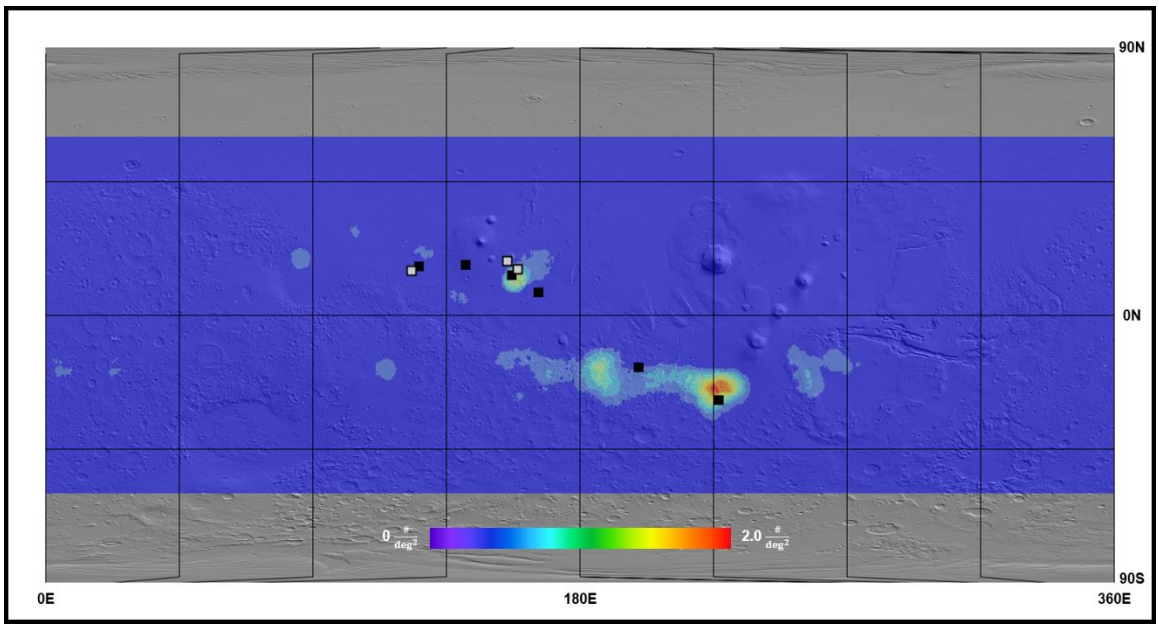

Figure 7.20. Point density map of the low-TI ejecta deposit (Types 3, 4, 5 & 6) locations overlaid on a MOLA (*Smith et al.*, 2001) shaded relief map, along with the probable (grey) and definitive (black) rayed craters identified by *Tornabene et al.* (2006) and *Tornabene and McEwen* (2008). The regions poleward of 60° were not included in the low-TI ejecta deposit survey.

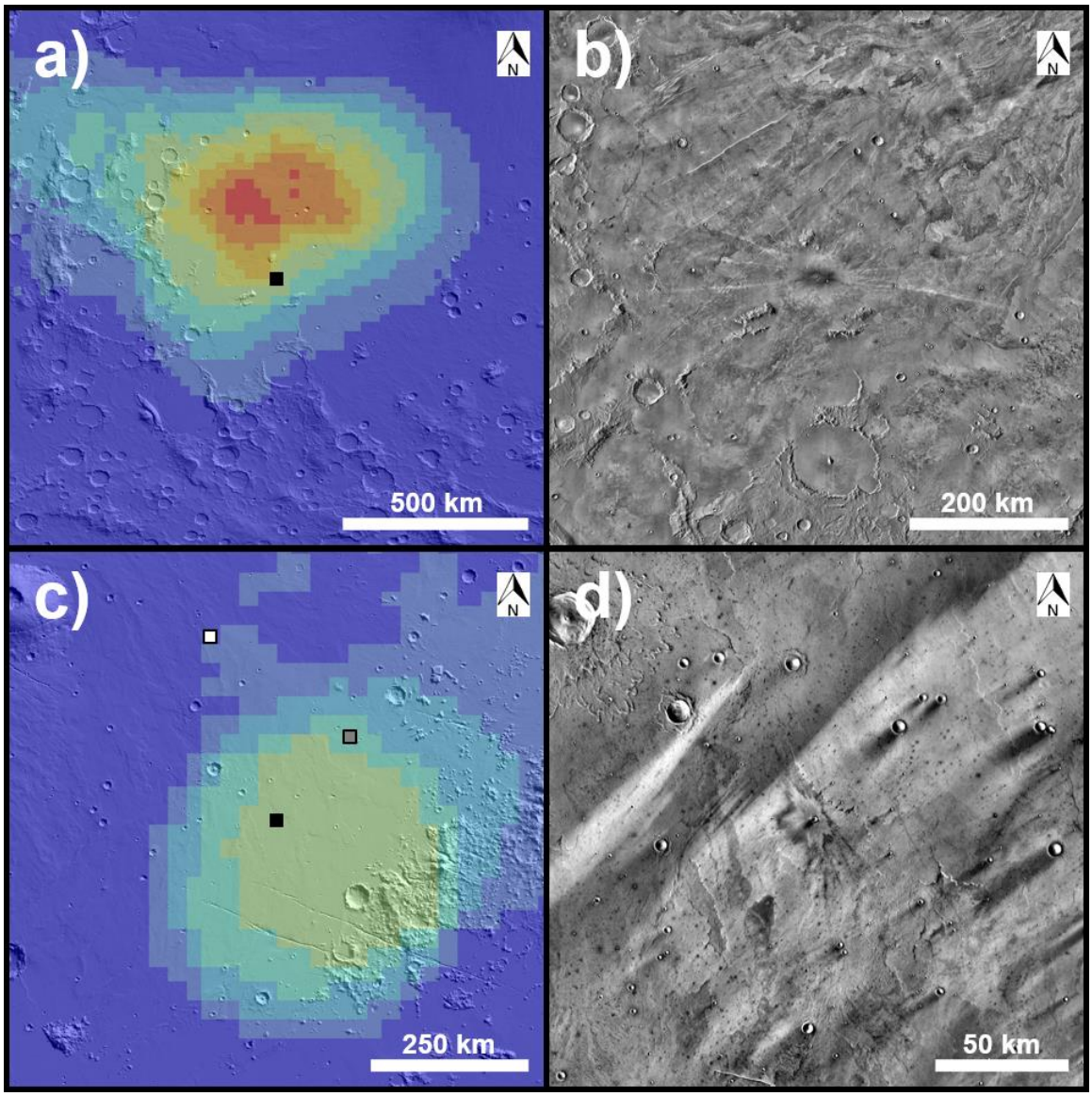

Figure 7.21. Low-TI ejecta deposit (Types 3, 4, 5 & 6) point density maps and the THEMIS Day IR global mosaic (*Hill et al.*, 2014) in the areas near the rayed craters Zumba and Dilly showing the relationship between the low-TI ejecta deposit concentrations and the ejecta patterns: (a) Low-TI ejecta deposit density map near Zumba Crater (in black), (b) THEMIS Day IR map of Zumba Crater, (c) Low-TI ejecta deposit density map near Dilly Crater (in black), Wiltz Crater (in grey) and Thila Crater (in white), (d) THEMIS Day IR map of Dilly Crater.

7.5 Conclusions

The low-TI ejecta deposits are composed of three concentric facies with radially decreasing thermal inertia values due to the decreasing average particle size of the ejecta material with radial distance from the crater. A near-global (60°N - 60°S) survey identified 4,024 low-TI ejecta deposits, which occur almost exclusively in regions with intermediate-to-high regional thermal inertias, which corresponds to low regional dust cover.

Compared to the recent primary impact craters, the low-TI ejecta deposits have different forms in infrared images and occur in regions with different dust cover thicknesses. Specifically, differences in the ejecta deposit textures, the sizes of the impact craters and the temperatures of the surface materials indicate they are not simply different expressions of the same feature, but are instead two distinct populations with related formation mechanisms.

Compared to the Zunil Crater secondary impact craters, they have well-defined edges and the ejecta rays emanating from the continuous ejecta blankets only extend tens of crater radii from the rim, both of which are characteristics of secondary crater ejecta. Clusters of low-TI ejecta deposits are found near the rayed craters Zumba and Dilly, with the cluster centers offset from the rayed crater locations. In the case of Zumba Crater, this offset is consistent with the primary direction of ejecta from the oblique impact. In the case of Dilly Crater, this offset is not consistent with the primary direction of ejecta from the oblique impact, but is complicated by the presence of two other nearby rayed craters and their less well-defined ejecta deposits.

We conclude that: 1) the low-TI ejecta deposits were formed by secondary impacts, many of which originated from the rayed crater primary impacts, and 2) the low-TI ejecta deposits are well-preserved and easily identifiable due to the absence of significant dust cover and relatively low aeolian erosion rates in the regions where they are located.

CHAPTER 8

CONCLUSION

Although chloride salts do not have any diagnostic spectral features in the thermal infrared wavelengths, this work has demonstrated that thermal infrared data can still provide valuable insight into the distribution and diversity of Martian chloride salts.

A globally-applicable covariance matrix was calculated for THEMIS daytime infrared images, which can be used to calculate globally-consistent decorrelation stretched images and principal component images. This not only enabled the development of an improved method for identifying chloride salt deposits, but it will also enable future researchers to more easily access the compositional data within the THEMIS infrared dataset.

The updated global survey of chloride salt deposits, which was based on the new THEMIS Principal Component Chloride Index, located 1,605 deposits, which represents a 250% increase in the number of known Martian chloride salt deposits. This catalog will provide current and future mission planners with an improved list of remote sensing targets, the data from which will aid future researchers in studying the full diversity of chloride salt deposits on Mars.

By examining all 257 chloride salt deposits in Early Noachian terrains, three distinct types were observed, which all have characteristics indicating that the chloride salts formed during the Early Noachian contemporaneously with the surrounding terrain. These deposits provide important insights about a geologic era that has largely been erased from the surfaces of both Earth and Mars.

In particular, a unique three-dimensional chloride salt structure was identified on the floor of Ares Vallis that has been interpreted as an exposed chloride salt diapir. If this interpretation is correct, it requires the existence of a substantial chloride salt layer more than a kilometer below the surrounding Early and Middle Noachian terrains, which would place its formation during the Pre-Noachian period. This is consistent with the results of other investigators who have independently come to the same conclusion regarding a large-scale subsurface chloride salt layer in the surrounding region.

In the process of completing this work, a previously undescribed population of 4,024 small young impact craters surrounded by low thermal inertia ejecta deposits were identified, which were determined to be the result of relatively low-velocity secondary impacts from the oblique young rayed crater impacts.

Additionally, the completed THEMIS Daytime Infrared Global Mosaic, which served as the foundation of this work, was printed on a basketball court-sized vinyl mat so students and the general public could physically explore the full resolution of the map. An assessment study demonstrated that the "Walk on Mars" map and its associated lessons are effective tools for teaching junior high school students about the geography of Mars and the history of Mars exploration.

By improving our understanding of the distribution and diversity of chloride salts on the Martian surface, this work has provided future investigators with new tools and avenues of research to explore the history of water on Mars.

REFERENCES

Abramov, O., & Mojzsis, S. J. (2009). Microbial habitability of the Hadean Earth during the late heavy bombardment. Nature, 459(7245), 419–422. https://doi.org/10.1038/nature08015.

Acuña, M., Connerney, J., Wasilewski, P., Lin, R., Anderson, K., Carlson, C., McFadden, J., Curtis, D., Reme, H., Cros, A., & others. (1992). Mars Observer magnetic fields investigation. Journal of Geophysical Research: Planets, 97(E5), 7799–7814.

Alley, R. (1996). Algorithm theoretical basis document for decorrelation stretch decorrelation stretch AST06. Manuscrito, Jet Propulsion Laboratory, Pasadena.

Anderson, J. A., Sides, S. C., Soltesz, D. L., Sucharski, T. L., & Becker, K. J. (2004). Modernization of the Integrated Software for Imagers and Spectrometers. In S. Mackwell & E. Stansbery (Eds.), Lunar and Planetary Science Conference (p. 2039).

Andrews-Hanna, J. C. (2009). A mega-landslide on Mars. Nature Geoscience, 2(4), 248–249. https://doi.org/10.1038/ngeo483.

Anthamatten, P., Bryant, L. M., Ferrucci, B. J., Jennings, S., & Theobald, R. (2018). Giant maps as pedagogical tools for teaching geography and mathematics. Journal of Geography, 117(5), 183–192.

Arizona Geographic Alliance, Arizona Giant Floor Map. Accessed 25 October 2021, https://geoalliance.asu.edu/GiantTravelingMap/.

Bandfield, J. L., Rogers, D., Smith, M. D., & Christensen, P. R. (2004). Atmospheric correction and surface spectral unit mapping using Thermal Emission Imaging System data. Journal of Geophysical Research: Planets, 109(E10).

Bandfield, J. L., Ghent, R. R., Vasavada, A. R., Paige, D. A., Lawrence, S. J., & Robinson, M. S. (2011). Lunar surface rock abundance and regolith fines temperatures derived from LRO Diviner Radiometer data. Journal of Geophysical Research: Planets, 116(E12).

Bandfield, J. L., Song, E., Hayne, P. O., Brand, B. D., Ghent, R. R., Vasavada, A. R., & Paige, D. A. (2014). Lunar cold spots: Granular flow features and extensive insulating materials surrounding young craters. Icarus, 231, 221–231.

Bardar, E. M., Prather, E. E., Brecher, K., & Slater, T. F. (2007). Development and validation of the light and spectroscopy concept inventory. Astronomy Education Review, 5(2), 103–113.

Becker, K. J., Anderson, J. A., Weller, L. A., & Becker, T. L. (2013). ISIS support for NASA mission instrument ground data processing systems. Lunar and Planetary Science Conference, 44, 2829.

Bell, E. A., Boehnke, P., Harrison, T. M., & Mao, W. L. (2015). Potentially biogenic carbon preserved in a 4.1 billion-year-old zircon. Proceedings of the National Academy of Sciences, 112(47), 14518–14521.

Bell, I., J. F., Malin, M. C., Caplinger, M. A., Fahle, J., Wolff, M. J., Cantor, B. A., James, P. B., Ghaemi, T., Posiolova, L. V., Ravine, M. A., Supulver, K. D., Calvin, W. M., Clancy, R. T., Edgett, K. S., Edwards, L. J., Haberle, R. M., Hale, A., Lee, S. W., Rice, M. S., … Williams, R. M. E. (2013). Calibration and Performance of the Mars Reconnaissance Orbiter Context Camera (CTX). International Journal of Mars Science and Exploration, 8, 1–14. https://doi.org/10.1555/mars.2013.0001.

Benz, W., Slattery, W., & Cameron, A. (1986). The origin of the Moon and the single-impact hypothesis I. Icarus, 66(3), 515–535.

Boynton, W., Feldman, W., Mitrofanov, I., Evans, L., Reedy, R., Squyres, S., Starr, R., Trombka, J., d'Uston, C., Arnold, J., & others. (2004). The Mars Odyssey gamma-ray spectrometer instrument suite. Space Science Reviews, 110(1), 37–83.

Boynton, W., Taylor, G., Evans, L. G., Reedy, R., Starr, R., Janes, D., Kerry, K., Drake, D., Kim, K., Williams, R., & others. (2007). Concentration of H, Si, Cl, K, Fe, and Th in the low-and mid-latitude regions of Mars. Journal of Geophysical Research: Planets, 112(E12).

Buchanan, L. B., Tschida, C. M., & Brown, S. N. (2016). Integrating mapping and ELA skills using giant traveling maps. Social Studies and the Young Learner, 29(2), 21–27.

Byrne, S., Dundas, C. M., Kennedy, M. R., Mellon, M. T., McEwen, A. S., Cull, S. C., Daubar, I. J., Shean, D. E., Seelos, K. D., Murchie, S. L., & others. (2009). Distribution of mid-latitude ground ice on Mars from new impact craters. Science, 325(5948), 1674–1676.

Calef III, F. J., Herrick, R. R., & Sharpton, V. L. (2009). Geomorphic analysis of small rayed craters on Mars: Examining primary versus secondary impacts. Journal of Geophysical Research: Planets, 114(E10).

Christensen, P. R., Bandfield, J. L., Hamilton, V. E., Ruff, S. W., Kieffer, H. H., Titus, T. N., Malin, M. C., Morris, R. V., Lane, M. D., Clark, R., & others. (2001). Mars Global Surveyor Thermal Emission Spectrometer experiment: Investigation description and surface science results. Journal of Geophysical Research: Planets, 106(E10), 23823–23871.

Christensen, P.R., Engle, E., Anwar, S., Dickenshied, S., Noss, D., Gorelick, N., Weiss-Malik, M., JMARS – A Planetary GIS, http://adsabs.harvard.edu/abs/2009AGUFMIN22A..06C.

Christensen, P. R., Fergason, R. L., Edwards, C. S., & Hill, J. (2013). THEMIS-Derived Thermal Inertia Mosaic of Mars: Product Description and Science Results. 44th Annual Lunar and Planetary Science Conference, 2822.

Christensen, P. R., Jakosky, B. M., Kieffer, H. H., Malin, M. C., McSween, H. Y., Nealson, K., Mehall, G. L., Silverman, S. H., Ferry, S., Caplinger, M., & Ravine, M. (2004). The Thermal Emission Imaging System (THEMIS) for the Mars 2001 Odyssey Mission. Space Science Reviews, 110(1), 85–130. https://doi.org/10.1023/B:SPAC.0000021008.16305.94.

Connerney, J., Acuña, M., Ness, N., Kletetschka, G., Mitchell, D., Lin, R., & Reme, H. (2005). Tectonic implications of Mars crustal magnetism. Proceedings of the National Academy of Sciences, 102(42), 14970–14975.

Crocker, L., & Algina, J. (1986). Introduction to classical and modern test theory. ERIC.

Daubar, I. J., Dundas, C. M., Byrne, S., Geissler, P., Bart, G., McEwen, A. S., Russell, P. S., Chojnacki, M., & Golombek, M. (2016). Changes in blast zone albedo patterns around new martian impact craters. Icarus, 267, 86–105.

Daubar, I., McEwen, A. S., Byrne, S., Kennedy, M., & Ivanov, B. (2013). The current martian cratering rate. Icarus, 225(1), 506–516.

Edwards, C., Christensen, P., & Hill, J. (2011). Mosaicking of global planetary image datasets: 2. Modeling of wind streak thicknesses observed in Thermal Emission Imaging System (THEMIS) daytime and nighttime infrared data. Journal of Geophysical Research: Planets, 116(E10).

Edwards, C., Nowicki, K., Christensen, P., Hill, J., Gorelick, N., & Murray, K. (2011). Mosaicking of global planetary image datasets: 1. Techniques and data processing for Thermal Emission Imaging System (THEMIS) multi-spectral data. Journal of Geophysical Research: Planets, 116(E10).

Ellison, R. A., Thomas, R. J., Jacobs, J., & Pharaoh, T. C. (2021). Anatomy and uplift history of the emergent salt domes of the United Arab Emirates. Arabian Journal of Geosciences, 15(1), 23. https://doi.org/10.1007/s12517-021-09034-7.

Ericksen, G. E. (1983). The Chilean Nitrate Deposits: The origin of the Chilean nitrate deposits, which contain a unique group of saline minerals, has provoked lively discussion for more than 100 years. American Scientist, 71(4), 366–374.

Farmer, J. D., & Des Marais, D. J. (1999). Exploring for a record of ancient Martian life. Journal of Geophysical Research: Planets, 104(E11), 26977–26995.

Fergason, R., Hare, T., & Laura, J. (2018). HRSC and MOLA blended digital elevation model at 200m v2, astrogeology PDS annex. US Geological Survey.

Fergason, R. L., Christensen, P. R., & Kieffer, H. H. (2006). High-resolution thermal inertia derived from the Thermal Emission Imaging System (THEMIS): Thermal model and applications. Journal of Geophysical Research: Planets, 111(E12).

Frey, H. (2006). Impact constraints on, and a chronology for, major events in early Mars history. Journal of Geophysical Research: Planets, 111(E8).

Galofre, A. G., Jellinek, A. M., & Osinski, G. R. (2020). Valley formation on early Mars by subglacial and fluvial erosion. Nature Geoscience, 13(10), 663–668.

Garry, W. B. @VolcanoCowboy. Accessed 22 March 2018, https://www.twitter.com/volcanocowboy.

Gault, D. E., Shoemaker, E. M., & Moore, H. J. (1963). Spray ejected from the lunar surface by meteoroid impact. National Aeronautics and Space Administration.

Gault, D. E., & Wedekind, J. A. (1978). Experimental studies of oblique impact. Lunar and Planetary Science Conference Proceedings, 9, 3843–3875.

Ghent, R. R., Gupta, V., Campbell, B. A., Ferguson, S., Brown, J., Fergason, R., & Carter, L. M. (2010). Generation and emplacement of fine-grained ejecta in planetary impacts. Icarus, 209(2), 818–835.

Gillespie, A. R., Kahle, A. B., & Walker, R. E. (1986). Color enhancement of highly correlated images. I. Decorrelation and HSI contrast stretches. Remote Sensing of Environment, 20(3), 209–235.

Greeley, R., Thompson, S., Whelley, P., Squyres, S., Neukum, G., Arvidson, R., Malin, M., Kuzmin, R., Christensen, P., & Rafkin, S. (2004). Coordinated observations of aeolian features from the Mars Exploration Rovers (MER) and the Mars

Express High Resolution Stereo Camera and other orbiters. Lunar and Planetary Science XXXV: Mars Missions.

Hake, R. R. (1998). Interactive-engagement versus traditional methods: A six-thousand-student survey of mechanics test data for introductory physics courses. American Journal of Physics, 66(1), 64–74.

Harrison, T. M. (2009). The Hadean Crust: Evidence from >4 Ga Zircons. Annual Review of Earth and Planetary Sciences, 37(1), 479–505. https://doi.org/10.1146/annurev.earth.031208.100151.

Hartmann, W. K. (1985). Impact experiments: 1. Ejecta velocity distributions and related results from regolith targets. Icarus, 63(1), 69–98.

Hartmann, W. K., Ryder, G., Dones, L., & Grinspoon, D. (2000). The Time-Dependent Intense Bombardment of the Primordial Earth/Moon System. In R. M. Canup, K. Righter, & et al. (Eds.), Origin of the Earth and Moon (pp. 493–512).

Hill, J., Edwards, C., & Christensen, P. (2014). Mapping the Martian surface with THEMIS global infrared mosaics. Eighth International Conference on Mars, 1791, 1141.

Hill, J. R., & Christensen, P. R. (2014). Identification and Characterization of Well-Preserved Impact Ejecta Deposits Using THEMIS Global Infrared Mosaics. AGU Fall Meeting Abstracts, 2014, P33A-4028.

Hill, J., & Christensen, P. (2017). Well-preserved low thermal inertia ejecta deposits surrounding young secondary impact craters on Mars. Journal of Geophysical Research: Planets, 122(6), 1276–1299.

Hill, J. R., & Christensen, P. R. (2019). Applying the THEMIS Quasi-Spectral Chloride Index to the Martian Southern Highlands. 50th Annual Lunar and Planetary Science Conference, 3213.

Hill, J. R., & Christensen, P. R. (2022). Visualizing the Maximum Compositional Variation within the Themis Multispectral Thermal Infrared Dataset, in prep.

Hill, J. R., & Christensen, P. R. (2022). A Principal Component Index for Identifying Chloride Minerals Using Themis Multispectral Thermal Infrared Images, in prep.

Hotelling, H. (1933). Analysis of a complex of statistical variables into principal components. Journal of Educational Psychology, 24(6), 417.

Hotelling, H. (1936). Relations between two sets of variates. Biometrika, 28(3/4), 321–377.

Jaumann, R., Neukum, G., Behnke, T., Duxbury, T. C., Eichentopf, K., Flohrer, J., Gasselt, S., Giese, B., Gwinner, K., Hauber, E., & others. (2007). The high-resolution stereo camera (HRSC) experiment on Mars Express: Instrument aspects and experiment conduct from interplanetary cruise through the nominal mission. Planetary and Space Science, 55(7–8), 928–952.

Jet Propulsion Laboratory, Solar System Ambassadors. Accessed 25 October 2021, https://solarsystem.nasa.gov/solar-system-ambassadors/events/.

Kadoya, S., Krissansen-Totton, J., & Catling, D. C. (2020). Probable cold and alkaline surface environment of the Hadean Earth caused by impact ejecta weathering. Geochemistry, Geophysics, Geosystems, 21(1), e2019GC008734.

Kieffer, H. H., Martin, T., Peterfreund, A. R., Jakosky, B. M., Miner, E. D., & Palluconi, F. D. (1977). Thermal and albedo mapping of Mars during the Viking primary mission. Journal of Geophysical Research, 82(28), 4249–4291.

Kite, E. S., & Mayer, D. P. (2017). Mars sedimentary rock erosion rates constrained using crater counts, with applications to organic-matter preservation and to the global dust cycle. Icarus, 286, 212–222.

Kranitz, R. A. (2018). The Effect of the State Giant Traveling Map of Montana on the Geographic Literacy of Fourth Graders in Western Montana.

Lucchitta, B., Ferguson, H., & Summers, C. (1987). Northern sinks on Mars? Martian Geomorphology and Its Relation to Subsurface Volatiles, 32.

Maher, K. A., & Stevenson, D. J. (1988). Impact frustration of the origin of life. Nature, 331(6157), 612–614.

Malin, M. C., Edgett, K. S., Posiolova, L. V., McColley, S. M., & Dobrea, E. Z. N. (2006). Present-day impact cratering rate and contemporary gully activity on Mars. Science, 314(5805), 1573–1577.

Malin, M. C., Bell, J. F., Cantor, B. A., Caplinger, M. A., Calvin, W. M., Clancy, R. T., Edgett, K. S., Edwards, L., Haberle, R. M., James, P. B., & others. (2007). Context camera investigation on board the Mars Reconnaissance Orbiter. Journal of Geophysical Research: Planets, 112(E5).

McEwen, A. S., Preblich, B. S., Turtle, E. P., Artemieva, N. A., Golombek, M. P., Hurst, M., Kirk, R. L., Burr, D. M., & Christensen, P. R. (2005). The rayed crater Zunil and interpretations of small impact craters on Mars. Icarus, 176(2), 351–381.

McEwen, A. S., Eliason, E. M., Bergstrom, J. W., Bridges, N. T., Hansen, C. J., Delamere, W. A., Grant, J. A., Gulick, V. C., Herkenhoff, K. E., Keszthelyi, L., &

others. (2007). Mars reconnaissance orbiter's high resolution imaging science experiment (HiRISE). Journal of Geophysical Research: Planets, 112(E5).

McGill, G. E., & Wise, D. U. (1972). Regional variations in degradation and density of Martian craters. Journal of Geophysical Research, 77(14), 2433–2441.

Michael, G. G., & Neukum, G. (2010). Planetary surface dating from crater size–frequency distribution measurements: Partial resurfacing events and statistical age uncertainty. Earth and Planetary Science Letters, 294(3), 223–229. https://doi.org/10.1016/j.epsl.2009.12.041

Montgomery, D. R., Som, S. M., Jackson, M. P., Schreiber, B. C., Gillespie, A. R., & Adams, J. B. (2009). Continental-scale salt tectonics on Mars and the origin of Valles Marineris and associated outflow channels. Geological Society of America Bulletin, 121(1–2), 117–133.

National Geographic Society, Giant Maps: Bring Geography to Your School in a Giant Way. Accessed 25 October 2021, https://www.nationalgeographic.org/education/giant-maps/.

Neukum, G., & Jaumann, R. (2004). HRSC: The high resolution stereo camera of Mars Express. Mars Express: The Scientific Payload, 1240, 17–35.

Nimmo, F., & Kleine, T. (2007). How rapidly did Mars accrete? Uncertainties in the Hf–W timing of core formation. Icarus, 191(2), 497–504.

Nowicki, K., Edwards, C., & Christensen, P. (2013). Removal of salt-and-pepper noise in THEMIS infrared radiance and emissivity spectral data of the Martian surface. 2013 5th Workshop on Hyperspectral Image and Signal Processing: Evolution in Remote Sensing (WHISPERS), 1–4.

Nunnally, J. (1978). Psychometric Theory 2nd edition (New York: McGraw).

Osterloo, M., Hamilton, V., Bandfield, J., Glotch, T., Baldridge, A., Christensen, P., Tornabene, L., & Anderson, F. (2008). Chloride-bearing materials in the southern highlands of Mars. Science, 319(5870), 1651–1654.

Osterloo, M. M., Anderson, F. S., Hamilton, V. E., & Hynek, B. M. (2010). Geologic context of proposed chloride-bearing materials on Mars. Journal of Geophysical Research: Planets, 115(E10).

Paige, D., Foote, M., Greenhagen, B., Schofield, J., Calcutt, S., Vasavada, A., Preston, D., Taylor, F., Allen, C., Snook, K., & others. (2010). The lunar reconnaissance orbiter diviner lunar radiometer experiment. Space Science Reviews, 150(1), 125–160.

Pasachoff, J. M., Padilla, M. J., Cyr, M., & Miaoulis, I. (2005). Astronomy. Pearson Prentice Hall.

Pearson, K., & Lines, L. O. (1901). Planes of Closest Fit to Systems of Points in Space, London Edinburgh Dublin Philos. Mag. J. Sci, 2(11), 559–572.

Peters, J. M., Filbrandt, J. B., Grotzinger, J. P., Newall, M. J., Shuster, M. W., & Al-Siyabi, H. A. (2003). Surface-piercing salt domes of interior North Oman, and their significance for the Ara carbonate 'stringer'hydrocarbon play. GeoArabia, 8(2), 231–270.

Pierens, A., & Raymond, S. N. (2011). Two phase, inward-then-outward migration of Jupiter and Saturn in the gaseous solar nebula. Astronomy & Astrophysics, 533, A131.

Piqueux, S., & Christensen, P. R. (2011). Temperature-dependent thermal inertia of homogeneous Martian regolith. Journal of Geophysical Research: Planets, 116(E7).

Putzig, N. E., & Mellon, M. T. (2007). Apparent thermal inertia and the surface heterogeneity of Mars. Icarus, 191(1), 68–94.

Putzig, N. E., Mellon, M. T., Kretke, K. A., & Arvidson, R. E. (2005). Global thermal inertia and surface properties of Mars from the MGS mapping mission. Icarus, 173(2), 325–341.

Rech, J. A., Quade, J., & Hart, W. S. (2003). Isotopic evidence for the source of Ca and S in soil gypsum, anhydrite and calcite in the Atacama Desert, Chile. Geochimica et Cosmochimica Acta, 67(4), 575–586.

Reed, S. E., Kreylos, O., Hsi, S., Kellogg, L. H., Schladow, G., Yikilmaz, M. B., Segale, H., Silverman, J., Yalowitz, S., & Sato, E. (2014). Shaping watersheds exhibit: An interactive, augmented reality sandbox for advancing earth science education. AGU Fall Meeting Abstracts, 2014, ED34A-01.

Reed, S., Hsi, S., Kreylos, O., Yikilmaz, M., Kellogg, L., Schladow, S., Segale, H., & Chan, L. (2016). Augmented reality turns a sandbox into a geoscience lesson. Eos, 97, 18–22.

Richardson, R., Sammons, D., & Delparte, D. (2018). Augmented affordances support learning: Comparing the instructional effects of the augmented reality sandbox and conventional maps to teach topographic map skills. Journal of Interactive Learning Research, 29(2), 231–248.

Robinson, M., Brylow, S., Tschimmel, M., Humm, D., Lawrence, S., Thomas, P., Denevi, B., Bowman-Cisneros, E., Zerr, J., Ravine, M., & others. (2010). Lunar

reconnaissance orbiter camera (LROC) instrument overview. Space Science Reviews, 150(1), 81–124.

Rogers, A. D., & Christensen, P. R. (2007). Surface mineralogy of Martian low-albedo regions from MGS-TES data: Implications for upper crustal evolution and surface alteration. Journal of Geophysical Research: Planets, 112(E1).

Ruff, S. W., & Christensen, P. R. (2002). Bright and dark regions on Mars: Particle size and mineralogical characteristics based on Thermal Emission Spectrometer data. Journal of Geophysical Research: Planets, 107(E12), 2–1.

Schoof, C. (2010). Ice-sheet acceleration driven by melt supply variability. Nature, 468(7325), 803–806.

Schubert, B. A., Lowenstein, T. K., & Timofeeff, M. N. (2009). Microscopic identification of prokaryotes in modern and ancient halite, Saline Valley and Death Valley, California. Astrobiology, 9(5), 467–482.

Schubert, B. A., Lowenstein, T. K., Timofeeff, M. N., & Parker, M. A. (2010). Halophilic archaea cultured from ancient halite, Death Valley, California. Environmental Microbiology, 12(2), 440–454.

Schultz, P. H., & Gault, D. E. (1979). Atmospheric effects on Martian ejecta emplacement. Journal of Geophysical Research: Solid Earth, 84(B13), 7669–7687.

Schultz, P. H., & Quintana, S. N. (2017). Impact-generated winds on Mars. Icarus, 292, 86–101.

Scott, D. H., & MH, C. (1978). Geologic Map of Mars. Scale 1: 25 000 000.

Scott, R., Damon, M., Chastain, J., Wiig, K., & Daniels, J. (2015, September 30). The Martian.

ShareSpace Foundation, The, Giant Mars Map Program. Accessed 17 September 2019, https://sharespace.org/education/mars-maps/.

Shoemaker, E. M. (1960). Impact mechanics at Meteor Crater, Arizona. Princeton University.

Simon, M. N., Prather, E. E., Buxner, S. R., & Impey, C. D. (2019). The development and validation of the Planet Formation Concept Inventory. International Journal of Science Education, 41(17), 2448–2464.

Smith, D. E., Zuber, M. T., Frey, H. V., Garvin, J. B., Head, J. W., Muhleman, D. O., Pettengill, G. H., Phillips, R. J., Solomon, S. C., Zwally, H. J., & others. (2001).

Mars Orbiter Laser Altimeter: Experiment summary after the first year of global mapping of Mars. Journal of Geophysical Research: Planets, 106(E10), 23689–23722.

Smith, M. D. (2009). THEMIS observations of Mars aerosol optical depth from 2002–2008. Icarus, 202(2), 444–452. https://doi.org/10.1016/j.icarus.2009.03.027.

Soha, J., & Schwartz, A. (1979). Multispectral histogram normalization contrast enhancement. 5th Canadian Symposium on Remote Sensing, 86–93.

Swanson, J., Personal Communication. Swanson.J@kubin.com. 7 February 2018.

Tanaka, K. L. (1986). The stratigraphy of Mars. Journal of Geophysical Research: Solid Earth, 91(B13), E139–E158.

Tanaka, K., Skinner Jr, J., Dohm, J., Irwin III, R., Kolb, E., Fortezzo, C., Platz, T., Michael, G., & Hare, T. (2014). Geologic map of Mars: US geological survey scientific investigations map 3292. Scientific Investigations Map.

Tornabene, L. L., Moersch, J. E., McSween Jr, H. Y., McEwen, A. S., Piatek, J. L., Milam, K. A., & Christensen, P. R. (2006). Identification of large (2–10 km) rayed craters on Mars in THEMIS thermal infrared images: Implications for possible Martian meteorite source regions. Journal of Geophysical Research: Planets, 111(E10).

Tornabene, L., McEwen, A., & Team, H. (2008). Recent channel systems emanating from Hale crater ejecta: Implications for the Noachian landscape evolution of Mars. 39th Annual Lunar and Planetary Science Conference, 1391, 2180.

Warner, N., Gupta, S., Muller, J.-P., Kim, J.-R., & Lin, S.-Y. (2009). A refined chronology of catastrophic outflow events in Ares Vallis, Mars. Earth and Planetary Science Letters, 288(1–2), 58–69.

Watson, E. B., & Harrison, T. (2005). Zircon thermometer reveals minimum melting conditions on earliest Earth. Science, 308(5723), 841–844.

Weir, A. (2014). The Martian (First edition). Crown Publishers.

Werner, S., & Tanaka, K. (2011). Redefinition of the crater-density and absolute-age boundaries for the chronostratigraphic system of Mars. Icarus, 215(2), 603–607.

Woods, T. L., Reed, S., Hsi, S., Woods, J. A., & Woods, M. R. (2016). Pilot study using the augmented reality sandbox to teach topographic maps and surficial processes in introductory geology labs. Journal of Geoscience Education, 64(3), 199–214.

APPENDIX A

MARS GEOGRAPHY SCAVENGER HUNT

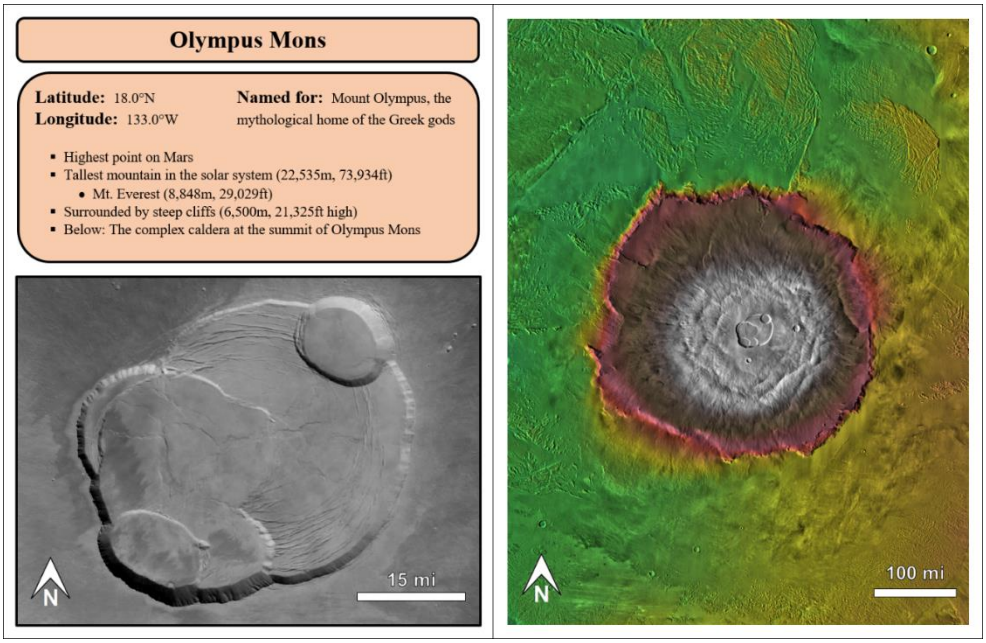

Figure A.1. Mars Geography Scavenger Hunt – Olympus Mons Entry

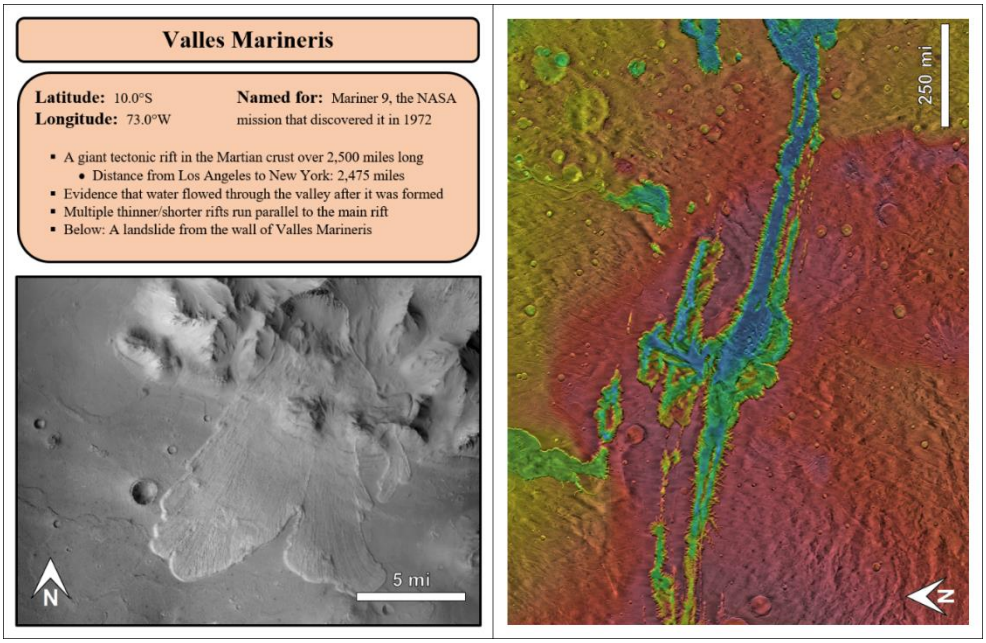

Figure A.2. Mars Geography Scavenger Hunt – Valles Marineris Entry

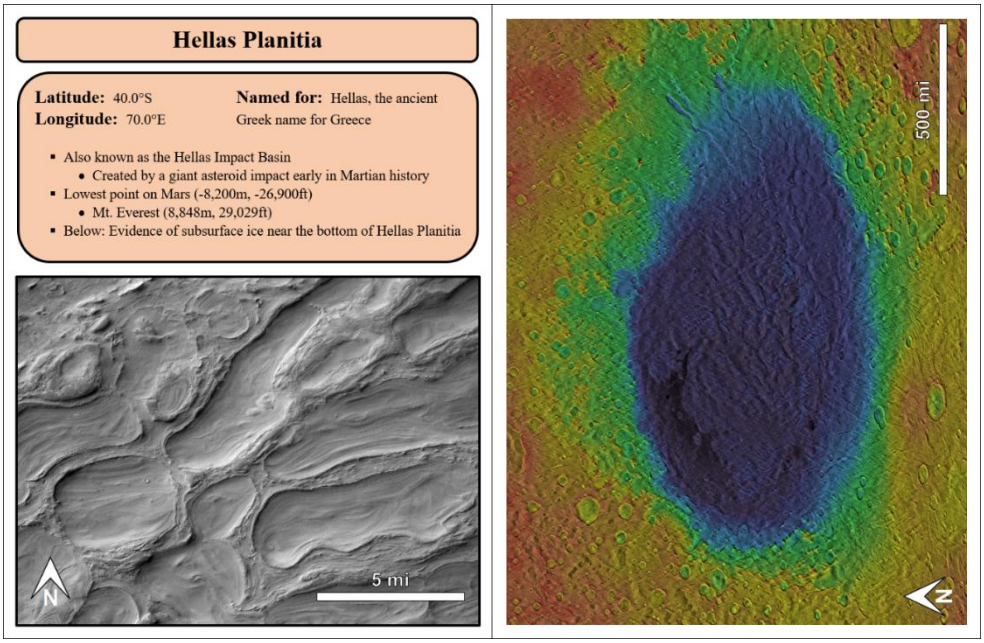

Figure A.3. Mars Geography Scavenger Hunt – Hellas Planitia Entry

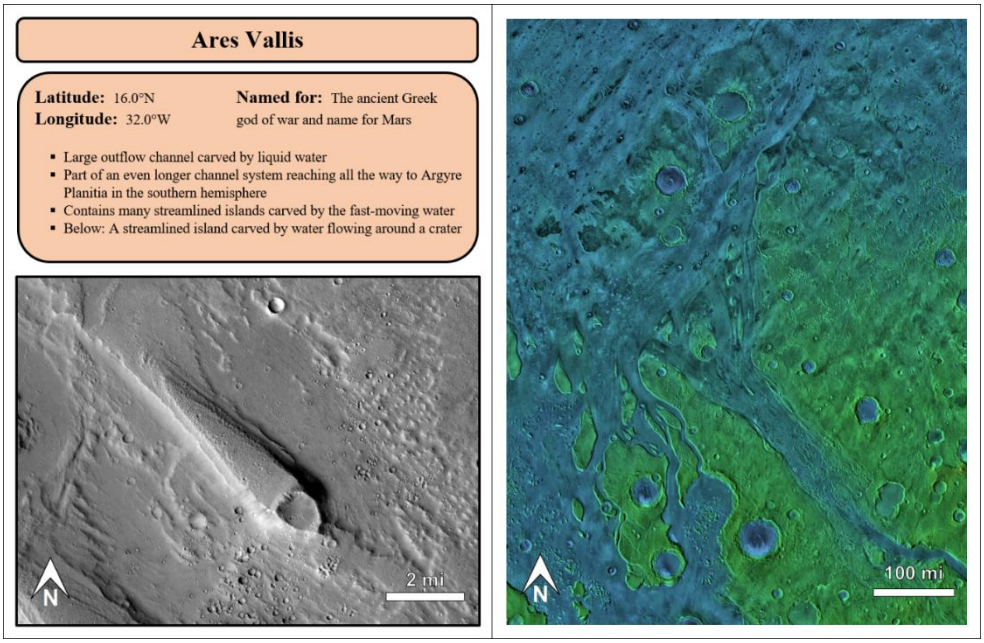

Figure A.4. Mars Geography Scavenger Hunt – Ares Vallis Entry

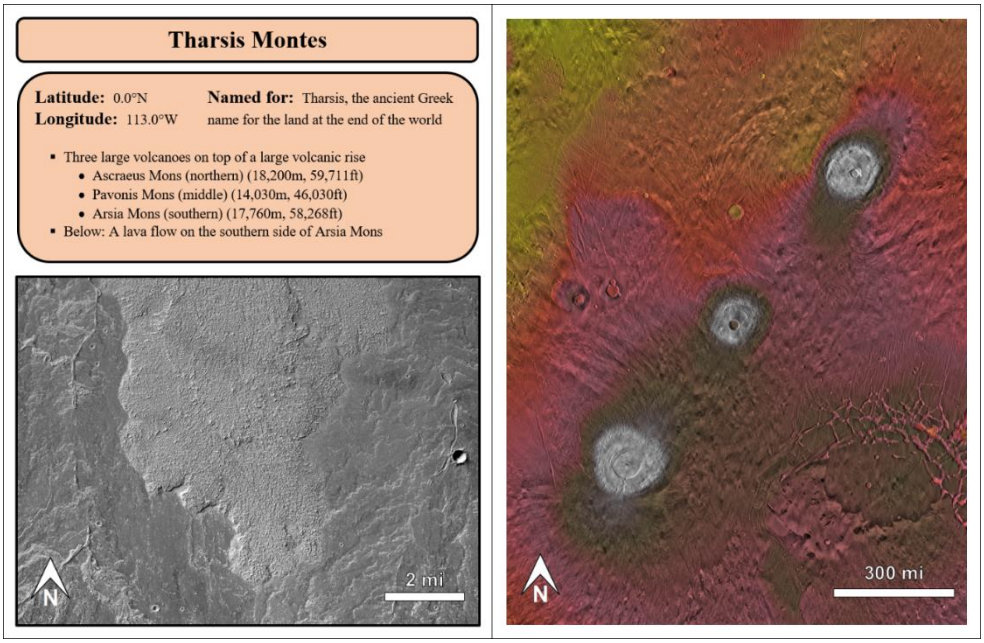

Figure A.5. Mars Geography Scavenger Hunt – Tharsis Montes Entry

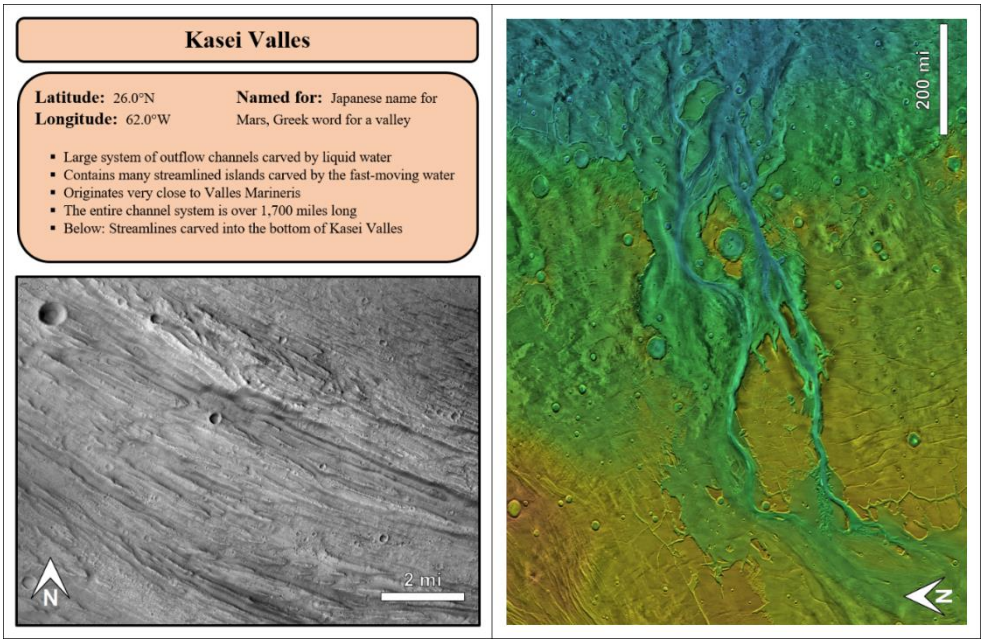

Figure A.6. Mars Geography Scavenger Hunt – Kasei Valles Entry

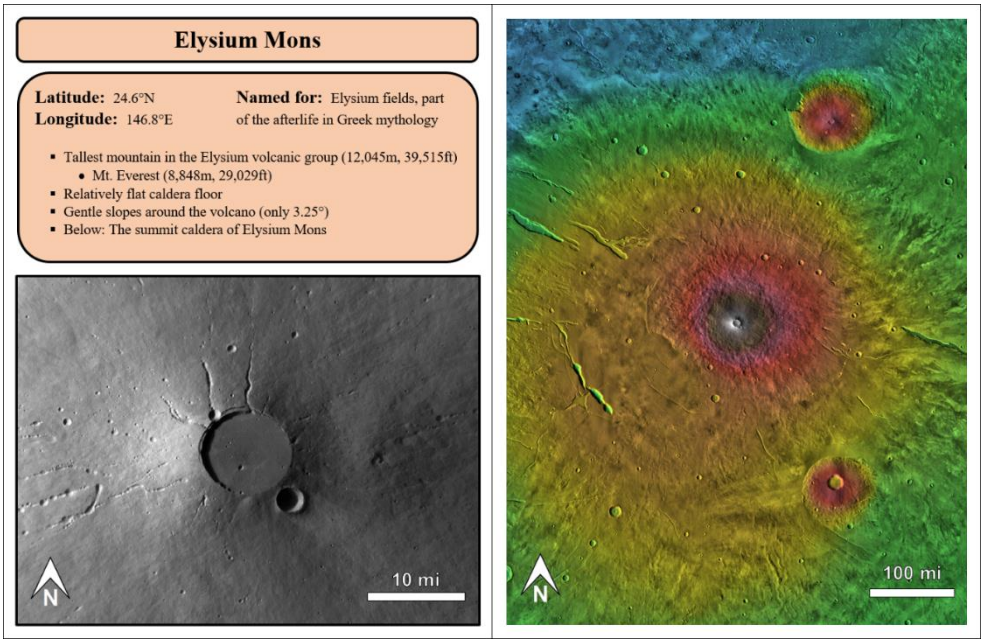

Figure A.7. Mars Geography Scavenger Hunt – Elysium Mons Entry

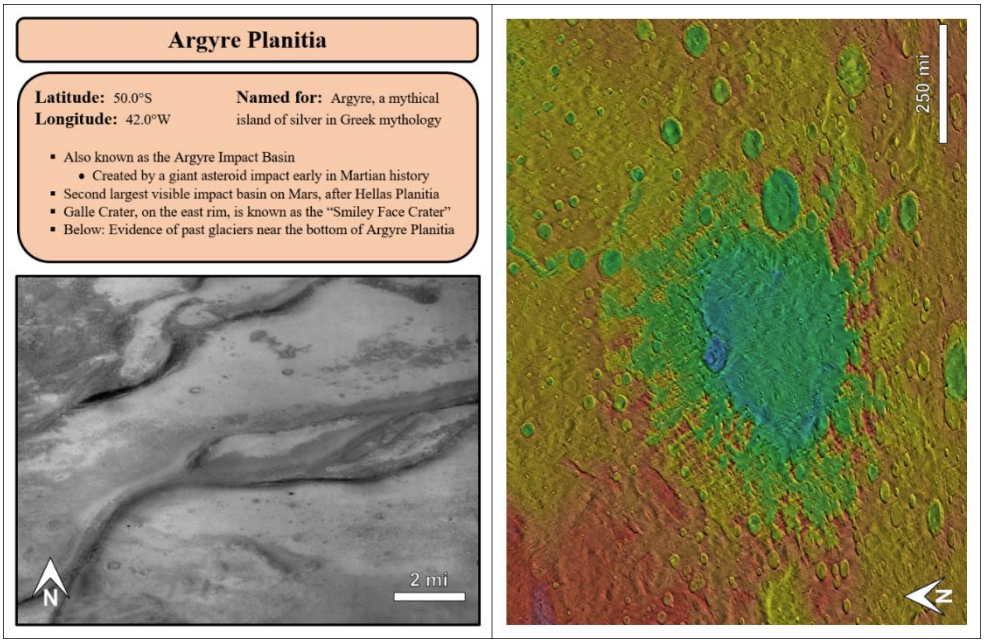

Figure A.8. Mars Geography Scavenger Hunt – Argyre Planitia Entry

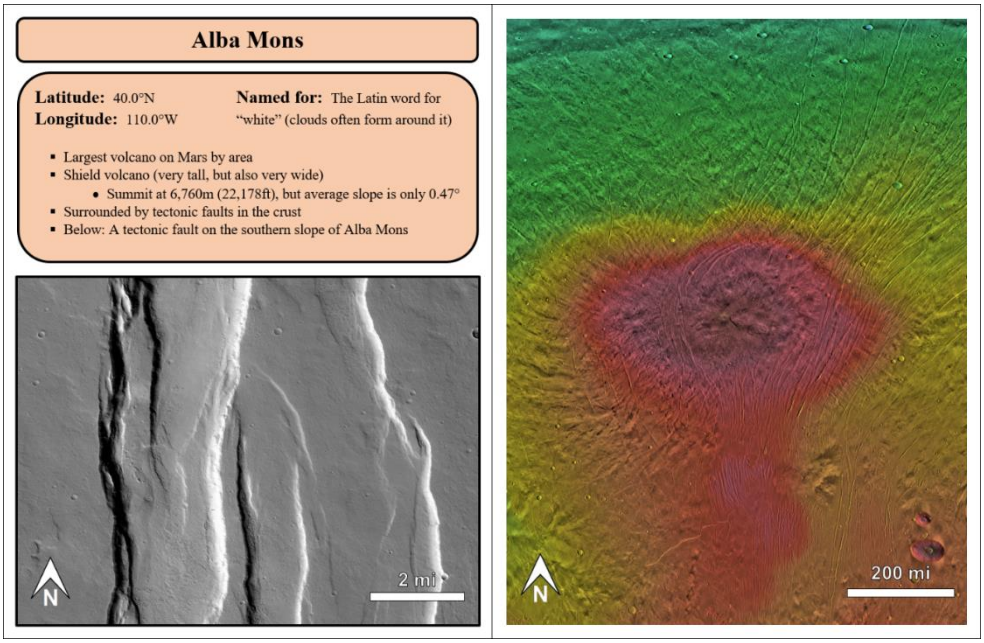

Figure A.9. Mars Geography Scavenger Hunt – Alba Mons Entry

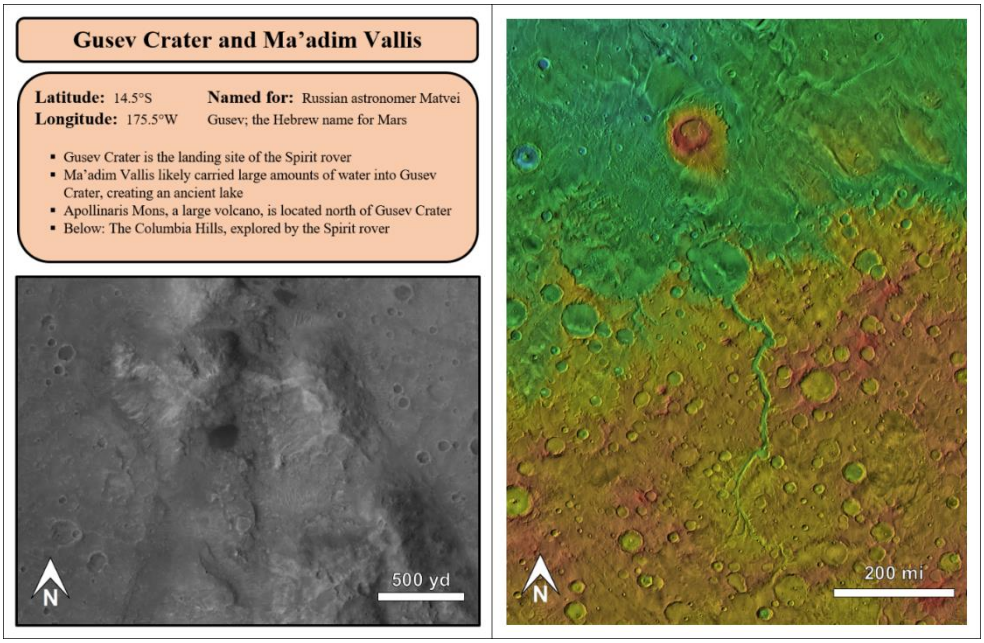

Figure A.10. Mars Geography Scavenger Hunt – Gusev Crater and Ma'adim Vallis Entry

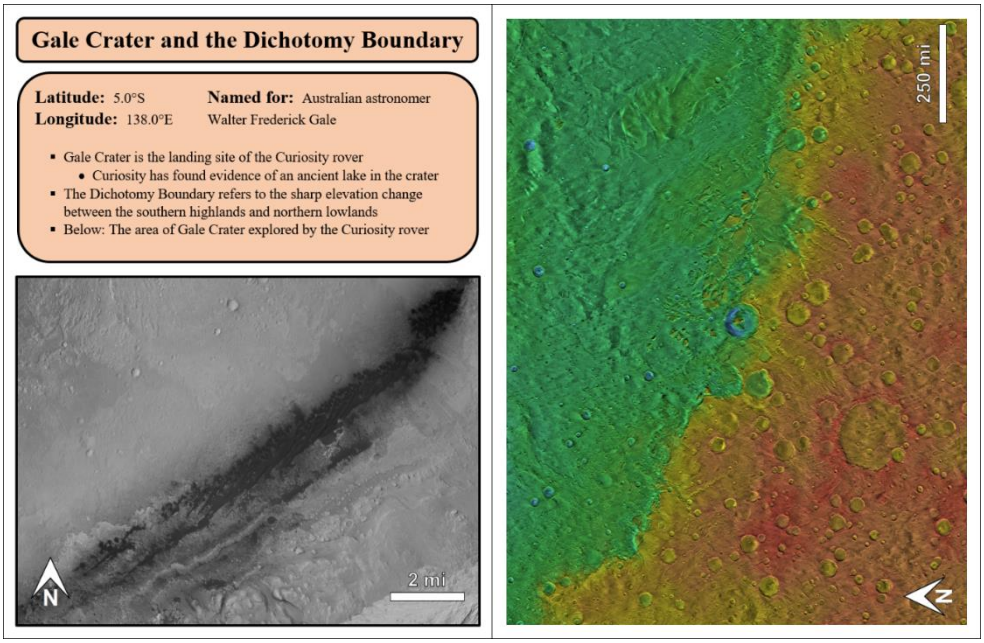

Figure A.11. Mars Geography Scavenger Hunt – Gale Crater and the Dichotomy Boundary Entry

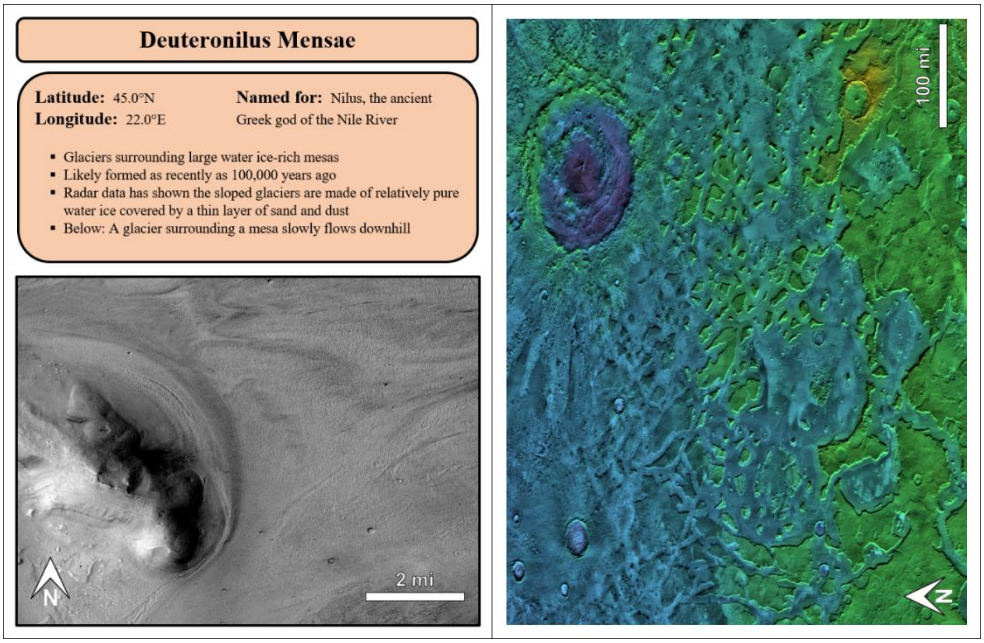

Figure A.12. Mars Geography Scavenger Hunt – Deuteronilus Mensae Entry

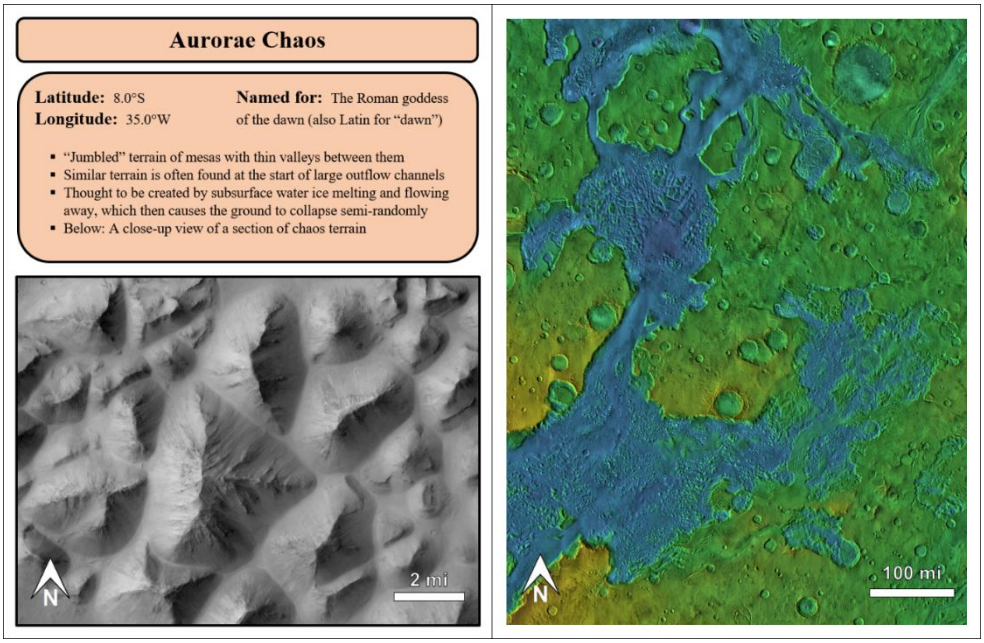

Figure A.13. Mars Geography Scavenger Hunt – Aurorae Chaos Entry

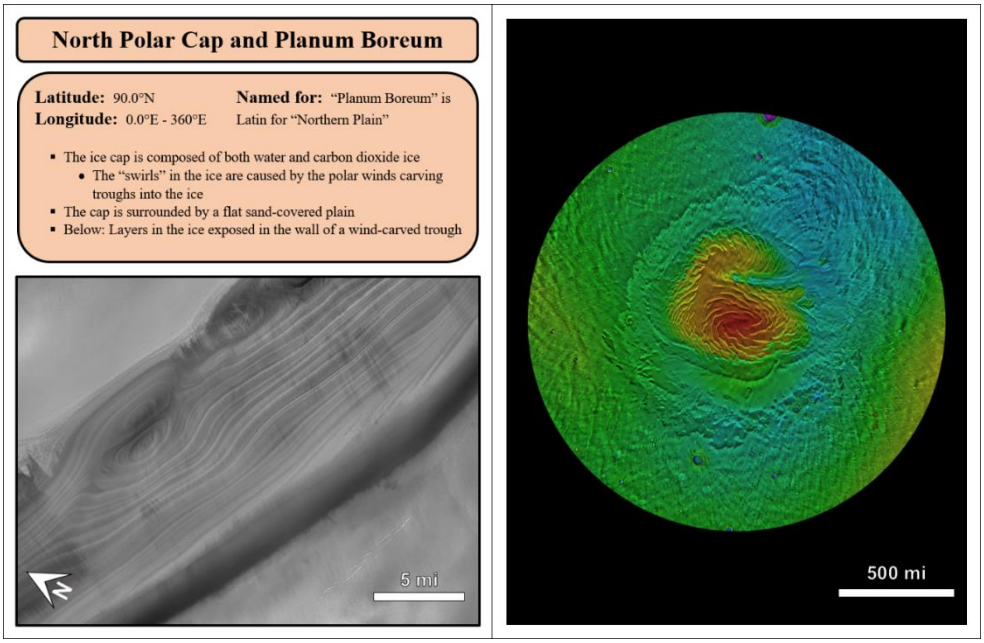

Figure A.14. Mars Geography Scavenger Hunt – North Polar Cap and Planum Boreum Entry

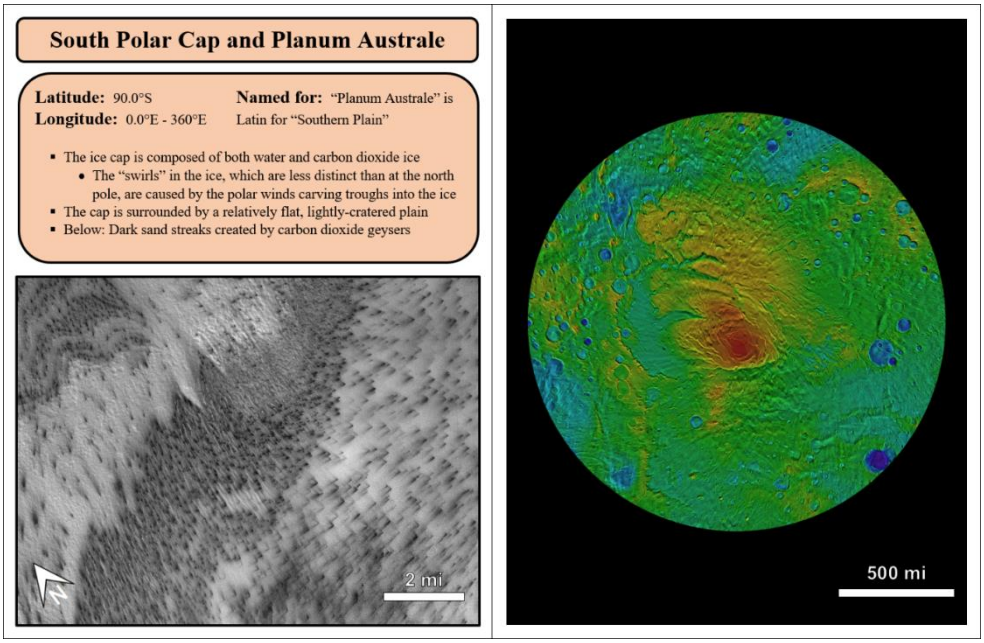

Figure A.15. Mars Geography Scavenger Hunt – South Polar Cap and Planum Australe Entry

APPENDIX B

MARS LANDING SITE SCAVENGER HUNT

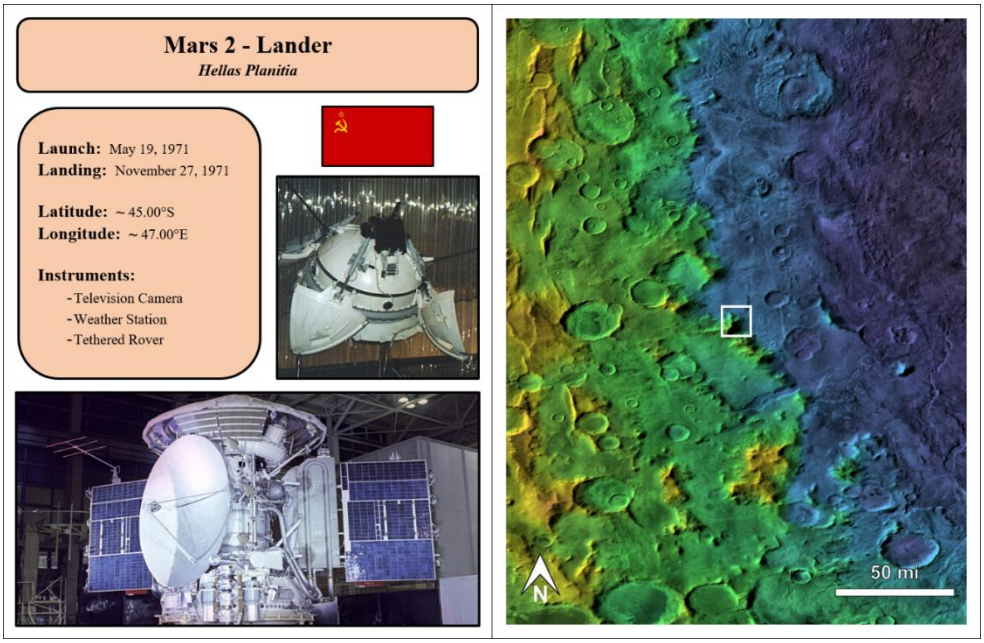

Figure B.1. Mars Landing Site Scavenger Hunt – Mars 2 Lander Entry

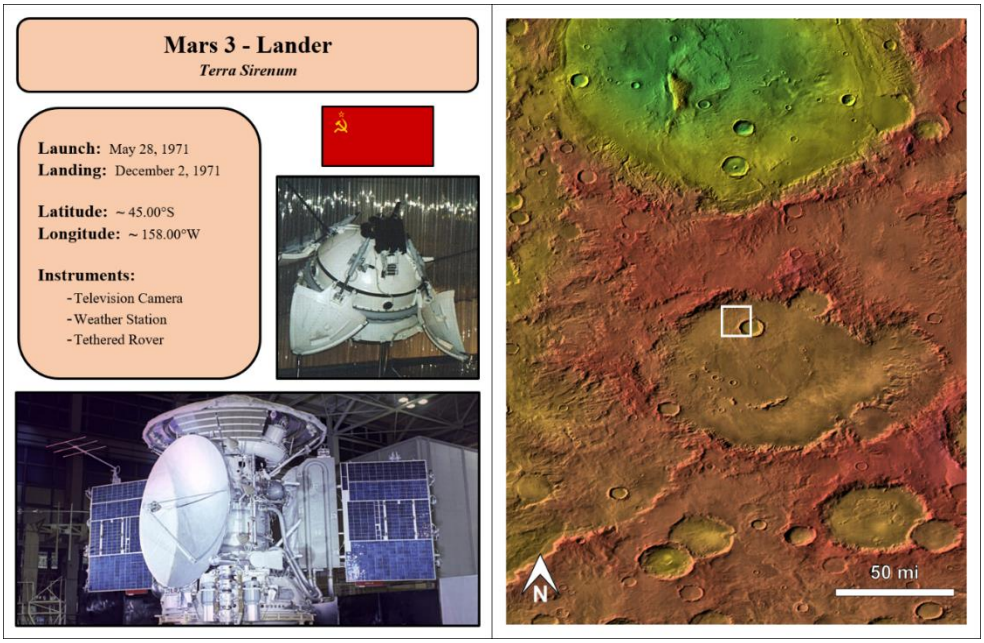

Figure B.2. Mars Landing Site Scavenger Hunt – Mars 3 Lander Entry

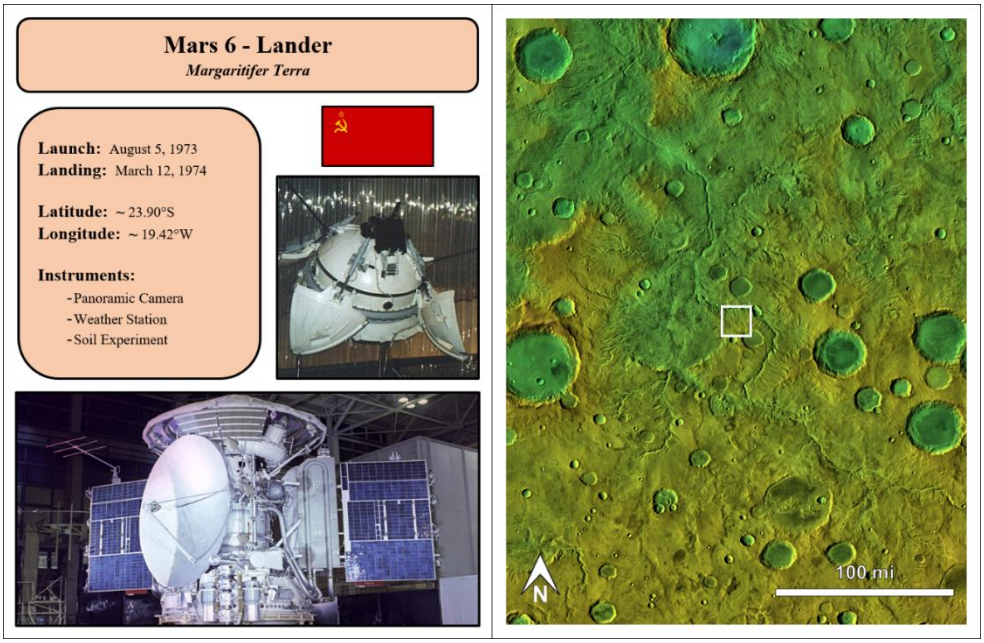

Figure B.3. Mars Landing Site Scavenger Hunt – Mars 6 Lander Entry

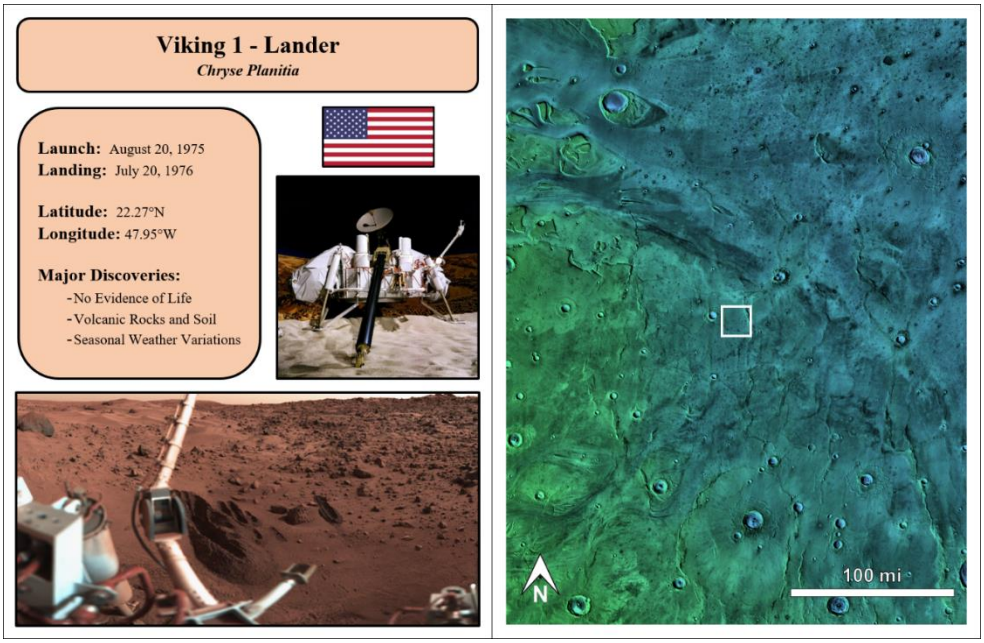

Figure B.4. Mars Landing Site Scavenger Hunt – Viking 1 Lander Entry

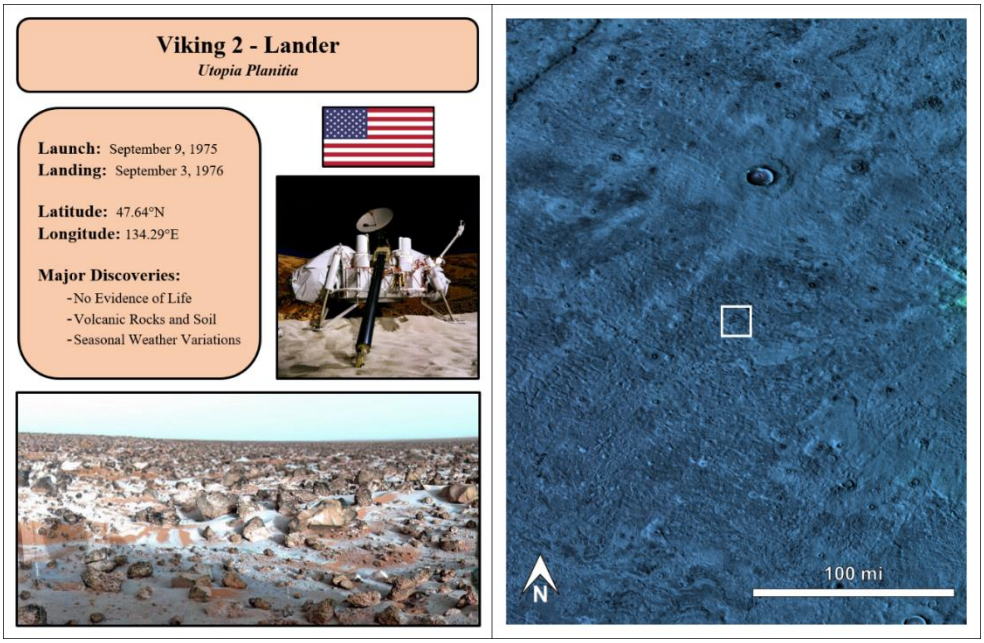

Figure B.5. Mars Landing Site Scavenger Hunt – Viking 2 Lander Entry

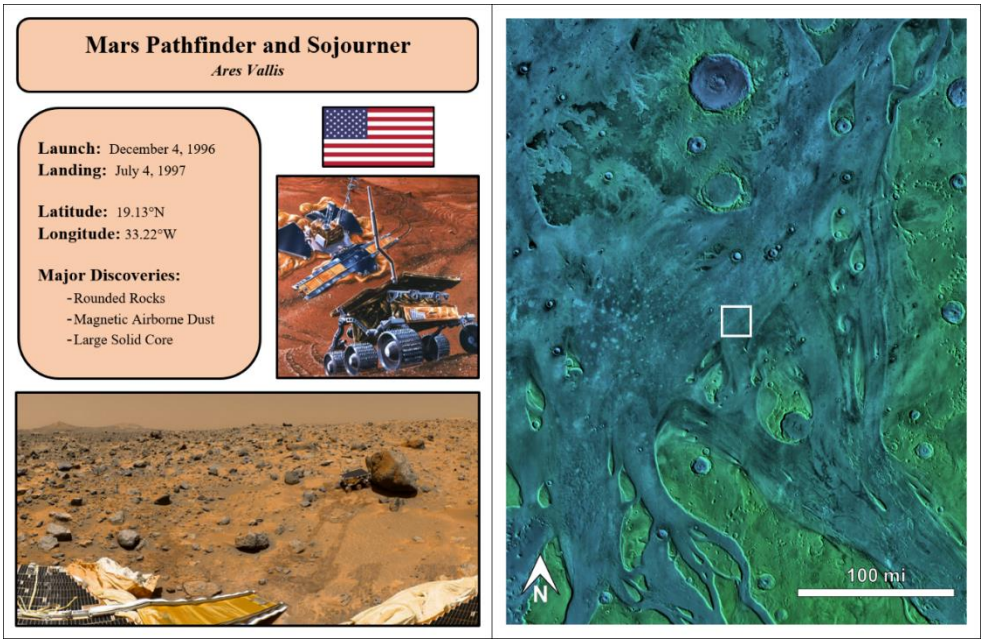

Figure B.6. Mars Landing Site Scavenger Hunt – Mars Pathfinder and Sojourner Entry

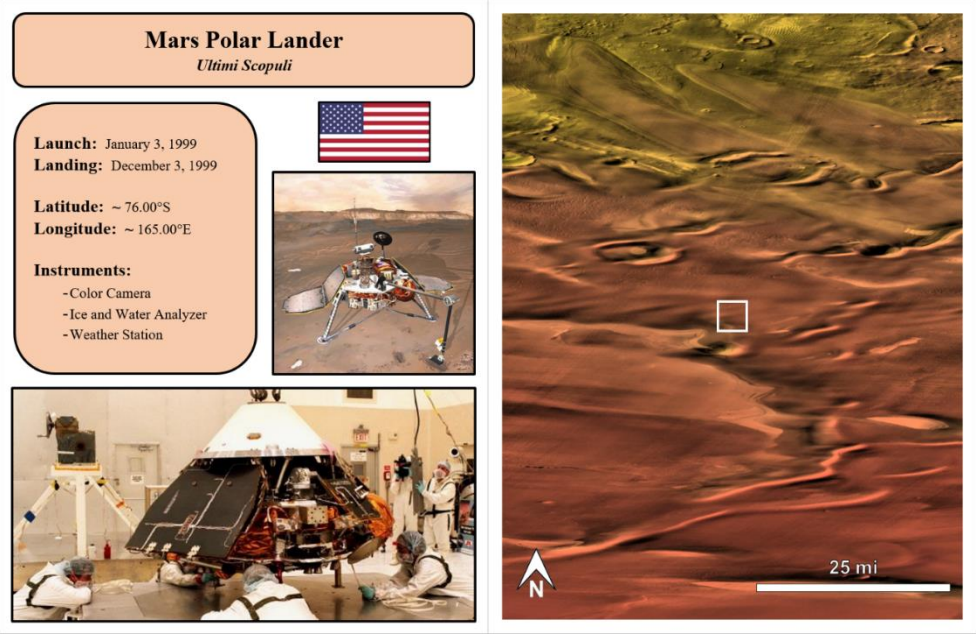

Figure B.7. Mars Landing Site Scavenger Hunt – Mars Polar Lander Entry

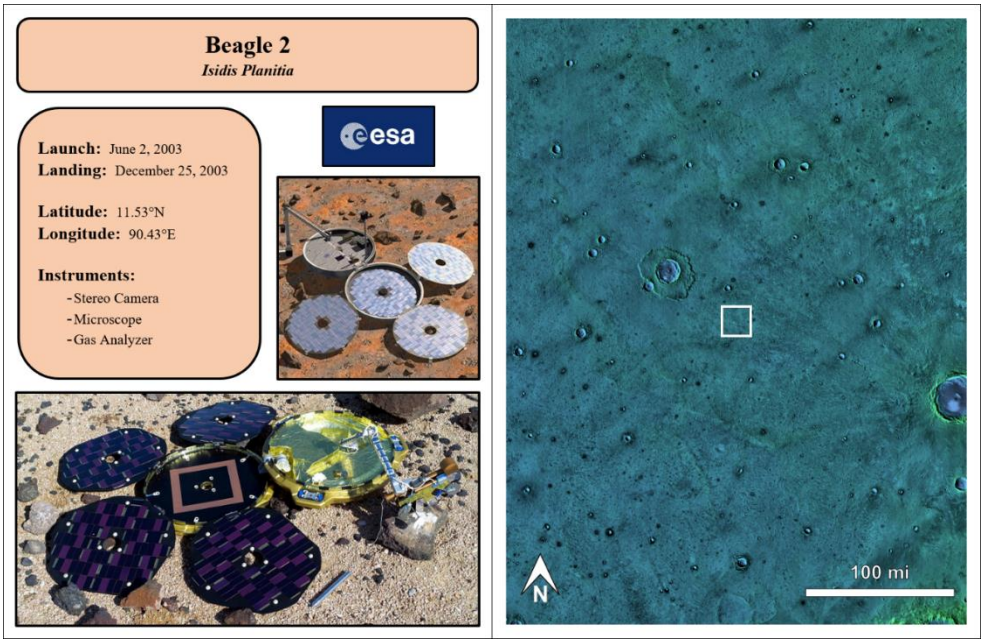

Figure B.8. Mars Landing Site Scavenger Hunt – Beagle 2 Entry

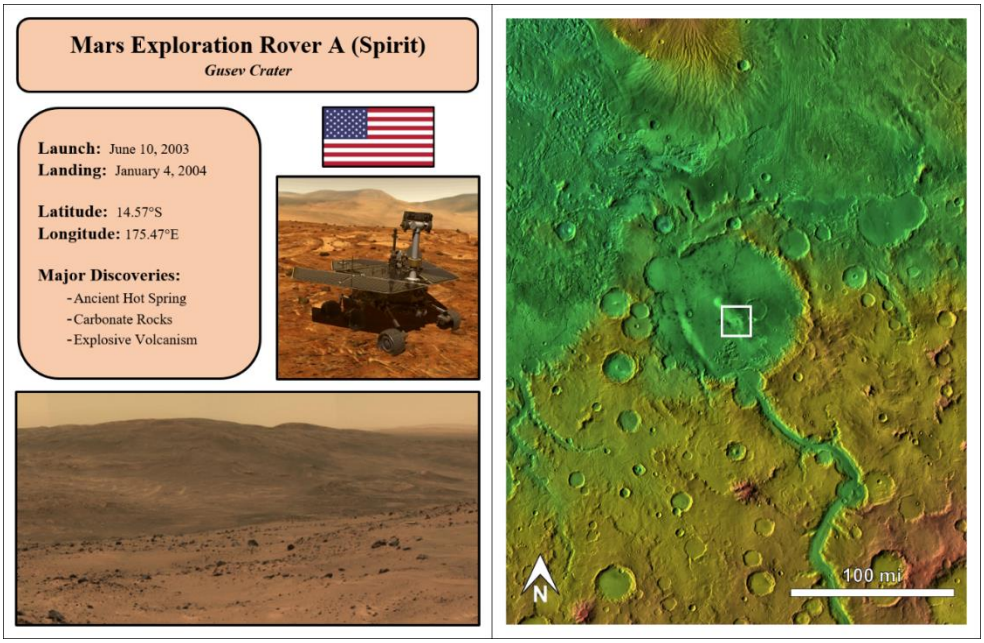

Figure B.9. Mars Landing Site Scavenger Hunt – Mars Exploration Rover A (Spirit) Entry

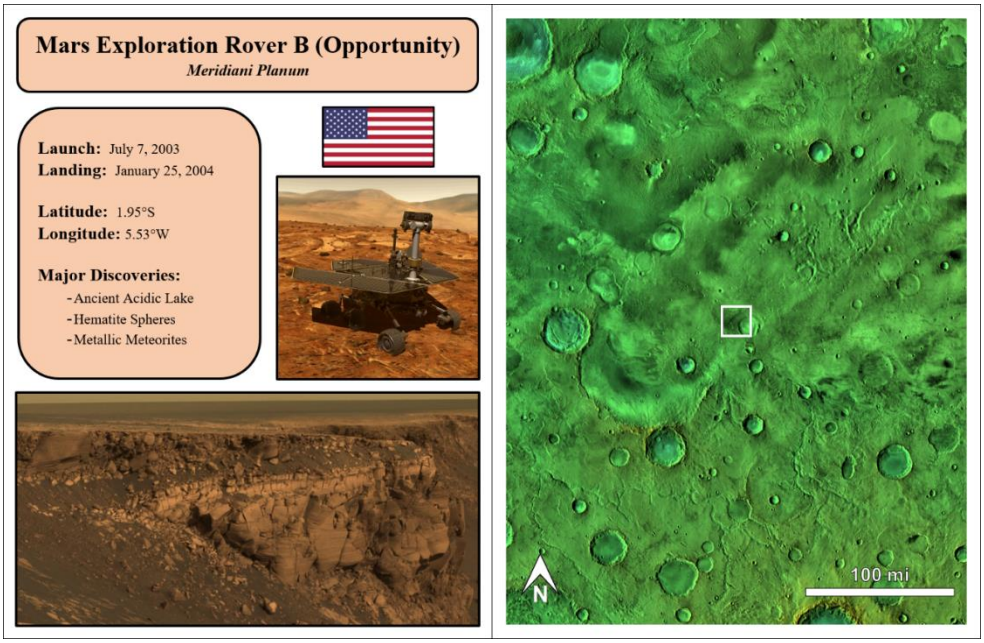

Figure B.10. Mars Landing Site Scavenger Hunt – Mars Exploration Rover B (Opportunity) Entry

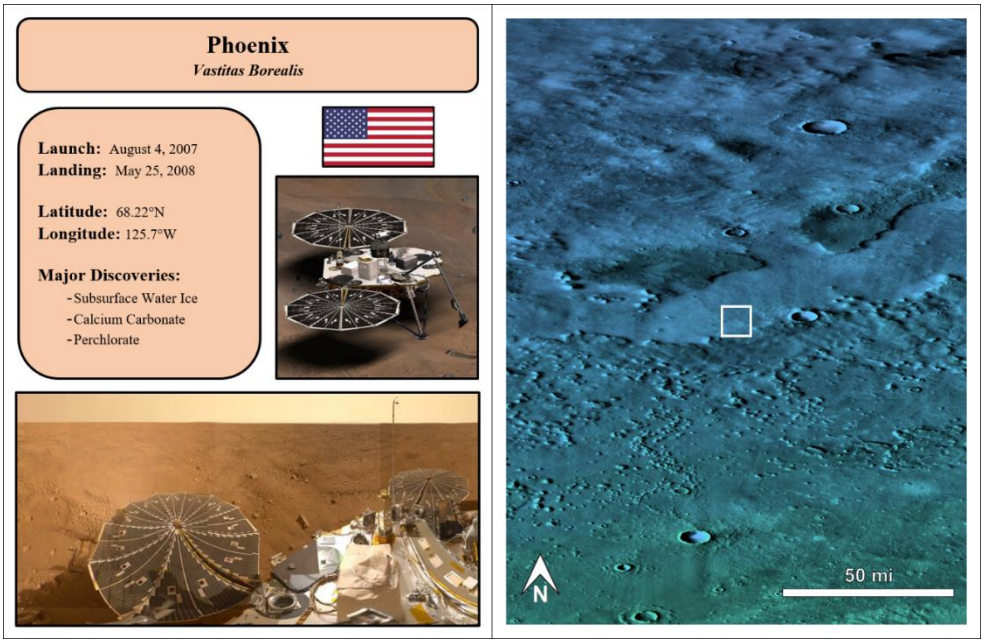

Figure B.11. Mars Landing Site Scavenger Hunt – Phoenix Entry

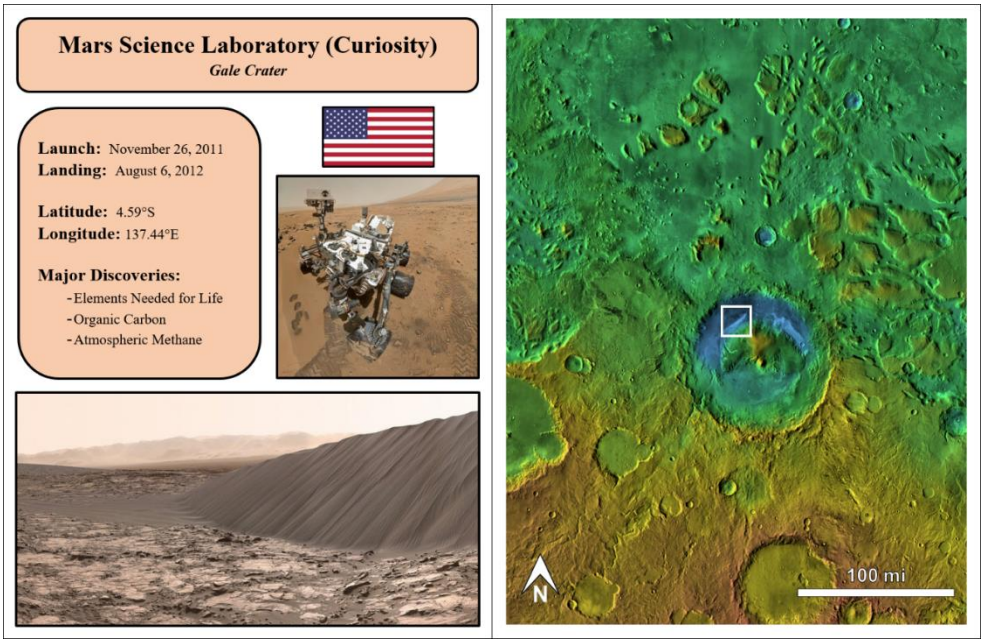

Figure B.12. Mars Landing Site Scavenger Hunt – Mars Science Laboratory (Curiosity) Entry

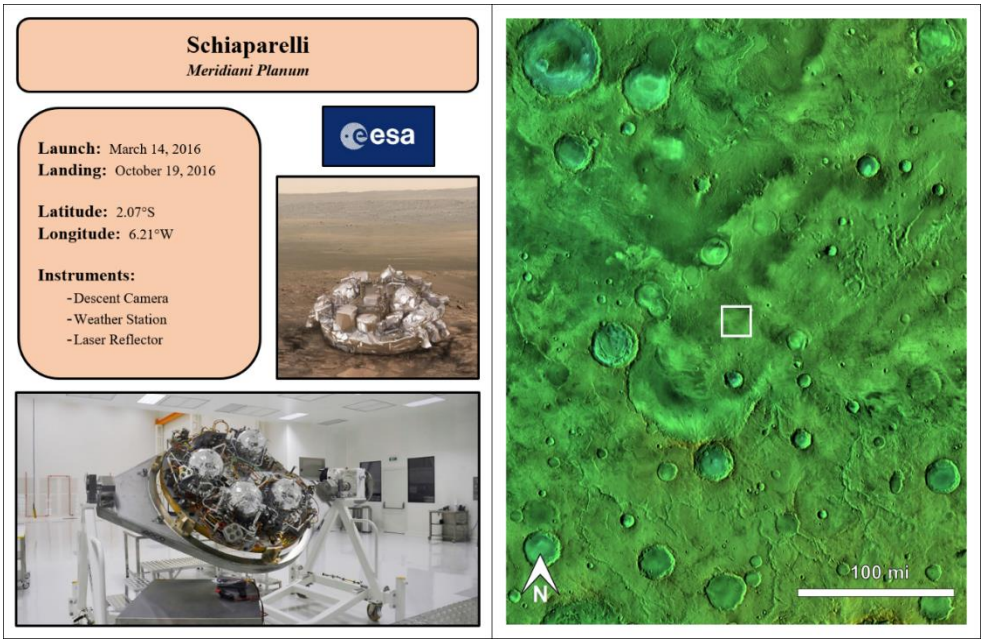

Figure B.13. Mars Landing Site Scavenger Hunt – Schiaparelli Entry

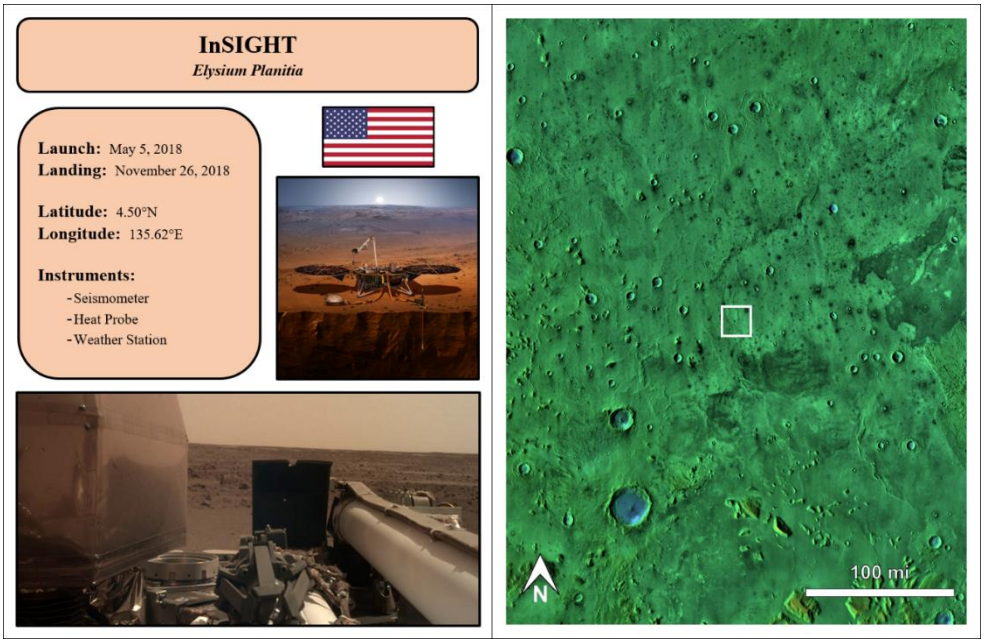

Figure B.14. Mars Landing Site Scavenger Hunt – InSIGHT Entry

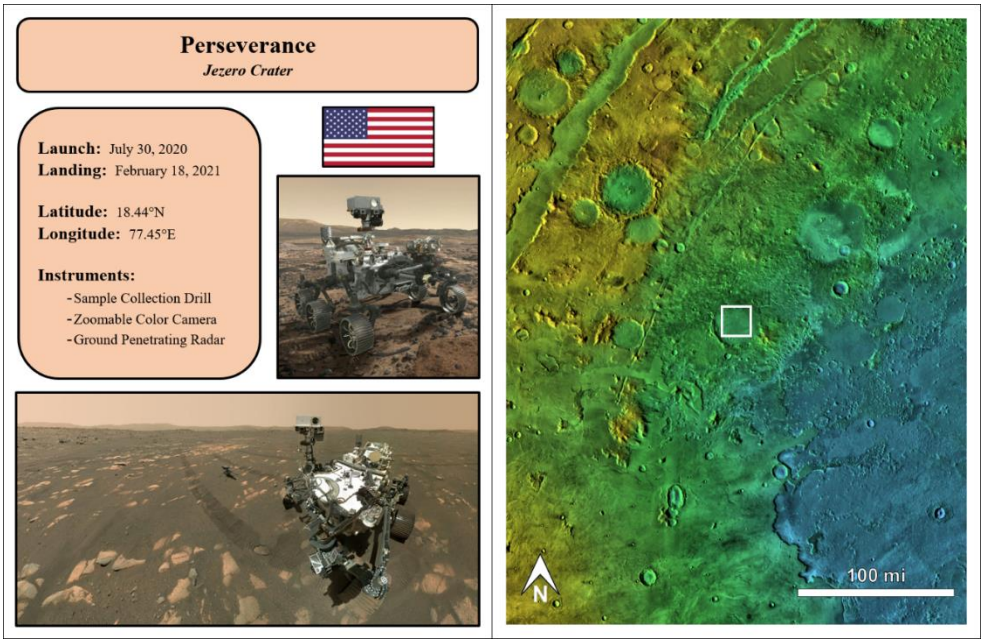

Figure B.15. Mars Landing Site Scavenger Hunt – Perseverance Entry

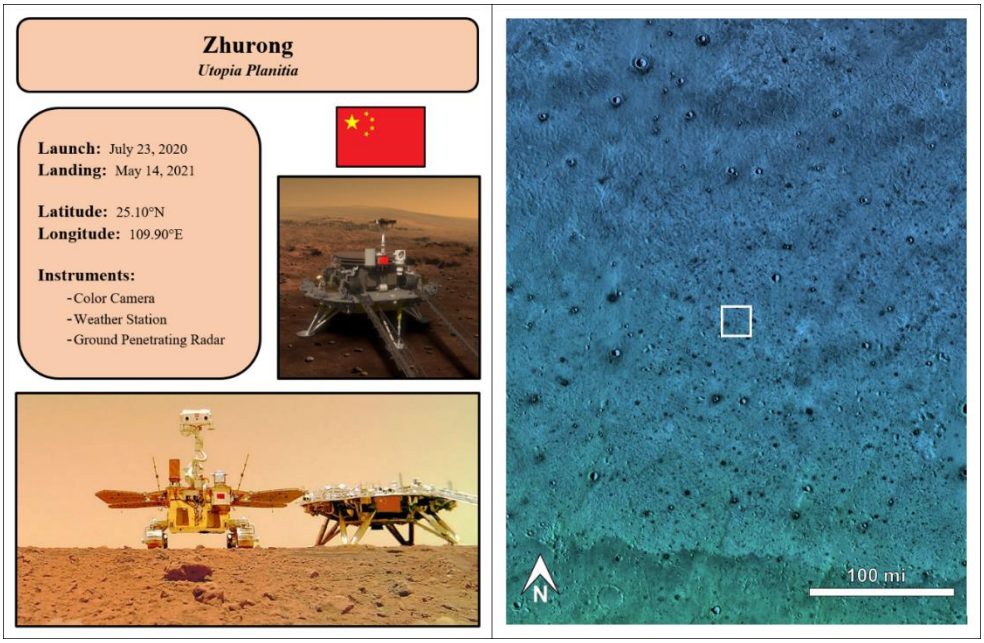

Figure B.16. Mars Landing Site Scavenger Hunt – Zhurong Entry

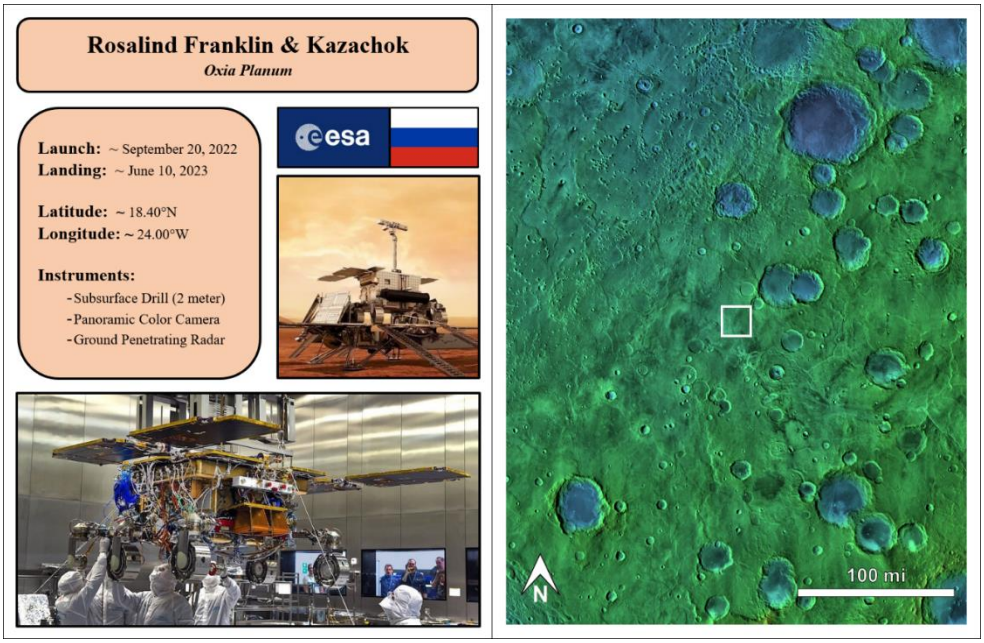

Figure B.17. Mars Landing Site Scavenger Hunt – Rosalind Franklin and Kazachok Entry

APPENDIX C

“THE MARTIAN” SCAVENGER HUNT

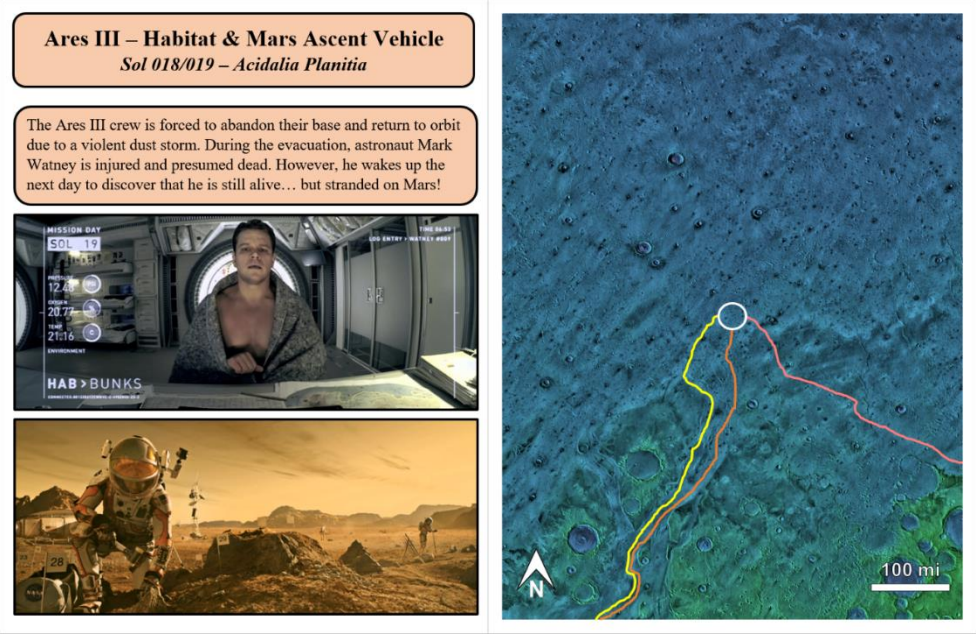

Figure C.1. "The Martian" Scavenger Hunt – Sol 018/019 Entry

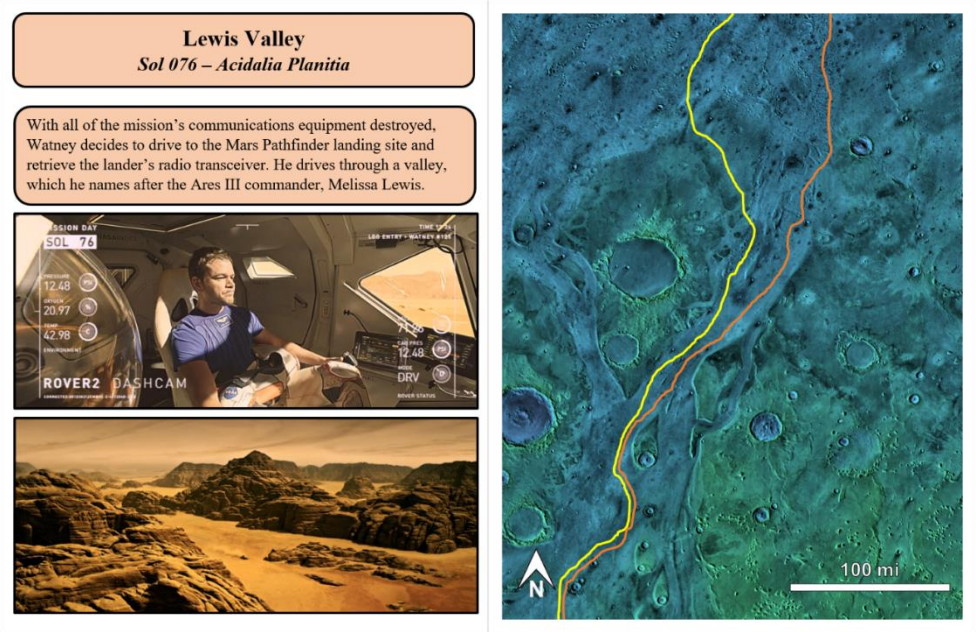

Figure C.2. "The Martian" Scavenger Hunt – Sol 076 Entry

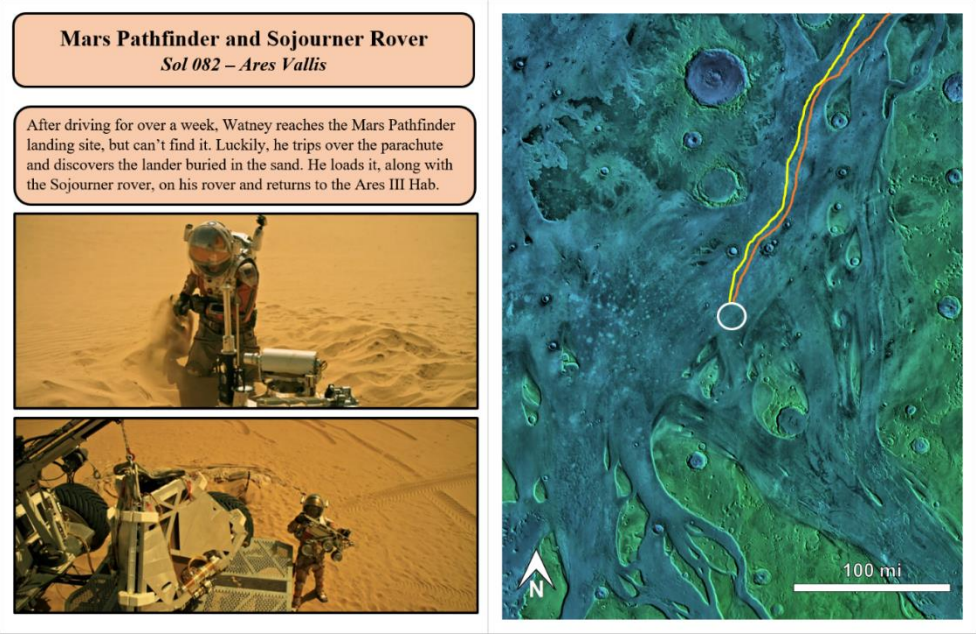

Figure C.3. "The Martian" Scavenger Hunt – Sol 082 Entry

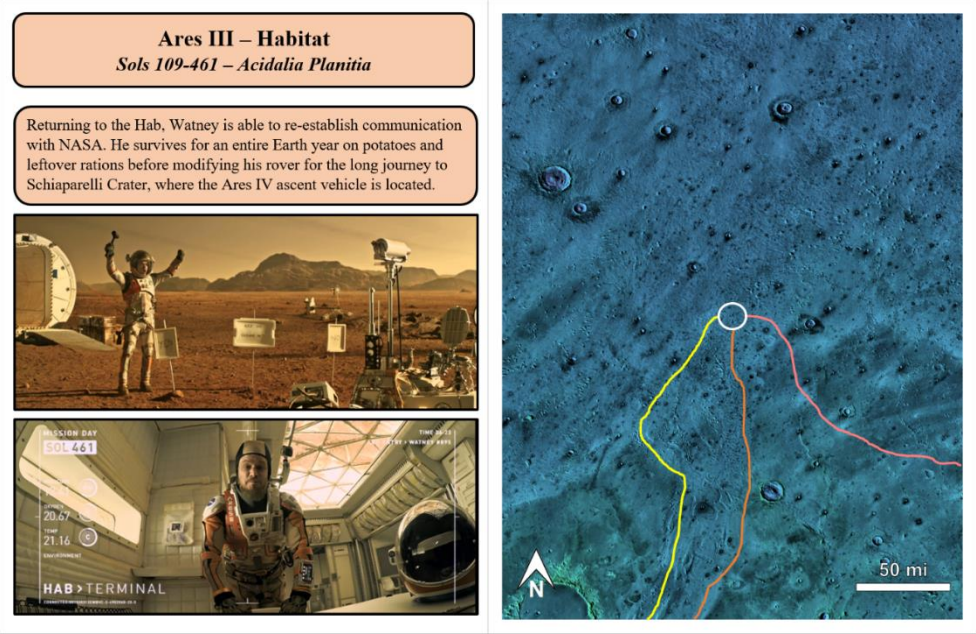

Figure C.4. "The Martian" Scavenger Hunt – Sol 109-461 Entry

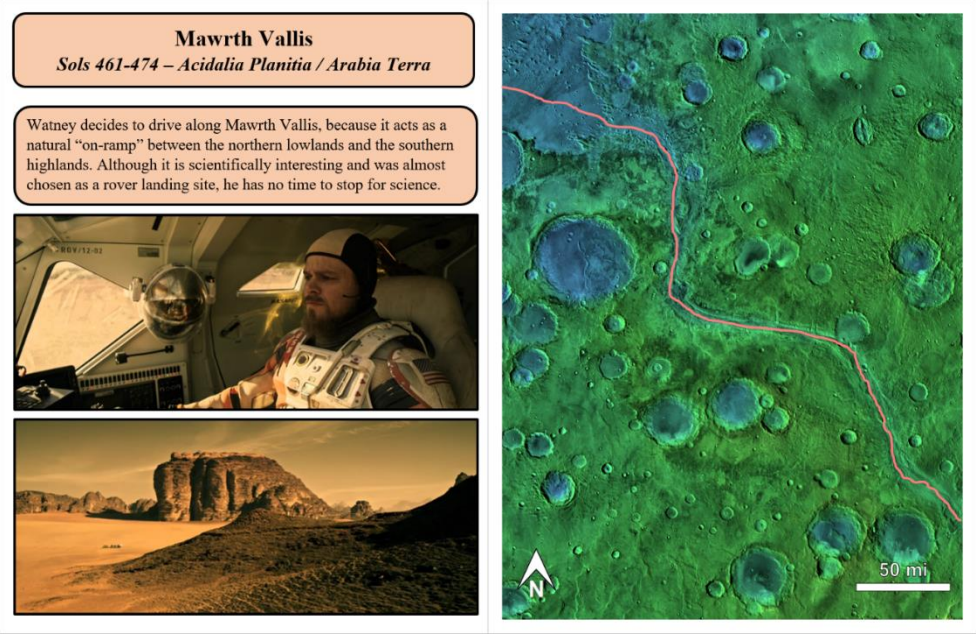

Figure C.5. "The Martian" Scavenger Hunt – Sol 461-474 Entry

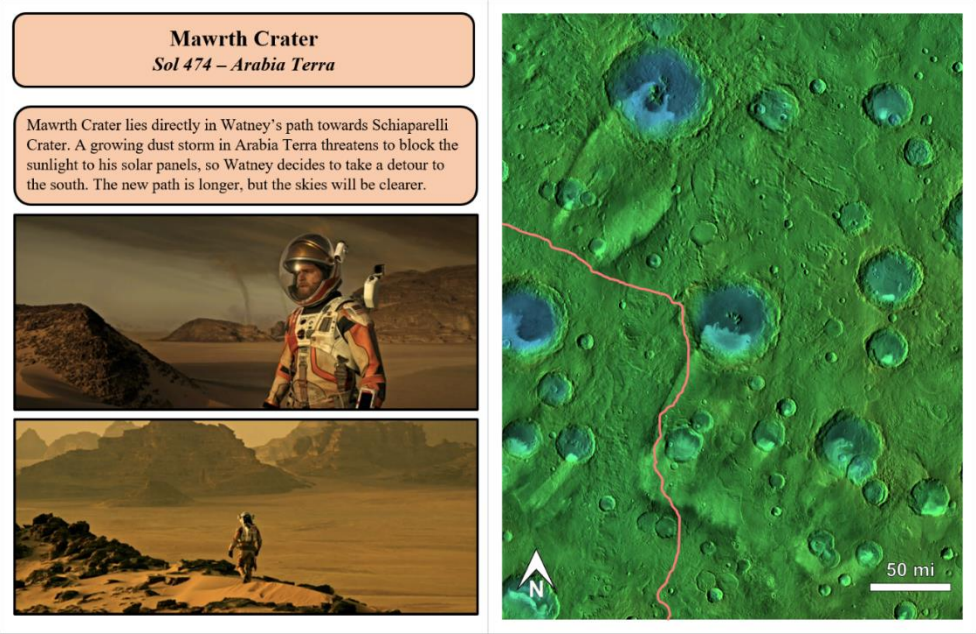

Figure C.6. "The Martian" Scavenger Hunt – Sol 474 Entry

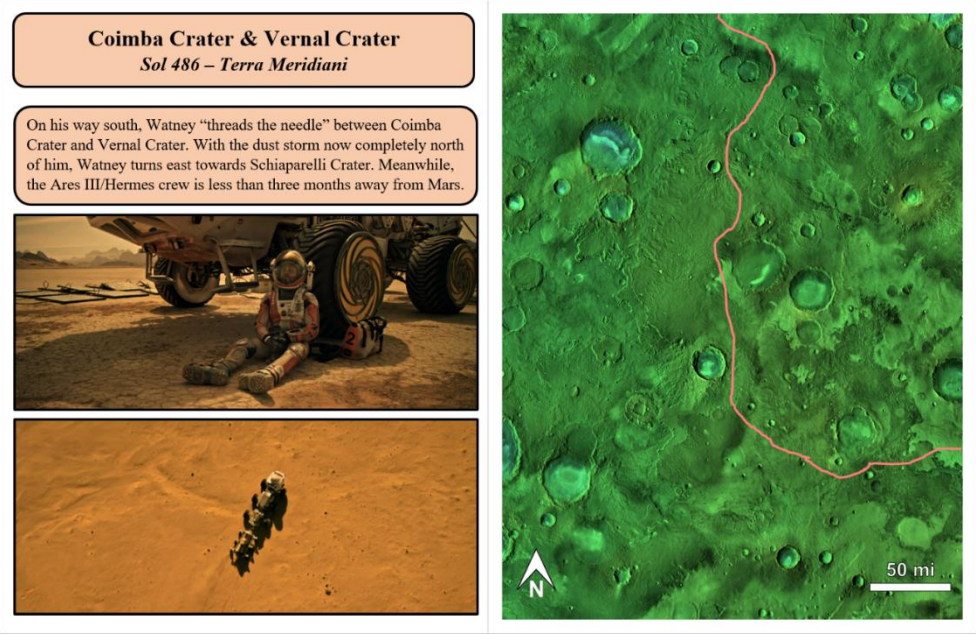

Figure C.7. "The Martian" Scavenger Hunt – Sol 486 Entry

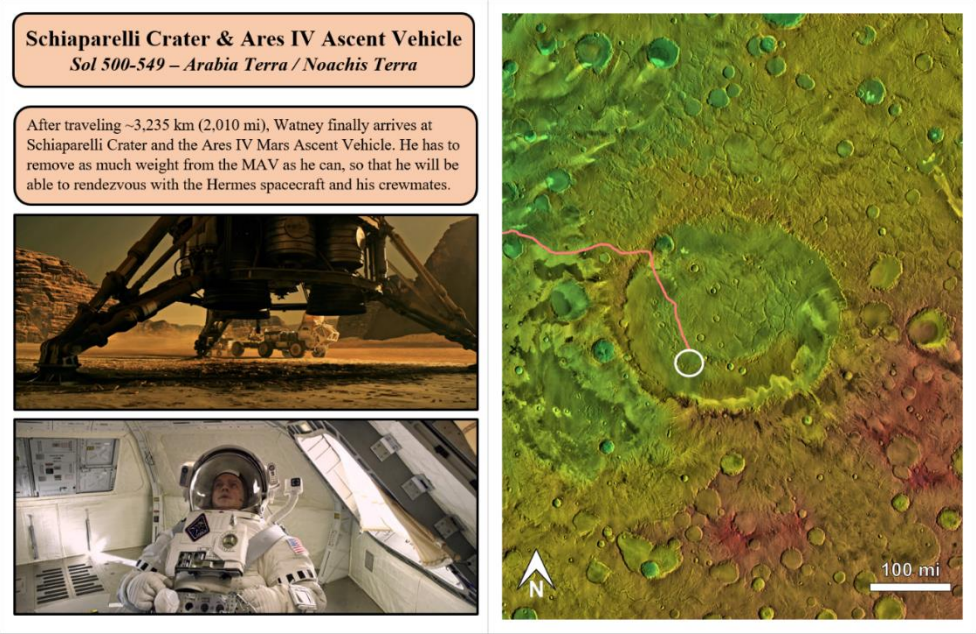

Figure C.8. "The Martian" Scavenger Hunt – Sol 500-549 Entry

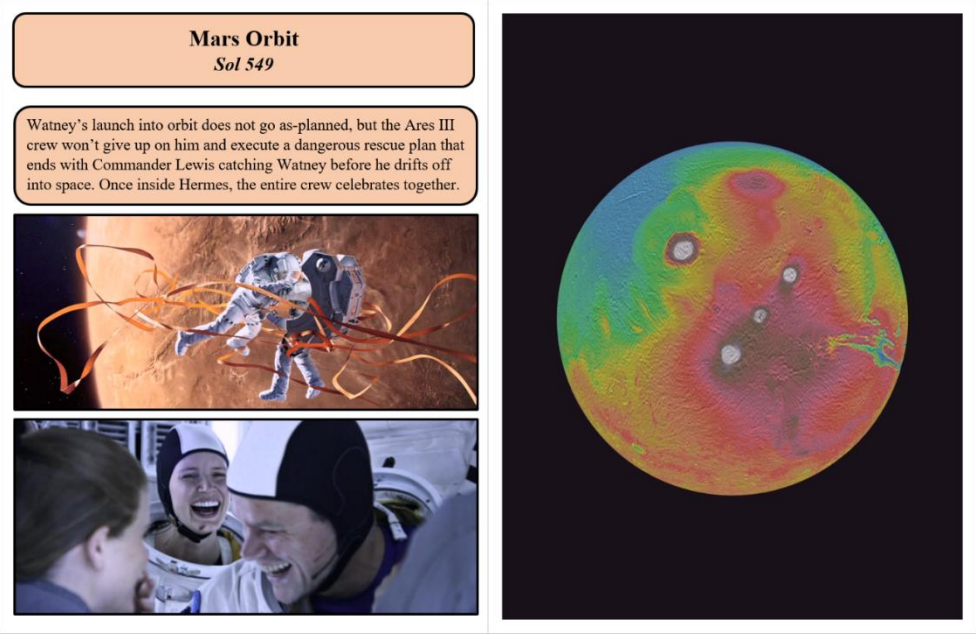

Figure C.9. "The Martian" Scavenger Hunt – Sol 549 Entry

APPENDIX D

"WALK ON MARS" EVENT ATTENDANCE

Table D.1. "Walk on Mars" event attendance.

Event Location	Attendance
ASU Map Preview	25
ASU Open Door 2018	325
Ss. Simon & Jude School – 1	250
LPSC 2018	250
COSPAR 2018	75
Flagstaff Festival of Science 2018	250
THEMIS Team Meeting	50
ASU Earth & Space Day 2018	250
Cal State East Bay – Concord	400
Bradshaw Mountain High School – 1	200
Bradshaw Mountain High School – 2	175
Desert Mirage Elementary School – 1	225
South Mountain Community College	125
Chandler Environmental Center	50
Classical Academy	850
Mesquite High School	300
Desert Mirage Elementary School – 2	225
ASU Open Door 2019	300
Garden Lakes Elementary School – 1	525
Kyrene de la Mariposa Middle School	150
Sunset Heights Elementary School	250
Ridgeline Academy	375
Gila Crossing Community School	250
Summit School of Ahwatukee	70
Chandler Environmental Center	15
Boys & Girls Club- Guadalupe	150
Flagstaff Festival of Science 2019	150
AGU Centennial – Mars on the Mall	1,000
Garden Lakes Elementary School – 2	300
Jacobson Elementary	200
Foothills Recreation and Aquatics Center	30
Ss. Simon and Jude School – 2	170
Flagstaff Festival of Science 2021	100
Total	**8,060**

APPENDIX E

“WALK ON MARS” ASSESSMENT STUDY PROTOCAL

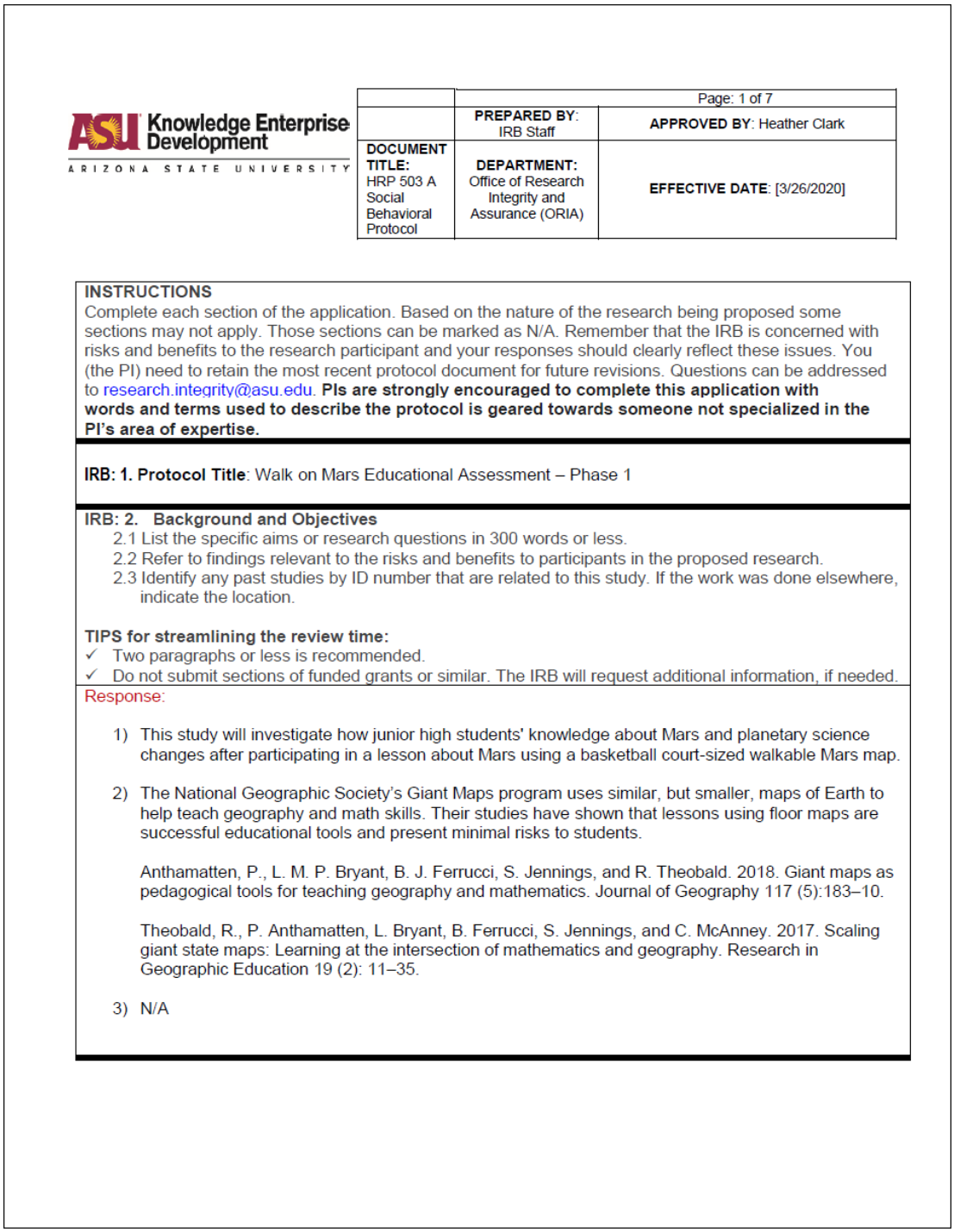

ASU Knowledge Enterprise Development
ARIZONA STATE UNIVERSITY

	Page: 1 of 7	
	PREPARED BY: IRB Staff	**APPROVED BY**: Heather Clark
DOCUMENT TITLE: HRP 503 A Social Behavioral Protocol	**DEPARTMENT:** Office of Research Integrity and Assurance (ORIA)	**EFFECTIVE DATE**: [3/26/2020]

INSTRUCTIONS
Complete each section of the application. Based on the nature of the research being proposed some sections may not apply. Those sections can be marked as N/A. Remember that the IRB is concerned with risks and benefits to the research participant and your responses should clearly reflect these issues. You (the PI) need to retain the most recent protocol document for future revisions. Questions can be addressed to research.integrity@asu.edu. **PIs are strongly encouraged to complete this application with words and terms used to describe the protocol is geared towards someone not specialized in the PI's area of expertise.**

IRB: 1. Protocol Title: Walk on Mars Educational Assessment – Phase 1

IRB: 2. Background and Objectives
2.1 List the specific aims or research questions in 300 words or less.
2.2 Refer to findings relevant to the risks and benefits to participants in the proposed research.
2.3 Identify any past studies by ID number that are related to this study. If the work was done elsewhere, indicate the location.

TIPS for streamlining the review time:
✓ Two paragraphs or less is recommended.
✓ Do not submit sections of funded grants or similar. The IRB will request additional information, if needed.

Response:

1) This study will investigate how junior high students' knowledge about Mars and planetary science changes after participating in a lesson about Mars using a basketball court-sized walkable Mars map.

2) The National Geographic Society's Giant Maps program uses similar, but smaller, maps of Earth to help teach geography and math skills. Their studies have shown that lessons using floor maps are successful educational tools and present minimal risks to students.

   Anthamatten, P., L. M. P. Bryant, B. J. Ferrucci, S. Jennings, and R. Theobald. 2018. Giant maps as pedagogical tools for teaching geography and mathematics. Journal of Geography 117 (5):183–10.

   Theobald, R., P. Anthamatten, L. Bryant, B. Ferrucci, S. Jennings, and C. McAnney. 2017. Scaling giant state maps: Learning at the intersection of mathematics and geography. Research in Geographic Education 19 (2): 11–35.

3) N/A

Figure E.1. Assessment study protocol: page #1

IRB: 3. Data Use - What are the intended uses of the data generated from this project?

Examples include: Dissertation, thesis, undergraduate project, publication/journal article, conferences/presentations, results released to agency, organization, employer, or school. If other, then describe.

Response:

Dissertation (Jonathon Ryan Hill)

IRB: 4. Inclusion and Exclusion Criteria

4.1 List criteria that define who will be included or excluded in your final sample.
Indicate if each of the following special (vulnerable/protected) populations is included or excluded:

- Minors (under 18)
- Adults who are unable to consent (impaired decision-making capacity)
- Prisoners
- Economically or educationally disadvantaged individuals

4.2 If not obvious, what is the rationale for the exclusion of special populations?
4.3 What procedures will be used to determine inclusion/exclusion of special populations?

TIPS for streamlining the review time.

✓ Research involving only data analyses should only describe variables included in the dataset that will be used.
✓ For any research which includes or may likely include children/minors or adults unable to consent, review content [here]
✓ For research targeting Native Americans or populations with a high Native American demographic, or on or near tribal lands, review content [here]
For research involving minors on campus, review content [here]

Response:

1) Minor students in 6th, 7th and 8th grade science classes at Ss. Simon and Jude Cathedral School will be included in the study.

2) N/A

3) N/A

IRB: 5. Number of Participants

Indicate the total number of individuals you expect to recruit and enroll. For secondary data analyses, the response should reflect the number of cases in the dataset.

Response:

1) 180

IRB: 6. Recruitment Methods

6.1 Identify who will be doing the recruitment and consenting of participants.
6.2 Identify when, where, and how potential participants will be identified, recruited, and consented.
6.3 Name materials that will be used (e.g., recruitment materials such as emails, flyers, advertisements, etc.) Please upload each recruitment material as a separate document, Name the document: recruitment_methods_email/flyer/advertisement_dd-mm-yyyy
6.4 Describe the procedures relevant to using materials (e.g., consent form).
✓

Figure E.2. Assessment study protocol: page #2

Response:

1) Student participants will be recruited by the 6th, 7th and 8th grade science teacher at Ss. Simon and Jude Cathedral School.

   An exemption/waiver of parental consent is requested consistent with Common Rule, Subpart D, since the only data collected will be an educational test without student names or other identifiable information, and therefore the consent/assent forms would be the only method of identifying a student who participated in the study.

   In addition, the school principal (Sr. Raphael Quinn) has specified in the site permission letter that she will act *in loca parentis* and give permission for the students to participate in these activities, since the parents regularly delegate such education-related decision-making to her. Also, the logistics of distributing, collecting and organizing ~180 parental permission slips would place an unreasonable burden on the junior high science teacher.

   The science teacher will still post a notification of the research to be conducted on the school's online FACTS-SIS portal, for both students and parents to review. As requested by the school, the notification will include an Opt-Out option, in the event that parents do not want their children to participate.

   The pre- and post-tests will not be graded or otherwise affect the students academically, and are therefore not part of the students' academic records as defined by FERPA.

2) Student participants will be identified and recruited through their regular science classes. (See above for exemption/waiver requested for parental consent and minor student assent.)

3) a) Student Portal - Notification of Research Activities
   (recruitment_methods_online_notification_18_08_2021.pdf)

4) a) The Notification of Research Activities document will be posted to the school's FACTS-SIS online portal. Parents and students are supposed to check this portal daily for homework assignments, grades, and other notifications/announcements from the teachers.

IRB: **7. Study Procedures**

7.1 List research procedure step by step (e.g., interventions, surveys, focus groups, observations, lab procedures, secondary data collection, accessing student or other records for research purposes, and follow-ups). Upload one attachment, dated, with all the materials relevant to this section. Name the document: supporting documents dd-mm-yyyy

7.2 For each procedure listed, describe **who** will be conducting it, **where** it will be performed, **how long** is participation in each procedure, and **how/what data** will be collected in each procedure.

7.3 Report the total period and span of time for the procedures (if applicable the timeline for follow ups).

7.4 For secondary data analyses, identify if it is a public dataset (please include a weblink where the data will be accessed from, if applicable). If not, describe the contents of the dataset, how it will be accessed, and attach data use agreement(s) if relevant.

TIPS for streamlining the review time.

- ✓ Ensure that research materials and procedures are explicitly connected to the articulated aims or research questions (from section 2 above).
- ✓ In some cases, a table enumerating the name of the measures, corresponding citation (if any), number of items, sources of data, time/wave if a repeated measures design can help the IRB streamline the review time.

Figure E.3. Assessment study protocol: page #3

Response:

1) Study Procedure

   a) Pre-Test: Students will be given a pre-test in order to assess their level of knowledge prior to the giant map lesson. The test will be given in their regular science class by their science teacher approximately 1 week before the giant map lesson and will last approximately 15 minutes. (See supporting documents for a copy of the pre-test.)

   b) Giant Map Lesson: Students will participate in an approximately 30 minute lesson about Mars while on the giant map. The lesson will be given by a member of the research team (Jonathon Hill). The lesson will take place during their normal science class, although the junior high teachers may re-arrange the normal period schedule in order to coordinate with times when the school gymnasium is available to display the giant map.

   c) Post-Test: Students will be given a post-test in order to assess how their knowledge changed after the giant map lesson. The test will be given in their regular science class by their science teacher approximately 1 week after the giant map lesson and will last approximately 15 minutes. (See supporting documents for a copy of the post-test.)

   d) Collation and De-identification of Tests: The junior high science teacher and/or aides will staple together each student's pre-test and post-test, record the student's gender and ELL (English language learner) status in the appropriate section, and then cut the student names from the bottom of the tests, making them anonymous.

   e) Data Analysis: Once the tests are de-identified, the teachers will return the completed and collated tests to the research team, who will compile quantitative statistics and qualitative assessments in order to address the research study's objectives.

2) See Description Above

3) The student portion of the study will last approximately 1 hour, spread out over two weeks (one week before and after the actual map lesson). The collation and de-identification by the school's teachers and/or aides will take approximately 4 person-hours, scheduled at their convenience within one week after the completion of the student portion of the study. The analysis by the research team is expected to last approximately 4 weeks, depending on the complexity and variability in the free-form answers given in the tests.

4) N/A

IRB: 8. Compensation

8.1 Report the amount and timing of any compensation or credit to participants.
8.2 Identify the source of the funds to compensate participants.
8.3 Justify that the compensation to participants to indicate it is reasonable and/or how the compensation amount was determined.
8.4 Describe the procedures for distributing the compensation or assigning the credit to participants.

TIPS for streamlining the review time.

- ✓ If partial compensation or credit will be given or if completion of all elements is required, explain the rationale or a plan to avoid coercion
- ✓ For extra or course credit guidance, see "Research on educational programs or in classrooms" on the following page: https://researchintegrity.asu.edu/human-subjects/special-considerations.
- ✓ For compensation over $100.00, review "Research Subject Compensation" at: https://researchintegrity.asu.edu/human-subjects/special-considerations for more information.

Figure E.4. Assessment study protocol: page #4

Response:

1) No compensation or academic credit will be given to participants
2) N/A
3) N/A
4) N/A

IRB: 9. Risk to Participants

List the reasonably foreseeable risks, discomforts, or inconveniences related to participation in the research.

TIPS for streamlining the review time.

- ✓ Consider the broad definition of "minimal risk" as the probability and magnitude of harm or discomfort anticipated in the research that are not greater in and of themselves than those ordinarily encountered in daily life or during the performance of routine physical or psychological examinations or tests.
- ✓ Consider physical, psychological, social, legal, and economic risks.
- ✓ If there are risks, clearly describe the plan for mitigating the identified risks.

Response:

1) Participants will be subjected to minimal risk for the duration of the study.

2) Student participants will wear masks throughout the study according to the school's masking rules at the time of the study. (The school has made clear to students that their masking rules may change depending on changing recommendations from the CDC and/or the current COVID environment in the area.) The ASU researchers will wear masks according to the ASU Community of Care guidelines at the time of the study.

IRB: 10. Potential Direct Benefits to Participants

List the potential direct benefits to research participants. If there are risks noted in 9 (above), articulated benefits should outweigh such risks. These benefits are not to society or others not considered participants in the proposed research. Indicate if there is no direct benefit. A direct benefit comes as a direct result of the subject's participation in the research. An indirect benefit may be incidental to the subject's participation. Do not include compensation as a benefit.

Response:

1) There will be no direct benefit to participants.

Figure E.5. Assessment study protocol: page #5

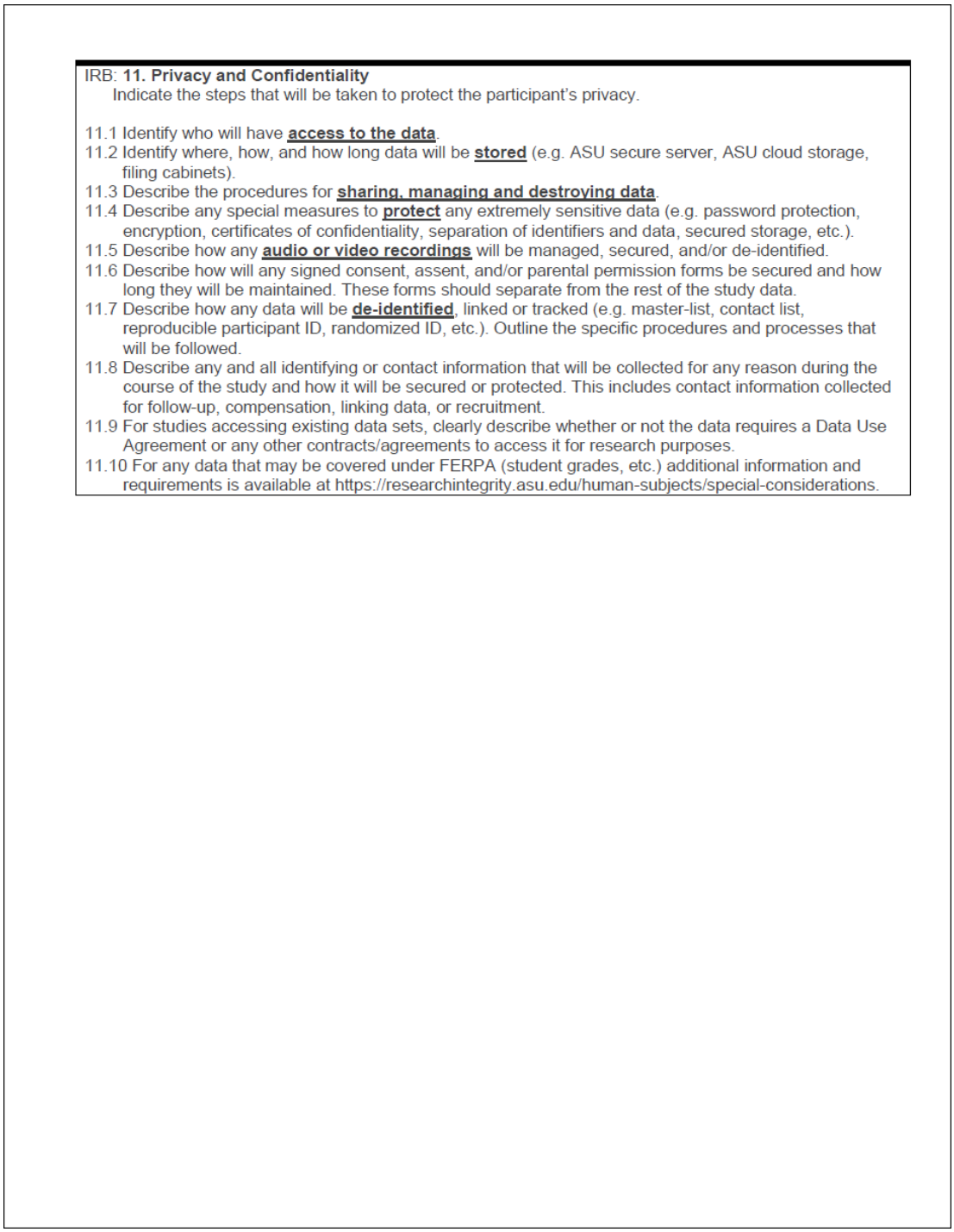

IRB: **11. Privacy and Confidentiality**

Indicate the steps that will be taken to protect the participant's privacy.

11.1 Identify who will have **access to the data**.
11.2 Identify where, how, and how long data will be **stored** (e.g. ASU secure server, ASU cloud storage, filing cabinets).
11.3 Describe the procedures for **sharing, managing and destroying data**.
11.4 Describe any special measures to **protect** any extremely sensitive data (e.g. password protection, encryption, certificates of confidentiality, separation of identifiers and data, secured storage, etc.).
11.5 Describe how any **audio or video recordings** will be managed, secured, and/or de-identified.
11.6 Describe how will any signed consent, assent, and/or parental permission forms be secured and how long they will be maintained. These forms should separate from the rest of the study data.
11.7 Describe how any data will be **de-identified**, linked or tracked (e.g. master-list, contact list, reproducible participant ID, randomized ID, etc.). Outline the specific procedures and processes that will be followed.
11.8 Describe any and all identifying or contact information that will be collected for any reason during the course of the study and how it will be secured or protected. This includes contact information collected for follow-up, compensation, linking data, or recruitment.
11.9 For studies accessing existing data sets, clearly describe whether or not the data requires a Data Use Agreement or any other contracts/agreements to access it for research purposes.
11.10 For any data that may be covered under FERPA (student grades, etc.) additional information and requirements is available at https://researchintegrity.asu.edu/human-subjects/special-considerations.

Figure E.6. Assessment study protocol: page #6

Response:

1) Only the science teachers and aides at Ss. Simon and Jude Cathedral School will have access to personally-identifiable data, in the form of student names on the pre- and post-tests. The teachers will physically remove these names from the tests after the pre- and post-tests have been physically stapled together and before releasing the tests to the study investigators. Afterwards, only the research team will have access to the physical tests.

2) The de-identified pre- and post-tests will be stored indefinitely at ASU's Mars Space Flight Facility by Jonathon R. Hill in a standard filing cabinet, at least until the final research work has been published.

3) The personally-identifiable information (ie: student names) will be removed (ex: cut off) and destroyed (ex: shredded) after the science teachers have stapled the pre- and post-tests together. The now-anonymous tests will be destroyed (ex: shredded) after the research work has been published and the research team has determined they are no longer useful.

4) N/A

5) N/A

6) An exemption/waiver from collecting parental consent and minor student assent documents is being requested. See Section 6.1 for further information.

7) The teachers will collate pre- and post-test documents, staple them together, and then the portion of the pages with student names will be physically cut off of the assessments.

8) If the consent/assent exemption is granted, there will be no identifying or contact information collected from the participants.

9) N/A

10) The pre- and post-tests will not be graded or otherwise affect the students academically, and are therefore not part of the students' academic records as defined by FERPA.

Figure E.7. Assessment study protocol: page #7

IRB: 12. Consent
Describe the procedures that will be used to obtain consent or assent (and/or parental permission).

12.1 Who will be responsible for consenting participants?
12.2 Where will the consent process take place?
12.3 How will the consent be obtained (e.g., verbal, digital signature)?

TIPS for streamlining the review time.

- ✓ If participants who do not speak English will be enrolled, describe the process to ensure that the oral and/or written information provided to those participants will be in their preferred language. Indicate the language that will be used by those obtaining consent. For translation requirements, see Translating documents and materials under https://researchintegrity.asu.edu/human-subjects/protocol-submission
- ✓ Translated consent forms should be submitted after the English is version of all relevant materials are approved. Alternatively, submit translation certification letter.
- ✓ **If a waiver for the informed consent process is requested, justify the waiver in terms of each of the following: (a) The research involves no more than minimal risk to the subjects; (b) The waiver or alteration will not adversely affect the rights and welfare of the subjects; (c) The research could not practicably be carried out without the waiver or alteration; and (d) Whenever appropriate, the subjects will be provided with additional pertinent information after participation.** Studies involving confidential, one time, or anonymous data need not justify a waiver. A verbal consent or implied consent after reading a cover letter is sufficient.
- ✓ ASU consent templates are [here].
- ✓ Consents and related materials need to be congruent with the content of the application.

Response:

1) An exemption to the parental consent and student assent process has been requested. This study involves the collection of anonymous educational tests, and therefore is not required to further justify a waiver. See section 6.1 for further details.

   Parents will be given the option to opt-out of the research study activities on behalf of their children. The Notification of Research Activities will be posted to the school's FACTS-SIS online portal ≥ 3 days (72 hours) prior to the start of the research activities, which will consist of the ~15-minute pre-test. Parents may also withdraw their children from participation at any time up until end-of-school-day on the date of the ~15-minute post-test (≥ 7 days after the notification is posted). After that time, the student participation portion of the research study will be completed and the pre-test and post-test will have been de-identified, making it impossible to single-out and remove a specific student's pre-test and/or post-test.

2) Same

3) Same

Figure E.8. Assessment study protocol: page #8

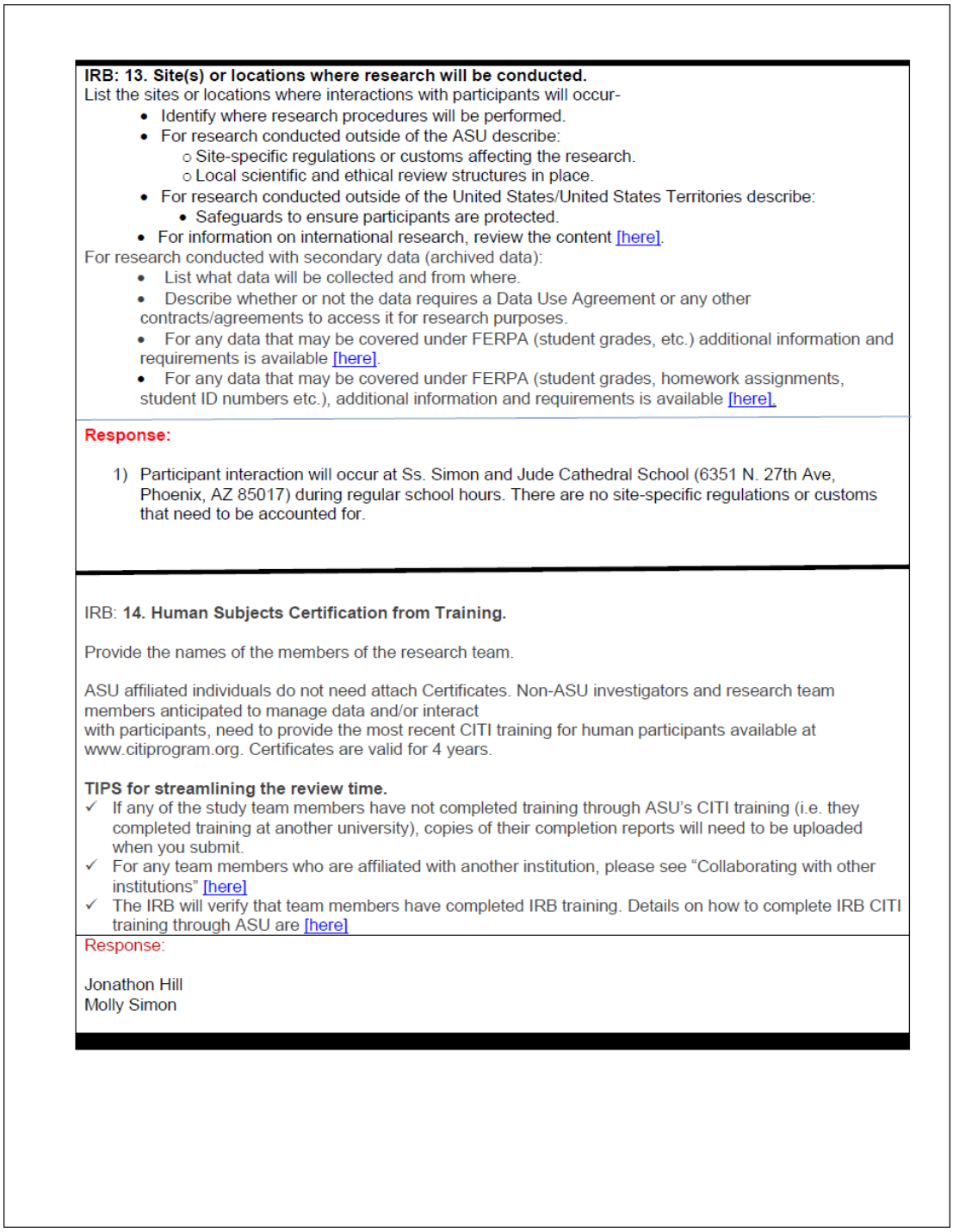

IRB: 13. Site(s) or locations where research will be conducted.
List the sites or locations where interactions with participants will occur-

- Identify where research procedures will be performed.
- For research conducted outside of the ASU describe:
  - Site-specific regulations or customs affecting the research.
  - Local scientific and ethical review structures in place.
- For research conducted outside of the United States/United States Territories describe:
  - Safeguards to ensure participants are protected.
- For information on international research, review the content [here].

For research conducted with secondary data (archived data):

- List what data will be collected and from where.
- Describe whether or not the data requires a Data Use Agreement or any other contracts/agreements to access it for research purposes.
- For any data that may be covered under FERPA (student grades, etc.) additional information and requirements is available [here].
- For any data that may be covered under FERPA (student grades, homework assignments, student ID numbers etc.), additional information and requirements is available [here].

Response:

1) Participant interaction will occur at Ss. Simon and Jude Cathedral School (6351 N. 27th Ave, Phoenix, AZ 85017) during regular school hours. There are no site-specific regulations or customs that need to be accounted for.

IRB: **14. Human Subjects Certification from Training.**

Provide the names of the members of the research team.

ASU affiliated individuals do not need attach Certificates. Non-ASU investigators and research team members anticipated to manage data and/or interact
with participants, need to provide the most recent CITI training for human participants available at www.citiprogram.org. Certificates are valid for 4 years.

TIPS for streamlining the review time.

- ✓ If any of the study team members have not completed training through ASU's CITI training (i.e. they completed training at another university), copies of their completion reports will need to be uploaded when you submit.
- ✓ For any team members who are affiliated with another institution, please see "Collaborating with other institutions" [here]
- ✓ The IRB will verify that team members have completed IRB training. Details on how to complete IRB CITI training through ASU are [here]

Response:

Jonathon Hill
Molly Simon

Figure E.9. Assessment study protocol: page #9

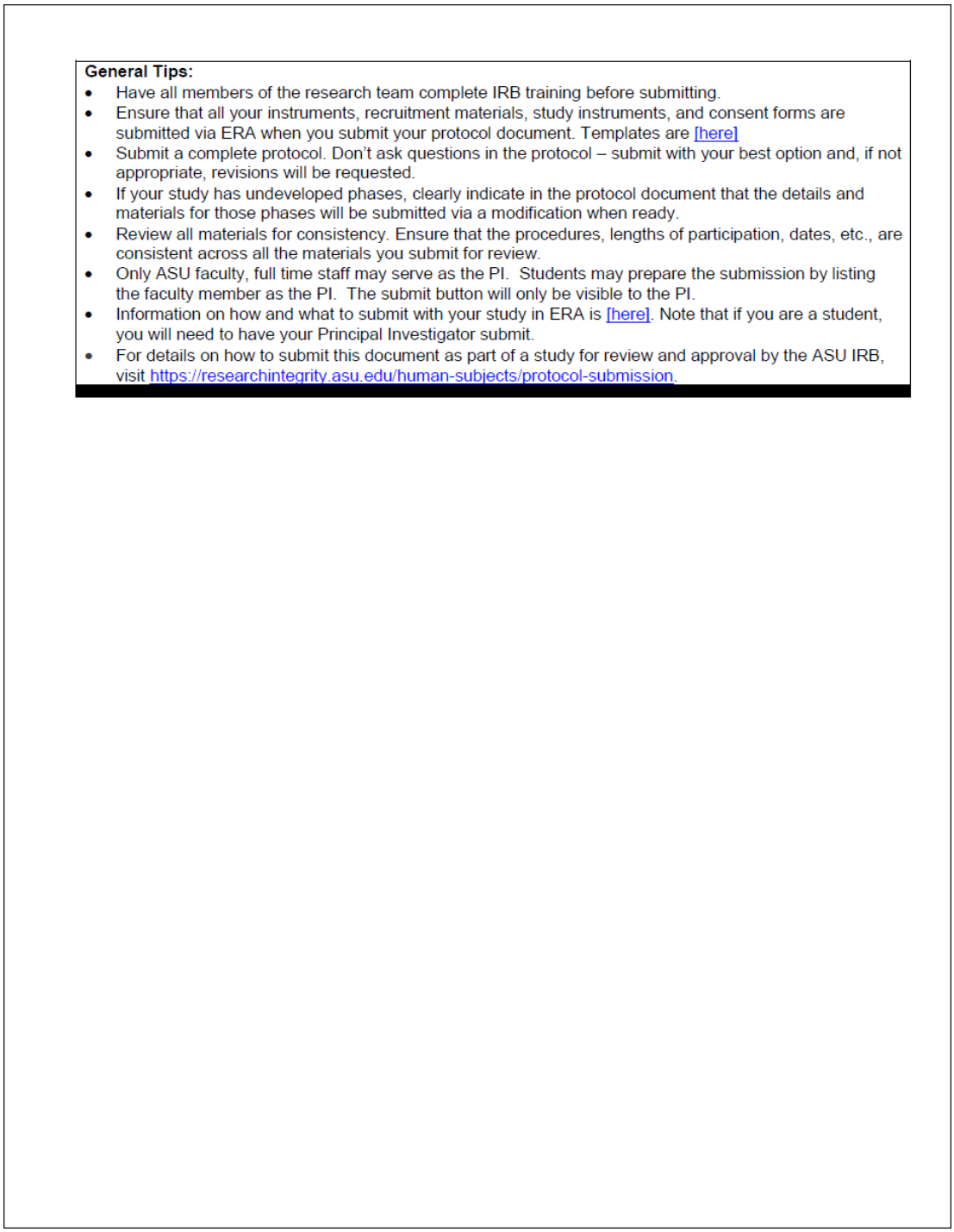

Figure E.10. Assessment study protocol: page #10

SS. SIMON & JUDE CATHEDRAL SCHOOL

6351 North 27th Avenue • Phoenix, AZ 85017
602.242.1299 • Fax: 602.433.7608
www.simonjudeschool.org

August 13, 2021

To the Arizona State University Institutional Review Board,

Based on my review of the proposed research by **Jonathon R. Hill**, I give permission for the study entitled **Walk on Mars Educational Assessment – Phase 1** to be conducted at **Ss. Simon and Jude Cathedral School**.

As part of this study, I authorize the researcher(s) to: 1) administer a pre-test to the 6th, 7th and 8th grade students regarding basic knowledge about Mars; 2) provide the 6th, 7th and 8th grade students with an approximately 30 minute lesson about Mars utilizing the "Walk on Mars" walkable floor map; and 3) administer a post-test to the 6th, 7th and 8th grade students regarding material covered during the in-person lesson.

Individual students' participation in the research activities will be voluntary. Students will not receive any academic credit or other reward for their participation in the research activities. Similarly, students will not be penalized if they choose not to participate in the research activities.

As principal, acting in loca parentis, I give permission for the students to participate in these research activities and will not require explicit parental permission in an effort to reduce the paperwork burden of the teacher(s) involved. However, parents will be notified in advance of the research activities and provided with an opt-out form in the event they do not wish for their children to participate.

We understand that our organization's responsibilities include having the junior high science teacher and/or aides: 1) post a notification and description of the research activities to the school's online FACTS-SIS system where students and parents will be able to review it, 2) proctor the pre-test and post-test; 3) staple together each student's pair of tests; 4) mark the gender and ELL (English language learner) status on each student's test pair; 5) physically cut the student name from the bottom of the test pages, and 6) deliver the de-identified tests to the researcher(s). We reserve the right to withdraw from the study at any time.

This authorization covers the time period of **August 15th, 2021** to **December 15th, 2021**.

I confirm that I am authorized to approve research activities at the school.

Sincerely,

Sister Raphael Quinn

Sister Raphael Quinn
Principal

Alive With the Spirit Since 1954

Figure E.11. Assessment study protocol: page #11

Parental Notification Regarding Participation in ASU Research Study

Principal Investigator: Molly Simon (Molly.N.Simon@asu.edu)

Primary Contact: Jonathon Hill (Jonathon.Hill@asu.edu)

Study Title: Walk on Mars Education Assessment – Phase 1

Researchers from Arizona State University will be conducting an educational research study at Ss. Simon and Jude Cathedral School in Grades 6, 7 & 8. This letter will explain why this study is being done and what you need to do if you DO NOT want your child to participate. We encourage you to take some time to read about the study and to discuss it with your child. We also encourage you to ask questions about the study at any time. If you decide to allow your child to participate, no further action is required. However, if you decide that you DO NOT want your child to participate, please sign the attached form and return it to Ms. Maureen Callaghan.

The purpose of this research study is to determine how the use of a basketball court-sized map of Mars during a lesson about planetary science changes and/or improves students' knowledge about Mars and planetary science. This research study will be conducted during the school day as part of the students' regular science classes. The junior high teachers may choose to adjust the daily schedule so that certain science classes occur when the school gymnasium is also available for displaying the Mars map.

The study will consist of three parts. First, students will be asked to complete an approximately 15-minute pre-test during their regular science class in order to determine how much they know about Mars and planetary science before the lesson. Second, the students will participate in an approximately 30-minute lesson about Mars while being guided around the map by an ASU Mars researcher. Third, the students will be asked to complete an approximately 15-minute post-test during their regular science class in order to determine how their knowledge about Mars and planetary science has changed and/or improved after the lesson.

Student names will be physically removed (ex: cut off) from the pre-test and post-test before Ss. Simon and Jude Cathedral School provides them to the ASU researchers. Therefore, the test results will be completely anonymous. The results of the pre-test and post-test will not affect the students' academic record in any way. The tests will not be graded, students will not be rewarded with credit or extra-credit for completing them, and students will not be penalized if they do not complete the tests.

The ASU researchers and the ASU Institutional Review Board have determined that this research study does not pose a risk to the students.

We will be happy to answer any question you may have about this study. Please feel free to contact Maureen Callaghan (ssjscience@hotmail.com) or Jonathon Hill (Jonathon.Hill@asu.edu) or Molly Simon (Molly.N.Simon@asu.edu)) with any questions you may have about the study.

Figure E.12. Assessment study protocol: page #12

If you have any questions concerning your child's rights as a research participant, you may contact the Arizona State University Institutional Review Board (IRB) at research.integrity@asu.edu or 480-965-6788.

Your child does not have to participate in this study if you do not want them to. If you decide to allow your child to be in the study, but later change your mind, you may withdraw your child at any time until the student names are removed from the tests, at which point the Ss. Simon and Jude Cathedral School teachers and the ASU researchers will not be able to identify and remove the pre-test and/or post-test completed by your child. There are no penalties or consequences of any kind if you decide that you DO NOT want your child to participate.

The pre-test portion of the study will begin on **September 7th, 2021** and post-test portion of the study will conclude on **September 9th, 2021**.

If you DO NOT want your child to participate in this research study, please sign and return the attached form to Ms. Maureen Callaghan by **September 7th, 2021**. You may also withdraw your child from participation in this research study at any time up until end-of-school-day on **September 9th, 2021**.

Notification of Refusal:
I have read this notification and decided that I DO NOT want my child to participate in the ASU research study described above.

_____
Print Child's Name:

_____ _____ _____
Parent/Guardian's Signature: Print Name: Date:

Relationship (e.g. mother, father, legal guardian):_____

Figure E.13. Assessment study protocol: page #13

APPENDIX F

“WALK ON MARS” ASSESSMENT STUDY TESTS

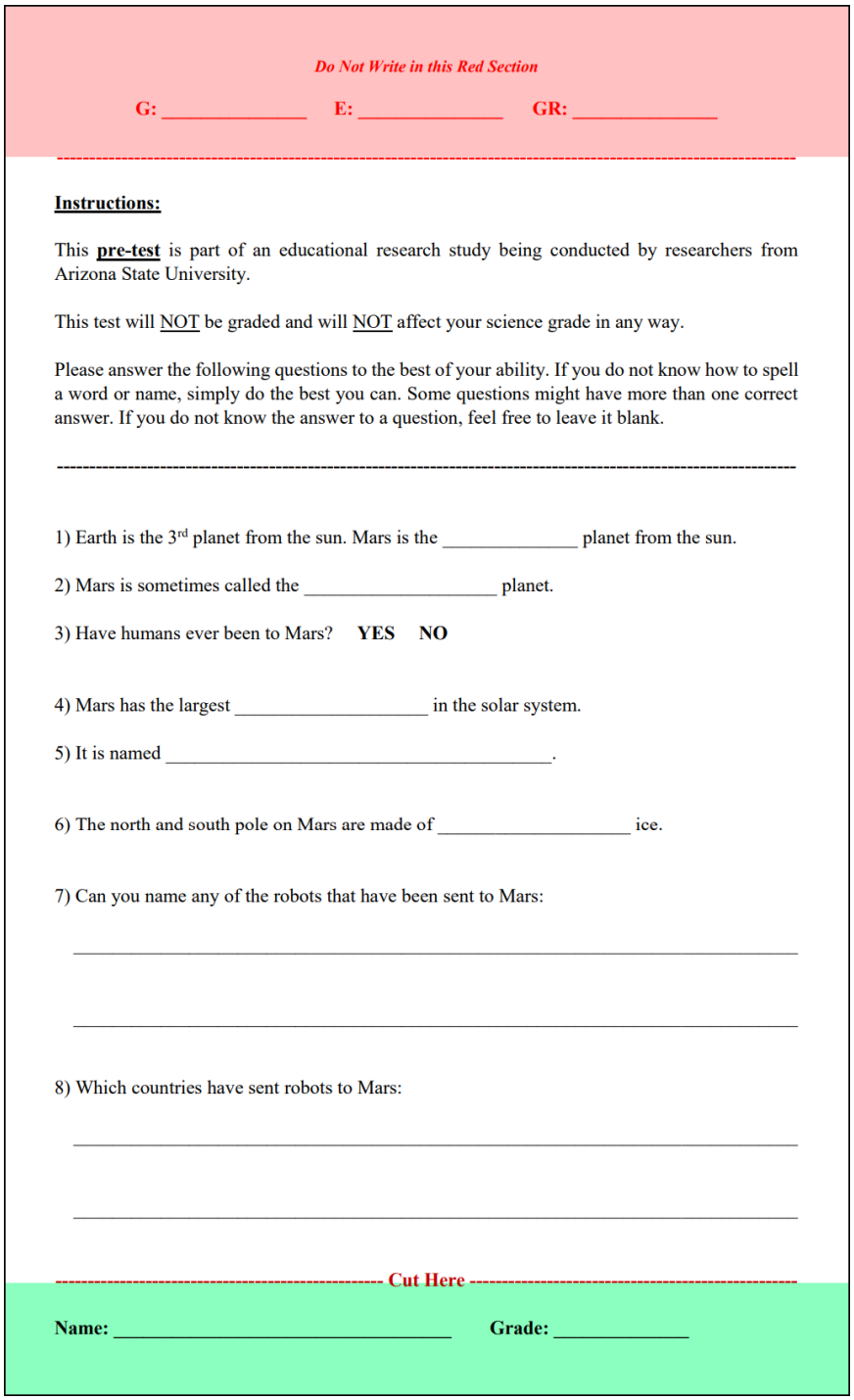

Do Not Write in this Red Section

G: _____ E: _____ GR: _____

Instructions:

This **pre-test** is part of an educational research study being conducted by researchers from Arizona State University.

This test will NOT be graded and will NOT affect your science grade in any way.

Please answer the following questions to the best of your ability. If you do not know how to spell a word or name, simply do the best you can. Some questions might have more than one correct answer. If you do not know the answer to a question, feel free to leave it blank.

---

1) Earth is the 3rd planet from the sun. Mars is the _____ planet from the sun.

2) Mars is sometimes called the _____ planet.

3) Have humans ever been to Mars? **YES** **NO**

4) Mars has the largest _____ in the solar system.

5) It is named _____.

6) The north and south pole on Mars are made of _____ ice.

7) Can you name any of the robots that have been sent to Mars:

_____

_____

8) Which countries have sent robots to Mars:

_____

_____

---------- Cut Here ----------

Name: _____ Grade: _____

Figure F.1. Assessment study: pre-test page #1.

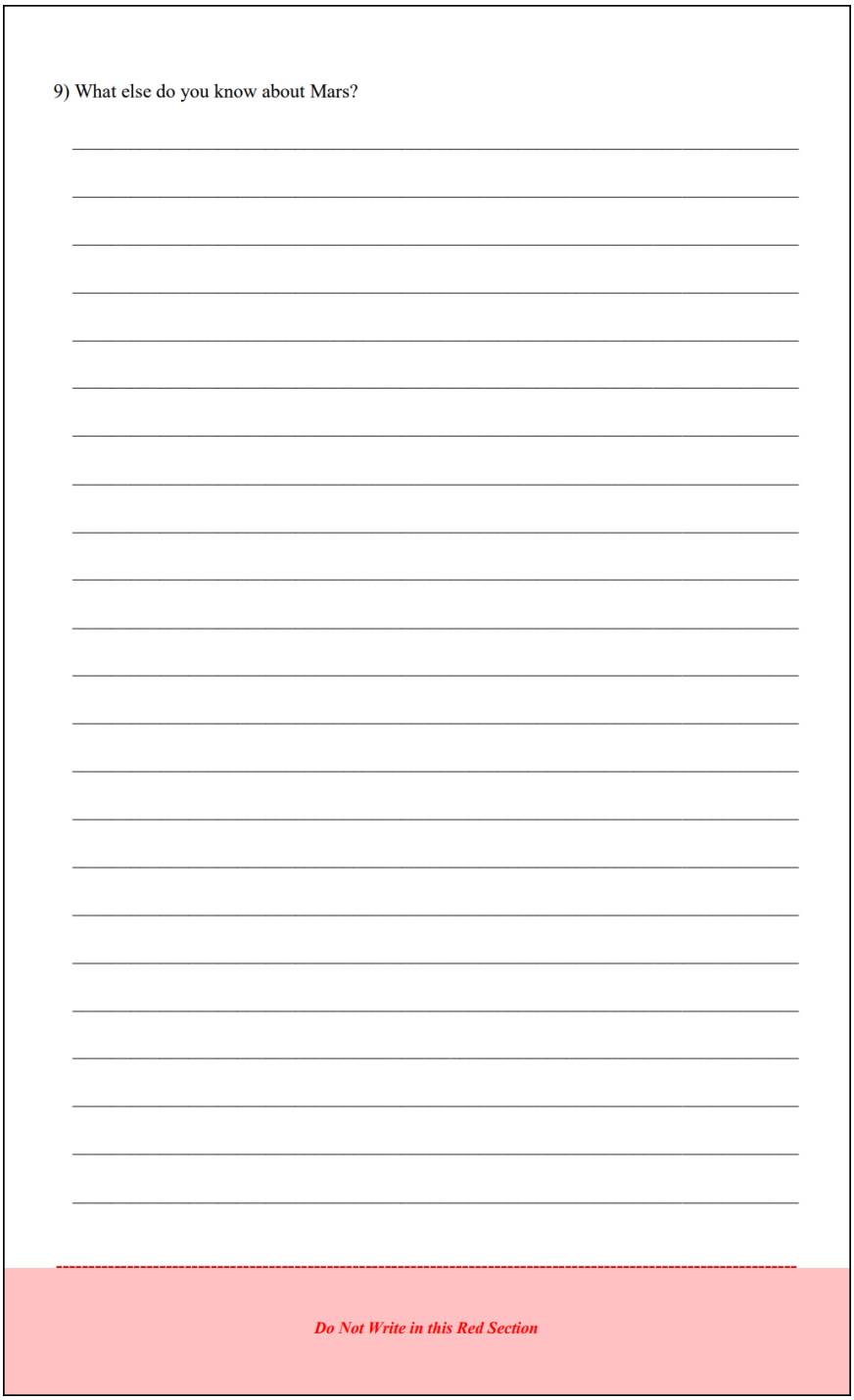

Figure F.2. Assessment study: pre-test page #2.

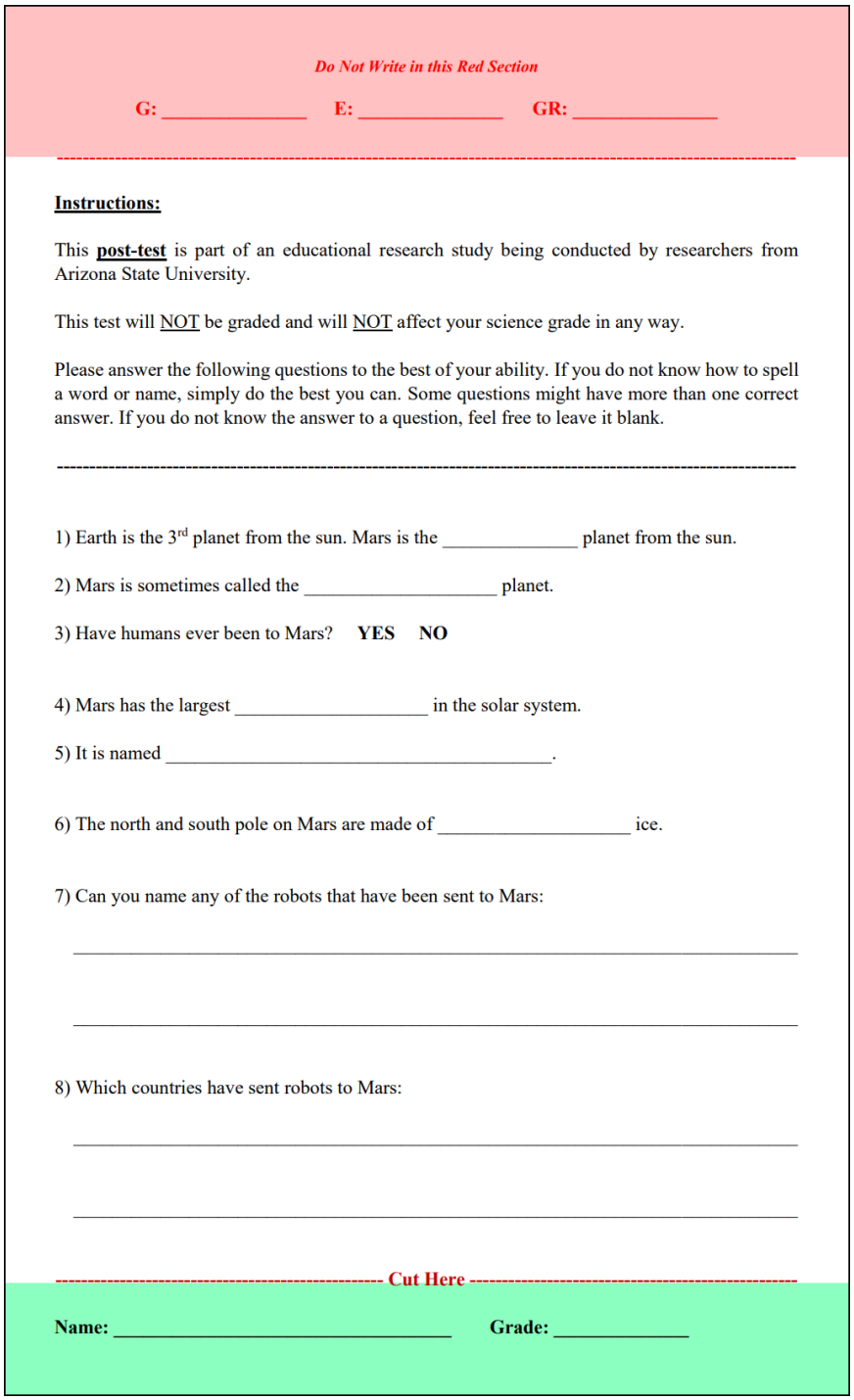

Do Not Write in this Red Section

G: _____ **E:** _____ **GR:** _____

Instructions:

This **post-test** is part of an educational research study being conducted by researchers from Arizona State University.

This test will NOT be graded and will NOT affect your science grade in any way.

Please answer the following questions to the best of your ability. If you do not know how to spell a word or name, simply do the best you can. Some questions might have more than one correct answer. If you do not know the answer to a question, feel free to leave it blank.

---

1) Earth is the 3rd planet from the sun. Mars is the _____ planet from the sun.

2) Mars is sometimes called the _____ planet.

3) Have humans ever been to Mars? **YES** **NO**

4) Mars has the largest _____ in the solar system.

5) It is named _____.

6) The north and south pole on Mars are made of _____ ice.

7) Can you name any of the robots that have been sent to Mars:

_____

_____

8) Which countries have sent robots to Mars:

_____

_____

---------- Cut Here ----------

Name: _____ **Grade:** _____

Figure F.3. Assessment study: post-test page #1.

9) What else did you learn about Mars while exploring the Giant Mars Map?

_____

_____

_____

_____

_____

_____

_____

_____

10) On the Giant Mars Map, what did the colors represent? _____

a) What did **red** represent? _____

b) What did **green** represent? _____

c) What did **blue** represent? _____

d) What did **white** represent? _____

e) What did **purple** represent? _____

11) What did you **like** about the Giant Mars Map?

_____

_____

12) What did you **dislike** about the Giant Mars Map?

_____

_____

Do Not Write in this Red Section

Figure F.4. Assessment study: post-test page #2.

APPENDIX G

"WALK ON MARS" ASSESSMENT STUDY – TOUR OUTLINE

G.1 Introduction

- Tour guide introduction
- Ask students to remove their shoes (keep socks on)
- Invite students to step onto the edge of the map

G.2 Stop #0: Colorized Topography

- Ask students what the map colors might represent.
- Explain that even though it looks like temperature, it is actually showing elevation
- Explain that high elevations = “hot” colors, low elevations = “cold” colors
- Ask students to predict what color the highest point on Mars will be.
- Ask students to predict what color the lowest point on Mars will be.
- Ask students to find, and stand on top of, the highest point on Mars.

G.3 Stop #1: Mount Olympus (Olympus Mons)

- Students will likely stand on one of the Tharsis volcanoes
- Explain that the Tharsis volcanoes are the four highest mountains on Mars, but that Mount Olympus is the tallest
    - Use the English version of the Latin names, to avoid confusion on the post-test
- Ask students to stand in a large circle around Mount Olympus so everyone can easily see it
- Ask the students if they know the name of the tallest mountain on Earth.

- Explain that Mount Olympus is ~2.5x as tall as Mount Everestt and is the tallest mountain/volcano in the solar system
    - Older students might know that Mauna Kea is actually the tallest mountain on Earth from base to summit. If they know this, explain that they're technically correct and that Mount Olympus is almost twice as tall as Mauna Kea. If they don't know this, don't mention Mauna Kea since explaining the difference with Mount Everest might introduce too much confusion and save for a later class.
- Explain that major features on Mars are named after gods and places from mythology, primarily Greek and Roman mythology
    - In Greek mythology, the gods lived on Mount Olympus, so it seemed like an appropriate name for the tallest mountain in the Solar System
- Explain that Mount Ascraeus, Mount Pavonis, and Mount Arsia are "smaller" and only ~2x the height of Mount Everest
- Ask students to now find, and stand on top of, the lowest point on Mars.

G.4 Stop #2: Hellas Basin

- Students will likely stand somewhere in Hellas Basin, but direct their attention to the absolute lowest point: Badwater Crater
- Ask students to stand in a large circle on the edge of Hellas Basin so that everyone can see the entire feature
- Explain that "Hellas" is the ancient Greek name for Greece (connection with Greek mythology)
- Ask the students what might have created such a large "hole" in Mars.

- Direct the students' attention to the many smaller craters at their feet, and explain that they were all made by asteroids/comets colliding with Mars over ~4.5 billion years
- Explain that Hellas is approximately the same width as the continental U.S.
- Explain that Hellas is approximately as deep as Mount Everest is tall
- Explain that the asteroid that hit Mars and created Hellas would have been VERY big
- Ask students to raise their hand if they've been to the Grand Canyon
- Ask students to find the "Grand Canyon of Mars"
    - many should realize they already walked over it on their way between Mount Olympus and Hellas Basin

G.5 Stop #3: Mariner Valley (Valles Marineris)

- Most students should return to various parts of Mariner Valley
- Ask student to form a large oval along the length of Mariner Valley proper, so everyone can see the entire feature
- Explain that Mariner Valley (from Noctis Labyrinthus to Aurorae Chaos) is approximately the length of the continental U.S., and that Mariner Valles (arguably) continues all the way to Chryse Planitia
- Explain that Mariner Valley is one of the few major Mars features not named after mythology; instead it is named after Mariner 9, the spacecraft that discovered it (it's too thin to see using telescopes on Earth)
- Ask student again to raise their hand if they've been to the Grand Canyon

- Explain that the Earth's Grand Canyon is the size of one of the small side canyons surrounding the rim of Mariner Valley
- Ask students what created the Earth's Grand Canyon (water erosion)
- Ask students to guess what might have created Mariner Valley
    - Explain that the lower part of Mariner Valley was likely formed by flowing water, but not the main section
    - Explain that Mariner Valley is like the Great Rift Valley in Africa, where the crust tried to break apart, but as Mars cooled, the process slowed until it stopped short of breaking the crust into plates
- Ask students to walk to the small circular maps on the side of the main map

G.6 Stop #4: North and South Poles

- Ask students to guess what the circular maps represent
    - Students usually guess that they are the north and south pole fairly quickly
- Ask students why the poles are shown in separate maps
    - Students usually don't guess correctly
    - Ask students why Greenland appears artificially big in world maps
    - Explain that similar polar distortions are present on the Mars map
    - Show students the edge of the main Mars map and how stretched it is
    - Explain that the polar maps are shown as if viewing a globe from above each pole, to help correct for the map distortions
    - Point out which map is the north pole and which map is the south pole
- Ask students to re-state what the map colors represent

- Ask students what the large “mountains” in both maps are
- If students don’t guess polar ice, ask them what is at the Earth’s poles, and explain that the “mountains” are giant mounds of ice
- Explain that the polar ice on Mars isn’t water ice, and ask what other types of ice exist
- Students usually guess “dry ice”, but then ask what dry ice is actually made of
    - Explain that Mars is so cold that even the carbon dioxide in the air freezes

G. 7 Stop #5: Jezero Crater

- Ask students to follow you to Jezero Crater on the main map and then form large circle around the small (temporary) star sticker within Jezero Crater
- Explain that Mars is the only planet in the solar system completely inhabited by robots, with a population of four: 3 American robots and 1 Chinese robot
- Explain that the U.S.’s newest robot landed in the small, indistinct Jezero Crater because we think it used to be a lake
- Explain that there is a small river channel that flows into the crater and forms a delta, which is a good place to search for preserved evidence of life
- State that Perseverance landed in Jezero Crater in February, 2021
- Explain that Perseverance is so large that it can’t use solar arrays, and instead has a small nuclear reactor on the back of it
- Explain that in addition to searching for life, Perseverance is going to collect ~30 rock samples the size of a pinky finger, which a future mission is going to

bring back to Earth, since we can study the rocks much better in our labs on Earth

- Add that Perseverance actually has a sort of “baby” robot, the Mars helicopter Ingenuity
- Explain that Ingenuity was supposed to only fly 4-5 times and prove that we could successfully fly on Mars, but it has worked so well, that it has flown over 13 times and is now acting as a scout for Perseverance

G.8 Stop #6: Gale Crater

- Ask the students to walk to Gale Crater with you, and then form a large circle around the small (temporary) star sticker within Gale Crater
- Explain that NASA’s other Mars rover, Curiosity, is a twin of Perseverance and landed in Gale Crater in August 2012
- Explain that Curiosity went to Gale because we also think it used to be a lake
    - Curiosity found lots of evidence of water at the bottom of the crater
- Explain that Curiosity has slowly been climbing the mountain in the middle of Gale Crater, investigating each rock layer as it goes, which is telling us about the past climate of Mars
- Point out that Curiosity has a neighbor on Mars, the InSIGHT lander

G.9 Stop #7: Elysium Planitia

- Ask students to shift their circle to center it on the small (temporary) star sticker to the northwest of Gale Crater

- Explain that unlike the other robots currently on Mars, InSIGHT is a lander, which doesn't move from the place where it landed
    - This is because InSIGHT has to stay very still to make measurements with its seismometer
- Ask the students what a seismometer measures
    - They will likely not know, so give them the clue that there are lots of seismometers in California
    - If they don't guess it relatively quickly, explain that seismometers measure the shaking from Earthquakes
- Explain that because InSIGHT is on Mars, it is actually measures the shaking from Mars-quakes
    - Students tend to find the idea of "Marsquakes" interesting, so put some emphasis on explaining it
- Explain that Marsquakes are very weak, and they would probably just barely feel the strongest Marsquake that InSIGHT has ever felt
- Explain that by measuring the Marsquakes, InSIGHT has found that Mars has layers just like the Earth (crust, mantle and core), but that Mars' core is unusually large for such a relatively small planet
- Tell the students that there is one more robot currently exploring Mars

G.10 Stop #8: Southern Utopia Planitia

- Ask the students to follow you to the small (temporary) star in southern Utopia Planitia, roughly halfway between InSIGHT and Perseverance

- Explain that this fourth Mars robot was sent by China, and they were able to successfully land on their very first attempt
- Add that the rover is named Zhurong, after one of the fire gods in ancient Chinese mythology
- Explain that Zhurong is about half the size of Curiosity and Perseverance and is 100% solar powered
- Explain that Zhurong's mission is to study water ice that is under the surface, using its radar instrument
    - Add that most of the blue area surrounding Zhurong's landing site has water ice under the surface, but we're not sure exactly how deep it is, which will be important to know if we send humans to Mars, so they can dig up the water and use it while on Mars

G.11 Question and Answer Session

- Ask students if they have any questions about Mars, either the places visited on the tour or about Mars in general
    - Answer the student questions as best you can

G.12 Conclusion

- Ask students to return to the edge of the map and put their shoes back on

APPENDIX H

“WALK ON MARS” ASSESSMENT STUDY – PRE-TEST RUBRIC

H.1 Basic Mars Questions Grading Instructions:

- Only the eight basic Mars questions will be graded, with each one worth 1 point
- Students may choose to not respond to questions, which simply results in 0 points
- Some questions have multiple correct answers, all worth 1 total point
- Incorrect spelling is acceptable, as long as it is close enough to interpret

---

1) Earth is the 3rd planet from the sun. Mars is the ____3rd____ planet from the sun.

2) Mars is sometimes called the ____Red____planet.

3) Have humans ever been to Mars? **YES** (**NO**)

4) Mars has the largest ____mountain / volcano / canyon____ in the solar system.

5) It is named ____Mount Olympus / Mariner Valley____.

6) The north and south pole on Mars are made of ____dry / CO_2 / carbon dioxide____ice.

7) Can you name any of the robots that have been sent to Mars:

____Zhurong, Perseverance, Ingenuity, InSIGHT, Curiosity, Phoenix, Spirit____

____Opportunity, Pathfinder/Sojourner, Viking 1 & 2____

____(any orbiters and unsuccessful landers also count)____

8) Which countries have sent robots to Mars:

____U.S.A., China, USSR/Russia, Europe/ESA____

____(orbiter-only countries also count) India, UAE, Japan____

APPENDIX I

"WALK ON MARS" ASSESSMENT STUDY – POST-TEST RUBRIC

I.1 Basic Mars Questions Grading Instructions:

- Only the eight basic Mars questions will be graded, with each one worth 1 point
- Students may choose to not respond to questions, which simply results in 0 points
- Some questions have multiple correct answers, all worth 1 total point
- Incorrect spelling is acceptable, as long as it is close enough to interpret

---

1) Earth is the 3rd planet from the sun. Mars is the ____3rd____ planet from the sun.

2) Mars is sometimes called the ____Red____planet.

3) Have humans ever been to Mars? **YES** (**NO**)

4) Mars has the largest ____mountain / volcano / canyon____ in the solar system.

5) It is named ____Mount Olympus / Mariner Valley____.

6) The north and south pole on Mars are made of ____dry / CO_2 / carbon dioxide____ice.

7) Can you name any of the robots that have been sent to Mars:

____Zhurong, Perseverance, Ingenuity, InSIGHT, Curiosity, Phoenix, Spirit____

____Opportunity, Pathfinder/Sojourner, Viking 1 & 2____

____(any orbiters and unsuccessful landers also count)____

8) Which countries have sent robots to Mars:

____U.S.A., China, USSR/Russia, Europe/ESA____

____(orbiter-only countries also count) India, UAE, Japan____

I.2 Topography Questions Instructions:

- Topography questions will be graded separately
- Students may choose to not respond to questions, which simply results in 0 points
- Some questions have multiple correct answers, all worth 1 point
- Incorrect spelling is acceptable, as long as it is close enough to interpret
- Wording may vary as long as relative relationships are correct

---

10) On the Giant Mars Map, what did the colors represent?

____elevation, height, altitude, topography____

a) What did **red** represent? ____high____

b) What did **green** represent? ____average____

c) What did **blue** represent? ____low____

d) What did **white** represent? ____very high____

e) What did **purple** represent? ____very low____